Title	Poleward transport of Circumpolar Deep Water off East Antarctica
Author(s)	山崎, 開平; Yamazaki, Kaihe
Degree Grantor	北海道大学
Degree Name	博士(環境科学)
Dissertation Number	甲第14766号
Issue Date	2022-03-24
DOI	https://doi.org/10.14943/doctoral.k14766
Doc URL	https://hdl.handle.net/2115/87076
Type	doctoral thesis
File Information	YAMAZAKI_Kaihe.pdf

Poleward transport of Circumpolar Deep Water off East Antarctica

Kaihe Yamazaki

Graduate School of Environmental Science

Hokkaido University

A thesis submitted for the degree of

Doctor of Philosophy

February 2022

Supervised by Prof. Shigeru Aoki

Poleward transport of Circumpolar Deep Water off East Antarctica

Kaihe Yamazaki (Institute of Low Temperature Science, Hokkaido University)

Circumpolar Deep Water (CDW) is the primary source of heat and salt for the Antarctic coast. In the meridional overturning circulation, the poleward CDW flux compensates for equatorward transport of Antarctic Surface and Bottom Waters. The onshore CDW intrusion is the leading cause of the accelerated ice shelf melting in West Antarctica. Meanwhile, in East Antarctica, stronger winds facilitate intensive sea ice production along the coast, and the onshore CDW flux interacts with both glacial melt and bottom water production. Our understanding of the ocean–atmosphere–cryosphere interaction is framed by the knowledge on deep ocean circulation, which governs the fate of CDW. However, the ocean circulation structure over the Antarctic margin, particularly to the south of the Antarctic Circumpolar Current, has been unconstrained because of in-situ data scarcity and inter-model discrepancy.

In this dissertation, I present a series of observational analyses focusing on the poleward transport of CDW off East Antarctica, including a ground-breaking finding on the deep ocean circulation in the Antarctic margin. Most of the description is based on compilations of in-situ data from ship, float, and biologging measurements, part of which I subjected by participating in research cruise or devising a novel utilization. Three key points follow: 1) the continental slope topography is essential for the poleward CDW flux as steering the structure of subpolar subgyres, 2) the isopycnal eddy advection achieves the cross-slope CDW transport, and 3) multidecadal variability of the poleward CDW flux is associated with the barotropic change of the Antarctic Circumpolar Current, the baroclinic change of the meridional overturning circulation, and the variability of the Antarctic Slope Current. These findings suggest that topography and isopycnal diffusion regulate the onshore CDW intrusion, providing a physical oceanography basis for the multidecadal-to-centennial climate projection, in which intensification of Southern Hemisphere westerlies is a dominant climatological driver.

TABLE OF CONTENTS

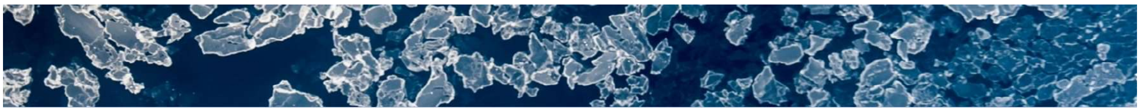

(This page is intentionally set blank)

INTRODUCTION

Deep poleward transport

Circumpolar Deep Water (CDW) is a warm, saline water mass that exists in the depths of the Southern Ocean. CDW is a mixture of deep waters from the Atlantic, Pacific, and Indian Oceans, each advected poleward in the global meridional overturning circulation (Fig. 1; Talley, 2011). Upper CDW, branching to the upper overturning cell, is marked as the oxygen minimum layer by its water age, and lower CDW of the lower overturning cell is marked as the salinity maximum layer (Fig. 2; Marshall and Speer, 2012). Particularly in the Antarctic continental margin, CDW is a major source of heat and salt, and is therefore of crucial climatological importance (Fig. 3; modified from Rintoul, 2018).

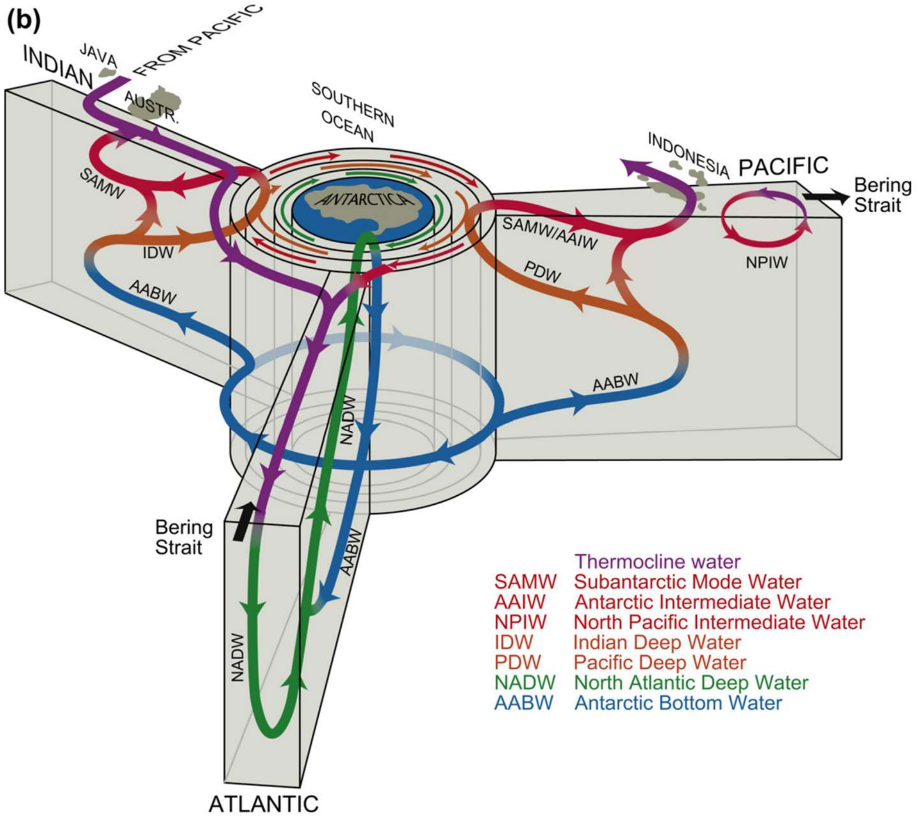

Figure 1. Global overturning circulation from a Southern Ocean perspective. Based on Lumpkin and Speer (2007).

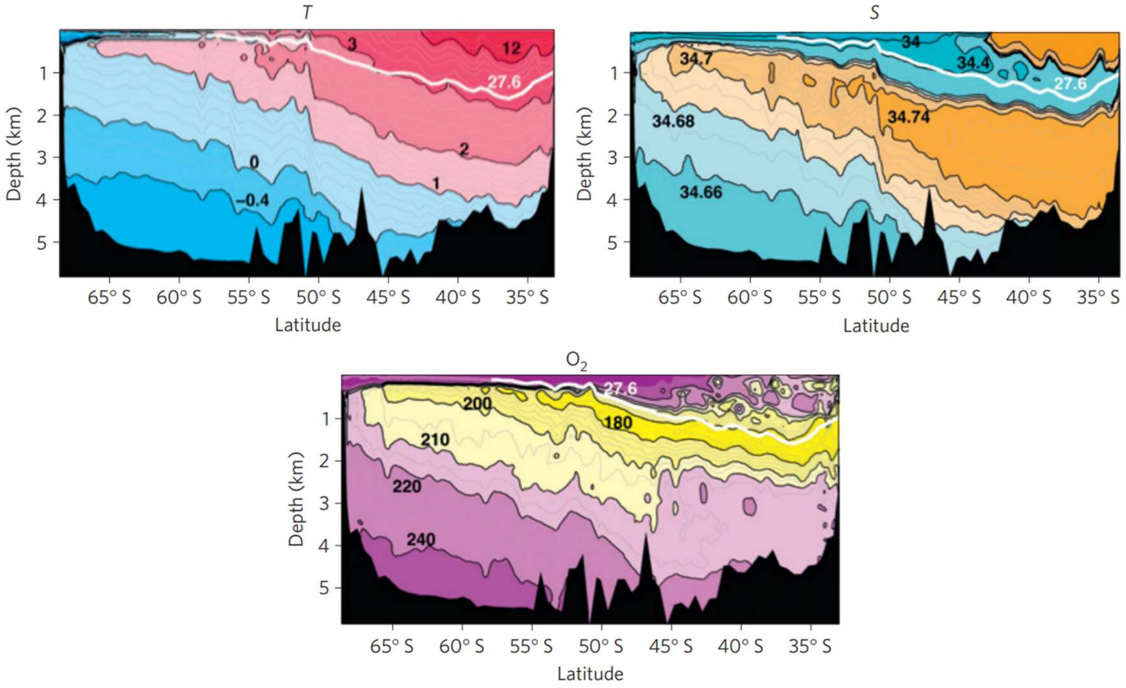

Figure 2. T (temperature), S (salinity), and O_2 sections along 30°E cutting across the ACC from Africa towards Antarctica. Black contours are labelled in°C for T, practical salinity unit for S and µmol kg^{-1} for O_2. The thick white line is the 27.6 kg m^{-3} potential density.

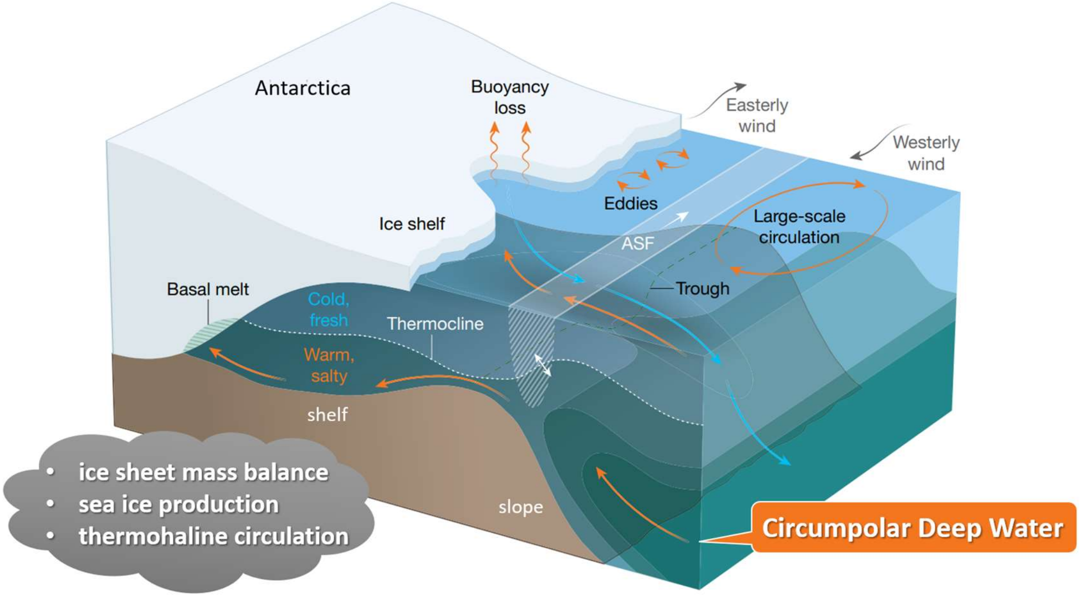

Figure 3. CDW intrusion towards the Antarctic continental margin. Physical processes that control the CDW transport from the open ocean to the base of the floating ice shelves are crucial for land ice melting, sea ice production, and bottom water formation.

Most area of the Southern Ocean is occupied by the Antarctic Circumpolar Current (ACC; Fig. 4). The ACC has a long history of study over the past 80 years, particularly in terms of its pivotal role in the global ocean circulation and the dynamics of eddy-mean flow interactions (e.g., Deacon, 1937; Munk and Palmén, 1951; Hidaka and Tsuchiya, 1953), and its dynamics remains the cutting-edge problem at present among the school of physical oceanography (e.g., Marshall and Radko, 2003; Ferrari and Nikurashin, 2010; Stewart and Hogg, 2017). To the Antarctic margin, the formation of Antarctic Bottom Water and the existence of the westward flowing Antarctic Slope Current (ASC) have also been known (e.g., Gill, 1973; Foster and Carmack, 1976). On the other hand, how the ACC connects with the ASC and how offshore CDW is transported towards Antarctica have been documented since the beginning of this century (e.g., Speer et al., 2000).

The southernmost extent of the ACC, the poleward limit of the oxygen-depleted upper CDW, is the Southern Boundary (SB; Orsi et al., 1995), which separates the offshore ACC from the inshore ASC. My investigation goes into the SB's vicinity, that is, the transition zone from the ACC to the ASC, properly corresponding to the subpolar gyre. In addition, I target the area off East Antarctica facing the Indian Ocean. One of the characteristics of the Indian Ocean sector is the narrow intervals between the ACC and the continent (Fig. 4), somewhat analogous to the Amundsen Basin in the Pacific Ocean sector. The Indian Ocean sector is less observed than the Ross Sea and Weddell Sea off West Antarctica due to its geographically remote location from the other continents and persistent sea ice conditions, leading to a lack of knowledge.

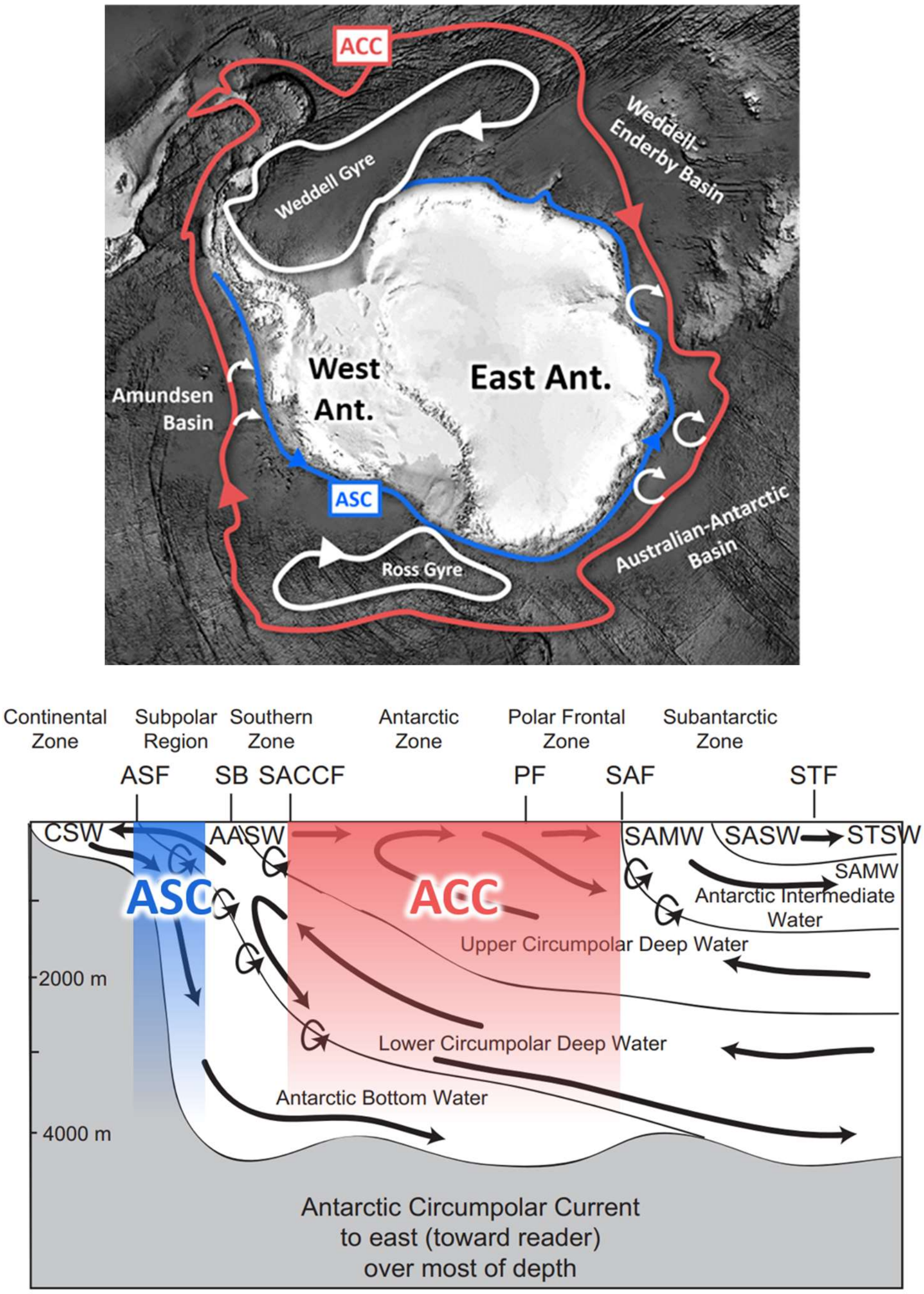

Figure 4. Horizontal (upper) and vertical (lower) structures of the ACC and the ASC. The lower panel is modified from Talley (2011), after Speer et al. (2000). ACC is majorly composed of three dynamical fronts: the Subantarctic Front (SAF), the Polar Front (PF), and the Southern ACC Front (SACCF; highlighted in upper panel). The Southern Boundary (SB) is the poleward limit of the ACC and the upper meridional overturning cell and separates offshore ACC from inshore ASC. The SACCF in the upper panel is based on Orsi et al. (1995), and the ASC is based on Thompson et al. (2018). White vectors represent the subpolar gyre.

Deep layers of the Southern Ocean have experienced gradual warming over decades (Fig. 5; Sallée, 2018), with a slightly higher rate in the Indian Ocean sector (Schmidtko et al., 2014; Kim and Orsi, 2014; Auger et al., 2021). It is suspected that the long-term change is caused by, via Ekman dynamics, strengthening of westerly winds in the southern hemisphere associated with ozone depletion and warming of the tropical troposphere (Pörtner et al., 2018). However, the exact oceanic response associated with the current and water mass changes has been unconstrained. The mechanism at play of the subpolar CDW warming is particularly arguable.

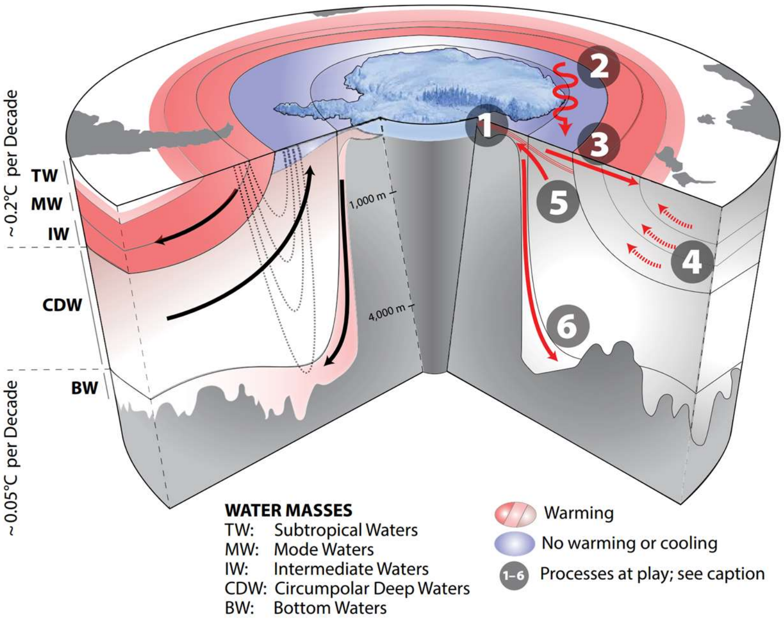

Figure 5. Schematic showing temperature trends in different layers of the Southern Ocean. The layers are defined as main water masses of the Southern Ocean: Subtropical Water (TW), Mode Water (MW), Intermediate Water (IW), Circumpolar Deep Water (CDW), and Bottom Water (BW). Black arrows show the main overturning pathways in the basin, and the dashed black contours show a vertical slice of the deep-reaching Antarctic Circumpolar Current circulating clockwise around the Antarctic continent. The red arrows and associated numbers represent processes at play in the warming of the Southern Ocean: 1) increased surface stratification and shallowing of CDW layer, 2) increased heat uptake in the subpolar basins, 3) increased northward heat transport associated with increased subpolar heat uptake, 4) reduced eddy-mediated southward heat transport at the northern flank of the ACC, 5) intrusion of CDW onto the continental shelves, and 6) warming of the bottom water ventilating the abyssal ocean.

Melting of the Antarctic ice sheet has incentivized studies on the CDW behavior. Over the past decades, a large amount of glacial melt has been observed in West Antarctica facing the Amundsen Sea of the Pacific Ocean sector (Fig. 6; Smith et al., 2020). Rapid melting has also been observed in parts of East Antarctica including Wilkes Land, to which the Totten Glacier encatchment belongs. The importance of East Antarctica lies in its potential: melting of the Wilkes Land would cause a 4-meters global sea-level rise (Pelle et al., 2021), which is as much as the potential sea-level rise by the entire West Antarctic melt. Since changes in the oceanic heat flux are primarily responsible for the ice sheet mass balance, understanding dynamics of the deep ocean circulation that governs the fate of CDW is essential for predicting global climate in the upcoming centuries.

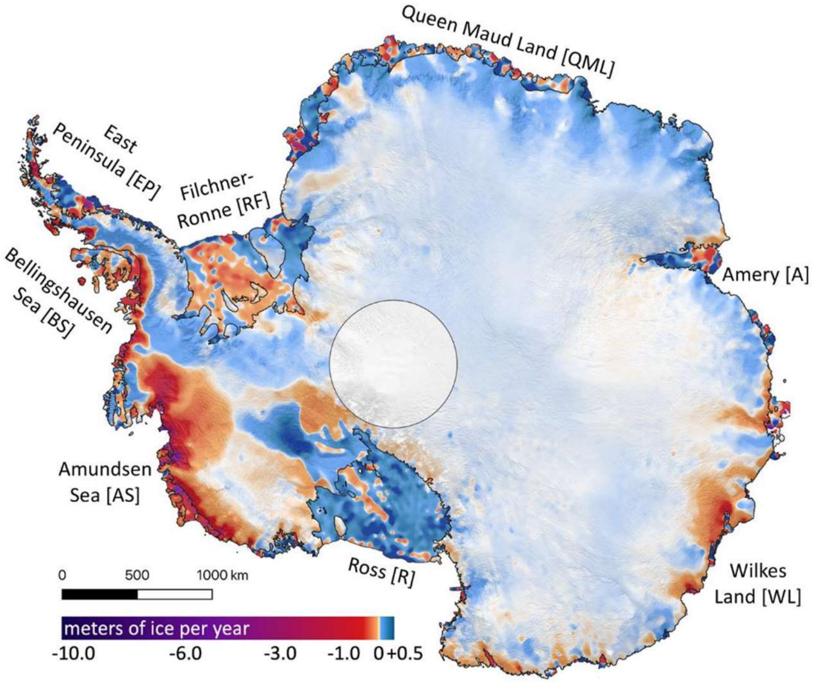

Figure 6. Mass loss from Antarctica from 2003 to 2019 based on satellite laser altimetry.

Recent advent of observational techniques and high-resolution numerical simulation updated the picture of the Southern Ocean circulation. Especially, profiling floats and biologging can exert an understanding of the ocean interior, which is partially covered by sea ice. Sophisticated use of satellite altimetry makes it possible to capture the spatial variation of ocean topography over the seasonal ice zone. Synthesizing them with the latest hydrography and a historical data inventory, the pathway and the mechanism of poleward CDW transport can be disclosed.

The thesis is comprised of the following chapters. The structure of the subpolar gyre as a prominent agent of CDW transport in this region is described in Chapter 1. Multidecadal variability from the 1990s to 2010s is highlighted in Chapter 2, in which the causes of the CDW warming are investigated. Chapter 3 further describes the oceanic structure over the continental slope, in which the ASC can be an obstacle for the onshore CDW intrusion. Chapter 4 quantifies the eddy diffusion of deep water using historical hydrographic data. What is common in these studies is that the analysis and discussion are based on in-situ observations.

References

Auger, M., Morrow, R., Kestenare, E., Sallée, J.-B., and Cowley, R. (2021). Southern Ocean in-situ temperature trends over 25 years emerge from interannual variability. *Nature Communications*, 12(1), 514.

Deacon, G. E. R., (1937). The hydrology of the Southern Ocean. *Discovery Reports*, 15, 1 124.

Ferrari, R., and Nikurashin, M. (2010). Suppression of eddy diffusivity across jets in the Southern Ocean. *Journal of Physical Oceanography*, 40(7), 1501–1519.

Foster, T. D., and Carmack, E. C. (1976). Frontal zone mixing and Antarctic Bottom water formation in the southern Weddell Sea. *Deep-Sea Research and Oceanographic Abstracts*, 23(4), 301–317.

Gill, A. E. (1973). Circulation and bottom water production in the Weddell Sea. *Deep-Sea Research and Oceanographic Abstracts*, 20(2), 111–140.

Hidaka, K., Tsuchiya, M. (1953). On the Antarctic Circumpolar Current. *Journal of Marine Research*, (12), 214–222.

Kim, Y. S., and Orsi, A. H. (2014). On the variability of antarctic circumpolar current fronts inferred from 1992-2011 altimetry. *Journal of Physical Oceanography*, 44(12), 3054–3071.

Lumpkin, R., and Speer, K. (2007). Global ocean meridional overturning. *Journal of Physical Oceanography*, 37(10), 2550–2562.

Marshall, J., and Radko, T. (2003). Residual-mean solutions for the Antarctic Circumpolar Current and its associated overturning circulation. *Journal of Physical Oceanography*, 33(11), 2341–2354.

Marshall, J., and Speer, K. (2012). Closure of the meridional overturning circulation through Southern Ocean upwelling. *Nature Geoscience*, 5(3), 171–180.

Munk, W. H., and Palmén, E. (1951). Note on the Dynamics of the Antarctic Circumpolar Current. *Tellus*, 3(1), 53–55.

Orsi, A. H., Whitworth, T., and Nowlin, W. D. (1995). On the meridional extent and fronts of the Antarctic Circumpolar Current. *Deep-Sea Research Part I*, 42(5), 641–673.

Pelle, T., Morlighem, M., and McCormack, F. S. (2020). Aurora Basin, the Weak Underbelly of East Antarctica. *Geophysical Research Letters*, 47(9).

Pörtner, H. O., Roberts, D. C., Masson-Delmotte, V., Zhai, P., Tignor, M., Poloczanska, E., and Weyer, N. M. (2019). The ocean and cryosphere in a changing climate. *A Special Report of the Intergovernmental Panel on Climate Change*.

Rintoul, S. R. (2018). The global influence of localized dynamics in the Southern Ocean. *Nature*, 558(7709), 209–218.

Sallée, J. B. (2018). Southern Ocean warming. *Oceanography*, 31(2 Special Issue), 52–62.

Schmidtko, S., Heywood, K. J., Thompson, A. F., and Aoki, S. (2014). Multidecadal warming of Antarctic waters. *Science*, 346(6214), 1227–1231.

Smith, B., Fricker, H. A., Gardner, A. S., Medley, B., Nilsson, J., Paolo, F. S., et al. (2020). Pervasive ice sheet mass loss reflects competing ocean and atmosphere processes. *Science*, 368(6496), 1239–1242.

Speer, K., Rintoul, S. R., and Sloyan, B. (2000). The diabatic Deacon cell. *Journal of Physical Oceanography*, 30(12), 3212–3222.

Stewart, A. L., and Hogg, A. M. C. (2017). Reshaping the Antarctic Circumpolar Current via Antarctic Bottom Water export. *Journal of Physical Oceanography*, 47(10), 2577–2601.

Talley, L. D. (2011). Descriptive physical oceanography: an introduction. *Academic press*.

Thompson, A. F., Stewart, A. L., Spence, P., and Heywood, K. J. (2018). The Antarctic Slope Current in a Changing Climate. *Reviews of Geophysics*, 56(4), 741–770.

(This page is intentionally set blank)

1

STRUCTURE OF THE SUBPOLAR GYRE

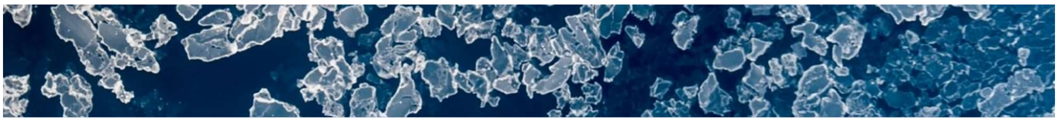

Abstract

The climatological structure of the subpolar cyclonic circulation off East Antarctica is delineated with Argo float data from the past decade. Up to 40% of the float profiles in the seasonal ice zone have been without satellite-positioning. We refined their position data as following the bathymetry to get appropriate positions in the continental margin. The error of the terrain-following interpolation was estimated by using positioned data to be 23 ± 27 (78 ± 70) km for 90 (390) day period. Profiles with the under-ice period shorter than 360 days are adopted. The float trajectories reveal the extent of the subpolar gyre adjoined to the westward Antarctic Slope Current to its south and the southernmost eastward jet of the Antarctic Circumpolar Current along 4,000 m isobath to its north. The subpolar circulation in the Australian-Antarctic Basin comprises of a series of quasi-barotropic "subgyre" circulations, which are bounded by bathymetric spurs in the continental slope. The temperature field reveals shoreward excursions of Circumpolar Deep Water (CDW) associated with the subgyres, effectively supplying heat to the continental shelves. An along-slope temperature variation up to 1°C in 27.7-27.8 kg/m^3 σ_θ indicates an active cross-slope exchange within the layer. Provided the velocity field and the water mass structure, the subsurface water mass exchange is likely accomplished by a combination of topographically-controlled mean flow and the eddy transports. Our findings suggest that the bathymetry primarily determines the structure of the subpolar gyre.

1.1 Background

The basin-scale circulation in the Antarctic continental margin is outlined by the eastward-flowing Antarctic Circumpolar Current (ACC, e.g., Orsi et al., 1995) to the north and the westward-flowing Antarctic Slope Current (ASC, e.g., Jacobs, 1991) to the south. Between the ACC and the ASC, clockwise subpolar gyres commonly exist. The southern boundary of ACC (SB, henceforth) is defined as the poleward limit of the upper core of Circumpolar Deep Water (CDW), which marked by the oxygen minimum layer (Orsi et al., 1995; hereinafter OWN95). The SB generally exists around the northern flank of subpolar gyres. Subpolar gyres are of paramount importance since they separate cold shelf water from offshore CDW, controlling heat intrusion onto the continental shelves.

The Weddell and Ross Gyres are archetypes of subpolar gyres, which are primarily shaped by the bathymetric features in the Weddell-Enderby Basin and the Southwest Pacific Basin, respectively (e.g., Gordon et al., 1981 Gouretsky, 1999). In contrast to these two gyres, the subpolar circulation off East Antarctica (from 50°E to 160°E in the Indian Ocean sector; Fig. 1) is not as evident, reflecting the proximity of the ACC to the continental shelves in the region. Satellite altimetry first revealed the basin-wide cyclonic circulations zonally split by the Kerguelen Plateau (Park and Gamberoni, 1995). To the east of the Kerguelen Plateau, Bindoff et al. (2000) proposed the presence of a clockwise circulation in the Australian-Antarctic Basin (AAB) spanning from 90°E to 120°E, based on systematic hydrographic sections of the Baseline Research on Oceanography, Krill and the Environment (BROKE) survey. The subpolar gyre in the AAB has occasionally been referred to as the Kerguelen Gyre (e.g., Kusahara and Hasumi, 2014; Rodehacke et al., 2007). McCartney and Donohue (2007) later presented a strong transport of the subpolar gyre in the AAB with a deeply-rooted barotropic flow based on the World Ocean Circulation Experiment hydrographies. To the west of the Kerguelen Plateau, a mid-sized cyclonic circulation has been reported in and off the Prydz Bay, referred to as the Prydz Bay Gyre (Heywood et al., 1999; Meijers et al., 2010; Smith et al., 1984). Aoki et al. (2010) reported a circulation pattern implicated by eddy-resolving simulation and iceberg trajectories, which is consistent with that reported by Bindoff et al. (2000) and McCartney and Donohue (2007), with a westward extension beyond the Princess Elizabeth Trough and into the Prydz Bay Gyre.

Some critical information is lacking about the structure of the subpolar gyre in the AAB. First, the gyre has not been delineated within the context of the cross-slope water exchange. Provided the quasi-barotropic nature of the circulation, we can expect that the topographic feature strongly influences the subpolar gyre and the associated water transport. Second, the spatial extent of the subpolar circulation has been unclear. Its zonal extent of the clockwise circulation is inconsistent among observation-based studies (Bindoff et al., 2000; McCartney and Donohue, 2007). Further, its meridional extent is also arguable, even though it would define the northern boundary of the gyre. The poleward extent of the ACC relates to the position of the southern ACC front (sACCf), which is one of three distinctive frontal features of the ACC just north of the SB (e.g., Orsi et al., 1995). The sACCf bifurcates due to the constriction of the Kerguelen Plateau (Sokolov and Rintoul, 2007), and its main stream is considered to be located far offshore of the gyre with its southern limit at 62°S in the AAB (Kim and Orsi, 2014). Both satellite altimetry and in-situ current measurements are required to capture the circulation because the SB is originally a boundary of upper CDW (Orsi et al., 1995), and a geostrophic shear maximum does not necessarily accompany with it. Although Bindoff et al. (2000) suggested the clockwise circulation by acoustic Doppler current profiler measurements, their description highly relies on snapshots to the south of 63°S.

The cross-slope water exchange is fundamental for the Antarctic coastal environment since it regulates the shoreward heat/salt flux through the CDW intrusion (e.g., Thompson et al., 2018). The oceanic heat is responsible for the ice sheet mass loss, which leads to freshwater discharge (e.g., Aoki et al., 2017; Brown et al., 2014), modification of bottom water production (e.g., Snow et al., 2016; Van Wijk and Rintoul, 2014), and sea-level rise (e.g., Purkey and Johnson, 2013; Rye et al., 2014). The West Antarctic Ice Sheet has experienced an accelerated mass loss since the 1990s, which is likely associated with the CDW intrusion from the Amundsen Sea (e.g., Kimura et al., 2017; Nakayama et al., 2018). Water mass distribution of coastal parts in the AAB is partly analogous to the Amundsen sector. Silvano et al. (2017) reported the similarity in the stratification between the Totten Glacier and the Pine Island Glacier ice fronts, with relatively warm modified CDW (mCDW henceforth) at the bottom. A recent study reported that the East Antarctic Ice Sheet had been a significant source in the ice sheet mass loss for the last 40 years (Rignot et al., 2019). Hence, the structure of the subpolar gyre and associated water exchange in the continental margin of the AAB needs to be scrutinized for future Antarctic thermal conditioning.

The knowledge on the circulation has been limited by the persistent sea ice within the region. For the last decade, Argo floats have greatly improved the spatial coverage of in-situ data in the seasonal ice zone. A number of Argo floats within the area are equipped with an ice-avoiding function, which stops their ascent when sea ice is expected by the temperature sensor (Klatt et al., 2007; Wong and Riser, 2011). While this protocol enables researchers to measure the CTD (conductivity, temperature, and depth) profile under sea ice, positions during the period cannot be obtained. Up to 40 % of the profiles within the seasonal ice zone in the Southern Ocean have no satellite-fixed position. A sound-tracking system can be used to track the under-ice position, and a regional array has been deployed in the Weddell Sea (Klatt et al., 2007). However, it is highly challenging to extend the system to the whole seasonal ice zone. As the number of under-ice data (without geolocations) will continue to increase, a proper way to interpolate their positions need to be discussed. The community using the under-ice data is growing (e.g., Chamberlain et al., 2018; Silvano et al., 2019; Pellichero et al., 2016; Williams et al., 2011; Wong and Riser, 2011, 2013), but its utilization remains limited despite its plentiful abundance.

This chapter is organized as follows. Section 2 provides the data information, including the treatment of the under-ice data. Section 3 illustrates the details of the subpolar gyre and the water mass distribution in the region. In Section 4, the validity of the results will be examined. A possible mechanism for water transport will be discussed here. Section 5 provides a summary and conclusion.

1.2 Data and methods

1.2.1 Environmental setting

The physical environments of the study region are first delineated. The region ranges from 30°E to 160°E and south of 60°S, off East Antarctica (Fig. 1). The Weddell and Ross Gyres are located to the west and east of the region, respectively, associated with the northward excursion of the ACC. Off East Antarctica, the Antarctic Divergence (i.e., the zero line of zonal mean wind stress; the surface wind by Large and Yeager, 2009 is adopted for Fig. 1) is located around 63°S. The Antarctic continent extends to about 66°S, and equatorward migrations of the isobaths on a spatial scale of several hundred kilometers characterize the topography of the continental margin. For clarity, the topographic spurs off the Shackleton Ice Shelf and the Cape Poinsett are referred to as the Bruce Spur (95–105°E) and the Poinsett Spur (105–120°E), respectively. The GEBCO One Minute Grid is adopted as the bathymetric dataset taking advantage of its data sources and reproducibility.

Temperature proxies for the characteristic frontal feature are introduced. The SB is defined as the 1.5°C temperature maximum based on OWN95. A proxy for the ASC axis is the 0°C isotherms at 400 dbar based on hydrographies (Bindoff et al., 2000; Whitworth et al., 1998). Since the subsurface temperature abruptly varies in a cross-isobath direction near the ASC axis (generally from -0.5 to 1°C) with a spatial scale of 50 km order, this index is not sensitive to the choice of temperature for the scale of our interest. The two proxies were derived from a climatological gridded dataset by Shimada et al. (2017; after this SAO17). The ASC axis was smoothed by a 7.5° running mean in the zonal direction. The SAO17 dataset was created from historical CTD station data, Argo data, and Nansen bottle data, and was optimally gridded with decorrelation scales deformed by the bathymetric structure. The resultant ASC axis is generally located within the 1,000-2,000 m isobaths, while the derived SB is typically located within the 3,000-4,000 m. For comparison, the SB and the sACCf presented by OWN95 are also introduced in Fig. 1.

1.2.2 Profiling floats

All float data were obtained from the Argo Global Data Assembly Center (Argo, 2018; downloaded on December 28th, 2018, from the United States Global Ocean Data Assimilation Experiment website https://www.usgodae.org/). Fig. 2a presents the distribution of all float profiles off East Antarctica from January 2007 to November 2018. CTD profiles were obtained for the pressure range of 0–2,000 dbar (including inshore profiles whose maximum pressure does not reach 2,000 dbar).

The profiles are not always accompanied by satellite-fixed positions. According to the positioning flag attached to each profile, the Argo data were categorized into two groups: accurately-positioned data and position-lacking data. The former is data with a position quality flag of either 1: Good data or 2: Probably good data, while the latter is data whose position quality flag is neither 1 nor 2 (without accurate position). Most position-lacking data are assigned linearly interpolated positions by default (with position quality flag being 8: interpolated) and are located within the seasonal ice zone.

The trajectories of Deep Argo floats are also introduced to complement the analysis. Japan Agency for Marine-Earth Science and Technology (JAMSTEC) provided the data after quality control. The parking depth of each float is 3,000 dbar (serial No. 13, 14, deployed in January 2014) or 3,500 dbar (serial No. 15, deployed in December 2014). The deep floats often obtain profiles from the sea bottom. Then, for under-ice profiles with bottom information, the latitudes were manually provided so that the sea depth matches with the seafloor, whereas the longitudes were linearly interpolated (Kobayashi, 2018).

1.2.3 Treatment of under-ice data

Conventionally, positioning for the under-ice float data is performed with linear interpolation (e.g., Wong and Riser, 2011). However, there is no guarantee that this method is always effective. On the contrary, the linear interpolation sometimes yields wrong positions, such as a trajectory crossing over the continental shelf shallower than the parking depth (triangles in Fig. 3). We introduce the terrain-following interpolation scheme, as it can yield a trajectory markedly following the isobaths (circles in Fig. 3). This scheme linearly interpolates the sea depth (instead of the distance) between two accurate positions. The procedure is detailed in Appendix A1. The terrain-following interpolation is effective near and on the continental slope because the current predominantly follows the isobath to conserve potential vorticity (PV), as was mentioned by Reeve et al. (2016) and demonstrated by Chamberlain et al. (2018). Since the present scheme is developed from the linear method, it can yield geolocations in any case even if the sea depth of one endpoint is far different from the other (i.e., the under-ice trajectory presumed to be cross-isobath), while the scheme of Chamberlain et al. (2018) needs computationally derived PV axes to intersect.

The interpolation error was evaluated for both linear and terrain-following methods by interpolation tests using the positioned data. The error is defined as the mean distance between the actual and interpolated positions during the interpolation period. Test trajectories were sampled from the positioned data with the interpolation period of 1, 3, 5, 9, 19, 29, and 39 cycles (1 cycle corresponds to 10 days), and then interpolation errors were estimated for each interpolation period. More than half of continuous sets of under-ice profiles have a duration shorter than 10 cycles. The positioned data used for the tests (total number of 4,924 casts) were chosen from the circumpolar domain south of 63°S with a sea depth shallower than 3,000 m (Fig. A2b) to focus on the interpolation errors near the continental slope, where the majority of the under-ice data are obtained.

The results of the tests are shown in Fig.s 4a and 4b (and summarized in Table A1). For both linear and terrain-following interpolations, the mean interpolation errors in longitude/latitude over the interpolation period increase as the duration of the interpolation period increases. Both methods yield almost the same errors when the interpolation period is shorter than 19 cycles; the average errors in longitude/latitude for periods shorter than 19 cycles are within 40 and 35 km for the terrain-following method and within 38 and 34 km for the linear method. The mean error of the terrain-following method becomes slightly smaller than that of the linear method for interpolation periods longer than 19 cycles; the error for the terrain-following method with the period of 39 cycles is about 93 km in longitude and 58 km in latitude, while for the linear method, the error is about 106 km in longitude and 63 km in latitude. Consequently, no significant difference in the positional error was found between the two methods. This result is probably because a considerable number of trajectories do not necessarily follow the isobaths (see also Fig. A2 for test examples). Since the terrain-following method can avoid the contradiction about the sea depths near the continental slope, which occurs at times by the linear method (Fig. 3), the terrain-following interpolation was adopted to perform the under-ice positioning in this study.

1.2.4 Data Processing

Based on the estimated positional errors with the terrain-following interpolation, the position-lacking data were categorized into three groups (Fig. 4c). Profiles with an interpolation period of 10 cycles or less were defined as “well-positioned data”; they were treated in the same way as data with the satellite-fixed position (or “accurately-positioned data”). Those with an interpolation period 36 cycles or less were defined as “mal-positioned data”; they were used only for the CTD data. Those with an interpolation period of more than 36 cycles were defined as “ill-positioned data” and were not used for any analysis. The error estimation (Fig.s 4a-b and Table A1) indicates that the well-positioned data can have errors as large as 24 ± 26 km in longitude and 22 ± 28 km in latitude (23 ± 27 km by their root-mean-square). In contrast, the mal-positioned data can have errors as large as 93 ± 84 km in longitude and 58 ± 54 km in latitude (78 ± 70 km by the root-mean-square distance). The number of profiles in each group is summarized in Table 1. Of all the position-lacking data (4,135 casts), the well-positioned data correspond to 14 %, the mal-positioned data to 72 %, and the ill-positioned data to 13 %.

The surface data were first extracted from the trajectory (not including the mal-positioned data) and CTD data (including both well-positioned and mal-positioned data). The absolute velocity at 1,000 dbar (standard parking pressure) was calculated from the float displacement during a consecutive observation cycle of 10 days simply by the change in distance over time (e.g., Lebedev et al., 2007; Ollitrault and Rannou, 2013). Besides, the geostrophic velocity from 1,000 to 50 dbar was calculated by taking the derivative of gridded surface data of the dynamic height derived from CTD data. Fig.s 2b and 2c separately show the data population for the velocity and the CTD data, respectively. A significant amount of data exists in the AAB to the east of 80°E. In those panels, suspicious positions in Fig. 2a by the linear method are absent. Rescuing the mal-positioned data substantially increases the number of data available for the analysis since most of them exist near the continental shelf covered by sea ice for a long time. The numbers of the velocity and CTD surface data are 10,946 and 13,927 points, respectively.

We performed two-dimensional gridding of the inhomogeneously distributed float data employing the radial basis function (RBF) interpolation (with a function of Scipy https://scipy.org/). This scheme approximates the best representative surface of noisy data in the least-squares sense (e.g., Vennell and Beatson, 2006). One advantage against the conventional optimal interpolation is its nonparametric nature. A linear function of the radius was chosen as the RBF. The smoothing factor, related to the magnitude of signal noise, was set to unity. The surface data obtained from each profile were gridded onto 0.25° (latitude)-0.66° (longitude) grids by the RBF interpolation. Areas with no data point in the radius of 100 km from the grid point and areas to the south of the ASC axis were masked. The interpolated surfaces are broadly consistent with the results obtained from the simple optimal interpolation with a 50 km decorrelation scale. The RBF interpolation turned out to better reproduce the detailed feature of original data than the simple interpolation with isotropic decorrelation scale (still, the choice of the interpolation scheme does not change the results qualitatively). Residuals of the original data from the interpolated values for zonal/meridional velocity and isopycnal temperature (Fig.s B1a–c) indicate that the interpolated field has no significant bias, suggesting its ability to fit the observation data faithfully. The standard deviation of the residual is spatially variant. For sea depths shallower than 3,000 m, the standard deviations of zonal/meridional velocity and isopycnal temperature are 1.96 cm/s, 1.72 cm/s, and 0.261°C, respectively, whereas those for sea depths deeper than 3,000 m are 3.85 cm/s, 2.86 cm/s, and 0.175°C. These values may approximate the interpolation error. The spatial dependency likely reflects the flow condition (e.g., flow is energetic, and water is homogeneous offshore). The absolute values of the residuals were re-mapped in Fig.s B2a-c to show the spatial variation of the standard deviations.

The results presented in the following section are considerably robust despite the interpolation error. First, the horizontal scale of circulation that we focus on is sufficiently large (greater than zonally 100 km and meridionally 50 km) relative to the scale of position error (Fig.s 4 and A3). Second, the reliability of the results is strongly supported by consistency with the positioned data. Notably, the velocity field is almost unaltered even if the under-ice dataset is absent (Figs. C1a–b), and thus it is unlikely contaminated by the terrain-following constraint. The position-lacking data likely improve the representativeness of CTD data at especially near the continental shelf. The validity of this processing for the position-lacking data will be further discussed in Section 4.1.

1.3 Results

1.3.1 Velocity fields

The zonal velocity field at 1000 dbar (Fig. 5a) reveals the presence of an eastward flow of the southern flank of the ACC to the north of 63°S and a westward flow to its south. The cyclonic circulation that appeared to the west of the Princess Elizabeth Trough (80°E) corresponds to the Prydz Bay Gyre (e.g., Meijers et al. 2012). The eastward flow is typically 6–10 cm/s, while the westward flow with 3–6 cm/s exists to the south (the maximum speed of the ASC is potentially underestimated due to the spatiotemporal smoothing and data deficits near the shelf). The zonal flow is eastward to the north of the SB (as the southernmost extent of the 1.5°C isotherms), whereas westward to its south. Thus, the SB is well aligned with the center of the subpolar gyre off East Antarctica.

The offshore ACC exhibits multiple jets; in the AAB (to the east of 80°E), there exist two eastward flow maxima (green lines in Fig. 5a). The northern jet flows southeastward from 60°S, 115°E to 62°S, 135°E, whereas the southern jet flows southeastward from 62°S, 100°E to 64.5°S, 150°E. The sACCf presented by OWN95 partly agrees with the northern jet in the west, though it rather overlays the southern jet near 135°E. Kim and Orsi (2014) reported the sACCf passes through the Kerguelen Plateau at 60°S and migrates southward to the east, and then achieves its southern limit at 62°S around 135°E, which is consistent with the location of the northern jet in the present result. Therefore, we refer to this northern jet as the sACCf.

The southern jet is located to the north of the SBs by about 100 km from 100°E to 140°E, generally along the 4,000 m isobath. This southernmost eastward jet likely corresponds to the "SACCF-S" (the southern branch of the sACCf) reported by Sokolov and Rintoul (2007, 2009). Other than the SACCF-S, there is no common name corresponding to the southernmost eastward jet to the north of the SB despite its importance in determining the northern extent of the subpolar gyre. From now on, we refer to it as the southern boundary front (SBf) and explicitly distinguish it from the SB and the sACCf. The speed of the SBf is as fast as 10 cm/s at a depth of 1,000 dbar. It is accompanied by an isopycnal inclination, whose baroclinicity yields a surface velocity of 14 cm/s (as mentioned later).

A closer look at the AAB reveals the spatial variation of zonal flow in detail (Fig. 5a). To the south of the SB, relatively weak westward flows appear in 108–113°E and 120–130°E between the spurs in the continental slope, and they are accompanied by shoreward excursions of the eastward flow offshore (areas deeper than the 3,000 m isobath) at 113°E and 123°E, respectively.

On the other hand, the meridional velocity field (Fig. 5b) presents the flow pattern, which reflects the direction of isobaths on the continental slope; the ASC is deflected northward on the eastern side of the spurs and southward on the western side. On the eastern side of the Bruce Spur (around 103°E), a northwestward flow exceeding 5 cm/s exists, whereas the flow is more than 5 cm/s to the east of Poinsett Spur (117–119°E; see also Fig. 6a). On the western side of the Poinsett Spur (110–115°E), the southwestward flow is around 3 cm/s, whereas the southwestward currents around 2 cm/s are detected in 121°E and 126–130°E. Together with the southward excursions of the eastward flow at 113°E and 120°E (Fig. 5a), two subgyres zonally bounded by the topographic spurs (located in 100–115°E and 115–130°E) are recognized inside the basin-scale subpolar circulation. Besides, provided the deflection of the along-slope flow around the smaller spur at 106°E (Fig. 5b), the western subgyre may include another small clockwise circulation split by the smaller spur between Bruce and Poinsett Spurs. In the Princess Elizabeth Trough, a northward flow is stripped from the upper slope (inshore of the 3,000 m isobath) at 82°E and connected to a strong northward current along the eastern flank of the Kerguelen Plateau (over 5 cm/s), whereas a systematic southward flow merges into the ASC at 90°E. The meridional flows indicates another cyclonic circulation bounded by the topographic feature in the Princess Elizabeth Trough.

The cross-isobath meridional flows around the SB are weaker than the along-isobath meridional flows shoreward of the 3,000 m isobath (Fig. 5b). Not only the average but also the variation of the flow is to be taken into account to comprehend the whole picture of CDW transport. In the vicinity of the SB, the standard deviation of meridional flow is as large as the mean value (about 2 cm/s; see Appendix B). The mean flow might reflect a net transport owing to the balanced and non-balanced (eddy) flows as the floats are exposed to both components. In contrast, the standard deviation corresponds to the temporal variation. The large temporal variation of the flow around the SB can be associated with the vigorous stirring of the ambient tracer field, and subsequently, the large downgradient tracer flux at the location (Foppert et al., 2019).

The current structure is generally barotropic in the Antarctic continental margin (e.g., Peña-Molino et al., 2016). Figs. 6a shows that the absolute velocities of the SBf and ASC at 1,000 dbar are 6–12 cm/s and 3–6 cm/s, respectively. They are representative of the gyre circulation because the geostrophic velocity from 1,000 dbar to 50 dbar merely yields baroclinic components of 3–5 cm/s for the SBf and 1–3 cm/s for the ASC (Fig. 6b). The result indicates that the geostrophic component above 1,000 dbar corresponds to roughly one-third of the absolute velocity at the surface. A sharp frontal feature of the ASC axis is unlikely resolved in Figs. 6a-6b. However, the flow structure of the SBf and the ASC with a minor baroclinic shear above 1,000 dbar is consistent with previous measurements (e.g., Peña-Molino et al., 2016; their Fig. 5). Southward geostrophic flow as fast as 3 cm/s appears around 115°E near the ASC, contributing to the onshore CDW transport in the upper slope (Fig. 6b; see Section 3.2 for the isopycnal structure). Deep floats further demonstrated the flow near the Bruce Spur at a depth of 3,000 or 3,500 dbar; their advective velocity ranges 2–5 cm/s (see Fig. 7 for their trajectories), which is comparable to the absolute velocity at 1,000 dbar. Thus, the circulation near the bottom is likely vigorous, as previously reported (e.g., McCartney and Donohue, 2007).

The zonal absolute velocity at 1,000 dbar (Fig. 5a) was integrated from south to north to capture the flow pattern (Fig. 7). Even though this is independent of the meridional velocity with a conceivable effect of the divergent term, the major features of meridional flow, such as the deflections of the ASC (Fig. 5b), are reproduced underpinning its validity as a proxy of the stream function. Provided that the circulation is generally barotropic above 1,000 dbar, these contours indicate the direction of the subsurface volume transport following the streamlines. In this figure, centers of clockwise circulation present at 62.5°S, 105°E (northeast of the Bruce Spur) and 63°S, 118°E (northeast of the Poinsett Spur) are consistent with the two subgyres bounded by the spurs discussed above (Figs. 5a–b). The SB locates near the center of the clockwise circulation, as seen in Fig. 5a. One of the deep floats (green) tracks the western subgyre in 100–115°E (between the Bruce and Poinsett Spurs), and the other two (pink and yellow) follow the 3,000 m isobath along the smaller spur in 106°E which may split the western subgyre (Fig. 5b). The western subgyre is meridionally elongated and analogous to the flow pattern of McCartney and Donohue (2007 see their Figs. 28 and 29). The deep float trajectories highlight the deeply-rooted structure of the subgyres (the trajectories mentioned here are solely based on satellite-positioned data).

1.3.2 Subsurface water mass distribution

The water properties derived from the CTD measurements are presented in this section. To the south of the SB, the local potential temperature maximum (θ-max; below the surface temperature minimum layer) represents the core of CDW. We henceforth refer to warm water in the θ-max layer as CDW for simplicity. The θ-max exhibits the synoptic-scale southward excursions of the shallow core of CDW in the AAB (Figs. 8a and 8b). Around 90°E, 110°E, and 120°E, the θ-max is particularly warm and shallow (about 200 dbar) near the shelf, indicating a localized CDW intrusion onto the shelves in these regions. To the west of the Princess Elizabeth Trough (80°E), shallow CDW is observed at 65°E (Fig. 8b), which likely supplies heat and salt to the Cape Darnley Polynya (Ohshima et al., 2013) and the Prydz Bay (Williams et al., 2016). Fig. 8a shows that the 1.5°C isotherms on the θ-max are generally in the proximity of the SBs of both SAO17 and OWN95. Thus, the float CTD data are consistent with the climatological SBs, which align the center of the subpolar gyre (Fig. 5a).

The density structures for the subsurface/deep layers are presented in Figs. 9a–b (the dynamic heights integrated for 50–800 dbar and 800–1,600 dbar, respectively). Note that the subsurface θ-max exclusively exists within 50–800 dbar (Fig. 8b). Above 800 dbar (Fig. 9a), the SB traces the northern limb of the dynamic height minima, while the local minima appear even shoreward around 64°S, 113°E (west of the Poinsett Spur) and around 64.5°S, 120°E (east of the Poinsett Spur). A relatively low dynamic height is also observed at 64.5°S, 90°E (west of the Bruce Spur), and these locations correlate well with the warm and shallow θ-max (Figs. 8a–b). These local minima correspond to isopycnal shoaling and are consistent with the cyclonic "eddies" above ridges reported by Wakatsuchi et al. (1994), while their baroclinic shear gives only a minor contribution to the surface mean flow in the gyre (Fig. 6b). Below 800 dbar (Fig. 9b), in contrast, contours of dynamic height spatially correlate well with the isobath of 3,000 m (white curve) rather than the SB because isopycnals within the layer are set along with the topography and monotonically decline toward the offshore. Isopycnals associated with CDW intrusion are likely confined within the subsurface layer above 800 dbar.

The core of CDW marked by the θ-max (Figs. 8a–b) generally exists within the subsurface isopycnal layer of $\sigma_\theta = 27.7–27.8$ kg/m^3 to the south of the SB. The potential temperature averaged for these isopycnals reveals a prominent along-slope variation (Fig. 10a); along the 3,000 m isobath, southward intrusions of warm water are found at 88–92°E (denoted as W1), 108–114°E (W2), and 119–130°E (W3), whereas cold signals are found at 80–88°E (denoted as C1), 101–105°E (C2), and 116–119°E (C3). The colder variations can be classified as mCDW since their density is comparable to CDW (e.g., Orsi and Wiederwohl, 2009). Note, the terminology mCDW has conventionally been used to refer to relatively warm water intruding onto the coastal region (e.g., Williams et al., 2010), not to colder water exported from the shelf. The potential density 27.7–27.8 kg/m^3 represents the cross-slope exchange between CDW and inshore water because the isopycnal of the temperature minimum layer (about 27.6 kg/m^3; which characterizes the bottom of the surface mixing layer) is exclusively shallower than the CDW layer. Since the colder variations in Fig. 10a likely originate from the shoreward, they may be referred to as shelf water in a broad sense rather than mCDW.

The warm water intrusion generally corresponds to the shallow θ-max (Fig. 8b) and the subsurface isopycnal shoaling (Fig. 9a), while the colder water corresponds to the deep θ-max. Fig. 10b specifies the isopycnal structure of the CDW layer. The layer is thicker in the north of the SB (more than 500 m) and thinner in the south, with a sharp thickness gradient around the SB (nearly halved in 100 km). The warm water intrusions (W1–W3) are accompanied by isopycnal shoaling with southward excursions of thick water, whereas the colder variations (C1–C3) are thinner and accompanied by thick surface water (as revealed by the depth of the isopycnal 27.7 kg/m^3). The isopycnal structure and the shoreward thickness gradient are likely associated with the cross-slope eddy transport (Foppert et al., 2019).

The along-slope potential temperature anomaly in the isopycnal coordinate reveals the regionality of water columns on the continental slope (Fig. 11a; the horizontal axis is shared with Fig. 11c, where a green-hatched area denotes the location). The prominent along-slope variation in temperature as much as 1°C within the CDW layer (27.7–27.8 kg/m^3) is emergent. Signals of warmer/colder water corresponding to those in Fig. 10a are recognized, consistently with the shallower/deeper isopycnal (Fig. 11b). Warm anomalies also appear near the Bruce Spur and to the east of 130°E, which simply reflect the location of isobaths close to the ACC (the anomaly over the Bruce Spur is isolated from the main axis of the ASC, so unlikely associated with the shoreward heat intrusion). The original CTD profiles further provide the fundamental water properties for each warm/cold signal (Figs. 12a–c). The upper and lower isopycnal surfaces of the CDW layer are denoted by circles and triangles, respectively. For the warm signals (red curves), the layer is consistently shallower than that for the cold signals (blue curves; will be further discussed in Section 4.3). Throughout the layer, the cold signals are considerably colder (by 1–2°C) and fresher (by 0.05–0.10) than the warm signals. Salinity profiles further show the depths of the CDW layer overlap a sharp halocline in contrast to the well-mixed shallower layer. Since the halocline with a stable stratification exists below the winter water layer, the local winter mixing does not reach the upper surface of the CDW layer (27.7 kg/m^3). Therefore, the colder variations within the CDW layer can be attributed to water advected from the shoreward. Regarding the source of warm/cold water within the CDW layer, the temperature anomalies shown in Fig. 11a might be associated with the cross-slope water mass exchange. The regionality in the water column properties will be discussed in Section 4.3.

1.4 Discussion

1.4.1 Utilization of under-ice data

A brand-new scheme that automatically refines the under-ice float positions was introduced. The interpolation error for the position-lacking data was evaluated by tests using the accurately-positioned data, allowing us to determine the extent to which the position-lacking data may be incorporated into the analysis. The choice of terrain-following interpolation rather than the conventional linear method was adopted to avoid a problematic trajectory crossing over a region shallower than the parking depth.

Chamberlain et al. (2018) discussed the utility of under-ice floats with the sound-tracking array in the Weddell Sea and particle-releasing numerical experiments. They first examined the error of under-ice position with the linear and PV-conservative interpolations, and their work compellingly encourages the utilization of the under-ice data. A difference from their results is that the error of the terrain-following method (functionally the same as the PV-conservative interpolation) is not so reduced from the linear method. A possible cause is the test dataset; we tested the positioned data from the circumpolar region inshore of the 3,000 m isobath, whereas Chamberlain et al. (2018) selected test samples in the Weddell Sea for which the PV-conservative interpolation is correctly performed. The presented result still seems acceptable since floats are always exposed to eddying flows, and actual trajectories can be cross-isobath at times. The estimated positional errors are consistent with their results regarding the scale of error in the linear and the PV-conservative methods.

To describe the velocity field, in addition to the accurately-positioned data, the position-lacking data with an interpolation period of 10 cycles or less are incorporated as the well-positioned data (Fig. 2b). The inclusion of the well-positioned data does not substantially increase the position error (Fig. A3a) and does not qualitatively affect the presented flow pattern (Figs. C1a-b) as the number of accurately-positioned data (10,342 casts) is much greater than the well-positioned data (604 casts). Meanwhile, the well-positioned data improve the data coverage at some locations offshore of the 3,000 m isobath and likely improve the representativeness of the flow speed since the effect of the terrain-following scheme on flow direction may be small with 10 cycles or less.

The mal-positioned data with an interpolation period 36 cycles or less (2,981 casts) are additionally incorporated to describe the water mass properties. This inclusion considerably recovered the data coverage (Fig. 2c) and modified the temperature field, particularly inshore of the 3,000 m isobath (Fig. C1c). The positioned data alone can reproduce the warm features corresponding to the W1, W2, and W3. For the cold signals in the upper slope, the C1 and cold water east of 120°E are amplified by this inclusion (coldness is emphasized by 0.5-1°C). Meanwhile, the C2 and the C3 can be reproduced without the under-ice data. Overall, the regionally different outcomes from the inclusion of the mal-positioned data are attributed to the local scarceness of the accurately-positioned data near the ASC axis (Fig. A3b) and possibly to the seasonality.

1.4.2 Circulation off East Antarctica

The structure of the subpolar gyre in the AAB corresponding to the Kerguelen Gyre was presented in Section 3.1. Our result is generally consistent with the synoptic flow pattern schematized by Bindoff et al. (2000), whereas it further provides new understandings of its structure (Section 3.1). First, the northern boundary of the subpolar gyre is defined by the southernmost jet of the ACC along the 4,000 m isobath (SBf), which was not fully resolved previously because the BROKE survey did not cover the north of 63°S, and the satellite altimetry has suffered from the presence of sea ice (Sokolov and Rintoul, 2007). Second, in contrast to the northward recirculation at 90°E inferred by Bindoff et al., the southward flow was obtained at that location (Fig. 5b). Regarding the weak recirculation in the Princess Elizabeth Trough, the western limb of the Kerguelen Gyre likely extends to the west of the Princess Elizabeth Trough, meeting the Prydz Bay Gyre as implicated by Aoki et al. (2010). Our result indicates that the Kerguelen Gyre is meridionally bounded by the ACC and the ASC and comprises a series of subgyres, rather than a broad recirculation from 90°E to 115°E proposed by Bindoff et al. (2000). The series of cyclonic eddies associated with the topographic spurs was previously documented by Wakatsuchi et al. (1994). The present study further suggests that the subgyres are quasi-barotropic controlled by the topographic spurs, whereas the baroclinic component has a minor contribution to the synoptic flow pattern (Figs. 6a–b).

The flow speeds based on float trajectories are quantitatively consistent with the direct observations. Moorings along 113°E (Peña-Molino et al., 2016) observed a westward flow at 64.5°S at 1,500 m of 5.1 cm/s and an eastward flow at 61.5°S near 1,000 m of 4.1 cm/s, while the zonal velocity by the float trajectories at each location was around -3 cm/s and +5 cm/s, respectively (Fig. 5a). A mooring at 140°E (Fukamachi et al., 2000) detected a mean flow of 5.3 cm/s at 1,000 m, which also agrees well with our results (Fig. 6a). Furthermore, these moorings revealed the flow fluctuations as large as the mean speeds, which seem consistent with the significant standard deviation of the advective velocity (Appendix B).

The subpolar gyres off East Antarctica are united with the ACC that travels to the proximity of the continental shelf. It contrasts with the situation of the Weddell and Ross Gyres, in which the SB is located well outside the clockwise circulations. The location of the Antarctic Divergence relative to the SB is likely vital for the water mass exchange; as the Antarctic Divergence is locally aligned with the SB (around 63°S), net cyclonic vorticity is supplied onto the sea surface wherein the ACC prevails. This wind forcing can promote the upwelling of CDW and allow effective heat transport onto the shelves. Buoyancy forcing due to the intensive air-sea interaction off East Antarctica might also characterize the gyre structure and the cross-slope flows.

1.4.3 Subsurface cross-slope exchange

The along-slope temperature variation in Fig. 10a has a remarkable relationship with the meridional velocity; i.e., warm CDW accompanies southward flow, whereas colder water accompanies northward flow (as annotated in Fig. 5b). This correlation highly indicates that the meridional flows associated with the topographically-controlled subgyre circulations facilitate the cross-slope exchange between offshore CDW and inshore cold water. The subsurface water mass exchange within the subpolar gyre is schematized in Fig. 13. CTD profiles along the 2,200–2,800 m isobaths revealed the presence of cold water too deep to be created by local winter mixing (Figs. 12a–c). The cold features are likely shelf water in a broad sense advected from the shoreward. It is naturally assumed that the subsurface cold water reflects intensive buoyancy loss in the coastal region (e.g., Guo et al., 2019; Tamura et al., 2016). As such, the spatial variation in the along-slope temperature likely reflects the regional difference in surface forcing over the continental shelves. The CDW intrusions can compensate heat and salt flux due to the continental processes, including sea ice production and/or glacial melting.

In the following paragraphs, regional differences in water mass properties on the continental slope that exhibited in Fig.s. 12a-12c are discussed. The extremely cold and fresh feature C1 (Fig. 12a) may be related to the icy coastal condition of the active Shackleton Polynya. Fig. 10a shows that some of the cold water escape from the ASC and are exported northward subsequently to the eastern flank of the Kerguelen Plateau (Fig. 5b). The CDW intrusion W1 off the Shackleton Ice Shelf may supply heat onto the shelf, with its systematic southward flow around 90°E. The W1 and C1 are likely associated with the subgyre bounded by the Princess Elizabeth Trough topography.

The signal C2 (Fig. 12b) can be shelf water advected from the Vincennes Bay, whereas the W2 corresponds to CDW, which broadly and intensively penetrates the shelf. As Kitade et al. (2014) reported that the Vincennes Bay Polynya at 110°E contributes to the bottom water production, the W2 intrusion can compensate the volume export from the Vincennes Bay into an abyssal layer. The W2 may also be relevant to the southward baroclinic flow at 115°E (Fig. 6b). Kitade et al. (2014) indicated that the exported bottom water follows the 3,000 m isobath along the small spur at 106°E between the Bruce and Poinsett Spurs. The meridional velocity (Fig. 5b) and the deep float trajectories (Fig. 7) support their result. The structure of the subgyre in 100-115°E split by the small spur likely influences the shoreward intrusion of CDW and the export of bottom water at the location.

Water properties in C3 (Fig. 12c) are close to that of mCDW located at the bottom of the Sabrina coast (Silvano et al., 2017), with a typical temperature (0°C) and salinity (34.5). The late winter hydrography reported by Williams et al. (2011) detected deepened Winter Water, corresponding to the thick surface layer above the subsurface cold signal C3. CDW likely enters the Sabrina and Banzare Coast sectors via the western and eastern paths of W3 (Fig. 10a). In Fig. 11, the western branch of W3 looks almost absent because it does not broadly intrude over the upper slope, and the warm signal was canceled out with the ambient cold water. The western branch of W3 (at 120°E) agrees with warm mCDW reported by Nitsche et al. (2017, their st. 23) with its location and properties. To the east of 120°E, vertical profiles exhibit active interleaving between warm and cold water within the CDW layer (in Fig. 12c, colder water is displayed by black curves), which indicates the energetic lateral mixing due to the sharp frontal structure. A corresponding frontal feature along 128°E was observed during the BROKE survey (reported in Williams et al., 2011). This strong meridional temperature gradient may be consistent with the significant standard deviation of temperature at the location obtained by the float data (see Appendix B).

The mean flow regulated by the spurs can contribute to the meridional transport in the subpolar gyre (Fig. 13). However, it alone should be insufficient to explain the entire transport because the cross-isobath component is required to close the circulation. In addition to the along-isobath transport by the mean flow, diffusive cross-slope transport is expected by 1) the significant standard deviation of absolute velocity (Section 3.1), which can enhance the downgradient tracer flux, and by 2) the shoreward thickness gradient (Section 3.2), likely associated with the onshore eddy diffusion of layer thickness (e.g., Stewart and Thompson, 2016; Foppert et al., 2019). Isopycnal eddy transports (advection and stirring) can explain why the CDW intrusions agree with the subsurface isopycnal shoaling, as they help adiabatic upwelling of CDW, compensating for diapycnal flux near the mixing layer. Aside from the isopycnal eddy transport, various processes (tidal variation, etc.) can contribute to the cross-isobath component. However, isopycnal eddies likely have a dominant contribution to the transports in the ocean interior away from the shelf break. We may conclude that the subsurface water mass exchange within the subpolar gyre is accomplished by a combination of topographically-controlled mean flow and eddy transport.

1.5 Summary

Argo data in the seasonal ice zone were analyzed to describe the structure of the subpolar gyre off East Antarctica (Fig. 13). In this region, the SB is systematically located to the south of the southernmost jet of the ACC along the 4,000 m isobath. The southernmost eastward jet, referred to as the southern boundary front (SBf), is consistent with SACCF-S reported by Sokolov and Rintoul (2007). The SB generally presents along the center of the Kerguelen Gyre and the Prydz Bay Gyre, whereas the SBf provides their northern extent. The topography highly constrains the flow pattern, constituting a series of subgyres within the basin-scale stretch of the subpolar region between the ACC and the ASC. The subgyres are bounded by the spurs in the continental slope and quasi-barotropic. The temperature field within the CDW layer (27.7–27.8 kg/m^3 in σ_θ) displays distinct warm and cold anomalies on the upper continental slope. This along-slope variation within the CDW layer is likely related to the cross-slope exchange. The shoreward CDW transport was implicated by the standard deviation of the velocity and the shoreward isopycnal thickness gradient. The eddy transport can explain the congruity between the isopycnal shoaling and the shoreward CDW intrusion. Overall, topographically-controlled mean flow and isopycnal eddy transport are likely responsible for the cross-slope exchange.

Reportedly, the ACC off East Antarctica has been shifted poleward during the past decades (Couldrey et al., 2013; Kim and Orsi, 2014), which may be associated with the atmospheric changes induced by the anthropogenic forcing (Goddard et al., 2017; Spence et al., 2014). Given the potential impact of the oceanic heat on the East Antarctic Ice Sheet (Greenbaum et al., 2015) and its significant reduction in the recent decades (Rignot et al., 2019), it is an urgent task to understand the dynamical response of the subpolar gyre to atmospheric variability. The present study would provide the observational basis for future investigation.

We propose a new terrain-following interpolation to utilize under-ice data without coordinates. This scheme is especially effective in the continental margin because the ocean current predominantly follows the isobaths, and unnatural positions inconsistent with the parking depth yielded by the conventional linear interpolation can be avoided. Spatial error in the interpolated position is estimated using the data with satellite-fixed coordinates. The interpolating tests enable us to evaluate the geolocational error, estimated to be 23 ± 27 (78 ± 70) km with a continuous under-ice period shorter than 90 (390) days. Since a substantial amount of the under-ice data already exists, the developed method can improve the data quality in the seasonal ice zone. We remark that the under-ice data are extremely valuable for studying the ocean structures that have yet to be documented. Their use will alleviate challenges in extensive monitoring of polar oceans all year round.

Appendix A. Position interpolation for the position-lacking Data

A.1. Implementation of the Terrain-following interpolation

Here, the procedure for the terrain-following interpolation adopted to infer under-ice positions is delineated. As an example, we consider the case of a float which sequentially failed satellite positioning (Fig. A1a). The positions before and after these position-lacking cycles are known (blue stars). The missing positions can be determined simply via linear interpolation, dividing the linear path into segments of equal length (blue circles). The direction parallel to the linear path is referred to as the "tangential axis," and the direction at the right angle of the path is referred to as the "normal axis" hereafter. Instead of the linear method, the positions are determined so that the trajectory follows the isobaths.

First, a reference depth is given to every position-lacking point by linearly interpolating the bottom depths of the two accurately-positioned endpoints (Fig. A1a). We assume that a candidate of position is located along the normal axis extended from the linearly interpolated positions, within a certain distance referred to as the "search range." Within this search range, the position is first determined to minimalize the difference between the local and the reference depth. Once the position is determined, the tangential and normal axes are updated and used for positioning of the next position-lacking point. The terrain-following trajectory can be obtained by repeating this procedure for all the position-lacking points. Lastly, as a check of the validity of the path, the known position of the downstream endpoint is compared to the last estimated point (Fig. A1b). The distance in the normal axis between them is called the "gap."

The interpolation is usually completed solely by an iteration of the procedure presented above (Case 1; Figs. A1a–b). However, if the gap exceeds the search range, the result is considered erroneous and another iteration is necessary (Case 2; Figs. A1c–d). In such cases, the revising procedure is performed as follows. We first introduce the angle α, whose value depends on the ratio of the search range R to the length of one segment of the linear path L: $\alpha = \arctan(R/L)$ (Fig. A1c). This is used to define the region where interpolated positions are deemed acceptable so that the boundary extended from the endpoint crosses the linear path with the angle α. The revising procedure starts from the last downstream accepted point. By connecting the start point to the endpoint with a linear path and dividing the distance equally, new referential points are defined (black circles in Fig. A1d). A second iteration is then carried out to minimalize a difference from the reference depth, using the referential points as the centers for the search range.

More than 1/3 of all sets of continuous position-lacking data required this second iteration to be run.

As the search range R, 22 km was found to be appropriate to yield trajectories with realistic advective speeds, whereas greater values could induce artificially meandering features. The choice of search range can be justified by the interpolation error associated with the linear method for one position-lacking cycle. As this scale approximates the radius of a circle where the float is likely located during one position-lacking cycle, the search range should be close to this error. The root-mean-square error with the linear method for one position-lacking cycle is 8.5 ± 9.4 km (Appendix A.2). Thus, the choice of 22 km is comparable to its mean plus one standard deviation.

A.2. Evaluated interpolation error

The positional errors accompanied by the interpolation, defined as the distance between the actual and interpolated positions, were evaluated by the interpolation tests using the accurately-positioned data. Table A1 summarizes the derived error values. The mean and the standard deviation of error were calculated at every cycle during a certain duration of the interpolation period then averaged over the period. In addition to the errors for longitude and latitude, their root-mean-square is also presented to provide a nondirectional measure of the error.

Two test examples are shown in Fig. A2a to represent the skill of the terrain-following interpolation. For both cases, the interpolation is properly performed in a terrain-following manner. It seems effective when a float follows isobaths with a scale comparable to the under-ice displacement (as in the blue trajectory). However, the actual trajectories do not necessarily follow isobaths as is the case for the red trajectory, because floats are exposed not only to PV-conservative flow but also to non-conservative flows. As a result, no significant difference between the terrain-following and the linear methods was obtained. This disagreement with the result by Chamberlain et al. (2018) can be attributed to the data locations; Fig. A2b provides the spatial distribution of test data used in the present study, which is from a circumpolar domain.

The distribution of the position-lacking data directly affects the position error of the two-dimensionally gridded fields. Figs. A3a–b demonstrate the spatial variation of the position error due to the position-lacking data, in which the mean position error was estimated per 2.5° × 0.25° box bin. The position error of each data point was evaluated by the root-mean-square interpolation error from the interpolation tests (Table A1). The error of the accurately-positioned data was assumed to be zero. The mean position error of the velocity data (Fig. A3a) is generally smaller than 20 km because the number of the well-positioned data is limited (Table 1) and the maximum interpolation period of the well-positioned data is 10 cycles (Section 2.4). The mean position error of the CTD data (Fig. A3b) is generally smaller than 40 km in the east of 110°E, whereas it is relatively larger in the west. This map reflects the spatial variation of the number of position-lacking data relative to the accurately-positioned data. In addition to Figs. A3a–b, the data population (Figs. 2b–c) further supports the credibility of the presented results against the position error.

Appendix B. Absolute deviation from the interpolated field

Residuals of the original data subtracted by the two-dimensional interpolated field were calculated to assess the possible error resulting from the RBF interpolation (Figs. B1a–c). The residuals were derived for the absolute velocity at 1,000 dbar and the isopycnal temperature (27.7–27.8 kg/m^3 σ_θ), with the sea depths shallower and deeper than 3,000 m. The 3,000 m isobath was chosen as the boundary since it likely separates the inshore region with a smaller flow variability and a larger temperature variability from the offshore region. The figures indicate that the averages of the residuals are nearly zero, which corresponds to the interpolation bias. Hence, a possible interpolation error is likely associated with the standard deviation of the residuals. The standard deviations in Figs. B1a-c (the values are provided in Section 2.4) were derived from the dataset reproduced from 10,000 times boot-strap resampling of the residuals. According to the resampled dataset, the 90 % confidence range of the residuals of the zonal/meridional velocity and isopycnal temperature for sea depths shallower than 3,000 m are −3.22–+2.85 cm/s, −2.84–+2.73 cm/s, and −0.458–+0.438°C, respectively. Those for sea depths deeper than 3,000 m are −6.52–+6.35 cm/s, −4.76–+4.64 cm/s, and −0.277–+0.251°C, respectively. The widths of the 90 % confidence range, as well as the standard deviation, are likely correlated with the amplitude of the temporal variation.

The standard deviation of the residual is spatially variant, as mentioned in Section 2.4. Spatial variations of the absolute deviation (absolute value of the residuals) of each parameter were objectively mapped with the RBF interpolation (Figs. B2a–c). Since a sufficient number of data exists within the scale of interest, the mean absolute deviation likely expresses each parameter's standard deviation. For the zonal velocity at 1,000 dbar (Fig. B2a), significant deviations comparable to the mean value are obtained to the north of SB. In contrast, for the meridional velocity (Fig. B2b), significant deviations are obtained even to the south of SB. The sum of these deviations may relate to the eddy kinetic energy at the depth. The deviation of the isopycnal temperature (for 27.7–27.8 kg/m^3 σ_θ) is correlated with the temperature gradient (Fig. B2c); significant deviations are obtained around the 3,000 m isobath. These results likely reflect the temporal variation and the flow condition.

Appendix C. Effect of the position-lacking data

To represent the effects of the position-lacking (under-ice) data, gridded fields were created only using the accurately-positioned data and compared to the presented results (Figs. C1a–C1c). As mentioned in Section 4.1, the inclusion of the under-ice data does not change the velocities qualitatively (Figs. C1a–b). As for the subsurface temperature, the effect of inclusion is generally confined inshore of the 3,000 m isobath (Fig. C1c). The inclusion seems to amplify the cold signal C1 and the cold water east of 120°E (Section 4.1). The remarkable features of shoreward CDW intrusion around the SB remain unaltered.

Figures and tables

Figure 1. Bathymetry in the study region. The contour interval is 500 m and the colormap is shown upper right. The coastlines are based on Mouginot et al. (2017). Fronts derived from the climatological temperature in Shimada et al. (2017) are denoted by solid curves for the Southern Boundary of ACC (SB, red) and the axis of the Antarctic Slope Current (ASC, blue). The SB and the southern ACC front (sACCf) by Orsi et al. (1995) are also introduced for comparison (red and yellow broken lines, respectively). The Antarctic Divergence is denoted by the solid white line.

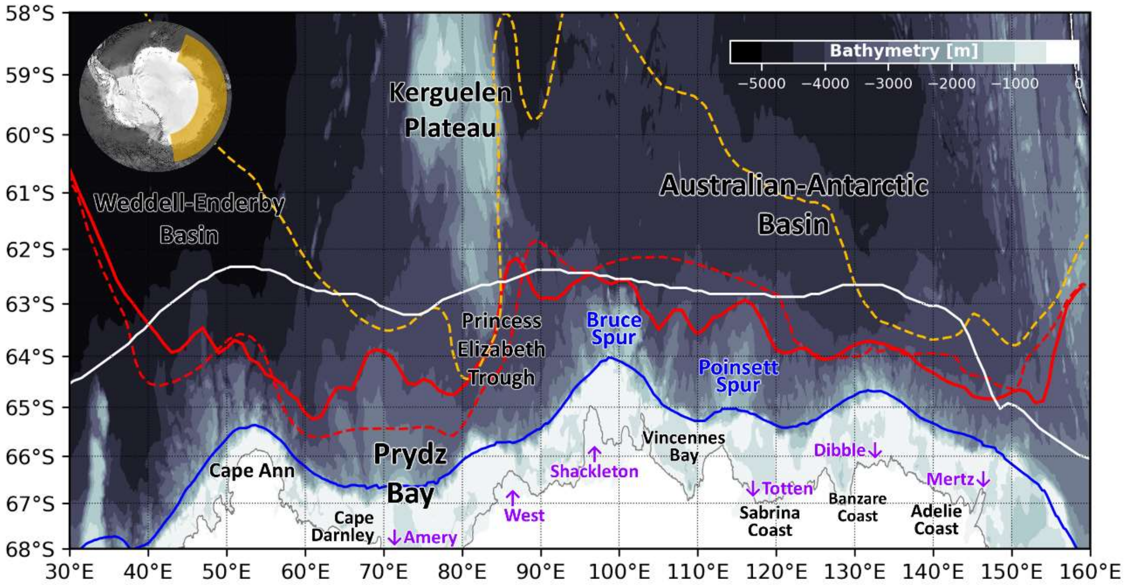

Figure 2. Distribution of the float data used in this study. (a) All available data. The positioned data are green dots, and the position-lacking data are pink dots (which are linearly interpolated in this figure). Climatological sea ice edges by Stroeve and Meier (2017) for September (solid white line) and March (broken white line) are also shown, delineating the seasonal ice zone. (b) Data population used for the velocity data per bin (2.5° in longitude and 0.25° in latitude), which include the accurately-positioned and well-positioned data. (c) Same as in (b), but for the CTD data, which include the mal-positioned data as well.

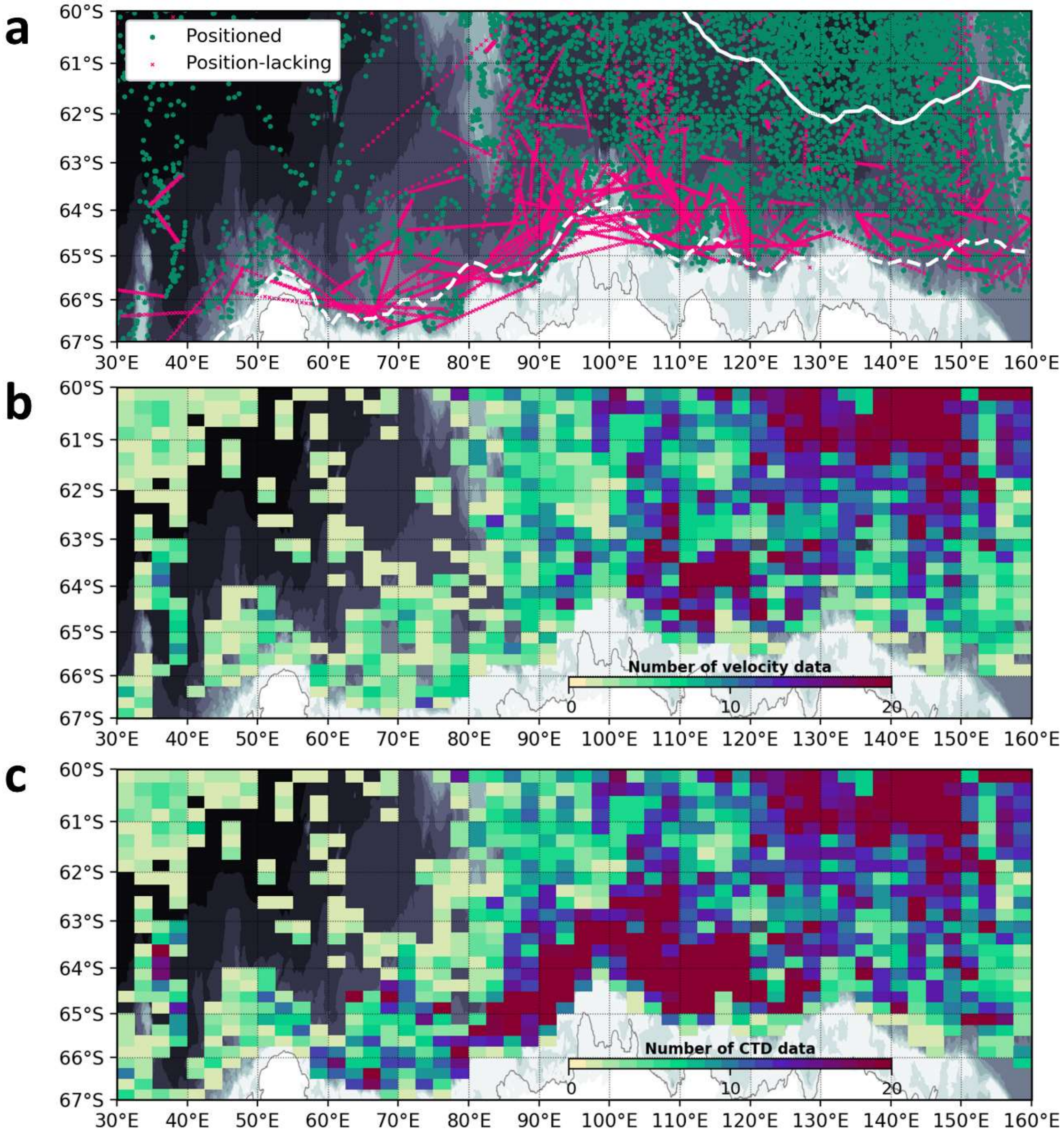

Table 1. Summary of the number of profiles for each data classification. Data are retrieved from 30–160°E, south of 60°S (Fig. 2). The accurately-positioned and well-positioned data were used for both CTD and velocity data, whereas the mal-positioned data were used only for the CTD data. The ill-positioned data were not used for any analysis.

Accurately-positioned	10,342			Used for Both CTD and Velocity
Position-lacking	4,135	Well-positioned	604	
		Mal-positioned	2,981	Used Only for CTD
		Ill-positioned	550	Not Used

Figure 3. Example of the under-ice positioning by two different methods (for float ID: 2900118). The float advected from east to west in the figure. Background color denotes the sea depth with a shallower region to the south. Black crosses denote the accurately-positioned casts. Circles are the positions obtained by the terrain-following interpolation, whereas triangles are the linearly interpolated points; they are continuously colored according to the date. In this case, linearly interpolated positions are not acceptable as the float crosses over the continental shelf shallower than its parking depth (1,000 dbar). The trajectory obtained by the terrain-following method (white broken curve) is adopted in this study.

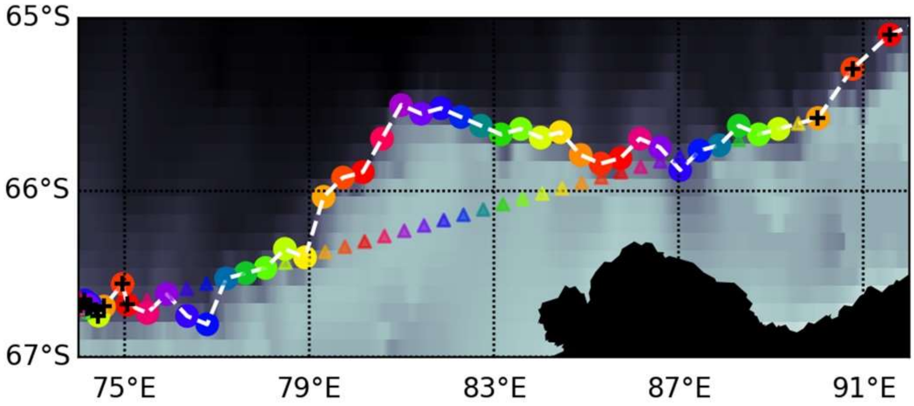

Figure 4. Estimated interpolation error of the position-lacking data. (a) Zonal and (b) meridional errors (in kilometer) for the interpolation period for the linear and the terrain-following methods derived from interpolation tests. Mean (solid line) and standard deviation (SD; colored hatch) of errors are calculated at every cycle of the period and then averaged over the period (see Table A1 for specific values). (c) The number of the position-lacking profiles (from 30°E to 160°E, to the south of 60°S) for the duration of the consecutive position-lacking period. Data with a position-lacking period of 1–10 cycles were defined as well-positioned data, and data with a position-lacking period of 11–36 cycles were defined as mal-positioned data (see also Table 1).

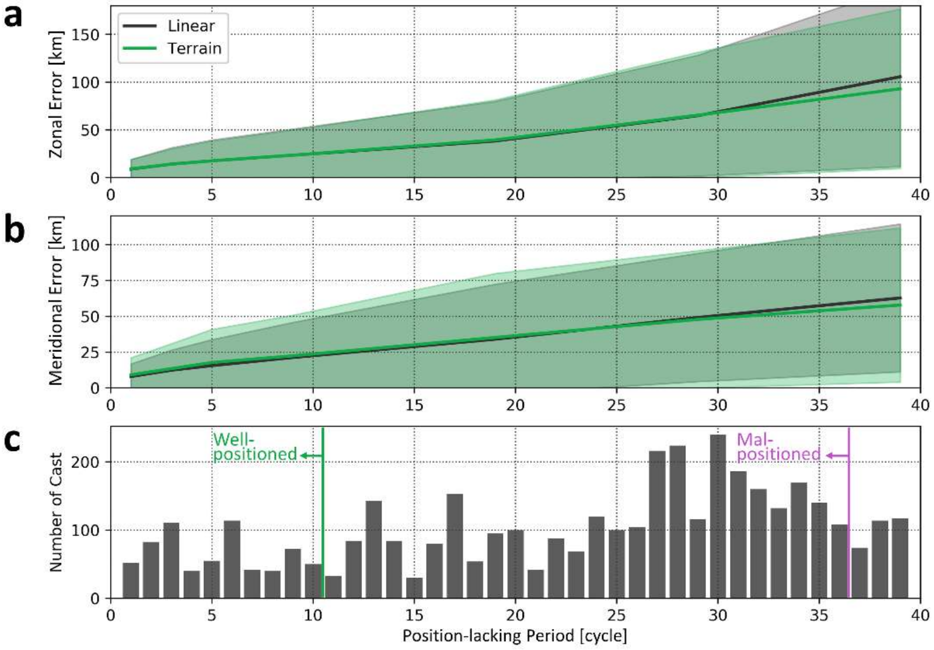

Figure 5. Absolute velocity field at 1,000 dbar derived from the float advective velocity. (a) Zonal velocity (background color; the colormap located lower center). Areas with no data point within 100 km and to the south of the ASC axis were masked. The SBs by SAO17 and OWN95, the ASC axis, and the sACCf by OWN95 are introduced as in Fig. 1. The 3,000 and 4,000 m isobaths and coastlines are shown by gray curves. The northern and the southern jets of the ACC are highlighted by green curves. (b) Meridional velocity. The red "W" and blue "C" denote the locations where remarkably warm/cold waters are observed (see Section 3.2 for these annotations).

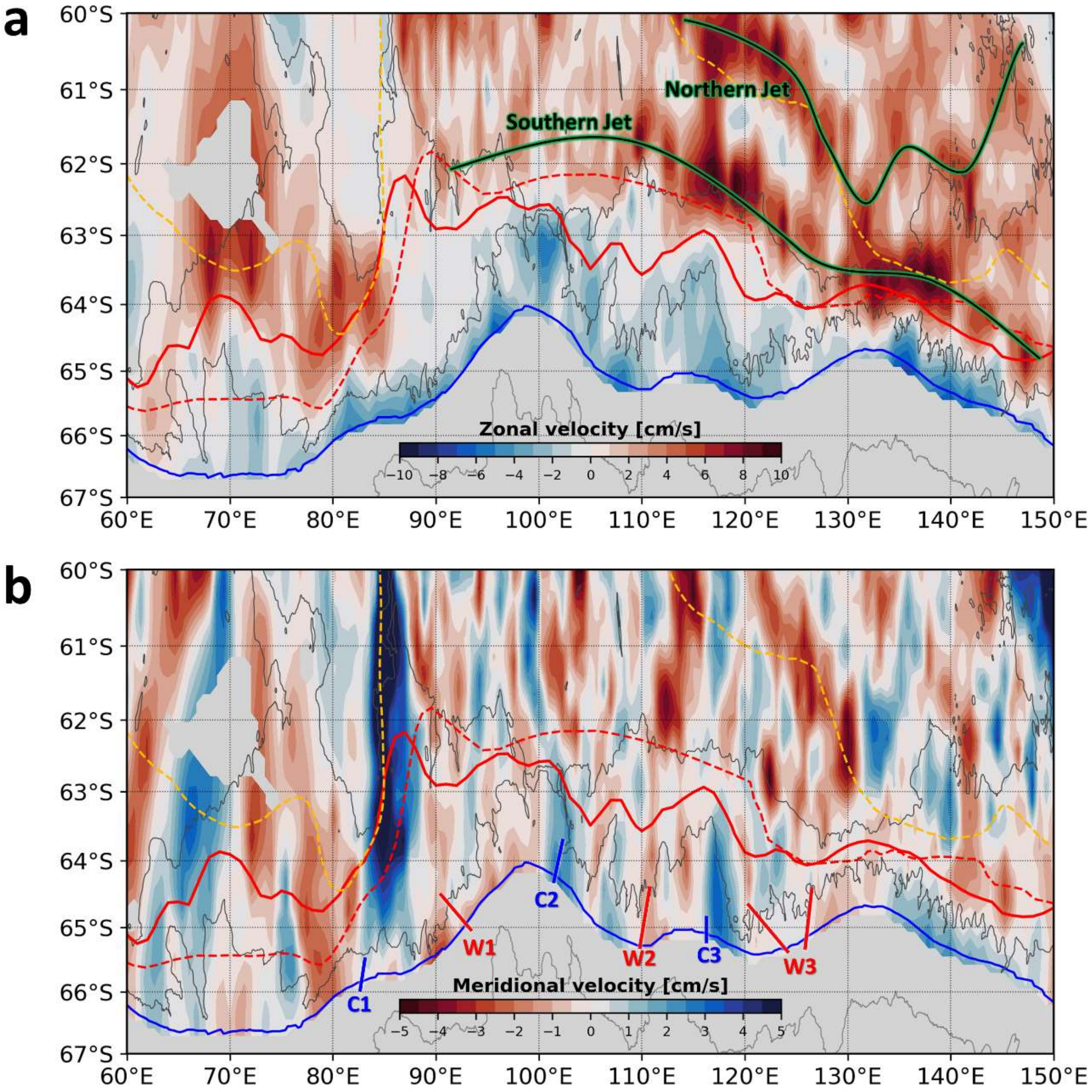

Figure 6. Comparison between the absolute velocity and the geostrophic velocity. (a) Mean absolute velocity at 1,000 dbar with the velocity vectors. (b) Geostrophic velocity (baroclinic flow) at 50 dbar relative to 1,000 dbar derived from the CTD data. Vectors are meridionally distorted for geographical consistency. The SB and the ASC axis by SAO17 (red and blue curves) and the isobaths (gray curves) are introduced as in Fig. 5.

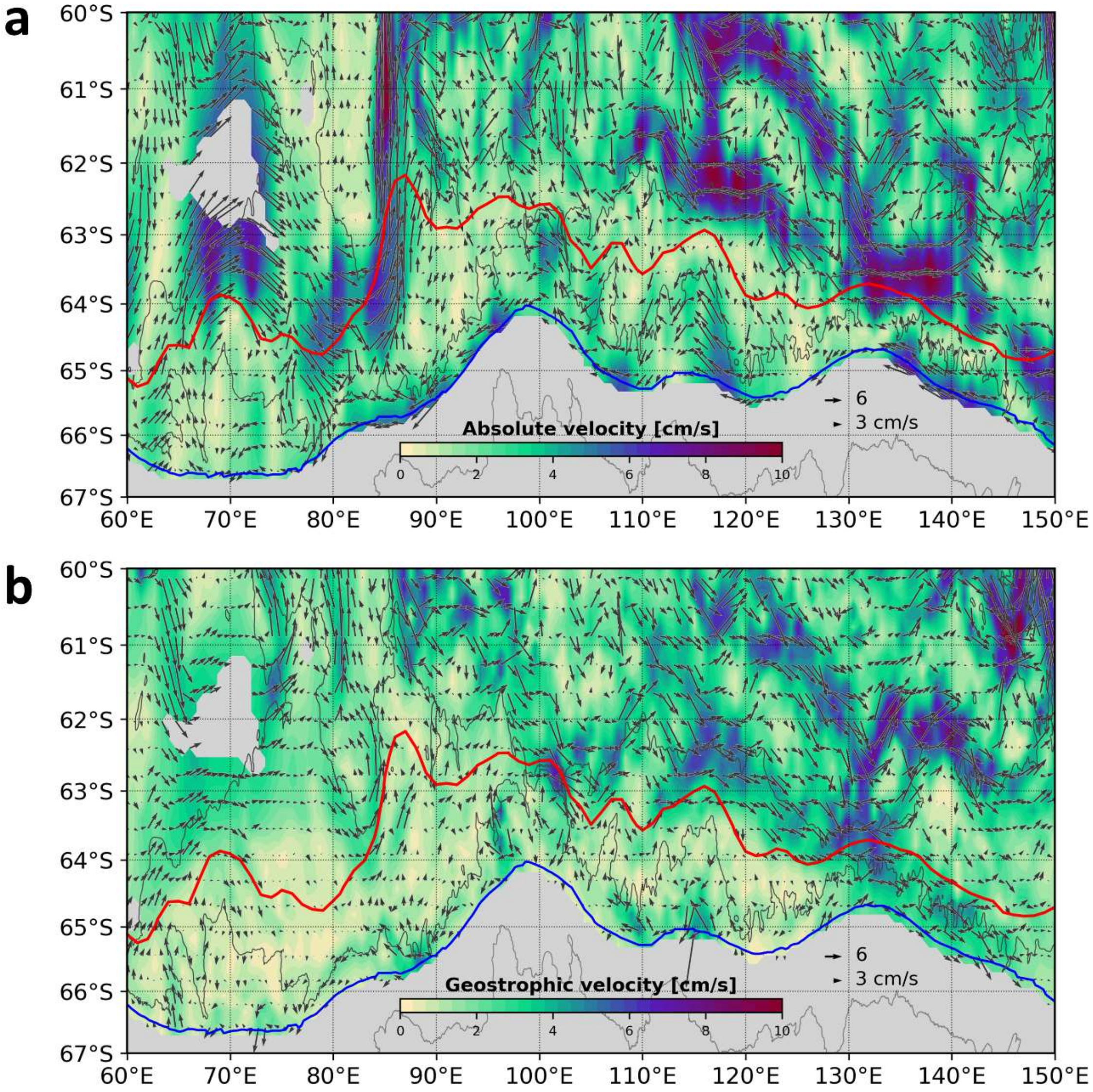

Figure 7. Meridionally integrated zonal velocity at 1,000 dbar as a proxy for the stream function. The circulation approximately follows the contour, seeing a bluer/redder area to its right/left-hand side. The isobaths of 3,000 and 4,000 m are shown by gray contour. Results from integration, which include the masked region of zonal velocity (Fig. 5a), are not shown. The trajectories of the deep floats are introduced; SN 13, 14 (at 3,000 dbar), and 15 (at 3,500 dbar) are denoted by pink, yellow, and green lines, respectively.

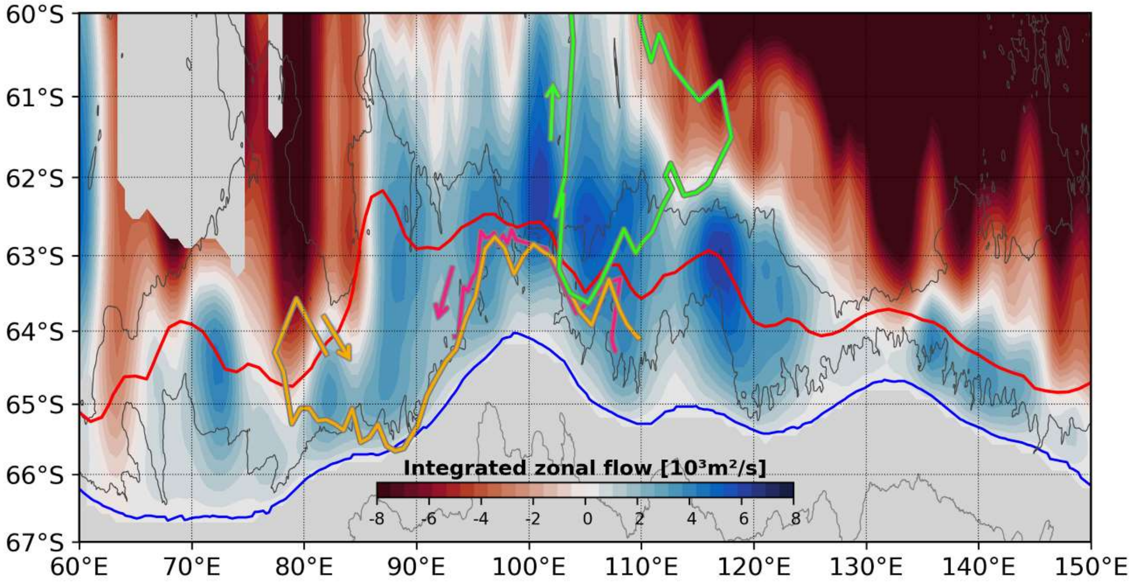

Figure 8. Property of the subsurface potential temperature maximum (θ-max). (a) Potential temperature at the θ-max below 100 dbar. The SB (southernmost extent of the 1.5°C isotherm) is assumed to locate near the white area. (b) Depth of the θ-max. Profiles without θ-max between 100 dbar and the maximum measured pressure are excluded. Areas with no data point within 100 km and to the south of the ASC axis were masked. The climatological fronts, topographic contours are denoted as in Fig. 5.

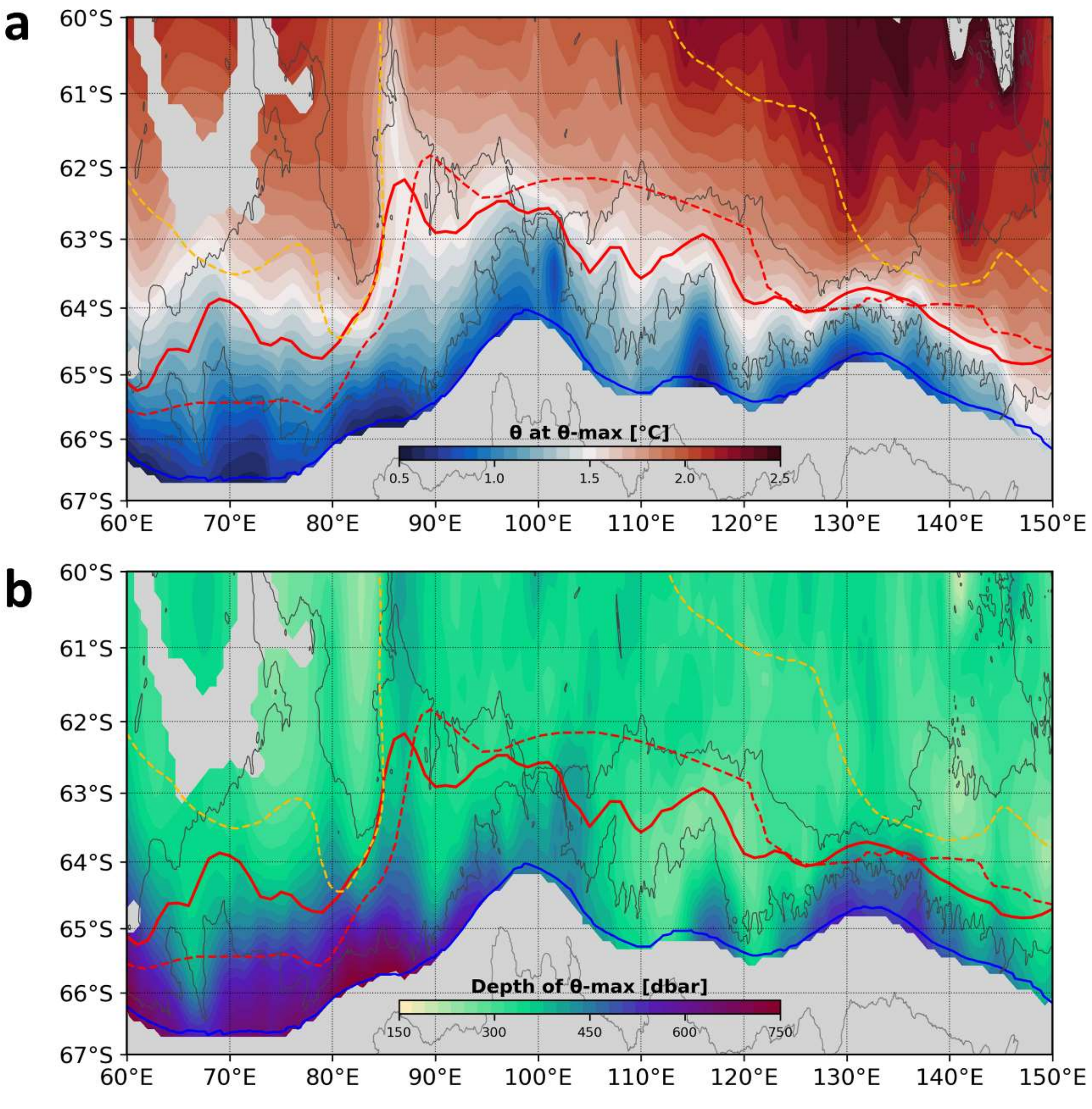

Figure 9. Dynamic heights integrated for (a) 800–50 dbar and (b) 1,600–800 dbar. The dynamic height was calculated by vertically integrating the specific volume anomaly derived from CTD data. The isobaths of 3,000 and 4,000 m are shown by white contour. The climatological fronts are denoted as in Fig. 5.

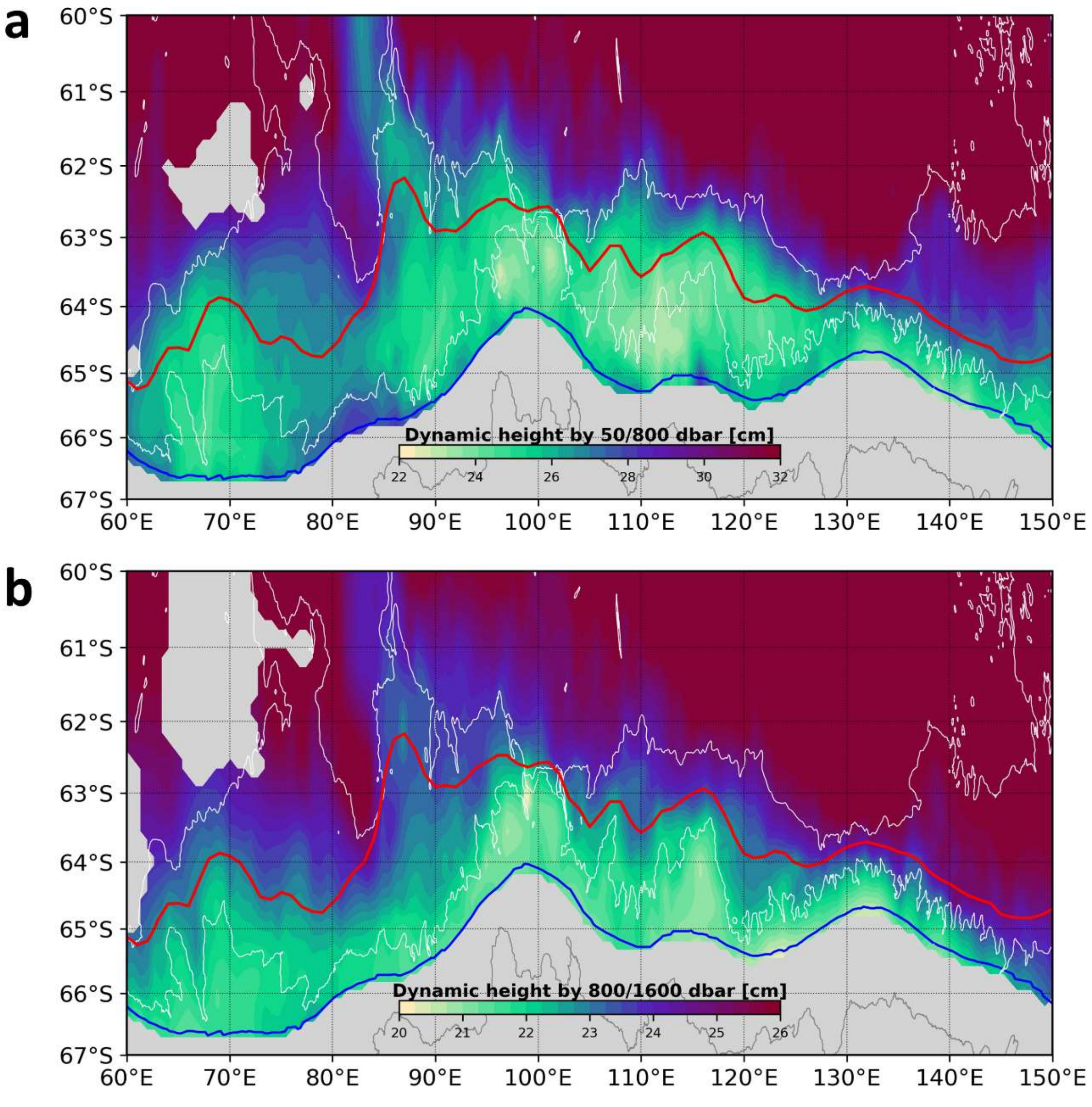

Figure 10. Subsurface water mass structure for the CDW layer (27.7–27.8 kg/m^3 σ_θ). (a) Layer-averaged potential temperature. Remarkably warm and cold features on the continental slope region are annotated by red and blue letters, respectively. (b) Thickness of the isopycnal layer (background color). Depth of the 27.7 kg/m^3 isopycnal (upper surface of the layer) is overlaid by gray contours.

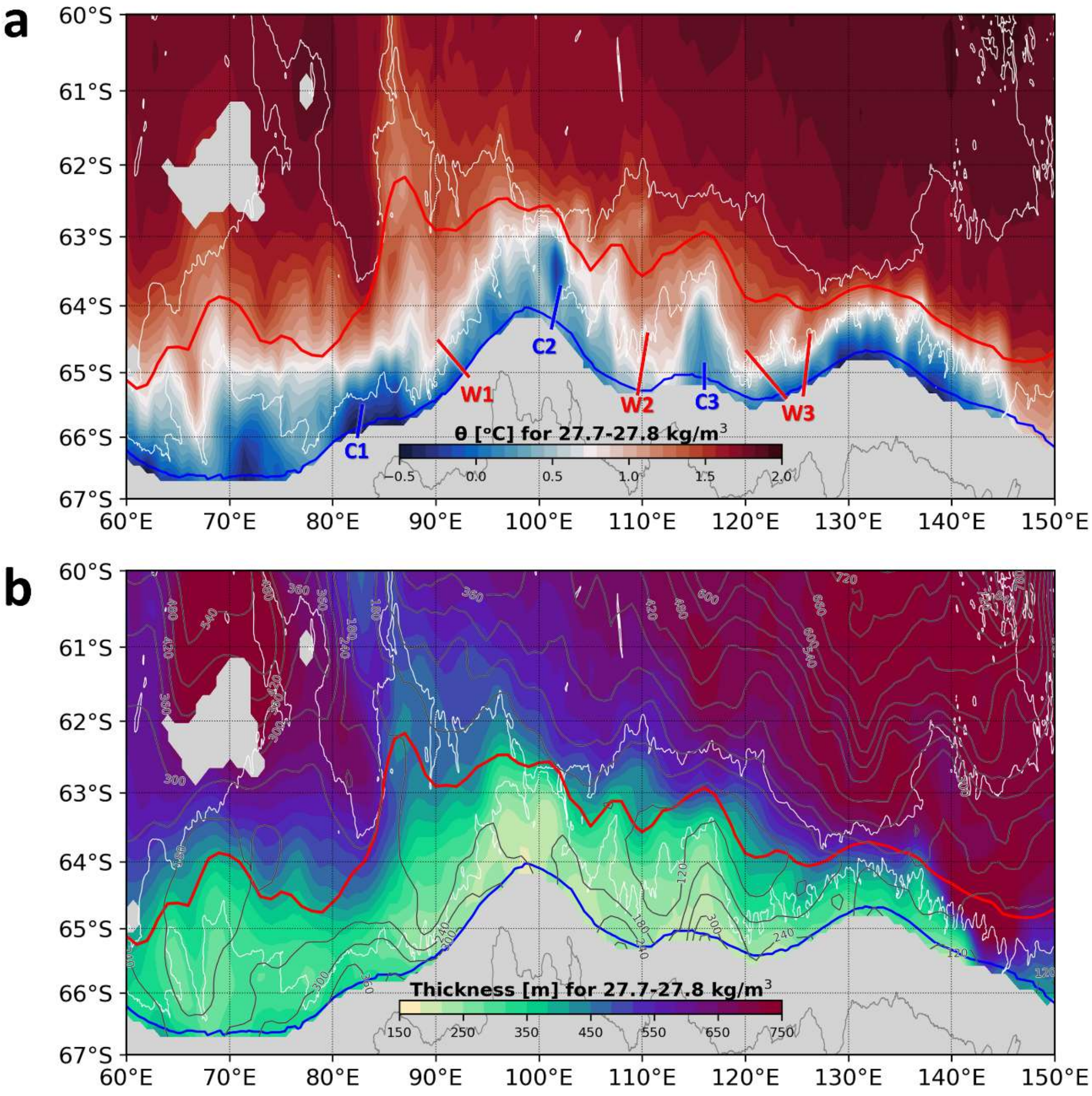

Figure 11. Along-slope temperature variation on the continental slope where the sea depth ranges from 2,200 to 2800 m. (a) Temperature anomaly from the isopycnal average in the longitude-potential density coordinates (averaged in meridional direction). Warm and cold signals presented in Fig. 10a are consistently annotated by red and blue letters, respectively. (b) Pressure variation of the upper (27.7 kg/m^3; solid curve) and the lower (27.8 kg/m^3; broken curve) surfaces of the CDW layer. (c) The data location (green-hatched area). The isobaths with 1,000 m intervals, the SB (red curve), and the ASC axis (blue curve) are also plotted. The horizontal axes of (a)–(c) are shared.

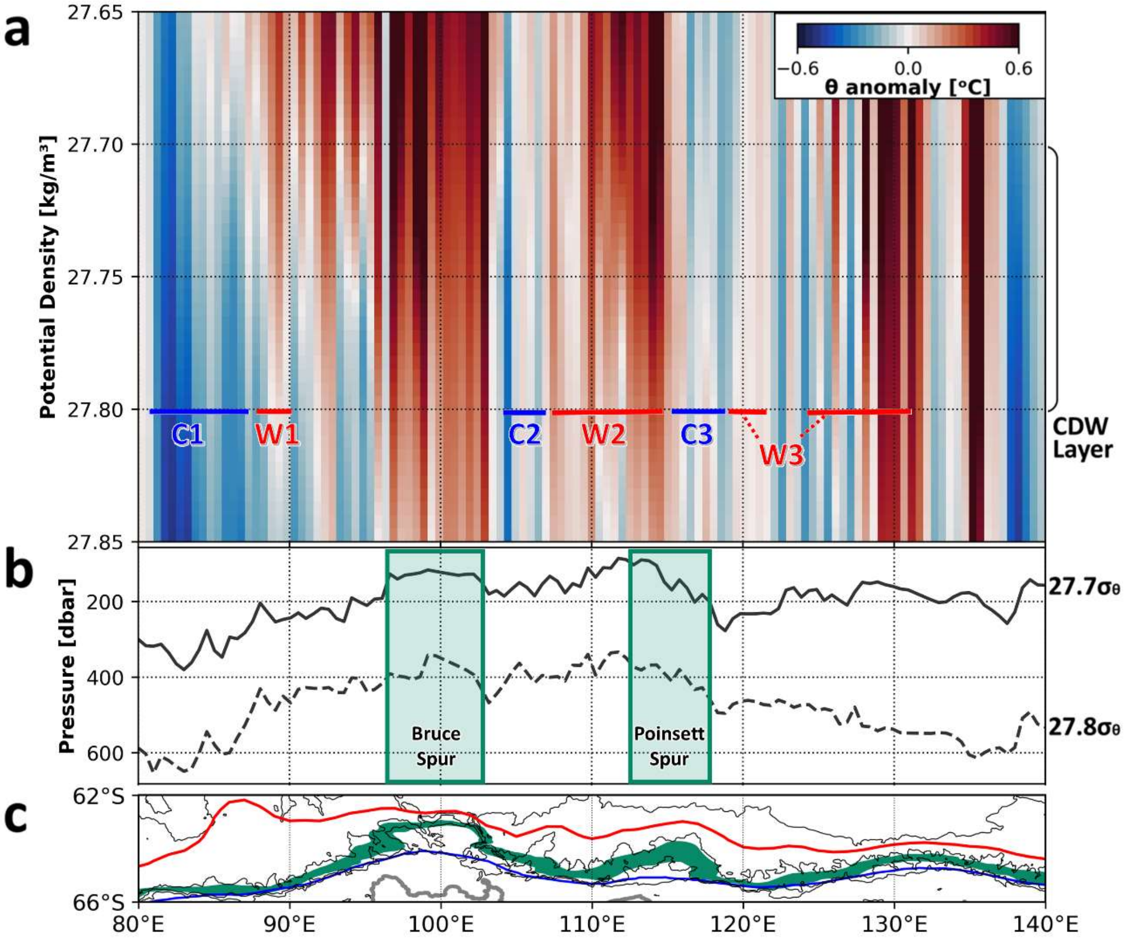

Figure 12. Potential temperature (right) and salinity (left) profiles on the continental slope (2,200–2,800 m) corresponding to each warm/cold signal in Fig. 10a (red and blue curves, respectively). They are divided into three panels corresponding to the location: (a) the Princess Elizabeth Trough, (b) the Vincennes Bay, and (c) off the Sabrina and Banzare Coasts. The isobaric average of all profiles is given by white broken curve. The potential density of 27.7 kg/m^3 and 27.8 kg/m^3 are overlaid (circles and triangles, respectively). For panel (c), cold water to the east of 120°E is also presented (black curve) to demonstrate the large along-slope variation at the location.

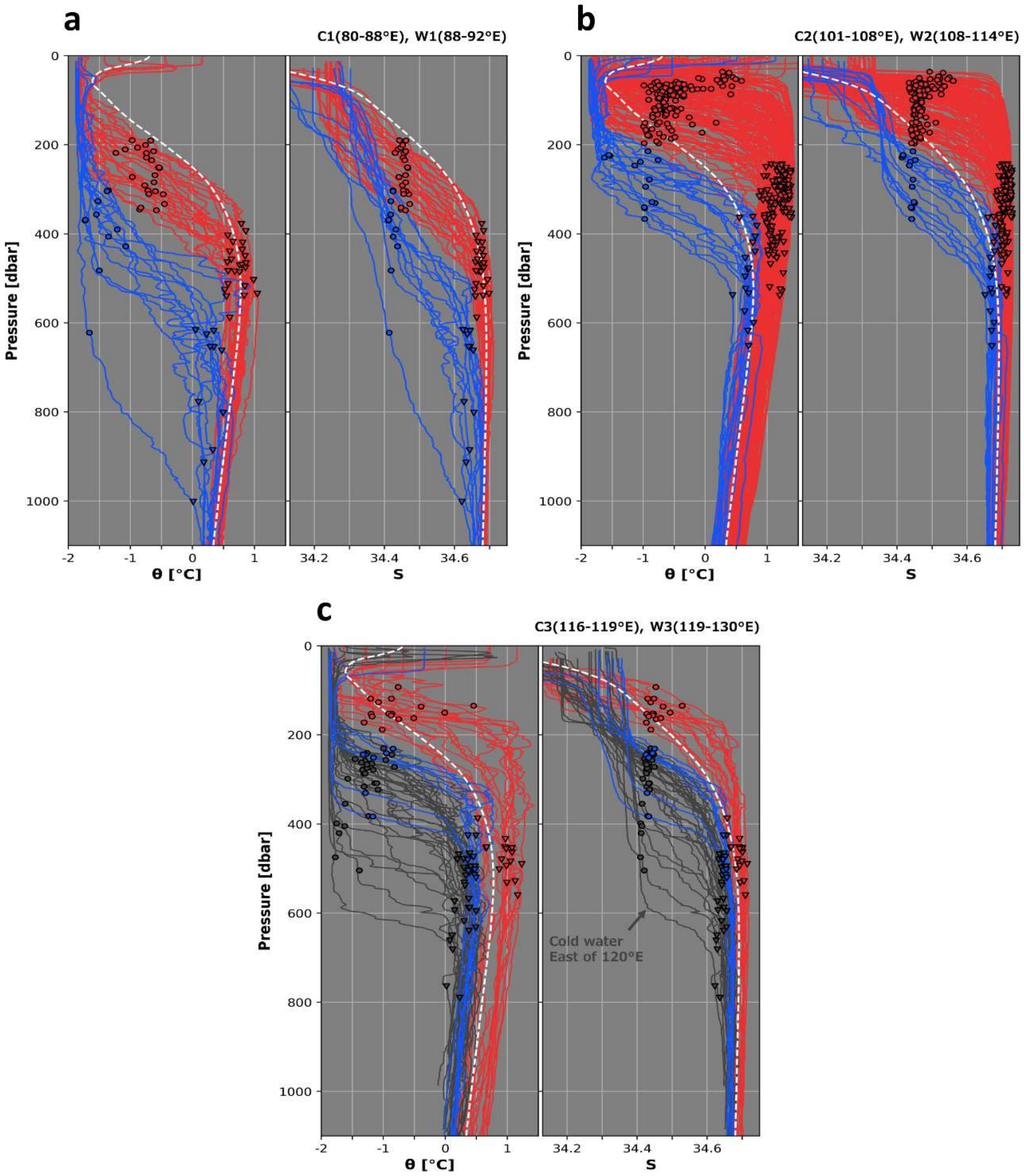

Figure 13. Schematic of the subpolar gyre in the AAB associated with the subsurface water exchange (represented by the isopycnal layer of 27.7–27.8 kg/m^3). Arrows are based on the velocity field (Figs. 5 and 6), and the background color corresponds to the potential temperature (Fig. 10a). The bathymetry is drawn by 1,000 m intervals (white contour). See the annotations in Figs. 5b, 10a, and 11a to check how each feature is consistently subscripted.

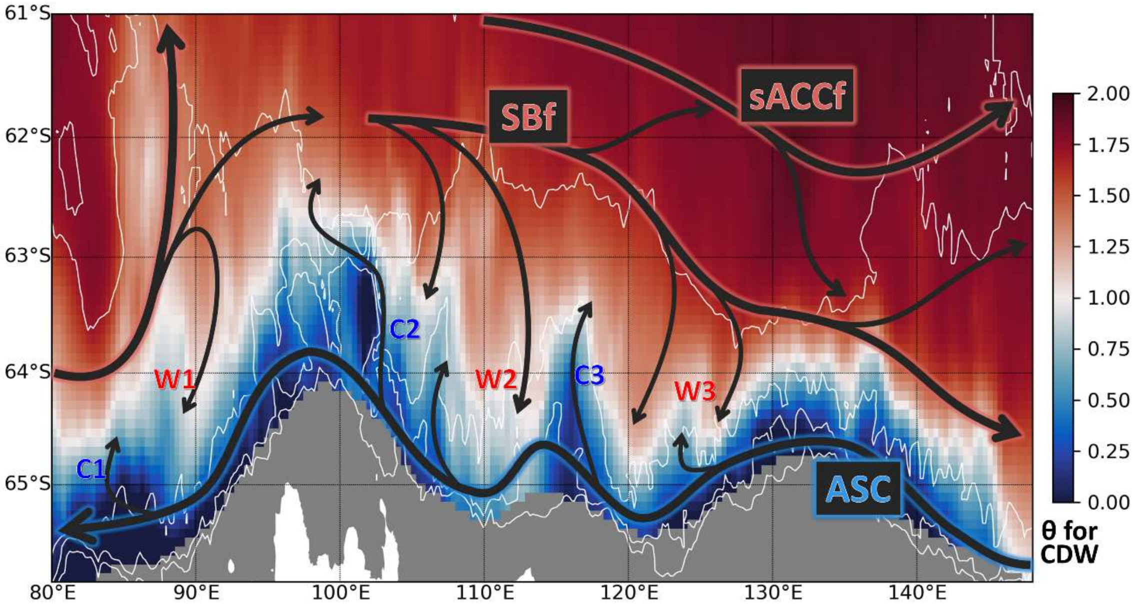

Table A1. The mean positional errors (in kilometers) and their standard deviation (*SD*) by the linear and terrain-following interpolations derived from interpolating tests using the satellite-positioned data. The *cycle* is the length of the interpolation period, and *N* is the number of test samples for each period. *RMS distance* is the root-mean-square of the longitudinal/latitudinal errors, which provides the nondirectional error measurement.

			Zonal distance		*Meridional distance*		*RMS distance*	
method	*cycle*	*N*	*Mean*	*SD*	*Mean*	*SD*	*Mean*	*SD*
Linear	1	2718	8.9	9.9	8.0	8.8	8.5	9.4
	3	1828	14.1	17.1	12.4	14.0	13.3	15.6
	5	1313	17.6	21.8	15.6	18.1	16.6	20.1
	9	724	23.5	27.4	21.3	24.5	22.4	26.0
	19	232	38.4	41.4	34.0	38.4	36.3	39.9
	29	102	64.9	63.3	49.2	44.8	57.6	54.9
	39	56	105.6	94.1	62.8	51.6	86.9	75.9
Terrain	1	2718	9.2	9.6	9.2	11.9	9.2	10.8
	3	1828	14.1	15.8	13.5	17.4	13.8	16.6
	5	1313	17.6	20.6	17.8	23.1	17.7	21.9
	9	724	23.5	26.3	22.4	28.3	23.0	27.3
	19	232	39.5	41.9	35.3	44.7	37.4	43.3
	29	102	65.4	65.9	47.8	48.0	57.3	57.6
	39	56	93.0	83.6	57.9	53.8	77.5	70.3

Figure A1. The terrain-following interpolation scheme. Panels (a) and (b) describe the first iteration. Blue stars are accurately-positioned points and blue dots are linearly interpolated positions for the position-lacking data. The scheme gives positions to minimalize the depth difference from the referential bottom depth within the search range. For the first iteration, search ranges are located on the tangential axis extended from the previous point. In some cases, the first iteration yields erroneous points due to the excessive distance (gap) between the estimated position and the actual endpoint (Case 2: (c) and (d)), and further step is required to reduce the gap. (c) The revising section is bounded by two straight lines extended from the endpoint with the angle α, enabling to find the acceptable points. (d) Then, the second iteration is conducted about a new linear path drawn between the last acceptable position and the endpoint.

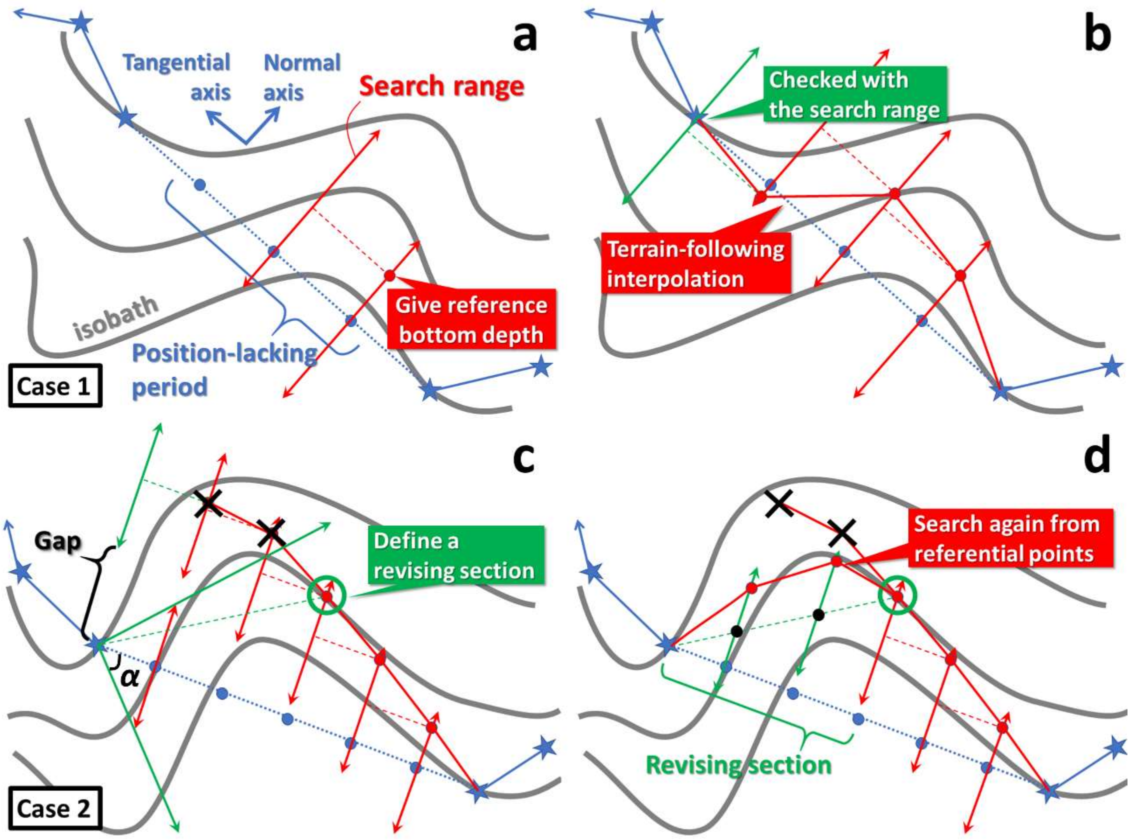

Figure A2. Description of test data for error estimation. (a) Interpolation test examples. Two sets of the test data with 19 interpolation cycles are presented in different colors (blue and red; the float ID 2900129 and 2900114, respectively). Solid lines are true trajectories and black dots denote the position of each profile. Arrows indicate the direction to travel. Interpolated positions obtained by the terrain-following method are colored circles, whereas the linear paths between the endpoints are shown by dotted lines. Bathymetric contours are presented by 500 m intervals. (b) All positioned data used in the interpolation tests (green dots), extracted from a circumpolar region south of 63°S with sea depth shallower than 3,000 m (white contour denotes the 3,000 m isobath).

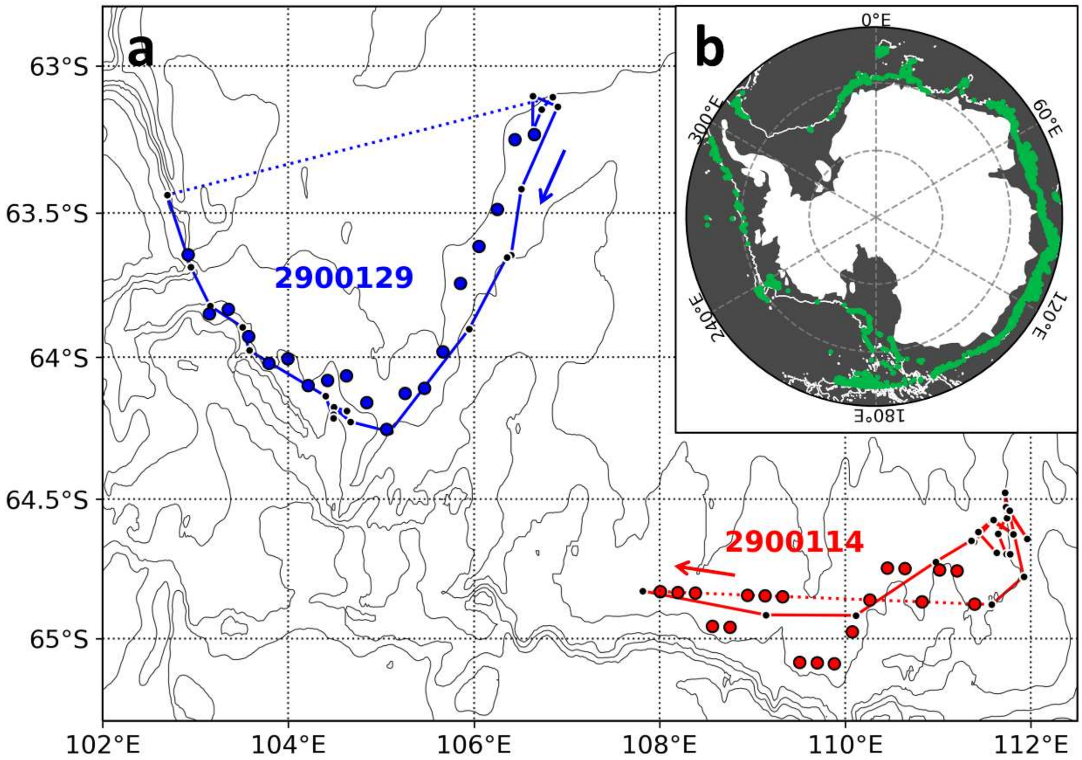

Figure A3. Mean position error due to the position-lacking data per bin (2.5° in longitude and 0.25° in latitude). (a) For the velocity data, which include the accurately-positioned and well-positioned data. (b) For the CTD data, which include the mal-positioned data as well. The error of the position-lacking data was estimated by the interpolation tests (RMS distance in Table A1). The accurately-positioned data were assumed no position error.

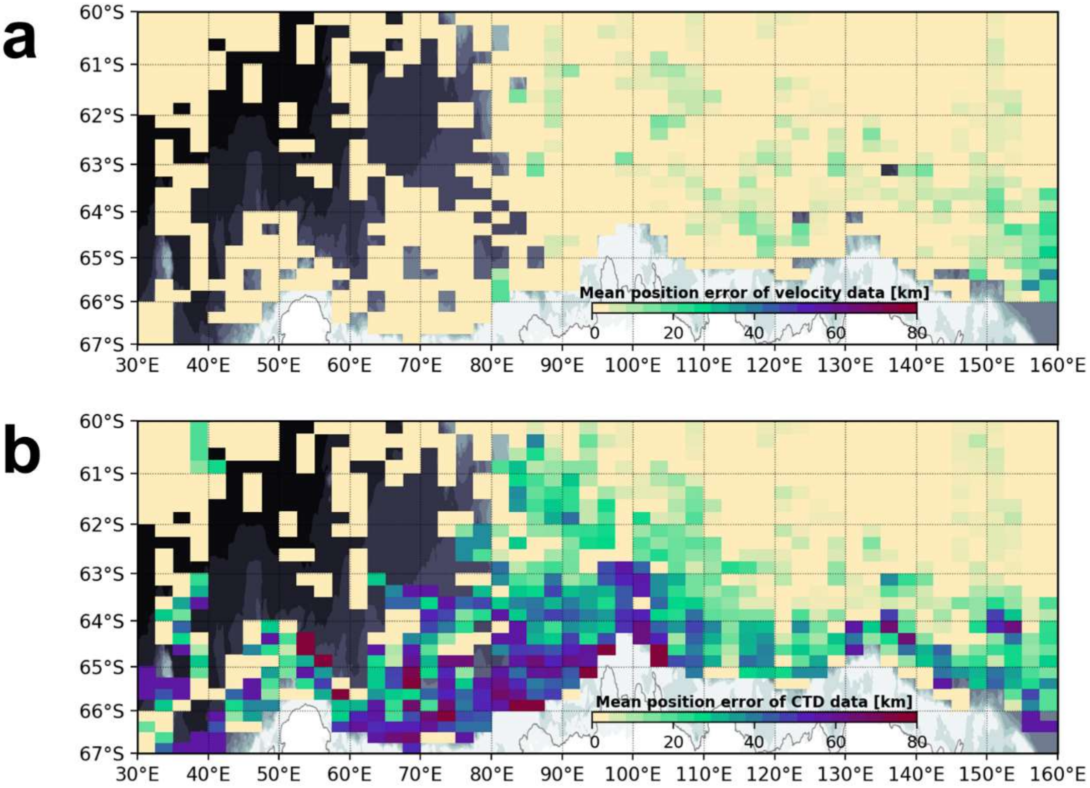

Figure B1. Histogram of residuals of the original data from the two-dimensionally gridded values for (a) zonal and (b) meridional velocity at 1,000 dbar, and (c) potential temperature within the CDW layer (27.7–27.8 kg/m^3 σ_θ). Residuals for sea depths shallower (deeper) than 3,000 m shown in blue (red). The range of one standard deviation is shown by broken vertical lines in the corresponding color. Bin sizes of histogram are (a): 0.2 cm/s, (b): 0.2 cm/s, and (c): 0.01°C.

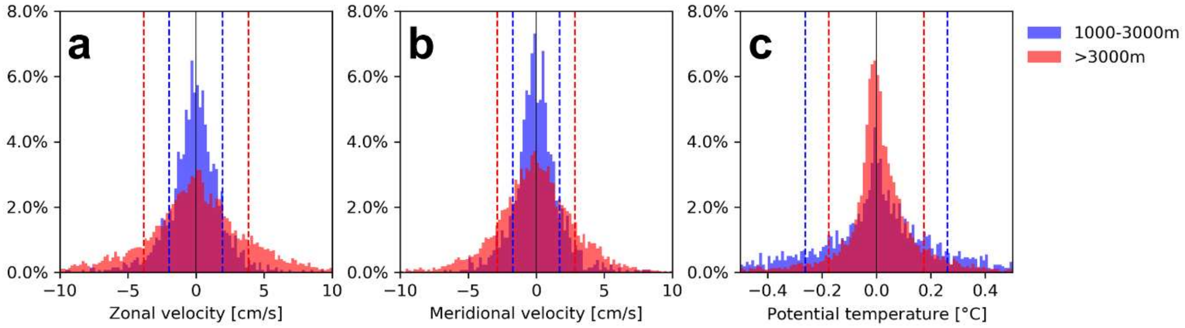

Figure B2. Absolute deviations from the interpolated surface (= absolute values of the residuals in Fig. B1) for (a) zonal and (b) meridional velocity at 1,000 dbar, and (c) isopycnal temperature for the CDW layer (their counterparts are Figs. 6a, 6b, and 10a, respectively). They approximate the standard deviation of each parameter. Red, blue, and black curves denote the SB, the ASC axis, and the 3,000 m isobath, respectively.

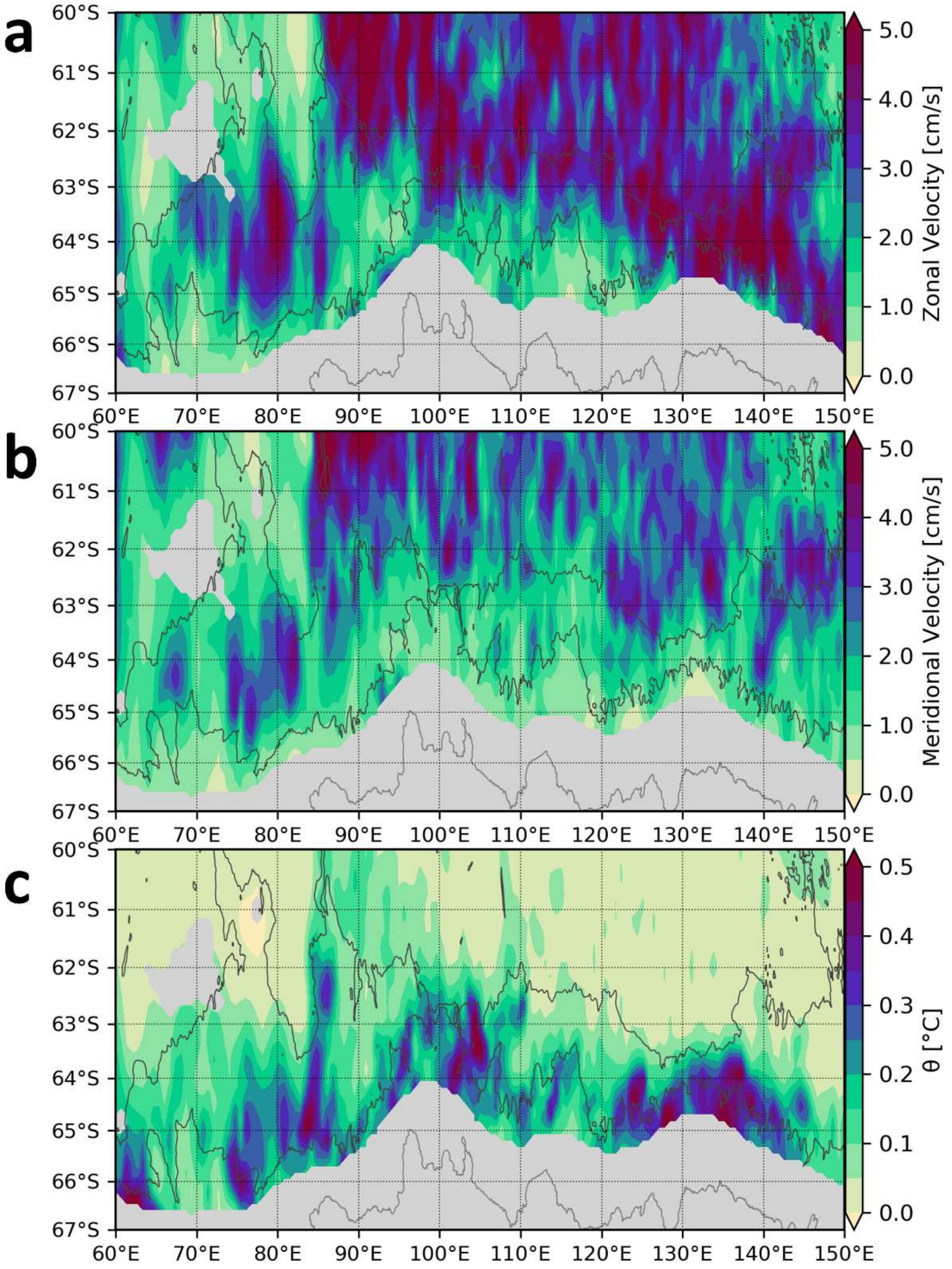

Figure C1. The difference of the presented mean fields from the results derived from the accurately-positioned data alone; for (a) zonal and (b) meridional velocity at 1,000 dbar, and (c) potential temperature within the CDW layer (their counterparts are Figs. 6a, 6b, and 10a, respectively).

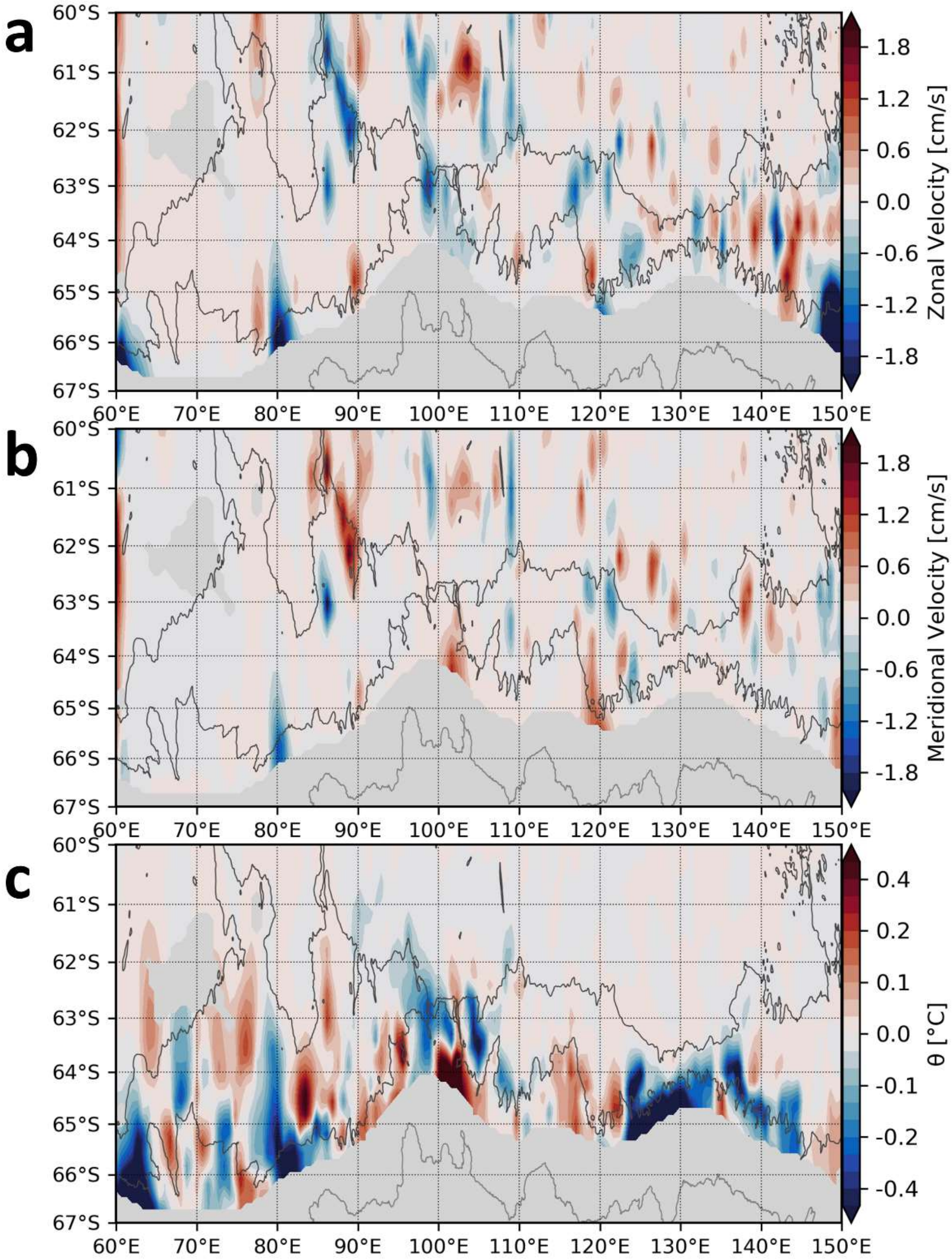

References and notes

Aoki, S., Kobayashi, R., Rintoul, S. R., Tamura, T., and Kusahara, K. (2017). Changes in water properties and flow regime on the continental shelf off the Adélie/George VLand coast, East Antarctica, after glacier tongue calving. Journal of Geophysical Research: Oceans, 122(8), 6277–6294.

Aoki, S., Sasai, Y., Sasaki, H., Mitsudera, H., and Williams, G. D. (2010). The cyclonic circulation in the Australian–Antarctic basin simulated by an eddy-resolving general circulation model. Ocean Dynamics, 60(3), 743–757.

Argo. (2018). Argo float data and metadata from Global Data Assembly Centre (Argo GDAC). Downloaded on December 28th, 2018. https://doi.org/10.17882/42182

Bindoff, N. L., Rosenberg, M. A., and Warner, M. J. (2000). On the circulation and water masses over the Antarctic continental slope and rise between 80 and 150°E. Deep Sea Research Part II: Topical Studies in Oceanography, 47(12–13), 2299–2326.

Brown, P. J., Meredith, M. P., Jullion, L., Naveira Garabato, A., Torres-Valdes, S., Holland, P., Leng, M. J., and Venables, H. (2014). Freshwater fluxes in the Weddell Gyre: results from 18O. Philosophical Transactions of the Royal Society A: Mathematical, Physical and Engineering Sciences, 372(2019), 20130298–20130298.

Chamberlain, P. M., Talley, L. D., Mazloff, M. R., Riser, S. C., Speer, K., Gray, A. R., and Schwartzman, A. (2018). Observing the Ice-Covered Weddell Gyre With Profiling Floats: Position Uncertainties and Correlation Statistics. Journal of Geophysical Research: Oceans, 123(11), 8383–8410.

Couldrey, M. P., Jullion, L., Naveira Garabato, A. C., Rye, C., Herráiz-Borreguero, L., Brown, P. J., Meredith, M. P., and Speer, K. L. (2013). Remotely induced warming of Antarctic Bottom Water in the eastern Weddell gyre. Geophysical Research Letters, 40(11), 2755–2760.

Foppert, A., Rintoul, S. R., and England, M. H. (2019). Along‐Slope Variability of Cross‐Slope Eddy Transport in East Antarctica. Geophysical Research Letters, 46(14), 8224‐8233.

Fukamachi, Y., Wakatsuchi, M., Taira, K., Kitagawa, S., Ushio, S., Takahashi, A., Oikawa, K., Furukawa, T., Yoritaka, H., Fukuchi, M., and Yamanouchi, T. (2000). Seasonal variability of bottom water properties off Adélie Land, Antarctica. Journal of Geophysical Research: Oceans, 105(C3), 6531–6540.

Goddard, P. B., Dufour, C. O., Yin, J., Griffies, S. M., and Winton, M. (2017). CO2-Induced Ocean Warming of the Antarctic Continental Shelf in an Eddying Global Climate Model. Journal of Geophysical Research: Oceans, 122(10), 8079–8101.

Gordon, A. L., Martinson, D. G., and Taylor, H. W. (1981). The wind-driven circulation in the Weddell-Enderby Basin. Deep Sea Research Part A, Oceanographic Research Papers, 28(2), 151–163.

Gouretski, V. (1999). The Large-Scale Thermohaline Structure of the Ross Gyre. In Oceanography of the Ross Sea Antarctica (pp. 77–100). Milano: Springer Milan.

Greenbaum, J. S., Blankenship, D. D., Young, D. A., Richter, T. G., Roberts, J. L., Aitken, A. R. A., Legresy, B., Schroeder, D. M., Warner, R. C., van Ommen, T. D., and Siegert, M. J. (2015). Ocean access to a cavity beneath Totten Glacier in East Antarctica. Nature Geoscience, 8(4), 294–298.

Guo, G., Shi, J., Gao, L., Tamura, T., and Williams, G. D. (2019). Reduced Sea Ice Production Due to Upwelled Oceanic Heat Flux in Prydz Bay, East Antarctica. Geophysical Research Letters, 46(9), 4782–4789.

Heywood, K. J., Sparrow, M. D., Brown, J., and Dickson, R. R. (1999). Frontal structure and Antarctic Bottom Water flow through the Princess Elizabeth Trough, Antarctica. Deep Sea Research Part I: Oceanographic Research Papers, 46(7), 1181–1200.

Jacobs, S. S. (1991). On the nature and significance of the Antarctic Slope Front. Marine Chemistry, 35(1–4), 9–24.

Kim, Y. S., and Orsi, A. H. (2014). On the Variability of Antarctic Circumpolar Current Fronts Inferred from 1992–2011 Altimetry*. Journal of Physical Oceanography, 44(12), 3054–3071.

Kimura, S., Jenkins, A., Regan, H., Holland, P. R., Assmann, K. M., Whitt, D. B., Van Wessem, M., van de Berg, W. J., Reijmer, C. H., and Dutrieux, P. (2017). Oceanographic Controls on the Variability of Ice-Shelf Basal Melting and Circulation of Glacial Meltwater in the Amundsen Sea Embayment, Antarctica. Journal of Geophysical Research: Oceans, 122(12), 10131–10155.

Kitade, Y., Shimada, K., Tamura, T., Williams, G. D., Aoki, S., Fukamachi, Y., Roquet, F., Hindell, M., Ushio, S., and Ohshima, K. I. (2014). Antarctic Bottom Water production from the Vincennes Bay Polynya, East Antarctica. Geophysical Research Letters, 41(10), 3528–3534.

Klatt, O., Boebel, O., and Fahrbach, E. (2007). A profiling float's sense of ice. Journal of Atmospheric and Oceanic Technology, 24(7), 1301–1308.

Kobayashi, T. (2018). Rapid volume reduction in Antarctic Bottom Water off the Adélie/George V Land coast observed by deep floats. Deep Sea Research Part I: Oceanographic Research Papers, 140(July), 95–117.

Kusahara, K., and Hasumi, H. (2014). Pathways of basal meltwater from Antarctic ice shelves: A model study. Journal of Geophysical Research: Oceans, 119(9), 5690–5704.

Large, W. G., and Yeager, S. G. (2009). The global climatology of an interannually varying air–sea flux data set. Climate Dynamics, 33(2–3), 341–364.

Lebedev, K. V, Yoshinari, H., Maximenko, N. A., and Hacker, P. W. (2007). YoMaHa'07: Velocity data assessed from trajectories of Argo floats at parking level and at the sea surface. IPRC Technical Note No. 4(2). available at: http://apdrc.soest.hawaii.edu/

McCartney, M. S., and Donohue, K. A. (2007). A deep cyclonic gyre in the Australian–Antarctic Basin. Progress in Oceanography, 75(4), 675–750.

Meijers, A. J. S., Klocker, A., Bindoff, N. L., Williams, G. D., and Marsland, S. J. (2010). The circulation and water masses of the Antarctic shelf and continental slope between 30 and. Deep Sea Research Part II: Topical Studies in Oceanography, 57(9–10), 723–737.

Mouginot, J., B. Scheuchl, and E. Rignot. (2017) MEaSUREs Antarctic Boundaries for IPY 2007-2009 from Satellite Radar, Version 2. Ice Shelf. Boulder, Colorado USA. NASA National Snow and Ice Data Center Distributed Active Archive Center. https://doi.org/10.5067/AXE4121732AD (accessed on 13th January, 2018)

Nakayama, Y., Menemenlis, D., Zhang, H., Schodlok, M., and Rignot, E. (2018). Origin of Circumpolar Deep Water intruding onto the Amundsen and Bellingshausen Sea continental shelves. Nature Communications, 9(1), 3403.

Nitsche, F. O., Porter, D., Williams, G., Cougnon, E. A., Fraser, A. D., Correia, R., and Guerrero, R. (2017). Bathymetric control of warm ocean water access along the East Antarctic Margin. Geophysical Research Letters, 44(17), 8936–8944.

Ohshima, K. I., Fukamachi, Y., Williams, G. D., Nihashi, S., Roquet, F., Kitade, Y., Tamura, T., Hirano, D., Herraiz-Borreguero, L., Field, I., Hindell, M., Aoki, S., and Wakatsuchi, M. (2013). Antarctic Bottom Water production by intense sea-ice formation in the Cape Darnley polynya. Nature Geoscience, 6(3), 235–240.

Ollitrault, M., and Rannou, J. P. (2013). ANDRO: An argo-based deep displacement dataset. Journal of Atmospheric and Oceanic Technology, 30(4), 759–788.

Orsi, A. H., Whitworth, T., and Nowlin, W. D. (1995). On the meridional extent and fronts of the Antarctic Circumpolar Current. Deep Sea Research Part I: Oceanographic Research Papers, 42(5), 641–673.

Orsi, A. H., and Wiederwohl, C. L. (2009). A recount of Ross Sea waters. Deep-Sea Research Part II: Topical Studies in Oceanography, 56(13–14), 778–795.

Park, Y.-H., and Gambéroni, L. (1995). Large-scale circulation and its variability in the south Indian Ocean from TOPEX/POSEIDON altimetry. Journal of Geophysical Research, 100(C12), 24911.

Pellichero, V., Sallée, J. B., Schmidtko, S., Roquet, F., and Charrassin, J. B. (2017). The ocean mixed layer under Southern Ocean sea‐ice: Seasonal cycle and forcing. Journal of Geophysical Research: Oceans, 122(2), 1608-1633.

Peña-Molino, B., McCartney, M. S., and Rintoul, S. R. (2016). Direct observations of the Antarctic Slope Current transport at 113°E. Journal of Geophysical Research: Oceans, 121(10), 7390–7407.

Purkey, S. G., and Johnson, G. C. (2013). Antarctic Bottom Water Warming and Freshening: Contributions to Sea Level Rise, Ocean Freshwater Budgets, and Global Heat Gain. Journal of Climate, 26(16), 6105–6122.

Reeve, K. A., Boebel, O., Kanzow, T., Strass, V., Rohardt, G., and Fahrbach, E. (2016). A gridded data set of upper-ocean hydrographic properties in the Weddell Gyre obtained by objective mapping of Argo float measurements. Earth System Science Data, 8(1), 15–40.

Rignot, E., Mouginot, J., Scheuchl, B., van den Broeke, M., van Wessem, M. J., and Morlighem, M. (2019). Four decades of Antarctic Ice Sheet mass balance from 1979–2017. Proceedings of the National Academy of Sciences, 116(4), 1095–1103.

Rodehacke, C. B., Hellmer, H. H., Beckmann, A., and Roether, W. (2007). Formation and spreading of Antarctic deep and bottom waters inferred from a chlorofluorocarbon (CFC) simulation. Journal of Geophysical Research: Oceans, 112(9), 1–17.

Rye, C. D., Naveira Garabato, A. C., Holland, P. R., Meredith, M. P., George Nurser, A. J., Hughes, C. W., Coward, A. C., and Webb, D. J. (2014). Rapid sea-level rise along the Antarctic margins in response to increased glacial discharge. Nature Geoscience, 7(10), 732–735.

Shimada, K., Aoki, S., and Ohshima, K. I. (2017). Creation of a Gridded Dataset for the Southern Ocean with a Topographic Constraint Scheme. Journal of Atmospheric and Oceanic Technology, 34(3), 511–532.

Silvano, A., Rintoul, S. R., Peña-Molino, B., and Williams, G. D. (2017). Distribution of water masses and meltwater on the continental shelf near the Totten and Moscow University ice shelves. Journal of Geophysical Research: Oceans, 122(3), 2050–2068.

Silvano, A., Rintoul, S. R., Kusahara, K., Peña-Molino, B., van Wijk, E., Gwyther, D. E., and Williams, G. D. (2019). Seasonality of Warm Water Intrusions Onto the Continental Shelf Near the Totten Glacier. Journal of Geophysical Research: Oceans, 4272–4289.

Smith, N. R., Zhaoqian, D., Kerry, K. R., and Wright, S. (1984). Water masses and circulation in the region of Prydz Bay, Antarctica. Deep Sea Research Part A, Oceanographic Research Papers, 31(9), 1121–1147.

Snow, K., Hogg, A. M., Sloyan, B. M., and Downes, S. M. (2016). Sensitivity of Antarctic Bottom Water to Changes in Surface Buoyancy Fluxes. Journal of Climate, 29(1), 313–330.

Sokolov, S., and Rintoul, S. R. (2007). Multiple Jets of the Antarctic Circumpolar Current South of Australia*. Journal of Physical Oceanography, 37(5), 1394–1412.

Sokolov, S., and Rintoul, S. R. (2009). Circumpolar structure and distribution of the Antarctic Circumpolar Current fronts: 1. Mean circumpolar paths. Journal of Geophysical Research, 114(C11), C11018.

Spence, P., Griffies, S. M., England, M. H., Hogg, A. M., Saenko, O. A., and Jourdain, N. C. (2014). Rapid subsurface warming and circulation changes of Antarctic coastal waters by poleward shifting winds. Geophysical Research Letters, 41(13), 4601–4610.

Stewart, A. L., and Thompson, A. F. (2016). Eddy Generation and Jet Formation via Dense Water Outflows across the Antarctic Continental Slope. Journal of Physical Oceanography, 46(12), 3729–3750.

Stroeve, J., and Meier., W. (2017). Sea Ice Trends and Climatologies from SMMR and SSM/I-SSMIS, Version 2., (Boulder, Colorado USA. NASA National Snow and Ice Data Center Distributed Active Archive Center.). https://doi.org/10.5067/EYICLBOAAJOU (accessed on 13th January, 2018)

Tamura, T., Ohshima, K. I., Fraser, A. D., and Williams, G. D. (2016). Sea ice production variability in Antarctic coastal polynyas. Journal of Geophysical Research: Oceans, 121(5), 2967–2979.

Thompson, A. F., Stewart, A. L., Spence, P., and Heywood, K. J. (2018). The Antarctic Slope Current in a Changing Climate. Reviews of Geophysics, 56(4), 741–770.

Vennell, R., and Beatson, R. (2006). Moving vessel acoustic Doppler current profiler measurement of tidal stream function using radial basis functions. Journal of Geophysical Research, 111(C9), C09002.

Wakatsuchi, M., Ohshima, K. I., Hishida, M., and Naganobu, M. (1994). Observations of a street of cyclonic eddies in the Indian Ocean sector of the Antarctic Divergence. Journal of Geophysical Research, 99(C10), 20417.

Whitworth, T., Orsi, A. H., Kim, S.-J., Nowlin, W. D., and Locarnini, R. A. (1998). Water masses and mixing near the Antarctic slope front. In Ocean, Ice, and Atmosphere: Interactions at the Antarctic Continental Margin, Antarctic Research Series Vol. 75, 1–27.

van Wijk, E. M., and Rintoul, S. R. (2014). Freshening drives contraction of Antarctic Bottom Water in the Australian Antarctic Basin. Geophysical Research Letters, 41(5), 1657–1664.

Williams, G. D., Aoki, S., Jacobs, S. S., Rintoul, S. R., Tamura, T., and Bindoff, N. L. (2010). Antarctic Bottom Water from the Adélie and George V Land coast, East Antarctica (140–149°E). Journal of Geophysical Research, 115(C4), C04027.

Williams, G. D., Meijers, A. J. S., Poole, A., Mathiot, P., Tamura, T., and Klocker, A. (2011). Late winter oceanography off the Sabrina and BANZARE coast (117–128°E), East Antarctica. Deep Sea Research Part II: Topical Studies in Oceanography, 58(9–10), 1194–1210.

Williams, G. D., Herraiz-Borreguero, L., Roquet, F., Tamura, T., Ohshima, K. I., Fukamachi, Y., ... and Hindell, M. (2016). The suppression of Antarctic bottom water formation by melting ice shelves in Prydz Bay. Nature Communications, 7(1), 1-9.

Wong, A. P. S., and Riser, S. C. (2011). Profiling Float Observations of the Upper Ocean under Sea Ice off the Wilkes Land Coast of Antarctica. Journal of Physical Oceanography, 41(6), 1102–1115.

Wong, A. P. S., and Riser, S. C. (2013). Modified shelf water on the continental slope north of Mac Robertson Land, East Antarctica. Geophysical Research Letters, 40(23), 6186–6190.

This chapter is adopted from:

Yamazaki, K., Aoki, S., Shimada, K., Kobayashi, T., and Kitade, Y. (2020). Structure of the subpolar gyre in the Australian‐Antarctic Basin derived from Argo floats. Journal of Geophysical Research: Oceans, 125(8), e2019JC015406.

(This page is intentionally set blank)

2

MULTIDECADAL POLEWARD SHIFT OF THE SOUTHERN BOUNDARY OF ANTARCTIC CIRCUMPOLAR CURRENT

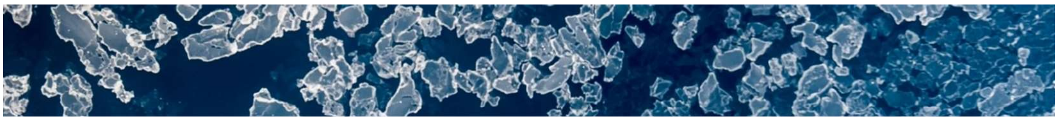

Abstract

The Southern Boundary (SB) of the Antarctic Circumpolar Current, the southernmost extent of the upper overturning circulation, regulates the Antarctic thermal conditions. The SB's behavior remains unconstrained since it does not have a clear surface signature. Revisited hydrographic data from off East Antarctica indicate full-depth warming from 1996 to 2019, concurrent with an extensive poleward shift of the SB subsurface isotherms (> 50 km), which is most prominent at 120°E off the Sabrina Coast. The SB shift is attributable to enhanced upper overturning circulation and a depth-independent frontal shift, generally accounting for 30% and 70%, respectively. Thirty years of oceanographic data corroborate the overall and localized poleward shifts that are likely controlled by continental slope topography. Numerical experiments successfully reproduce this locality and demonstrate its sensitivity to mesoscale processes and wind forcing. The poleward SB shift under intensified westerlies potentially induces multidecadal warming of Antarctic shelf water.

2.1 Background

In recent decades, the Southern Ocean has undergone widespread but spatially heterogeneous warming. In the northern part of the Antarctic Circumpolar Current (ACC, 45°–55°S), the temperature of the upper 1,000 m has increased rapidly (0.1°–0.2°C per decade), partly due to enhanced surface heat uptake (Sallée, 2018). In contrast, multidecadal warming in the southern part of the ACC (55°–65°S, subpolar zone), is confined to a deeper layer (below 200 m) and is relatively gradual (~0.1°C per decade; Sallée, 2018; Schmidtko et al., 2014; Auger et al., 2021; Aoki et al., 2005; Strass et al., 2020). Upwelling of subsurface cold water (< 0°C), reinforced by intensified westerlies, has cooled the subpolar ocean surface (Armour et al., 2016). Deep warm salty water (below 200 m, temperature > 0°C, salinity > 34.85 g kg^{-1}), called Circumpolar Deep Water (CDW), compensates volumetrically for the near-surface divergence, and subsequent enhancement of poleward CDW upwelling may lead to warming below 200 m. CDW primarily supplies heat to the Antarctic continental shelves. Thus, multidecadal warming of the subpolar CDW layer has enormous implications for Antarctic ice shelves (Gille et al., 2016), global overturning circulation (Morrison et al., 2020), and marine ecosystems (Tynan, 1998).

Poleward CDW upwelling constitutes the upper and lower cells of the global overturning circulation (Marshall and Speer, 2012). The poleward flank of the upper meridional overturning circulation has been identified as the southernmost extent of the oxygen-depleted layer, which dynamically corresponds to the Southern Boundary (SB) of the ACC (Orsi et al., 1995). The SB is represented by the poleward limit of the 1.5°C isotherm in Upper CDW (Orsi et al., 1995). In the upper overturning circulation, baroclinic (with depth-dependent structure) eddies transport CDW poleward, as the potential energy imposed by the westerlies is released through baroclinic instability (Gille et al., 2016, Marshall and Speer, 2012). Given the lagged correlation between eddy kinetic energy and surface winds (Hogg et al., 2015; Meredith and Hogg, 2006) and isopycnal temperature increases (Meijers et al., 2011), we expect that the multidecadal warming of the CDW layer is associated with enhanced eddy fluxes in response to wind intensification. Despite this dynamic background, the role of eddies in the multidecadal trend of wind-driven upper overturning circulation is not evident. CDW upwelling has been hypothesized to react to wind changes more slowly than the immediate response of surface water (Ferreira et al., 2015), whereas the contributions of eddy fluxes to multidecadal warming have not been constrained by previous studies that used both idealized ACC simulations and coupled climate models (Doddridge et al., 2019). In addition to eddy transport, the poleward displacement of the ACC fronts also results in warming of the CDW layer. The zonally averaged ACC position has not shifted decadally (Gille et al., 2016; 1992–2013) under the intensified westerlies (Swart et al., 2015; from 1990 onwards). However, this stability of the ACC does not preclude any regional trends (Meredith, 2016) because the bathymetry globally steers zonal asymmetry of the ACC through its barotropic (depth-independent) nature (Thompson and Naveira Garabato, 2014; Nadeau and Ferrari, 2015).

Historical temperature records from the Southern Ocean have indicated significant warming of CDW off East Antarctica over the past several decades (Schmidtko et al., 2014; Aoki et al., 2005). Hydrography of the eastern Indian sector of the Southern Ocean (or the Australian-Antarctic Basin; 80°–150°E) along 62°S, corresponding to the southern part of the ACC, has revealed a patchy pattern of poleward CDW migration from 1995 to 2012, which is concurrent with warming throughout the entire water column by 0.1°–0.4°C along pressure surfaces (Katsumata et al., 2015). Satellite altimetry has indicated that the Polar and Southern ACC Fronts have shifted further poleward (by 60–120 km) in the eastern Indian sector than in the other sectors from 1993 to 2010 (Kim and Orsi, 2014). Observed sea-level rise that significantly exceeds the global mean trend (1992–2011; Rye et al., 2014) supports this rapid poleward shift of ACC fronts in the eastern Indian sector. The latest reanalysis of a 25 year record along hydrographic section at 140°E has shown that multidecadal warming of CDW around the Southern ACC Front (61°S to 55°S) dominates the interannual variability of 0.04 ± 0.01°C per decade (Auger et al., 2021) (where ± indicates one standard deviation).

Nevertheless, little is currently known about the multidecadal trend of the SB. A previous study documented that the regional sea-level rise of 3.4 ± 0.48 cm from 1996 to 2008 in the western Indian sector (30°–80°E) is equivalent to a poleward SB shift of 100–200 km (Counldrey et al., 2013). However, the meridional location of the SB derived from hydrographic data often differs by more than 100 km from the location derived from altimetry (Counldrey et al., 2013). The effects of global sea-level rise and increased freshwater discharges from land ice account for a substantial portion of the altimetric change (Rye et al., 2014). Regarding the physical configuration of the SB, which does not necessarily follow a geostrophic jet detectable by a peak in the sea surface height gradient (Chapman et al., 2020), the use of satellite altimetry alone is insufficient to determine its variability. Therefore, we analyze the ocean interior to examine the connection between the SB and the multidecadal warming in the subpolar zone.

Off East Antarctica (including eastern/western Indian sectors), the SB is located along the center of subpolar gyres and is meridionally bounded by the offshore ACC and the shoreward Antarctic Slope Current (Chapter 1; Mizobata et al., 2020). Subpolar gyres are clockwise circulations that are typical along the continental margin near the Antarctic Divergence. At the eastern flank of the clockwise circulation, onshore CDW intrusion is maintained by southward flows that branch from the ACC (Fig. 1A; Chapter 1; Hirano et al., 2020; Nakayama et al., 2018). Motivated by the ongoing mass loss of the East Antarctic Ice Sheet and its potential impact on the global sea-level rise (Rignot et al., 2019), we delineate multidecadal changes in the SB in the eastern Indian sector. Results from hydrographic observations conducted in 2019 during the austral summer (Fig. 1A) are presented. This cruise revisited hydrographic sections surveyed in the summer of 1996 (Bindoff et al., 2000). Comparisons between the 1996 and 2019 measurements highlight a poleward shift of the SB in the eastern Indian sector and suggest possible mechanisms of observed multidecadal warming in the subpolar zone. Thirty years of oceanographic records from off East Antarctica support findings obtained from the 1996 and 2019 datasets. Furthermore, we conducted numerical experiments to investigate the possible factors controlling the changes in the SB.

2.2 Data and methods

2.2.1 Hydrographic data

High-quality hydrographic observations in the Australian-Antarctic Basin were obtained during the austral summers of 1996 (R/V Aurora-Australis: Expocode 09AR9604_1; Bindoff et al., 2000) and 2019 (R/V Kaiyo-maru: Expocode 490S20181205 and 490S20190121; documented in Aoki et al., 2020) and were compared. The year in the text denotes the new year of the season (i.e., cruises from December 2018 to March 2019 are denoted as 2019). Both hydrographic datasets are available through the CLIVAR (Climate and Ocean: Variability, Predictability and Change) and Carbon Hydrographic Data Office website (https://cchdo.ucsd.edu/). The position of the SB was determined in each meridional section as the southernmost extent of the 1.5°C isotherm. Temperature values of the temperature maximum surface at each station were linearly interpolated to obtain the meridional temperature profile. The poleward limit of the 1.5°C isotherm was then determined from the interpolated profile. For the 1996 observations, the SB at 150°E did not correspond to the southernmost isotherm isolated by the cold eddy at 64.6°S. This choice of SB is supported by the robust isobaric/isopycnal temperature increases from 1996 to 2019 (Figs. 2A and 3A) and the smoothed meridional profile of the dynamic height (Fig. 2C) along this section. The accuracies of the temperature and salinity data from the two measurements are ~0.002°C and ~0.003 g kg^{-1}, respectively. We used the thermodynamic equation of state TEOS-10 (http://teos-10.org/) for the analysis. Bathymetric data shown in the figures are the General Bathymetric Chart of the Oceans website (https://www.gebco.net/).

2.2.2 Isopycnal analysis

To determine the cause of the isopycnal water property changes, the following derivative rule was applied for the isopycnal temperature change:

$$\mathrm{d}\Theta_{\mathrm{y}} = \mathrm{d}\Theta_{\psi} + \left.\frac{\mathrm{d}\Theta}{\mathrm{d}\psi}\right|_{\mathrm{y}} \mathrm{d}\psi_{\mathrm{y}} \quad \text{(i)}$$

where Θ, y, ψ are the Conservative Temperature, latitude, and dynamic height, respectively, and the subscript denotes manipulation by fixing the variable. The left-hand side of Equation (i) is the Eulerian change on the latitude coordinates, simply the observed isopycnal change. The first term on the right-hand side corresponds to the along-streamline water transformation term, i.e., the temperature change along the geostrophic contour of the barotropic ACC front ψ. The second term is the temperature change due to the meridional shift of ψ, referred to as the frontal shift term. The frontal shift term was explicitly calculated, whereas the water transformation term was derived as the residual of Equation (i). The dynamic height at 300–1,800 dbar was adopted as the proxy for ψ based on the fact that the dynamic height above 2,000 dbar accurately represents the position of the barotropic ACC fronts (Chapter 1). The dynamic height was calculated by vertically integrating the specific volume (inverse potential density anomaly). The presented results are not sensitive to the choice of depth range, while the temperature above 300 dbar may have been more influenced by short-lived surface features than by the frontal position. To estimate the dynamic height change on the latitude coordinates, the meridional profile of the dynamic height was created by fitting the dynamic height value at each station with a quartic polynomial curve (Fig. 2C). This fitting smoothed out eddy-like features that are irrelevant to the frontal position (e.g., cold eddy at 150°E during the 1996 observations) and enabled us to obtain dynamic height profiles monotonically increasing northward. Using the meridional dynamic height profiles, the mean isopycnal temperature gradients on the ψ coordinates were calculated, and subsequently, the frontal shift term was derived.

2.2.3 Historical data analysis

A dataset of Conservative Temperature on the temperature maximum surface (which characterizes Upper CDW) was constructed from the historical data from 1990 to 2019 (Figs. 4, 5, and 6A). This dataset comprises shipboard conductivity-temperature-depth (CTD), eXpendable CTD (XCTD), Argo float, and biologging profiles. The shipboard CTD, XCTD, and float data used in the analysis are available through the National Centers for Environmental Information (https://www.ncei.noaa.gov/) and the Japanese Institute of Cetacean Research (https://icrwhale.org/) websites, and the biologging data are available through the Marine Mammals Exploring the Oceans Pole to Pole website (http://www.meop.net/). First, the temperature profiles were vertically interpolated every 1 dbar using Akima-interpolation. The targeted temperature was extracted as the temperature maximum in the interpolated vertical profile below the temperature minimum above 500 dbar. When calculating the Conservative Temperature, a climatological salinity field from the gridded climatological dataset (Shimada et al., 2017) was used. The consistency of the climatological position of the SB reproduced from this climatological product supports its fidelity (Figs. 1A and 5). The error associated with this treatment of salinity data has only a minor effect on the Conservative Temperature relative to the measurement error of the dataset (accurate to 0.01°C). The errors in the pressure/depth measurements are also negligible for the Conservative Temperature values at the detected temperature maximum surface. Objective mapping of the sparsely distributed surface data onto

1/4° grids was performed using radial basis function interpolation with a linear weighting function, which can smoothly interpolate noisy data in a least-squares sense (Chapter 1). Areas with less than 3 data points within a radius of 150 km from the grid point were masked (Figs. 4 and 5). The standard deviation of the meridional position of the SB (Fig. 7A) was derived as follows: the interpolated absolute deviation (residuals) of the temperature maximum surface was first calculated as the root-mean-square residual from the objectively mapped surface of the climatological dataset. Second, the mean temperature gradient of the objectively interpolated field was calculated to derive the standard deviation of the horizontal displacement of the SB. By multiplying this by the meridional factor of the mean temperature gradient vector at each location, we obtained the standard deviation of the meridional position of the SB as 56 ± 10 km between 100°–150°E (Fig. 7A). This analysis enabled us to evaluate the significance of the multidecadal poleward shift of the SB recorded in the historical data. To determine the statistic applicable for Welch's t-test of the objectively interpolated fields (Figs. 5D and 5E), we made two assumptions: 1) the interpolated absolute deviation closely approximates the standard deviation field, 2) the sample size in each grid is given by the number of surface data points within a radius of 150 km from the grid point.

2.2.4 Numerical simulations

High-resolution numerical simulations were conducted using the Massachusetts Institute of Technology general circulation model (MITgcm; http://mitgcm.org/) and compared with the observed changes (Figs. 6B and 6D). The model grid size was set to nominally 1/30° (3–4 km) with 50 vertical levels. The simulation was configured with hydrostatic approximations, dynamic/thermodynamic sea ice, and a thermodynamic ice shelf. The model domain covers 90°–150°E and 60°–70°S, spanning the period from 1992 to 2017. The bathymetry was prescribed by ETOPO1 (https://ngdc.noaa.gov/mgg/), with updates from recent hydrography over the continental shelves. Since the bathymetry in the target region is consistent among the different datasets, the choice of bathymetric data was unlikely to have affected our results. We adopted the ECCO estimate (https://www.ecco-group.org/), the multidecadal ocean state estimate powered by MITgcm, as the lateral boundary condition. LLC270 optimization data (nominally 1/4° grid and 50 vertical levels) were used (Zhang et al., 2018). The LLC270 data were also analyzed to evaluate the simulation's sensitivity to the grid size (Fig. 6C). Atmospheric forcing is based on the ERA-Interim reanalysis data (https://www.ecmwf.int/). Initial conditions were derived from a 25 year spin-up from an initial resting state. As we did for the in-situ historical data, the output was vertically interpolated every one dbar using Akima-interpolation to precisely derive the temperature maximum surface. The halved wind experiment (Fig. 6D) was performed by setting the overall scaling of the neutral drag coefficient (“exf_scal_BulkCdn”) to 0.5, which halved the air–sea interfacial stress.

2.3 Results

2.3.1 Water column property trends from 1996 to 2019

The revisited meridional sections are located over the continental slope between the 1,000–4,000 m isobaths, with zonal intervals of 10° (Fig. 1A). The temperature maximum layer (represented by 1.5°C) presents around the 28.0 kg m^{-3} neutral density unit, which characterizes the upper meridional overturning (Marshall and Speer, 2012). The salinity maximum layer (represented by 34.89 g kg^{-1} Absolute Salinity) presents around the 28.1 kg m^{-3} isopycnal, which characterizes the lower meridional overturning. The abyssal oxygen-rich, cold, fresh water is Antarctic Bottom Water (AABW), which is present below the 28.2 kg m^{-3} isopycnal (defined by the extent of the salinity maximum layer). The 1.5°C isotherm observed in 2019 agrees with the 195 μmol kg^{-1} dissolved oxygen contour where the oxygen-depleted layer abruptly attenuates poleward (Fig. 1B). The oxygen value at the southernmost extent of the 1.5°C isotherm coincides with the original description by Orsi et al. (1995) and the 1996 measurements (Bindoff et al., 2000), underpinning the oxygen invariance along the isotherm required for a proxy of the SB. Thus, we define the SB as the poleward limit of the 1.5°C isotherm for the following analyses.

A poleward shift of the SB by 50–120 km is observed in the five meridional sections between the 1996 and 2019 measurements, with an isobaric temperature increase in the upper 1,500 dbar of more than 0.1°C (Fig. 2A, Table 1). The SB shift is greater than the meridional sampling intervals (< 0.5° in latitude; indicated by triangles in Figs. 1B–1D) except 112°E, where the SB is absent in 1996. This temperature change is comparable to the reported warming of CDW further north (Schmidtko et al., 2014; Katsumata et al., 2015; Auger et al., 2020). The poleward shift of the SB is most pronounced at 120°E off the Sabrina Coast (120 km). This displacement is accompanied by a deepening of the isopycnals throughout the entire water column by 100–400 dbar, with a density decrease that exceeds 0.02 kg m^{-3}. Freshening prevails throughout most of the water column (Fig. 2B), likely associated with increased glacial water discharge (e.g., Aoki et al., 2005; Rye et al., 2014) and changes in the properties of AABW (Katsumata et al., 2015; Van Wijk and Rintoul, 2014; Purkey and Johnson, 2013). In contrast to the widespread freshening, a poleward migration of the salinity maximum layer (blue contour) appears with salinification in the CDW layer above 1,500 dbar in the vicinity of the SB (see dS_A in Table 1), and the salinification exceeding 0.06 g kg^{-1} spreads up to the surface further south of the SB at 112°, 120°, and 150°E. Although the freshening contributes to volume reduction of AABW denser than 28.2 kg m^{-3} (Rye et al., 2014; Van Wijk and Rintoul, 2014), the salinity change is not the cause of isopycnal deepening since temperature overwhelms salinity in the steric changes below 1,500 m by a factor of 6–8 (based on Table 1). The temperature-driven volume reduction of AABW is previously reported and attributed to isotherm heaving (Purkey and Johnson, 2013). We interpret the full-depth isopycnal deepening near the SB as being due to the poleward shift of the barotropic ACC fronts, which reasonably explains the isotherm heaving.

To further quantify the effects of the displacement of the barotropic ACC fronts offshore, the dynamic height (geopotential) between 300–1,800 dbar is calculated (see Materials and Methods). Air–sea interactions do not penetrate this layer because oxygen-depleted water presents at 300 dbar in the vicinity of the SB (Fig. 1B). A poleward shift of the dynamic height contour is observed in the five meridional sections as well as the 1.5°C isotherm (Fig. 2C). The SB generally corresponds to a dynamic height of 4.0–4.5 $m^2 s^{-2}$. Near the SB, the poleward shift of the dynamic height contour (40 km by the five-section average; Table 1) is comparable to but notably smaller than the displacement of the isotherm (73 km) by about 40%. Although baroclinic eddies may partially influence local dynamic height values, it is known that the dynamic height consistently reproduces the position of the barotropic ACC fronts north of the SB (Meijers et al., 2011). The SB is a baroclinic water mass boundary, not a dynamical front, and hence is not necessarily accompanied by a barotropic front (Orsi et al., 1995; Chapter 1). Orsi et al. indicated a spatial difference between the 1.5°C isotherm and the dynamic height contour in the Indian sector. Therefore, the significant disagreement between the displacements of the SB and the dynamic height contour can be explained by baroclinic changes. The isopycnal flux (due to eddies and baroclinic flows) can cause this by baroclinically transporting warm CDW poleward.

2.3.2 Frontal shifts and enhanced overturning

The poleward shift of the SB can be induced by both shifting the barotropic fronts and changing the water properties. The temperature trend is mapped onto the neutral density coordinates to eliminate transient features due to isopycnal heaving (Fig. 3A). The isopycnal analysis enables us to diagnose the cause of the meridional SB shift. Below the 28.0 kg m^{-3} isopycnal, the effect of air–sea interactions is negligible by the presence of oxygen-depleted water (Fig. 1B). Near the SB, the isopycnal temperature increases substantially in the Upper CDW layer (28.0–28.1 kg m^{-3}) by about 0.31°C (by the five-section average; Table 1), but no significant increase is visible in the Lower CDW layer (28.1–28.2 kg m^{-3}). The warming signal is generally confined above the 28.2 kg m^{-3} isopycnal (Fig. 3A), in contrast to the full-depth isobaric temperature increase (Fig. 2A). On isopycnals, a temperature change must be accompanied by a salinity change because seawater density at reference pressure is determined by temperature and salinity. Temperature decrease by 0.04°C in the AABW layer (28.2–28.3 kg m^{-3}) is thus associated with salinity decrease by 0.007 g kg -1, consistent with the previously reported freshening trend (Van Wijk and Rintoul, 2014; Purkey and Johnson, 2013).

We decompose the isopycnal temperature change into two terms: the lateral movement of the water column and the along-streamline water transformation. The former results from the displacement of barotropic ACC fronts, whereas the latter results from baroclinic changes such as enhanced isopycnal fluxes (due to eddies and baroclinic flows), buoyancy forcing (e.g., freshwater inputs), and modified mixing. The effect of the barotropic frontal shift can be quantified by assuming that the dynamic height contours (Fig. 2C) accurately represent the ACC's streamlines, which is supported by the gravest empirical mode methodology (Meijers et al., 2011). Based on this assumption, the isopycnal warming due to the barotropic frontal shift (referred to as "frontal shift term") is derived (see Materials and Methods). The frontal shift term (Fig. 3B) suggests that the poleward shift of the offshore ACC fronts generally explains the total temperature increase on isopycnals (0.21°C in Upper CDW and 0.05°C in Lower CDW; Table 1). At 64.8°S, 150°E, partial cooling occurs due to the eddy-like feature encountered in 1996 (Bindoff et al., 2000). The temperature increase due to the frontal shift term reaches the southern end of the meridional sections.

The along-streamline component of the isopycnal change (referred to as "water transformation term") is obtained as the residual term. The water transformation term (Fig. 3C) indicates that temperature decreases associated with the widespread freshening of surface, bottom, and intermediate waters counteract the isopycnal warming caused by the poleward frontal shift (Fig. 3B) and the isopycnal flux. A substantial temperature increase exceeding 0.1°C due to the water transformation term is discernable at the poleward flank of Upper CDW (Fig. 3C; between the 1.5°C isotherms in 2019 and 1996). This along-streamline warming is not apparent to the north of the SB from the 1996 measurement. To the south of the SB, warming due to the water transformation term is observed at 112°, 120°, and 150°E, but not at 128° or 140°E. Since surface forcing is negligible below the oxygen-depleted layer (Fig. 1B) and the isopycnal flux likely overwhelms the diapycnal flux within the region of interest away from topographic boundaries, the most plausible explanation for the along-frontal warming is an intensification of isopycnal transport due to enhanced upper overturning circulation, which is likely driven by the poleward eddy flux (Gille et al., 2016; Marshall and Speer, 2012). Since the mean flow is likely directed southward at 112°, 120°, and 150°E spatially associated with the southward excursion of the SB (Chapter 1), the zonal difference to the south of the SB (Figs. 2 and 3) may be attributable to changes in the subpolar gyre. A relatively small temperature increase in the water transformation term (up to 0.1°C) is observed in a few sections (e.g., 150°E) below the 28.1 kg m-3 isopycnal, where the upper overturning circulation is unlikely to affect the temperature. This change may be related to a modified mixing ratio of the locally produced AABW (Katsumata et al., 2015, Van Wijk and Rintoul, 2014) and salinification of the ambient Ross Sea Bottom Water (Aoki et al., 2020). By the five-section average (Table 1), the warming of Upper CDW associated with the poleward shift of the SB (0.31°C) is about 70% (0.21°C) due to the frontal shift term and about 30% (0.10°C) due to the water transformation term.

2.3.3 Spatial variations in the multidecadal trend

We further investigate the multidecadal temperature trends using different datasets. Historical in-situ measurements from the 1990s onwards are compiled (Fig. 4) to determine the decadal temperature variations at the subsurface temperature maximum. The climatological SB position (defined by the 1.5°C isotherm) reproduced from the compiled datasets is generally consistent with previous estimates (Fig. 1A; Chapter 1; Orsi et al., 1995). The decadal climatology further supports our finding that the SB has shifted poleward over the past three decades (Figs. 6A and 7A). We estimate the overall poleward shift from 1990–1999 to 2010–2019 as 49 ± 25 km (between 100°–150°E; see Fig. 5 for the decadal temperature fields off East Antarctica). The SB shift accompanies a significant temperature increase by 0.1°–0.6°C (95% confidence level) from 1990–1999 to 2000–2009 (Fig. 5D) and by 0.1°–0.4°C from 2000–2009 to 2010–2019 (Fig. 5E). Therefore, the comparisons of the observations made in 1996 and 2019 (Figs. 2 and 3, Table 1) very likely represent the multidecadal trend, rather than possible aliasing due to interannual variations.

The poleward displacement of the SB is the greatest at 120°E among the five meridional sections (120 km; Table 1). This regionality is consistent with the compiled historical data, which exhibit a maximum shift of ~80 km at this longitude (from 1990–1999 to 2010–2019; Figs. 6A and 7A). The displacement of the SB and the temperature increase (Figs. 5D, 5E, and 6A) are likely prominent between the topographic spurs in the continental slope (particularly at 105°, 110°, and 120°E) where the climatological SB deviates southward. The SB derived from pre-1990 data (Orsi et al., 1995) is also presented in Fig. 6A (dashed black curve). Despite the limited number of synoptic sections at the time used to determine its position (generally 10° longitude intervals), poleward shifts from the pre-1990 data are visible at 105°–120°E and east of 140°E. From the continental rise (3,000 m) to the shelf break (1,000 m) at 100°–115°E and around 125°E, the temperature increases continuously for the three decades (Figs. 5D and 5E). The localized shifts and warming patterns are likely related to the cross-slope water exchange maintained by the clockwise subgyres bounded by the continental slope (Chapter 1; Mizobata et al., 2020). The larger isotherm shifts in the CDW intruding locations may be caused by enhanced subpolar gyre transport.

Our numerical simulations with an eddy-resolving grid spacing (nominally 1/30°), laterally constrained by a simulation-based historical state estimate (ECCO: Estimating the Circulation and Climate of the Ocean, see Materials and Methods; Zhang et al., 2018), successfully reproduced the multidecadal poleward shift of the SB with a regionality similar to that of the compiled historical dataset (Figs. 6B and 7B). An overall poleward shift of 43 ± 36 km occurs from 1992–1999 to 2010–2017 at 100°–150°E, and the most prominent displacement of ~60 km occurs at 120°E. The SB is located southward of the 3,000 m isobath east of 125°E and northward of 61°S west of 100°E, possibly because the simulated subpolar gyre is stronger than the reality. Despite this inevitable difference between the simulated and observed SB positions, the multidecadal poleward shift is reproduced over a wide range of longitudes, consistent with the observations (Figs. 7A and 7B; 105°–110°E and 120°–140°E). The ECCO data used for the simulation (nominally 1/4° grid) generally reproduce the multidecadal warming of Upper CDW further north (Ferster et al., 2018). However, the poleward shift of the SB is not evident as in the eddy-resolving experiment (Figs. 6B and 6C). This result may be caused by differences in the model configuration or the grid spacing since mesoscale processes with a horizontal scale of ~10 km (Mckee et al., 2019) are not resolved in the 1/4° grid. The barotropic transport of the simulated subpolar gyre significantly increases from 1992–1999 to 2010–2017 (between 115°–125°E; Fig. 8). This result is consistent with that of a circumpolar study, in which the intensified westerlies yielded enhanced gyre transport (Kusahara, 2020). Furthermore, halving the air–sea drag coefficient in the simulation (see Materials and Methods), which effectively halves the eastward wind stress over the ACC, qualitatively modifies the locality in the trend (Fig. 6D). The poleward shift at 120°–125°E disappears, whereas the position of the SB between 110°–120°E changes from along-slope to cross-slope and becomes temporally transient. This experiment suggests that the multidecadal trend is partially driven by regional wind forcing, which likely alters shoreward eddy transport (Gille et al., 2016; Hogg et al., 2015; Meredith and Hogg, 2006) and the strength of the barotropic flow (Langlais et al., 2015; Naveira Garabato et al., 2019).

2.4 Discussion and conclusion

Based on in-situ hydrographic measurements and numerical eddy-resolving simulations, we found evidence for a multidecadal poleward shift of the SB off East Antarctica. This study sheds light on the mechanism of multidecadal warming of the CDW layer in the subpolar zone (Sallée, 2018; Schmidtko et al., 2014; Auger et al., 2021; Aoki et al., 2005; Strass et al., 2020) and extends our knowledge on the multidecadal variability of the ACC in a changing climate.

The comparisons between the 1996 and 2019 measurements suggest that the poleward shift of the SB is driven by the poleward shift of barotropic ACC fronts (Fig. 3B) and enhanced upper overturning circulation due to increased isopycnal fluxes by eddies and/or baroclinic flows (Fig. 3C). The enhanced isopycnal fluxes associated with the upper overturning can compensate for the subsurface volume removal due to the anomalous northward transport at the surface driven by the intensified westerlies over the past decades (Armour et al., 2016; Doddridge et al., 2019). Since the Upper CDW temperature change governs the position of the SB, its poleward shift (accounting for +0.31°C; Table 1) can be attributed to enhanced upper overturning and the poleward shift of offshore barotropic fronts, generally accounting for 30% (+0.10°C) and 70% (+0.21°C), respectively. Thus, the effect of the barotropic frontal shift is likely no less than the baroclinic water transformation. This result is supported by the displacement of dynamic height contour (40 km) that explains more than half of the observed SB shift (73 km). The significance of barotropic changes may manifest as unsaturated eddy conditions in the subpolar zone, sometimes referred to as Hughes's "southern mode," in which the barotropic response to wind forcing is likely more sensitive than in the ACC (Langlais et al., 2015; Naveira Garabato et al., 2019).

Uncertainty in the frontal term decomposition likely arises from an assumption that the displacement of the dynamic height contours represents the frontal shift of the ACC since baroclinic eddies can also affect the water column density. Previous studies have reported that temperature and salinity fields in the ACC constructed by the gravest empirical mode with a dynamic height of upper 2,000 dbar capture over 90% of the property variance below the thermocline (Meijers et al., 2011), and that the quasi-barotropic flow structure of the study region is well represented by dynamic height (Chapter 1; Mizobata et al., 2020) as in the north. These facts assure that dynamic height approximates the position of barotropic ACC fronts in the presented result.

Even without the isopycnal analysis, a contribution from the poleward shift of barotropic fronts is evident. Neither enhanced eddy transport, altered mixing ratio, nor the freshening-driven volumetric contraction of AABW can explain the isobaric temperature increase with the deepening of the isopycnals throughout the water column (Fig. 2A) observed in this and previous studies (Katsumata et al., 2015; Purkey and Johnson, 2013). Although the circumpolar-averaged ACC position has not shifted over the past decades (Gille et al., 2016), the regional shift of the ACC fronts represented by the dynamic height (Fig. 2C) and detectable by satellite altimetry (Kim and Orsi, 2014) has contributed significantly to full-depth warming in the subpolar zone. In contrast, we can expect that enhanced upper overturning caused the baroclinic poleward shift of the isotherms because this pertains to the discrepancy between the shifts in SB and dynamic height (Table 1). The isopycnal eddy flux likely increases in response to wind intensification (Hogg et al., 2015). In the presented results, enhancement of eddy flux does not necessarily occur locally. Baroclinic changes can be transferred from upstream where active eddy generation is observed, such as the eastern flank of the Kerguelen Plateau (Thompson and Naveira Garabato., 2014; Tamsitt et al., 2018). Enhanced isopycnal CDW upwelling in the upper overturning cell is consistent with the widely observed shoaling of the subsurface temperature maximum (Auger et al., 2021; Schmidtko et al., 2014). Since the poleward shift of the barotropic fronts likely deepens the isopycnals, enhanced isopycnal transport can reasonably reconcile the shoaling of CDW (Tamsitt et al., 2018).

The zonal variation in the poleward SB shift obtained from the 1996 and 2019 observations (Figs. 2–3) is consistent with that reproduced from the historical dataset (Fig. 6A), indicating that the SB shifted further poleward around 120°E associated with the continental slope topography. The eddy-resolving simulation reproduced the similar locality (Fig. 6B), supporting the topographic control on the poleward SB shift. Our simulation implicates the effect of mesoscale processes in the observed trend, which are characterized by the baroclinic Rossby radius (~10 km at the shelf break; Mckee et al., 2019) and are unresolved in the ECCO model (Fig. 6C). The configurations of the simulation (e.g., atmospheric forcing and eddy parameterization scheme), however, are not the same as the ECCO model (differences in the zonal wind stress between the models are unlikely to explain the absence of SB shift in the ECCO). The effects of mesoscale processes need to be scrutinized further. The locality in the multidecadal trend is likely related to a topographically controlled flow structure (Chapter 1; Mizobata et al., 2020). The sea depth near the SB shallows by ~250 m over the three decades (averaged between 100°–150°E), whereas the depth change at 120°E is the smallest (~150 m). Because the barotropic flow tends to follow the isobath to conserve potential vorticity, the furthest poleward shift at 120°E (Fig. 6) is likely explained by the flat bathymetry and the southward excursion of the continental slope at this longitude. The localized shifts correlated with the shoreward CDW intrusions (Figs. 6A and S3), the zonally asymmetric baroclinic warming (Fig. 3C), and the barotropic transport increase (Fig. 8) support the idea that the subpolar gyre strengthened over the period. This idea is consistent with implications from observations in the Weddell Sea (Strass et al., 2020), idealized models (Nadeau and Ferrari, 2015), and realistic circumpolar simulations (Kusahara, 2020).

The sensitivity experiment demonstrates the role of eastward wind stress over the domain (Figs. 6B and 6D), which likely enhances the poleward eddy flux and the wind-driven upper overturning. Since the manipulation halves the air–sea drag coefficient and the effect of wind intensification from the 1990s onwards (Swart et al., 2015), the smaller shift compared to the reference experiment (Fig. 7B) can be interpreted as being due to a decreased wind effect. Although the westerlies do not strengthen from the 1990s to the 2000s on a decadal mean basis (Hogg et al., 2015), the historical data indicate persistent warming and the poleward SB shift during this period (Figs. 5D and 6A). The warming during the 2000s may have been induced by the cyclonic wind stress curl anomaly around the Antarctic Divergence, which likely enhanced CDW upwelling towards the Sabrina Coast (120°E) and accelerated land ice discharge (Greene et al., 2017). The linkage between the localized SB shift off the Sabrina Coast favored by topography and this on-shelf warming event requires further investigation.

The poleward shift of the SB under intensified westerlies potentially enhances onshore heat intrusion, leading to multidecadal warming of Antarctic shelf water (Schmidtko et al., 2014). The extensive poleward shift of the SB (Fig. 6A) may result from the multidecadal wind intensification, while it may also be induced by the intrinsic variability of the ACC (Meredith, 2016). The dominant intrinsic variability of the Southern Ocean is a multidecadal mode of the Weddell Gyre in the Atlantic sector with a 40–50 year duration (Le Bars et al., 2016). The eddy activity relative to the intrinsic variability in the Indo-Pacific sector is more dependent on external wind forcing than the Atlantic sector (Meredith, 2016; Patara et al., 2016). In contrast to the Weddell and Ross Gyres, a synoptic-scale subpolar gyre is absent off East Antarctica (Chapter 1). These facts imply a minor effect of the intrinsic variability within the domain and the sensitivity of the circulation to the projected wind intensification due to anthropogenic forcing (Armour et al., 2016; Gille et al., 2016; Thompson et al., 2018). Isopycnal barriers of the Antarctic Slope Current are partially weak in the Indian sector (Thompson et al., 2018), which may allow immediate onshore heat access in response to the offshore poleward SB shift. The presented result indicates the localized warming towards the shelf break (Figs. 5D and 5E), which is likely consistent with the continental shelf warming (Schmidtko et al., 2014). Our findings remark the importance of sustained observations of the ocean interior off East Antarctica.

Figures and tables

Figure 1. Revisited hydrography off East Antarctica. (A) Hydrographic arrays along the continental margin of the Australian-Antarctic Basin. Conductivity-Temperature-Depth (CTD) stations from the R/V Aurora-Australis 1996 cruise are blue dots, and CTD stations from the R/V Kaiyo-maru 2019 cruise are pink crosses. White boxes highlight the five revisited CTD sections. Background color indicates bathymetry (isobaths at 1,000 m intervals). Black curves denote the climatological position of the SB (solid: historical dataset from this study, broken: Orsi et al., dotted: based on the gridded dataset of Shimada et al.). Five sections of the 2019 measurements of (B) dissolved oxygen, (C) Conservative Temperature, and (D) Absolute Salinity. Isopycnal contours (neutral density) are shown in black (from 28.0 to 28.3 kg m^{-3} at 0.1 kg m^{-3} intervals). Yellow, red, and blue curves are the 195 μmol/kg oxygen, 1.5°C isotherm (represents Upper CDW), and 34.89 g kg^{-1} isohaline (represents Lower CDW), respectively. Black/white triangles at the top of each graph indicate the location of the CTD stations for the 2019 and 1996 observations.

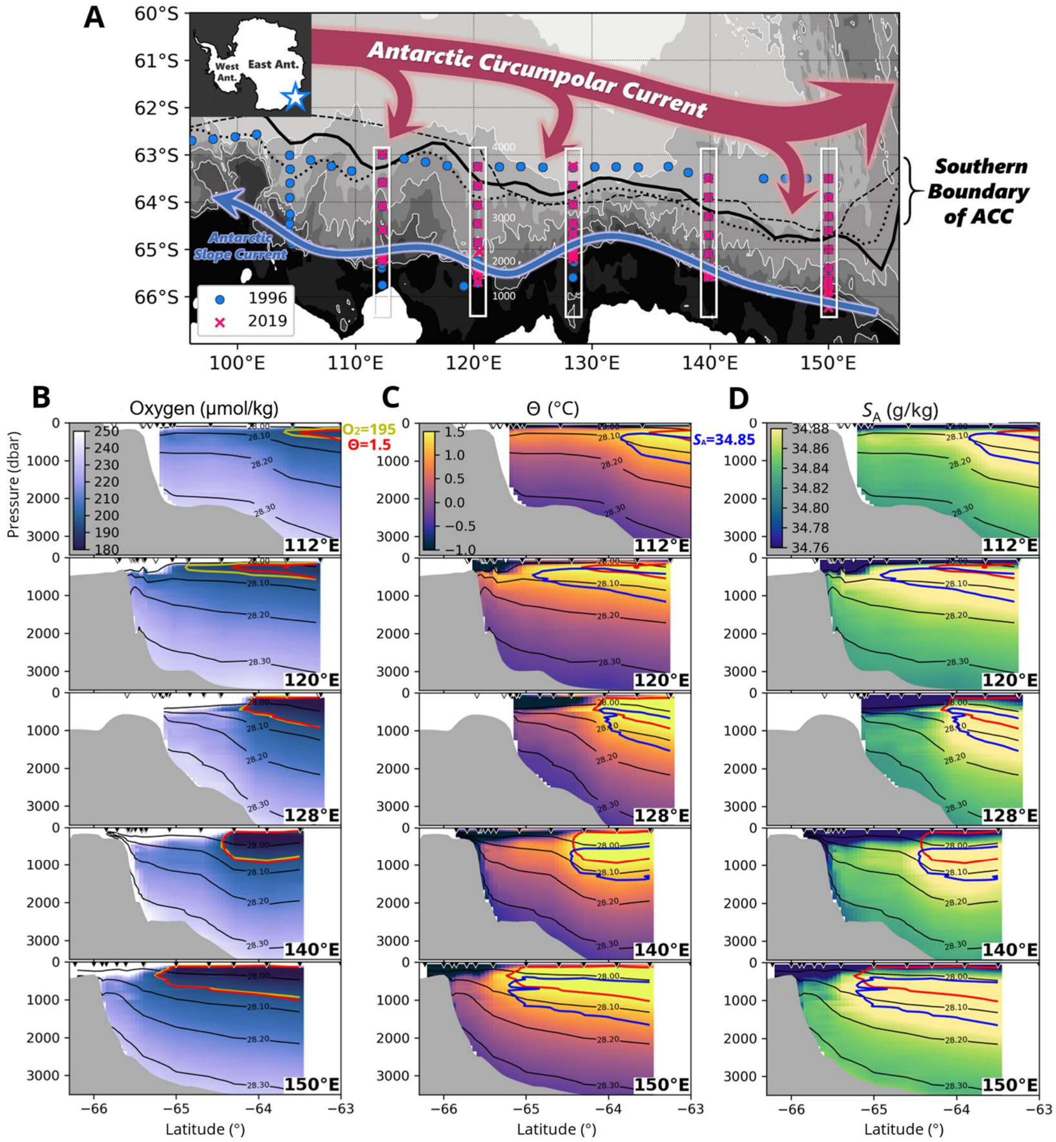
A
B
C
D
Antarctic Circumpolar Current
Southern Boundary of ACC
Antarctic Slope Current
West Ant.
East Ant.
1996
2019
4000
3000
2000
1000
60°S
61°S
62°S
63°S
64°S
65°S
66°S
100°E
110°E
120°E
130°E
140°E
150°E
Oxygen (μmol/kg)
Θ (°C)
S_A (g/kg)
O₂=195
Θ=1.5
S_A=34.85
Pressure (dbar)
Latitude (°)
112°E
120°E
128°E
140°E
150°E
28.00
28.10
28.20
28.30
0
1000
2000
3000
−66
−65
−64
−63
250
240
230
220
210
200
190
180
1.5
1.0
0.5
0.0
−0.5
−1.0
34.88
34.86
34.84
34.82
34.80
34.78
34.76

Figure 2. Isobaric trends from 1996 to 2019. Differences between 1996 and 2019 in (A) Conservative Temperature and (B) Absolute Salinity at the latitude–pressure coordinates. The isotherms, isohalines, and isopycnals are the same as in Fig. 1. The dotted lines denote those from 1996. The red vertical line is the position of the SB determined by the poleward limit of the 1.5°C. (C) The dynamic height between 300–1,800 dbar. Dots are the values at each station, which are least-squares fitted by quartic polynomials. Black (white) dots and solid (dashed) profiles are from 2019 (1996).

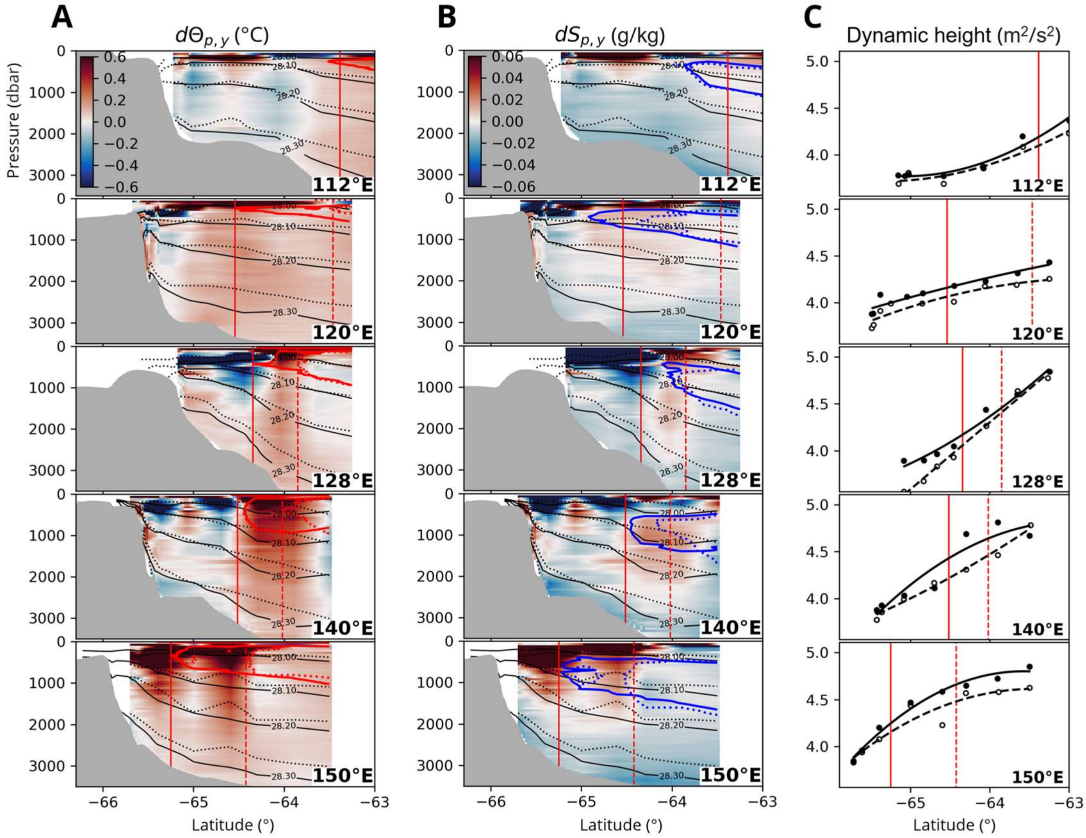

Table 1. Water column changes associated with the poleward SB shift. The poleward shift of the SB by the 1.5°C isotherm and the water property changes averaged over the latitudinal ranges of the 1996 and 2019 positions of the SB (with standard deviation) for the five meridional sections. Isobaric changes above/below 1,500 dbar are shown separately for Conservative Temperature, Absolute Salinity, and neutral density. In addition to the total isopycnal change, the frontal shift and the residual (water transformation) terms are presented for Upper CDW (28.0–28.1 kg m^{-3}), Lower CDW (28.1–28.2 kg m^{-3}), and AABW (28.2–28.3 kg m^{-3}). The underbar denotes the dominant source of the isopycnal change in each layer. The rightmost column presents the five-section average, and the ratio of the frontal shift/residual term to the total isopycnal change is shown in brackets. For 112°E, the leastwise SB shift is shown due to its absence from the 1996 measurement.

From 1996 to 2019			**112°E**	**120°E**	**128°E**	**140°E**	**150°E**	**Average**
Poleward SB shift [km]		1.5°C	> 43	120	55	55	92	73
		Dynamic height	27 ± 2	74 ± 20	13 ± 4	49 ± 1	38 ± 14	40
Isobaric change	$d\Theta$ [°C]	Upper 1500 dbar	+0.10 ± 0.04	+0.10 ± 0.04	+0.10 ± 0.16	+0.32 ± 0.12	+0.30 ± 0.21	+0.18
		Lower 1500 dbar	+0.10 ± 0.02	+0.12 ± 0.03	+0.13 ± 0.03	+0.17 ± 0.06	+0.11 ± 0.06	+0.13
	dS_A [g kg^{-1} 10^{-3}]	Upper 1500 dbar	+1 ± 4	+3 ± 4	+0 ± 19	+8 ± 12	+18 ± 17	+6
		Lower 1500 dbar	−6 ± 4	−3 ± 5	−0 ± 5	+1 ± 8	−5 ± 6	−3
	$d\gamma_n$ [kg m^{-3} 10^{-3}]	Upper 1500 dbar	−16 ± 3	−13 ± 8	−17 ± 7	−37 ± 12	−21 ± 14	−21
		Lower 1500 dbar	−27 ± 4	−26 ± 4	−25 ± 4	−30 ± 6	−27 ± 11	−27
Isopycnal change	$d\Theta$ [°C]	Upper CDW	+0.23 ± 0.19	+0.42 ± 0.44	+0.20 ± 0.40	+0.23 ± 0.25	+0.49 ± 0.38	+0.31
		Lower CDW	−0.04 ± 0.02	−0.00 ± 0.04	−0.06 ± 0.11	+0.02 ± 0.03	+0.04 ± 0.07	−0.01
		AABW	−0.07 ± 0.01	−0.03 ± 0.02	−0.03 ± 0.02	−0.02 ± 0.03	−0.04 ± 0.04	−0.04
	Frontal shift	Upper CDW	+0.06 ± 0.08	$\underline{+0.32 \pm 0.45}$	$\underline{+0.10 \pm 0.07}$	$\underline{+0.38 \pm 0.33}$	+0.19 ± 0.47	$\underline{+0.21\ (0.7)}$
		Lower CDW	+0.01 ± 0.00	$\underline{+0.05 \pm 0.04}$	+0.05 ± 0.03	$\underline{+0.08 \pm 0.05}$	$\underline{+0.07 \pm 0.07}$	+0.05 (−5)
		AABW	+0.00 ± 0.00	+0.03 ± 0.03	+0.01 ± 0.01	+0.03 ± 0.03	+0.02 ± 0.02	+0.02 (−0.5)
	Residual	Upper CDW	$\underline{+0.15 \pm 0.11}$	+0.10 ± 0.44	$\underline{+0.10 \pm 0.40}$	−0.15 ± 0.40	$\underline{+0.30 \pm 0.60}$	+0.10 (0.3)
		Lower CDW	$\underline{-0.05 \pm 0.02}$	$\underline{-0.06 \pm 0.06}$	$\underline{-0.11 \pm 0.14}$	−0.05 ± 0.06	−0.03 ± 0.10	$\underline{-0.06\ (6)}$
		AABW	$\underline{-0.07 \pm 0.01}$	$\underline{-0.06 \pm 0.05}$	$\underline{-0.03 \pm 0.03}$	$\underline{-0.05 \pm 0.03}$	$\underline{-0.06 \pm 0.04}$	$\underline{-0.05\ (1.4)}$

Figure 3. Isopycnal trends and frontal term decomposition. (A) Difference in Conservative Temperature in the latitude-neutral density coordinates between 1996 and 2019. The 1.5°C contour and the SB position (derived from the isobaric field; Fig. 2A) for the 1996 and 2019 measurements are presented as in Fig. 2. Above 200 dbar, the data are hatched to hide transient surface features. The total isopycnal change (A) is decomposed into (B) the frontal shift and (C) residual (water transformation) terms. Upper CDW (28.0–28.1 kg m^{-3}), Lower CDW (28.1–28.2 kg m^{-3}), and AABW (28.2–28.3 kg m^{-3}) are defined based on the extent of the temperature/salinity maximum layer (Figs. 1C and 1D).

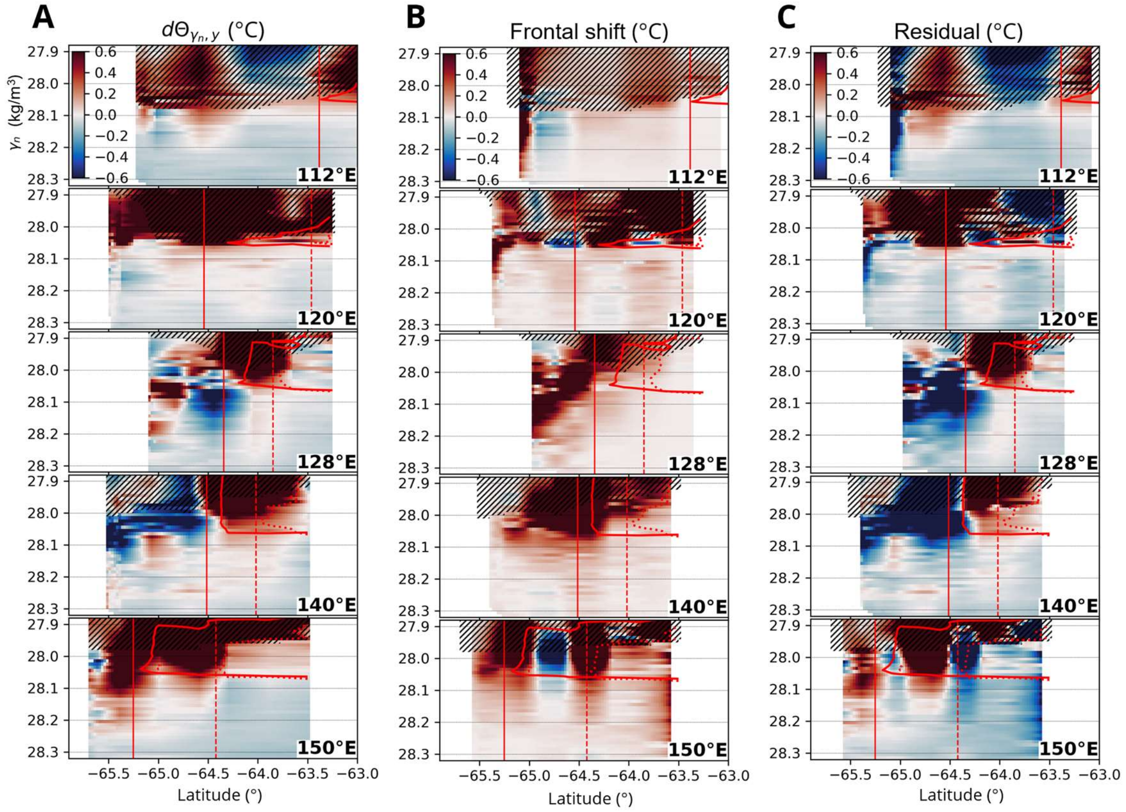

Figure 4. In-situ historical data. The historical dataset used to create the temperature surfaces of the temperature maximum layer from (A) 1990–1999, (B) 2000–2009, and (C) 2010–2019. Dots are colored according to the data type shown in the legend.

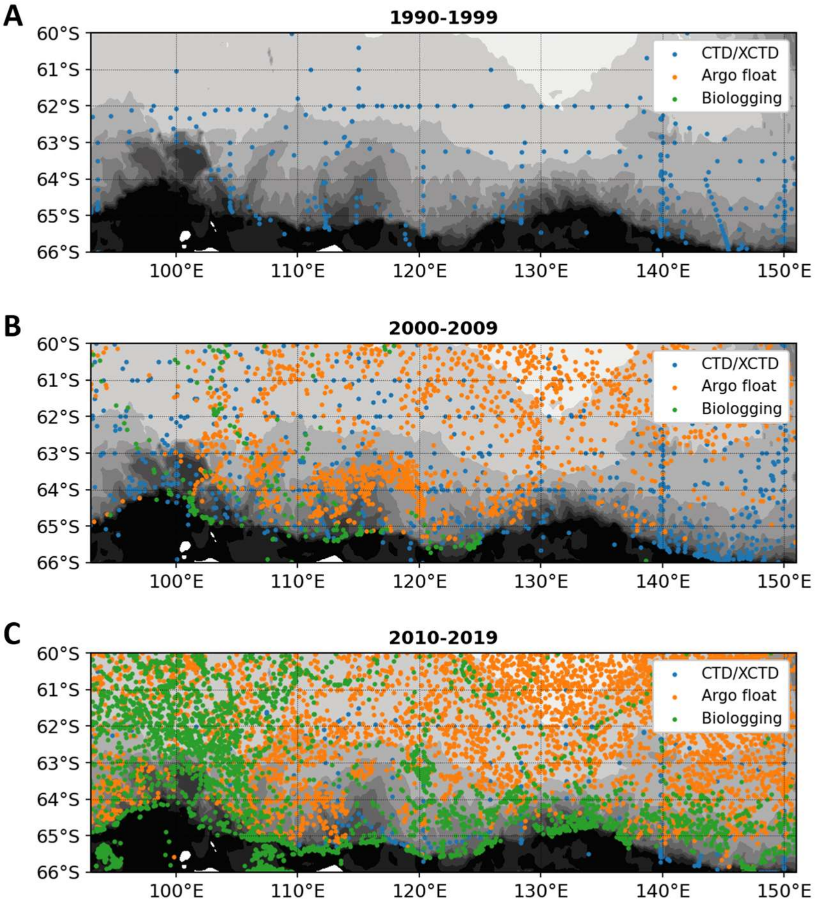

Figure 5. Multidecadal temperature changes off East Antarctica. Conservative Temperature at the temperature maximum surface reconstructed from the in-situ historical data for (A) 1990–1999, (B) 2000–2009, and (C) 2010–2019. Blue, purple, and red contours are the 1.5°C isotherm (SB) during each period. Areas with a standard deviation above 0.5°C are hatched. (D) Difference in Conservative Temperature at the temperature maximum surface between the 1990s–2000s decadal averages. Areas with confidence levels below 95% are hatched. (E) Same as (D), but for the 2000s–2010s decadal averages. Green (gray) contour is the 3,000 (1,000) m isobath. White dashed curve denotes the climatological SB based on Shimada et al.

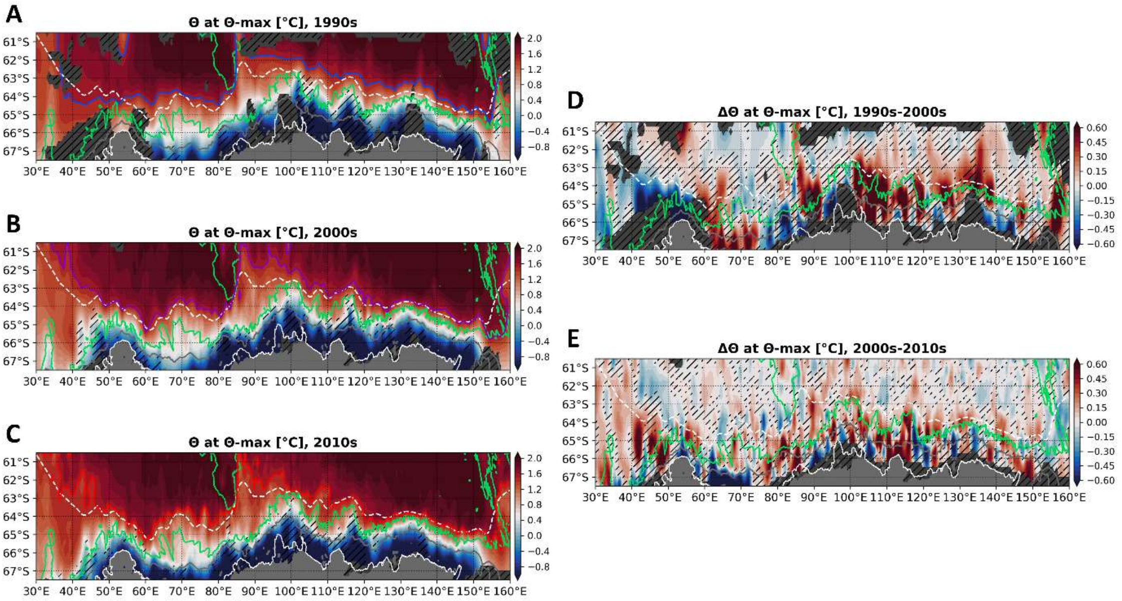

Figure 6. Regionality in the multidecadal trend of SB. (A) The SB position obtained from the 1996/2019 hydrographic measurements (dots) and the decadal climatology (curves; Fig. 5). The triangle at 112°E for 1996 denotes the absence of the SB, assumed to exist northward of this position. The white dashed curve denotes the climatological position (three-decade average), and the dashed black curve is the SB from Orsi et al. Background color indicates the bathymetry, and the 3,000 m isobath is highlighted in green. (B) The SB position reproduced from the high-resolution numerical simulations by MITgcm (nominally 1/30° grid). (C) Same as (B), but from the ECCO LLC270 ocean state estimate product (nominally 1/4° grid), which is used for the lateral boundary condition of (B). (D) Same as (B) but from the halved wind experiment of the high-resolution simulation.

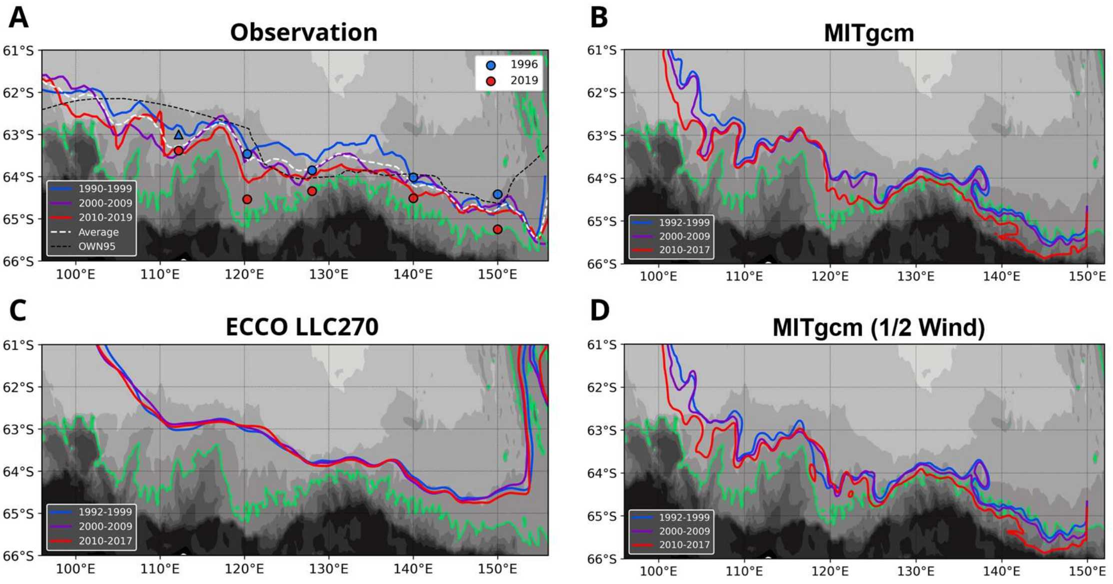

Figure 7. Meridional shift of the SB. (A) The meridional displacement of the SB derived from the historical dataset (Fig. 6A) from 1990–1999 to 2010–2019 (red) and 2000–2009 (purple). Shading with the corresponding color denotes the climatological standard deviation of the meridional position of the SB estimated from the absolute deviation and the temperature gradient of the temperature maximum surface (see Materials and Methods). The red and purple figures are the zonal averages of the corresponding period for 100°–150°E, with its zonal standard deviation. "SD" is the zonal average of the climatological standard deviation of the meridional position. The poleward shift from the 1996 and 2019 snapshots is also shown (for 112°E, its least value). (B) The meridional displacements of the SB reproduced from MITgcm (Fig. 6B; solid curve), ECCO (Fig. 6C; dashed curve), and the halved wind experiment (Fig. 6D; dotted curve) from 1992–1999 to 2010–2017 (red) and 2000–2009 (purple). The zonal average for 100°–150°E is presented for each period with its corresponding color. "Out of the simulated area" is shaded in gray.

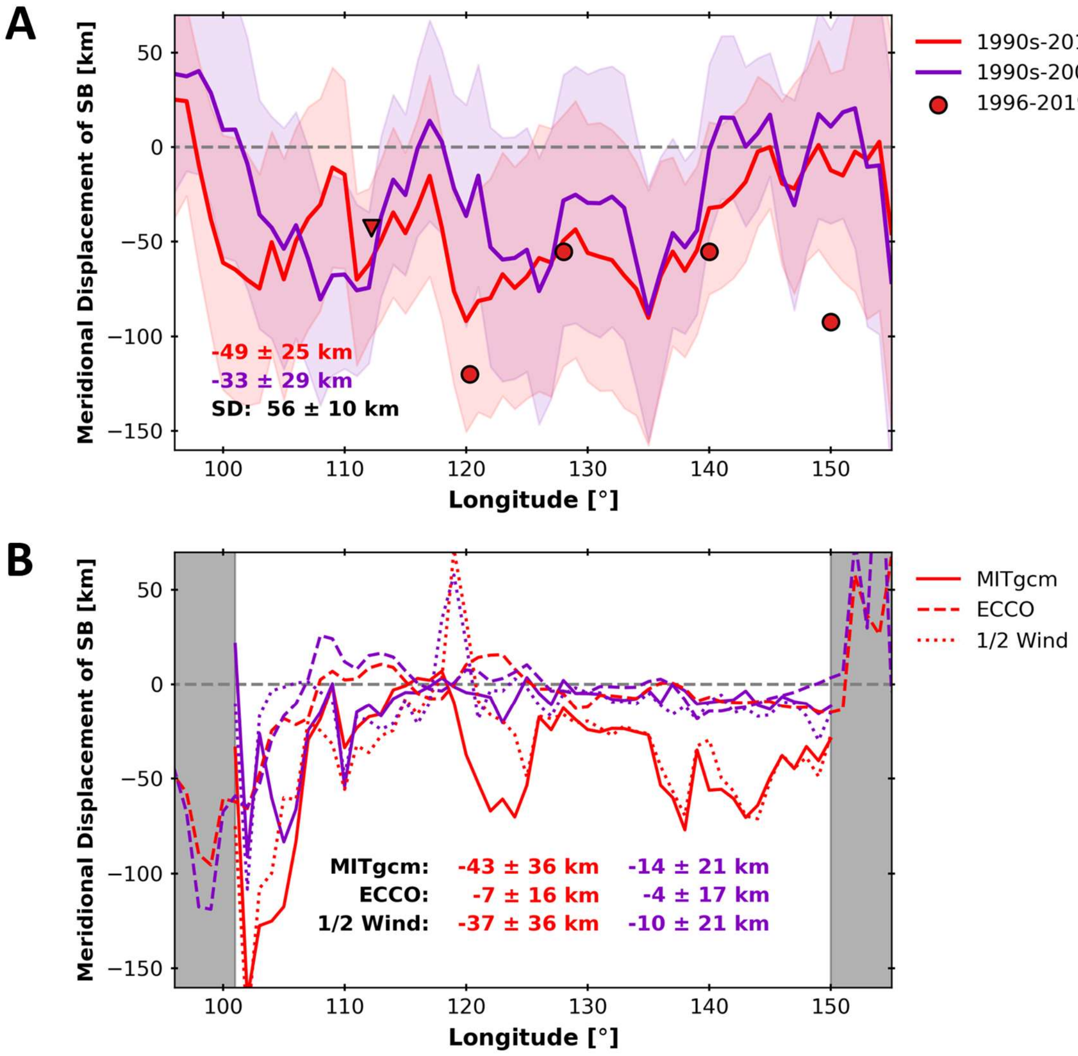

Figure 8. Simulated circulation. The barotropic streamfunction (Sv = 10^6 m^3 s^{-1}) averaged for (A) 1992–1999, (B) 2000–2009, and (C) 2010–2017 from the high-resolution numerical simulation. Water flows along the contour with higher values to its right. The SB as the poleward limit of the 1.5°C isotherm is shown by the black contour. (D) Differences in the streamfunction from the 1992–1999 to the 2010–2017 averages. Areas with confidence levels below 95% are hatched. Green contour denotes the 3,000 m isobath.

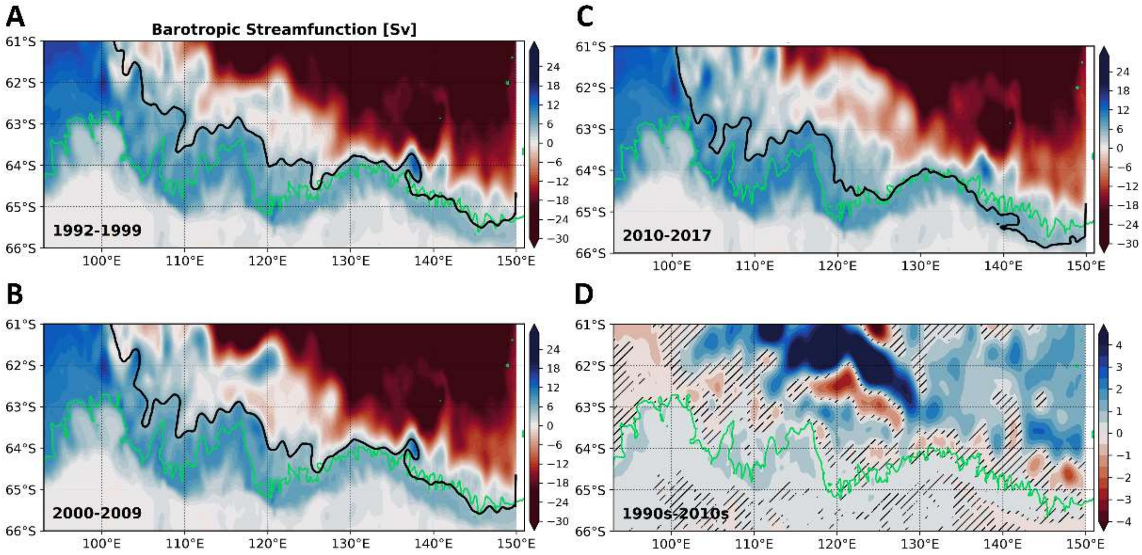

Figure 9. Concluding schematics. In upper panel, solid and dashed lines are the positions of SB for the 2010s and 1990s, respectively. Lower panel shows the meridional section around the SB.

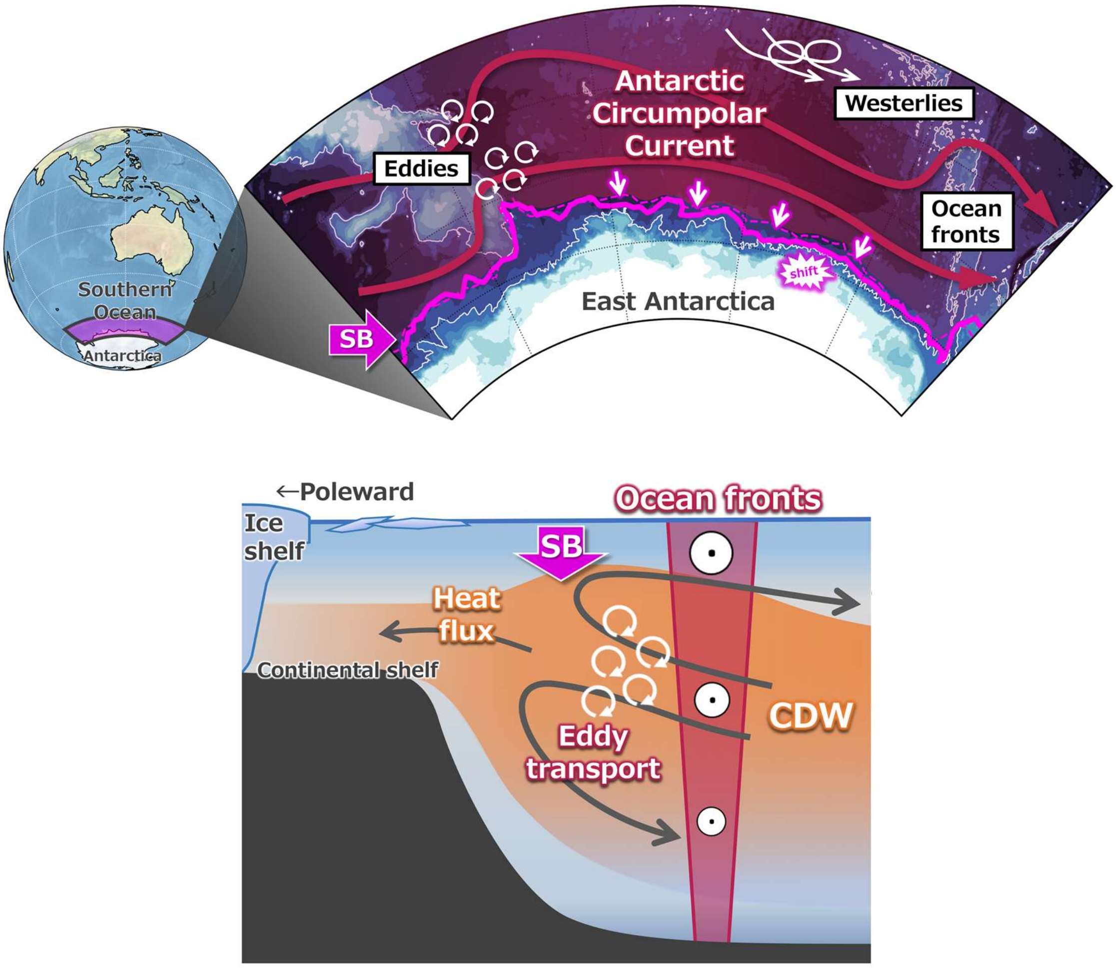

References and notes

Aoki, S., Yamazaki, K., Hirano, D., Katsumata, K., Shimada, K., Kitade, Y., et al. (2020). Reversal of freshening trend of Antarctic Bottom Water in the Australian-Antarctic Basin during 2010s. Scientific Reports, 10(1), 1–7.

Aoki, S., Bindoff, N. L., and Church, J. A. (2005). Interdecadal water mass changes in the Southern Ocean between 30°E and 160°E. Geophysical Research Letters, 32(7), 1–5.

Armour, K. C., Marshall, J., Scott, J. R., Donohoe, A., and Newsom, E. R. (2016). Southern Ocean warming delayed by circumpolar upwelling and equatorward transport. Nature Geoscience, 9(7), 549–554.

Auger, M., Morrow, R., Kestenare, E., Sallée, J.-B., and Cowley, R. (2021). Southern Ocean in-situ temperature trends over 25 years emerge from interannual variability. Nature Communications, 12(1), 514.

Bindoff, N. L., Rosenberg, M. A., and Warner, M. J. (2000). On the circulation and water masses over the Antarctic continental slope and rise between 80 and 150°E. Deep-Sea Research Part II: Topical Studies in Oceanography, 47(12–13), 2299–2326.

Chapman, C. C., Lea, M. A., Meyer, A., Sallée, J. B., and Hindell, M. (2020). Defining Southern Ocean fronts and their influence on biological and physical processes in a changing climate. Nature Climate Change, 10(3), 209-219.

Couldrey, M. P., Jullion, L., Naveira Garabato, A. C., Rye, C., Herráiz-Borreguero, L., Brown, P. J., et al. (2013). Remotely induced warming of Antarctic Bottom Water in the eastern Weddell gyre. Geophysical Research Letters, 40(11), 2755–2760.

Doddridge, E. W., Marshall, J., Song, H., Campin, J. M., Kelley, M., and Nazarenko, L. (2019). Eddy Compensation Dampens Southern Ocean Sea Surface Temperature Response to Westerly Wind Trends. Geophysical Research Letters, 46(8), 4365–4377.

Ferreira, D., Marshall, J., Bitz, C. M., Solomon, S., and Plumb, A. (2015). Antarctic ocean and sea ice response to ozone depletion: A two-time-scale problem. Journal of Climate, 28(3), 1206–1226.

Ferster, B. S., Subrahmanyam, B., Fukumori, I., and Nyadjro, E. S. (2018). Variability of southern ocean transports. Journal of Physical Oceanography, 48(11), 2667–2688.

Gille, S. T., McKee, D. C., and Martinson, D. G. (2016). Temporal changes in the Antarctic circumpolar current: Implications for the Antarctic continental shelves. Oceanography, 29(4), 96–105.

Greene, C. A., Blankenship, D. D., Gwyther, D. E., Silvano, A., and van Wijk, E. (2017). Wind causes Totten Ice Shelf melt and acceleration. Science Advances, 3(11), e1701681.

Hirano, D., Tamura, T., Kusahara, K., Ohshima, K. I., Nicholls, K. W., Ushio, S., et al. (2020). Strong ice-ocean interaction beneath Shirase Glacier Tongue in East Antarctica. Nature Communications, 11(1), 1–12.

Hogg, A. M. C., Meredith, M. P., Chambers, D. P., Abrahamsen, E. P., Hughes, C. W., and Morrison, A. K. (2015). Recent trends in the Southern Ocean eddy field. Journal of Geophysical Research: Oceans, 120(1), 257–267.

Katsumata, K., Nakano, H., and Kumamoto, Y. (2015). Dissolved oxygen change and freshening of Antarctic Bottom water along 62°S in the Australian-Antarctic Basin between 1995/1996 and 2012/2013. Deep-Sea Research Part II: Topical Studies in Oceanography, 114, 27–38.

Kim, Y. S., and Orsi, A. H. (2014). On the variability of antarctic circumpolar current fronts inferred from 1992-2011 altimetry. Journal of Physical Oceanography, 44(12), 3054–3071.

Kusahara, K. (2020). Interannual-to-multidecadal responses of antarctic ice shelf-ocean interaction and coastal water masses during the twentieth century and the early twenty-first century to dynamic and thermodynamic forcing. Journal of Climate, 33(12), 4941–4973.

Langlais, C. E., Rintoul, S. R., and Zika, J. D. (2015). Sensitivity of antarctic circumpolar current transport and eddy activity to wind patterns in the Southern Ocean. Journal of Physical Oceanography, 45(4), 1051–1067.

Le Bars, D., Viebahn, J. P., and Dijkstra, H. A. (2016). A Southern Ocean mode of multidecadal variability. Geophysical Research Letters, 43(5), 2102–2110.

Marshall, J., and Speer, K. (2012). Closure of the meridional overturning circulation through Southern Ocean upwelling. Nature Geoscience, 5(3), 171–180.

Mckee, D. C., Martinson, D. G., and Schofield, O. (2019). Origin and attenuation of mesoscale structure in Circumpolar Deep Water intrusions to an Antarctic shelf. Journal of Physical Oceanography, 49(5), 1293–1318.

Meijers, A. J. S., Bindoff, N. L., and Rintoul, S. R. (2011). Frontal movements and property fluxes: Contributions to heat and freshwater trends in the Southern Ocean. Journal of Geophysical Research: Oceans, 116(8), 1–17.

Meredith, M. P. (2016). Understanding the structure of changes in the Southern Ocean eddy field. Geophysical Research Letters, 43(11), 5829–5832.

Meredith, M. P., and Hogg, A. M. (2006). Circumpolar response of Southern Ocean eddy activity to a change in the Southern Annular Mode. Geophysical Research Letters, 33(16), 2–5.

Mizobata, K., Shimada, K., Aoki, S., and Kitade, Y. (2020). The Cyclonic Eddy Train in the Indian Ocean Sector of the Southern Ocean as Revealed by Satellite Radar Altimeters and In Situ Measurements. Journal of Geophysical Research: Oceans, 125(6).

Morrison, A. K., McC. Hogg, A., England, M. H., and Spence, P. (2020). Warm Circumpolar Deep Water transport toward Antarctica driven by local dense water export in canyons. Science Advances, 6(18), 1–10.

Nadeau, L. P., and Ferrari, R. (2015). The role of closed gyres in setting the zonal transport of the Antarctic Circumpolar Current. Journal of Physical Oceanography, 45(6), 1491–1509.

Nakayama, Y., Menemenlis, D., Zhang, H., Schodlok, M., and Rignot, E. (2018). Origin of Circumpolar Deep Water intruding onto the Amundsen and Bellingshausen Sea continental shelves. Nature Communications, 9(1), 3403.

Naveira Garabato, A. C., Dotto, T. S., Hooley, J., Bacon, S., Tsamados, M., Ridout, A., et al. (2019). Phased Response of the Subpolar Southern Ocean to Changes in Circumpolar Winds. Geophysical Research Letters, 46(11), 6024–6033.

Orsi, A. H., Whitworth, T., and Nowlin, W. D. (1995). On the meridional extent and fronts of the Antarctic Circumpolar Current. Deep Sea Research Part I: Oceanographic Research Papers, 42(5), 641–673.

Patara, L., Böning, C. W., and Biastoch, A. (2016). Variability and trends in Southern Ocean eddy activity in 1/12° ocean model simulations. Geophysical Research Letters, 43(9), 4517–4523.

Purkey, S. G., and Johnson, G. C. (2013). Antarctic bottom water warming and freshening: Contributions to sea level rise, ocean freshwater budgets, and global heat gain. Journal of Climate, 26(16), 6105–6122.

Rignot, E., Mouginot, J., Scheuchl, B., Van Den Broeke, M., Van Wessem, M. J., and Morlighem, M. (2019). Four decades of Antarctic ice sheet mass balance from 1979–2017. Proceedings of the National Academy of Sciences of the United States of America, 116(4), 1095–1103.

Rye, C. D., Garabato, A. C. N., Holland, P. R., Meredith, M. P., Nurser, A. J. G., Hughes, C. W., et al. (2014). Rapid sea-level rise along the Antarctic margins in response to increased glacial discharge. Nature Geoscience, 7(10), 732–735.

Sallée, J. B. (2018). Southern ocean warming. Oceanography, 31(2 Special Issue), 52–62.

Schmidtko, S., Heywood, K. J., Thompson, A. F., and Aoki, S. (2014). Multidecadal warming of Antarctic waters. Science, 346(6214), 1227–1231.

Shimada, K., Aoki, S., and Ohshima, K. I. (2017). Creation of a gridded dataset for the southern ocean with a topographic constraint scheme. Journal of Atmospheric and Oceanic Technology, 34(3), 511–532.

Strass, V. H., Rohardt, G., Kanzow, T., Hoppema, M., and Boebel, O. (2020). Multidecadal warming and density loss in the Deep Weddell Sea, Antarctica. Journal of Climate, 33(22), 9863–9881.

Swart, N. C., Fyfe, J. C., Gillett, N., and Marshall, G. J. (2015). Comparing trends in the southern annular mode and surface westerly jet. Journal of Climate, 28(22), 8840–8859.

Tamsitt, V., Drake, H. F., Morrison, A. K., Talley, L. D., Dufour, C. O., Gray, A. R., et al. (2017). Spiraling pathways of global deep waters to the surface of the Southern Ocean. Nature Communications, 8(1), 172.

Thompson, A. F., and Garabato, A. C. N. (2014). Equilibration of the Antarctic Circumpolar Current by standing meanders. Journal of Physical Oceanography, 44(7), 1811–1828.

Thompson, A. F., Stewart, A. L., Spence, P., and Heywood, K. J. (2018). The Antarctic Slope Current in a Changing Climate. Reviews of Geophysics, 56(4), 741–770.

Tynan, C. T. (1998). Ecological importance of the Southern Boundary of the Antarctic Circumpolar Current. Nature, 392(6677), 708–710.

Van Wijk, E. M., and Rintoul, S. R. (2014). Freshening drives contraction of Antarctic Bottom Water in the Australian Antarctic Basin. Geophysical Research Letters.

Yamazaki, K., Aoki, S., Shimada, K., Kobayashi, T., and Kitade, Y. (2020). Structure of the Subpolar Gyre in the Australian-Antarctic Basin Derived From Argo Floats. Journal of Geophysical Research: Oceans, 125(8).

Zhang, H., D. Menemenlis, I. Fenty, ECCO LLC270 Ocean-Ice State Estimate. http://hdl.handle.net/1721.1/119821 (California Institute of Technology, 2018).

This chapter is adpoted from:

Yamazaki, K., Aoki, S., Katsumata, K., Hirano, D., and Nakayama, Y. (2021). Multidecadal poleward shift of the southern boundary of the Antarctic Circumpolar Current off East Antarctica. *Science Advances*, 7(24), eabf8755.

(This page is intentionally set blank)

3

HYDROGRAPHIC CHANGES BETWEEN 1996 AND 2019 OVER THE EAST ANTARCTIC MARGIN

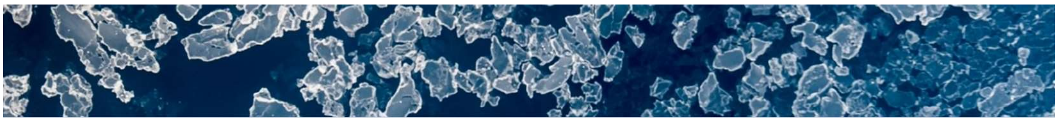

Abstract

In 2018/2019 austral summer, full-depth CTD sections of the BROKE experiment (over the Antarctic margin of 80–150°E; Bindoff et al., 2000) were first revisited in the past 23 years. The observation captured changes in the ocean structure over the decades, from the southern flank of the Antarctic Circumpolar Current (ACC) to the continental shelves. The poleward shift of the southern boundary of ACC outstands near the continental rise, and the simultaneous displacement of barotropic ACC fronts and full-depth warming (> 0.1°C) contributed to bottom warming over the shelf break. Coastal freshening further modified the structure of Antarctic Slope Current (ASC). Along the five meridional sections, its westward transport decreased by up to 20 Sv, and its axis was located offshore. These changes partly pertain to a decreased baroclinic transport due to freshwater input, reminiscent of the meltwater–ASC feedback hypothesis for coastal ice melt; i.e., meltwater can strengthen the coastal stratification, deform the ASC structure, and weaken its barrier effect, allowing more cross-slope CDW flux.

3.1. Background

The Australian-Antarctic Basin is characterized by a closer position of the Antarctic Circumpolar Current (ACC) to the Antarctic continent downstream of the Kerguelen Islands (Orsi et al., 1995, Sokolov and Rintoul, 2007). This ACC's proximity, along with strong westerlies in this sector, favors the onshore heat transport, leading to the strong ocean–atmosphere–cryosphere interaction. Intensive sea ice formation in the coastal region produces Antarctic Bottom Water (AABW), supplying freshwater, oxygen, and carbon into the global abyss (Foster 1995; Whitworth, 2002; Williams et al., 2010; Kitade et al., 2014). The temperate and windy climate in this basin flourishes marine ecosystems (e.g., Antarctic Krill).

The Baseline Research on Oceanography, Krill and the Environment (BROKE) experiment in 1996 austral summer first investigated the Antarctic margin between 80–150°E and unveiled the basin-wide clockwise circulation (Bindoff et al., 2000), later referred to as Kerguelen gyre. The CCAMLR KY1804 survey in 2018/2019 summer conducted by R/V Kaiyo-maru of Japan Fisheries Agency (KY18 onwards; see Murase et al., 2019 for the cruise report) revisited CTD sections in the BROKE experiment for the first time in the past 23 years (Fig. 1a) to identify full-depth ocean changes. The cruise was a part of the Global Ocean Ship-based Hydrographic Investigations Program (GO-SHIP; Sloyan et al., 2019). This chapter describes the large-scale flow pattern and subsurface water mass distributions observed in the KY18 survey, with an emphasis on ocean changes from 1996 to 2019.

The structure of circulation and water masses in the continental margin is schematized in Fig. 1b. Subsurface water masses are categorized into Upper Circumpolar Deep Water (UCDW), Lower Circumpolar Deep Water (LCDW), and AABW. UCDW and LCDW constitute the upper/lower cells of the meridional overturning circulation (Lumpkin and Speer, 2007). In the subpolar zone, Antarctic Surface Water (AASW) horizontally diverges due to cyclonic wind stress, and the upwelling of UCDW compensates for this surface volume removal. The poleward limit of UCDW corresponds to the southernmost extent of ACC (Orsi et al., 1995). Buoyancy loss at coastal polynyas produces dense Shelf Water (SW), the precursor of AABW. The coastal volume export and heat loss are primarily compensated by the onshore intrusion of LCDW (Morrison et al., 2020).

The horizontal circulation is shaped by the eastward ACC and the westward Antarctic Slope Current (ASC; e.g., Jacobs, 1991; Whitworth, 1998), imparted momentum by westerlies and easterlies, respectively. As a result of the cyclonic shear between ACC and ASC, clockwise subpolar gyres commonly exist in the Antarctic margin (e.g., Weddell and Ross gyres). In the

Australian-Antarctic Basin, the spatial extent of the subpolar zone is relatively narrow with O(100 km) so that the subpolar gyre is divided into multiple standing eddies referred to as subgyres, each bounded by the continental slope ridges (Mizobata et al., 2020; Chapter 1). Recent studies have pointed out the zonal connectivity between the recirculations off East Antarctica (i.e., Kerguelen and Prydz Bay gyres), interpreted as a subpolar version of "supergyre" (Aoki et al., 2010; Naveira Garabato et al., 2014; Chapter 1). The Australian-Antarctic Basin is connected to the Weddell-Enderby Basin through the Princess Elizabeth Trough, where the fronts exhibit complex structures with wild meandering (Heywood et al., 2004; Bestley et al., 2018). The interbasin connectivity infers that circulation and water mass variabilities in the BROKE and BROKE-West regions (Bindoff et al., 2000; Meijers et al., 2010) are mutually linked, and the following results potentially have an extensive implication.

Some of the intriguing results from the KY18 survey have already been reported. The freshening trend of AABW in the Indian sector (Purkey and Johnson, 2013; Van Wijk and Rintoul, 2014; Katsumata et al., 2015) was reversed from the mid-2010s, likely due to the recovery of bottom water formation in the Ross Sea (Aoki et al., 2020; Silvano et al., 2021). Further, the multidecadal warming in the sector (Schmidtko et al., 2014; Katsumata et al., 2015; Auger et al., 2021) was induced by a poleward shift of the ACC's southern flank (Chapter 2). These results likely reflect oceanic responses to a surface forcing change over the decades (e.g., Swart et al., 2018; Silvano et al., 2020; Purich and England, 2021). This chapter describes subsurface physical oceanography by the KY18 survey and hydrographic changes between 1996 and 2019 not documented in Aoki et al. (2020) and Chapter 2. Data and methods used are detailed in section 2. In section 3, frontal positions and their changes are described based on subsurface temperature criteria. In section 4, water mass properties and their changes are delineated. In section 5, changes in large-scale circulation are presented with an emphasis on the variability of ASC over the continental slope.

3.2. Data and methods

3.2.1 CTD and oxygen measurements

This study details CTD measurement during the KY18 cruise. 54 CTD stations were arrayed over the continental margin between 80-150°E following the stations in the BROKE experiment (Bindoff et al., 2000; Fig. 1a) and partly the World Ocean Circulation Experiment Hydrographic Programme (WOCE) S04I line (Katsumata et al., 2015). In addition, 18 stations off Adelie Coast and 29 stations off Sabrina Coast were located to survey water distributions over the continental shelves, as detailed in Hirano et al. (2021, 2023). The cruise was conducted over two legs; Leg 1 from December 15, 2018, to January 7, 2019, surveyed Line 1–11 from the west, and Leg 2 from January 26 to February 23, 2019, surveyed Line 12-18 from the east (Fig. 1a). The CTD stations off Sabrina and Adelie Coasts were surveyed during Leg 2.

CTD and oxygen measurements were carried out conforming to the GO-SHIP standard, with 0.001°C precision in temperature, 0.002 accuracy in practical salinity, and reproducibility within 1% in dissolved oxygen (Hood et al., 2010). Pressure measurement was performed with Sea-Bird Electronics (SBE) 9 plus. Temperature values taken by SBE 3 plus (dual sensor) were collected with SBE 35 high-precision temperature sensor, and conductivity values taken by SBE 4C (dual sensor) were calibrated with bottle water sampling as a function of pressure, temperature, and time, then converted into practical salinity unit. Oxygen values taken by RINKO III (JFE Advantech co.) were calibrated with bottle data following Garcia and Gordon (1992). As for the BROKE experiment, oxygen values are only available for bottle data (sampled with WOCE standard layers) and hence relatively sparce in depth. These data are available from the CLIVAR and Carbon Hydrographical Data Office website (https://cchdo.ucsd.edu/).

During the KY18 survey, eXpendable CTD (XCTD) measurement was also conducted to enhance the spatial coverage. The MK-130 XCTD system (Tsurumi Seiki Co.) was used. 150 XCTD probes were deployed during the cruise. The probe type was mainly XCTD-1 (1000 m range), while 17 probes of XCTD-4 (1850 m range) were deployed off Sabrina Coast. The temperature and salinity measurements are accurate to 0.02°C and 0.04, while special attention is required for the depth uncertainty of ~2%. In this study, the only temperature profiles are used to locate subsurface isotherms during the cruise.

Variables are based on the Thermodynamic Equation Of Seawater-2010 (TEOS-10; McDougall and Barker, 2011). Absolute Salinity SA (in gram per kilogram) and Conservative Temperature Θ (in degrees Celsius) were computed using the Gibbs Sea Water package translated to Python (https://github.com/TEOS-10/python-gsw). Θ almost equals traditional potential temperature to the extent of our interest, while SA is generally higher than traditional practical salinity by about 0.02 parts per thousand in the study region. Neutral density γn (Jacket and McDougall, 1997) was adopted to minimize thermobaric effects on seawater neutral surface. Definitions of water masses (Section 4) are based on neutral density following convention (Bindoff et al., 2000; Meijers et al., 2011), while potential density criteria are also presented regarding its consistency with TEOS-10 variables.

3.2.2 Velocity measurements

Shipboard acoustic Doppler current profiler (SADCP) data were collected throughout the voyage. The 38 kHz SADCP of Teledyne Instruments operated with 16-m bin sizes, pinging once a second. 64 bins were used, although the range was practically narrower than 1000 m. Ensemble averaging occurs over 5 minutes intervals and half-hour intervals for the final processing. Headings and positions were determined using a ship-mounted GPS. Post-processing, including heading collection and time-averaging, were performed using Common Ocean Data Access System (CODAS). Using this software, we manually removed presumable contaminations by ship acceleration, acoustic ringing due to the hull geometry, and resonance with a ship-borne precision depth recorder.

Lowered ADCP (LADCP) Workhorse Monitor 300 kHz (Teledyne Instruments) was mounted on the CTD frame looking downward and recorded velocity shear throughout the water column, pinging every second. The LADCP data were translated to absolute velocity by vertical integration of the velocity shear, bottom tracking velocity, and the SADCP and shipboard satellite positioning system as boundary conditions (Visbeck 2002). As being close to the magnetic pole, the machine-fixed coordinate was referenced for the CTD frame direction. 4-m bin data were averaged into 20-m bins in the final product. Incorporating bottom tracking and the SADCP into the shear profile means that the LADCP velocities in the surface 100–200 dbar and bottom 100 dbar are the most reliable measurement. Although LADCP measurement generally has large uncertainties, cumulative zonal transports based on LADCP velocities are quantitatively consistent with transport derived from SADCP and CTD-based geostrophic velocities. The post-processed SADCP/LADCP data are available from the National Institute of Polar Research repository (https://ads.nipr.ac.jp/).

Satellite altimetry data was also used to complement the ADCP velocity field. Since the study region suffers from persistent sea ice, we adopt a monthly dynamic topography dataset developed by Mizobata et al. (2020), incorporating synthetic aperture interferometric radar altimetry, interpolated with topographically-deformed decorrelation scales (Shimada et al., 2017), and smoothed with an empirical orthogonal function filter.

3.3. Frontal positions

3.3.1 Definitions of fronts and zones

The global definition of Southern Ocean fronts has been based on subsurface isotherms (e.g., Orsi et al., 1995; Giglio and Johnson, 2016). As was remarked by Chapman et al. (2020), sea surface height in the Southern Ocean reflects the water column thickness associated with mean balanced flow, and the local surface height gradient maximum approximates a jet of quasi-barotropic ACC front. Subsurface isotherms likely follow subsurface isopycnals associated with the ACC fronts (in contrast to sea surface temperature, which is heavily affected by the air-sea-ice interaction) and have an advantage in continuously positioning fronts over different places relative to the sea surface height definitions. We later define frontal features based on the subsurface temperatures to characterize the frontal position globally. Readers are recommended to note that the isotherm does not necessarily follow a dynamical jet because it can shift due to baroclinic changes such as variation of isopycnal flux and mixing ratio.

The southern ACC front (SACCF; Orsi et al., 1995; Sokolov and Rintoul, 2007) partly overlaps the study region, and offshore eastward currents encountered in the KY18 survey are regarded as SACCF. The SACCF bifurcates upstream of the Kerguelen Plateau, and its southern branch enters the Australian-Antarctic Basin through the Princess Elizabeth Trough (Heywood et al., 1999; Bestley et al., 2018). To distinguish from its northern branch (SACCF-N; Sokolov and Rintoul, 2007) associated with a more significant surface height gradient, the southern branch of SACCF (SACCF-S) may be referred to as the southern boundary front (SBF; Chapter 1). The SBF generally follows the 4,000 m isobath and constitutes the northern limb of subpolar gyres. The isotherm of SACCF introduced by Orsi et al. (1995; 1.8°C at Θ-max; orange contour in Fig. 3a) actually follows the SBF rather than the SACCF-N. Henceforth, this temperature criterion is used to infer the position of SBF, and it is simply referred to as SACCF following the definition by Orsi et al. (1995).

One characteristic isotherm is 1.5°C of UCDW, corresponding to the ACC's southern boundary (SB, red curve in Fig 3a). The SB is defined by the poleward limit of the upper meridional overturning circulation, which is recognizable as the southernmost extent of the oxygen-depleted UCDW (Orsi et al., 1995). This configuration means the SB is not a dynamical front associated with a surface height gradient maximum but a baroclinic water mass boundary (Chapman et al., 2020). Off East Antarctica, the SB is located along the center of clockwise gyre circulations (Fig. 1b; Chapter 1), unlike the Weddell and Ross Seas, where the SB exists outside the gyre circulation.

Since the dissolved oxygen value along the 1.5°C on Θ-max has minimal changes from the original description by Orsi et al. to the KY18 data (~195 μmol/kg; Chapter 2), this criterion may be used to define the SB in 1996 and 2019.

The ASC circumvents Antarctica westward, isolates cold SW from warm CDW, and creates a sharp Antarctic Slope Front (ASF) over the continental slope (Jacobs, 1991; Whitworth et al., 1998; Thompson et al., 2018). The sharpest structure of ASF presents off East Antarctica (Whitworth et al., 1998; Pauthenet et al., 2021), reflecting the strong easterlies within the sector (Hazel and Stewart, 2019). The structure of ASF dramatically varies along the slope, likely due to the distribution of coastal polynyas, the topographically-controlled flow field, and eddy variability (Foppert et al., 2019; Chapter 4). For illustration, 0°C at 400 dbar was used to proxy the ASF (blue contour in Fig. 3a), which approximates the cross-slope temperature gradient maxima (Whitworth et al., 1998) and is analogous to the temperature range by Pauthenet et al. (2021).

Based on the frontal definitions, the study region was categorized into the Southern, Subpolar, and Continental Zones (Fig. 3b). The SB divides the Southern and Subpolar Zones, whereas the ASF divides the Subpolar and Continental Zones (Orsi et al., 1995). Although these categories do not rigorously represent the circulation regimes, we may consider that water property changes within the zone generally reflect water changes along streamlines. As a reference for the climatological frontal position, we adopt a gridded dataset created by Shimada et al. (2017), which likely reproduces the frontal structure associated with the continental slope topography (Fig. 3a).

3.3.2 Changes in frontal positions

The frontal positions derived from the two occupations (including XCTD measurements) are presented in Fig. 3a. The SB to the east of 112°E in 2019 was located southward than 1996 by 50–120 km, as reported in Chapter 2. Meanwhile, between 120–140°E, the ASF in 2019 was located offshore than in 1996 by 10–40 km. The positional change of ASF is concurrent with a change in the velocity structure (discussed in Section 5). The CTD stations in the KY18 and BROKE surveys are tagged with the Southern, Subpolar, and Continental Zones according to their temperature profiles. As a result, more stations in 2019 (Fig. 3b) were classified into the Southern Zone than in 1996 (Fig. 3c) and less into the Subpolar Zone. Because of the shoreward data scarcity in 2019, the position of ASF could not be determined to the west of 115°E, and the comparison between the two occupations is only possible to the east of 100°E.

3.4. Water properties

3.4.1 Definitions of water masses

The water mass definitions are updated from Bindoff et al. (2000) and Meijers et al. (2011) based on TEOS-10 variables (Table 1), categorizing observed water properties in the T-S diagram (Fig. 4). The following definitions may be compared to Bestlay et al. (2018) and Bensi et al. (2021). The vertical extent of the 1.5°C isotherms (Fig. 2), corresponding to the oxygen-depleted layer (dissolved oxygen > 195 μmol/kg), defines UCDW as γ_n of 27.93–28.10 (in kg/m^3), alternatively, bounded by σ_θ of 27.70 and σ_1 of 34.85. The temperature inversion layer (interface between UCDW and AASW) is stratified by salinity, generally characterized by S_A of 34.6 g/kg. The salinity criterion for AASW is applicable for the Subpolar and Continental Zones since WW remarked by the near-freezing temperature (below –1.5°C) extends to around 34.3–34.6 g/kg, corresponding to σ_θ of 27.50–27.70. Bindoff et al. (2000) and Meijers et al. (2011) adopted γ_n of 28.03 as the lower surface of AASW; however, this definition includes UCDW in the Southern Zone. Instead, σ_θ of 27.70 (or γ_n of 27.93) is a safer choice as its definition. Warm, fresh AASW created by solar heating and sea ice melt generally exists shallower than σ_θ of 27.50.

The core of UCDW is the subsurface Θ-max, whereas LCDW corresponds to the SA-max. Between UCDW and AABW, LCDW is defined by γ_n of 28.10–28.27 (alternatively, bounded by σ_1 of 34.85 and σ_3 of 41.68). Although LCDW and AABW are weakly stratified, and there is no physical basis for the definition of AABW, γ_n of 28.27 has conventionally been adopted as its upper limit (Orsi et al., 1999). This isopycnal generally corresponds to σ_3 of 41.68 and the 0°C isotherm. The term SW may imply various kinds of water observed over the continental shelf (e.g., Chapter 1), while the definition here is somewhat narrow as dense water potent of forming AABW ($\gamma_n > 28.27$). LCDW and a part of UCDW (γ_n of 28.03–28.27) intrude onshore with transforming to modified CDW (mCDW; γ_n of 28.03–28.27). Onshore salt flux is primarily maintained by mCDW intrusion, whereas brine rejection in coastal polynyas creates high salinity SW locally saltier than mCDW (e.g., Williams et al., 2010).

3.4.2 Changes in water properties

Pressure and isopycnal averages were compared between 1996 and 2019 measurements (Fig. 5). In the Southern Zone, temperature and salinity around the Θ-max (200–500 dbar) were almost unchanged by the isopycnal average, while 2019 was slightly warmer and saltier (by ~0.1°C and ~0.01 g/kg) than 1996 in the pressure average, as a result of poleward migration of UCDW. Below the Θ-max pressure, the 2019 data were cooler and fresher (by ~0.1°C and ~0.01 g/kg) than 1996 in both Southern and Subpolar Zones, reflecting the widespread freshening likely associated with glacial meltwater discharge (Purkey and Johnson, 2013; Rye et al., 2014). The signal of freshening can be seen in ASW inshore (< 400 dbar; by ~0.4°C and ~0.05 g/kg). In contrast, subsurface temperature and salinity in the Continental Zone (> 400 dbar and γ_n > 28.03) significantly increased (by ~0.3°C and ~0.03 g/kg). As this difference necessarily asymptotes to zero near 400 dbar by the definition of ASF, these results indicate that the coastal freshening increased vertical gradient of temperature and salinity in the Continental Zone. The change in stratification may be relevant to the offshore shift of the ASF's isotherm (Fig. 3). The possibility of onshore warming is discussed in the next section.

Five meridional sections are available to compare 1996 and 2019 measurements (Figs. 6–8). The general temperature increase on pressure surface in the vicinity of SB (Figs. 6a–b; by 0.1–1.6°C) is caused by the poleward migration of UCDW corresponding to the 1.5°C isotherms (red contour). This trend is partly counteracted by the coastal freshening (Figs. 7a–b; by 0.01–0.12 g/kg) associated with shoreward cooling (remarkable to the south of 64.5°S in 128 and 140°E). Isopycnal warming in UCDW (Fig. 6c; γ_n of 27.93–28.10) is generally observed to the north of SB. Its poleward extensions are detected in 112, 120, and 150°E, unlikely in 128 and 140°E. These results suggest that the isopycnal onshore transport of anomalous heat due to the poleward SB shift caused onshore warming in 112, 120, and 150°E, while freshwater near the shelf break partly blocked the heat intrusion. On the other hand, onshore warming may also be induced by the heaving of ASF isopycnals. The shallow sections above 800 dbar (Fig. 6b and Fig 7b) indicate that isopycnal heaving in 120, 128, 140°E caused mCDW intrusion below the freshened layer near the shelf break (temperature increase up to 0.4°C). Overall, either enhanced isopycnal heat flux or isopycnal heaving of ASF likely caused onshore warming in all five sections. Since the poleward SB shift is emergent as a multidecadal trend (Chapter 2; Auger et al., 2021), it is suspected that the continental shelf has experienced successive warming over the past decades. Isopycnal warming is generally confined to the UCDW layer (Fig. 6c; above γ_n of 28.10). In contrast, LCDW and AABW (below γ_n of 28.10) experienced slight isopycnal cooling due to the widespread freshening (Fig. 7c; ~0.02 g/kg). As the S_A-max (represented by 34.89 g/kg; blue contour) migrated poleward with salinity increase (Figs. 7a–b), the isopycnal cooling at depth results from freshening cancellation of temperature increase by the poleward SB shift.

We also examine the dissolved oxygen change using bottle data from the BROKE survey (Fig. 8). The extent of the oxygen-depleted water (represented by195 μmol/kg; green contour) was in accordance with the 1.5°C isotherm (Fig. 6) for both occupations, underpinning the validity of

SB/UCDW definitions. The oxygen trends are generally anti-correlated with the changes in temperature/salinity; i.e., temperature/salinity increases by the poleward CDW migration were associated with oxygen decrease, and temperature/salinity decreases by the extra freshwater flux were associated with oxygen increase. The poleward SB shift generally reduces dissolved oxygen, as seen on the pressure surface (Fig. 8a). Nevertheless, dissolved oxygen of LCDW and AABW increased from 1996 to 2019, suggesting that oxygen supply from SW exceeded the deoxygenation effect of the poleward SB shift. Along with the enhanced onshore CDW intrusion, the results possibly indicate enhancement of lower meridional overturning.

3.5. Large scale circulation and transport

3.5.1 Surface and bottom velocities

Shipboard ADCP (Fig. 9a) captured the general eastward flow of the SACCF (~15 cm/s) and the westward flow of the ASC along the continental slope (~10 cm/s). The surface flow direction significantly varies in space and time, presumably reflecting waves, turbulence, and transient air–sea interaction. In the SB's vicinity, exceptionally, surface velocity tends to be small, indicating a divergent flow condition. Subsurface flow (200–1,000 m; Fig. 9b) likely controls the position of SB, as defined by the Θ-max temperature. The southernmost eastward jet likely exists around the 4,000 m isobath, broadly consistent with the climatological circulation (Mizobata et al., 2020; Chapter 1). Poleward velocities in 120 and 128°E up to 10 cm/s may be consistent with the poleward CDW intrusion at the longitudes. We can observe bottom-intensified ASC (~10 cm/s) over the continental slope (Fig. 9c), likely driven by coastal buoyancy loss and downslope geostrophy (Gill, 1973; Williams et al., 2010). Furthermore, southward flows at the northern ends of 110 and 120°E were also bottom-intensified (up to 10 cm/s), which may manifest the intensity of the deeply-rooted recirculating gyre (McCartney and Donohue, 2006).

3.5.2 Zonal transport

Geostrophic calculation was applied for the five meridional sections to derive zonal transport due to baroclinic flows (Fig. 10a). The geostrophic flows mostly direct eastward in both 1996 and 2019 occupations due to poleward inclination of dynamic height, and hence baroclinity of the ASC is insignificant for its westward transport. This result is consistent with the previous observation in the western Indian Ocean sector (Meijers et al., 2010). Eastward geostrophic transports over the sections were relatively larger in 128, 140, 150°E (~20 Sv) than in 112 and 120°E (~10 Sv), reflecting the ACC's proximity in the east. Eastward geostrophic transport in 2019 was slightly larger than in 1996 (up to 5 Sv; except 128°E), likely associated with the poleward SB shift and a change in the geostrophic transport of the ASC.

In contrast to the geostrophic transport, absolute transport based on the ADCP measurements generally directs westward (Fig. 10b), indicating the quasi-barotropic structure of the ASC over the slope. LADCP integration and SADCP combined with geostrophic velocity are in accordance, so the circulation is largely in geostrophic balance. Westward transports of 1996 (10–55 Sv; white circles; adopted from Bindoff et al., 2000) are greater than 2019 (10–25 Sv; black circles), and the ASC's transport maxima in 1996 are located significantly shoreward than in 2019 by ~100 km except for 150°E. Hence, the ASC in 2019 was likely weaker and located northward than in 1996, and this can partly pertain to the slightly increased eastward geostrophic component (Fig. 10a). A cross-slope mooring array in 113°E (17 months for 2010–2011) suggested that the westward ASC transport is ~19 Sv (Pena-Molino et al., 2016; south of 62°S), generally falling into the estimated range by the 2019 hydrography (see also Fig. 11b). The ASC transport in 2019 thus likely reflects its typical value over the decade, while the multidecadal change of the ASC transport may also affect the result. The cause of the ASC's change is argumented in the next section.

3.5.3 Dynamic topography

We evaluate the interannual variability of the circulation pattern using altimetry-based dynamic topography. Dynamic topography during the KY18 survey is presented in Fig. 11a with the climatological frontal positions. The southernmost eastward jet of SACCF exists along the 4000 m isobath, whereas the isolines of –1.95 m generally represent the clockwise subpolar recirculations. The SB, defined as the poleward limit of the UCDW isotherm (1.5°C), is aligned with the center of the subpolar recirculations, as previously observed by a velocity field reconstructed from the advection of profiling floats (Chapter 1). Although the dynamic topography is further presented inshore of the ASF, its structure over the continental shelf is highly uncertain due to the lack of geoid information over the continental shelf (Mizobata et al., 2020; Fecher et al., 2017). Nevertheless, the dynamic topography appears to represent the along-slope contours corresponding to the ASC.

The interannual variation of the –1.95 m isoline is shown in Fig 11b, in which the SB positions during the 1996 and 2019 measurements are denoted by red markers. The contour in 2019 January is highlighted by a dotted line, whereas the longitude of the mooring section during 2010–2011 (Pena-Molino et al., 2016) is indicated by a green broken line. The available period of the dynamic topography data is from 2010 November. Except for a sudden poleward shift of the northern limb in 2011–2012 (by 30–60 km), any systematic trend in the flow pattern is not noticeable during the data period. The stability of the barotropic flow structure over the decade infers the relative importance of baroclinity for the change in the ASC transport. In 2019 January, the eastward velocity near the northern limb of clockwise circulation is relatively strong (Fig. 11c; by ~1cm/s) due to poleward displacement of the SACCF contour. At that time, no significant decrease in the ASC velocity (i.e., its eastward anomaly) is observed, indicating that the poleward shift of the barotropic ACC front does not necessarily weaken the ASC's barotropic velocity. This result contrasts with the weakening of ASC’s baroclinic velocity concurrent with the poleward shift of geostrophic contours (Figs. 6a and 11b).

3.6. Discussion and conclusion

The observations unveil a new aspect of the ASC's variability. The position of 0°C isotherms representative for the ASF core shifts offshore from 1996 to 2019 (Fig. 3) as the axis of the westward ASC does (Fig. 10b). The offshore ASC shift is attributable to the cooling and thickening of AASW by freshwater input originating from the coast (Figs. 5a–b). The westward transport of ASC in 2019 likely falls within the typical value over the 2010s (Figs. 10b and 11b) despite the relatively poleward location of the SACCF jet (Fig. 11c). In contrast, the ASC transport in 1996 was significantly larger than in 2019 in all available cross-slope sections (generally by 5–30 Sv; Fig. 10b). The decrease in the ASC transport between 1996 and 2019 may be interpreted as follows; the poleward frontal shift is associated with the steric height increase (Fig. 7a; see also Chapter 2), likely contributing to a decrease in the baroclinic westward velocity of ASC (Fig. 10a). However, the poleward displacement of SACCF does not necessarily lead to a decrease of the barotropic transport of ASC (Fig. 10c), and the dynamic topography change of the ASC is insignificant over the past decade (Fig. 10b). On the other hand, the offshore shift of the ASF isotherm (Fig. 3a; caused by coastal freshening) between 120–140°E is consistent with the offshore displacement of the ASC. Since the ASC's structure is remarkably modified by freshwater input (in position and stratification; Figs. 7–9), the primary cause of the decrease in the ASC transport from 1996 to 2019 might be the weakening of its baroclinic velocity by coastal freshening. In addition, barotropic response to easterly winds (Pena-Molino et al., 2016) may also be essential for the observed changes as the geostrophic transport (Fig. 10a) does not explain all changes in westward transport (Fig. 10b).

Our findings from the revisited hydrography can be summarized as in Fig. 12. From 1996 to 2019, there have been three significant changes in the ocean structure: i) contraction of AABW (Van Wijk and Rintoul, 2014; Aoki et al., 2020), ii) poleward migration of the SB (Chapter 2; due to frontal shift and isopycnal transport), and iii) weakening of baroclinic ASC transport. The AABW contraction is attributable to its freshening (Van Wijk and Rintoul, 2014), vanishment of abyssal water, and poleward shift of barotropic front; however, the dominance of thermosteric change in the AABW volume over the halosteric change (Purkey and Johnson, 2013; Chapter 2) support the latter two as plausible causes. Further, isopycnal oxygenation of AABW and LCDW (Fig. 8) likely reflects enhancement of SW ventilation and the lower meridional overturning cell, possibly associated with the coastal freshening.

Although we observed a remarkable change in the ASF stratification, the cause of weakened baroclinic transport of ASC remains not evident. Our result suggests that the stronger cross-slope temperature gradient due to the coastal freshening and the poleward SB shift does not necessitate reinforcement of ASC barrier (sometimes observed in climate model; Goddard et al., 2017). Alternatively, it might have increased mCDW intrusion via stronger stratification and weaker baroclinic ASC. This speculation is consistent with eddy-resolving numerical experiments (Nakayama et al., 2021) and reminiscent of positive feedback for coastal melting; i.e., more meltwater discharge can weaken the ASC barrier, enhance onshore heat intrusion, thus further melt coastal ice. The likelihood of the "meltwater–ASC feedback" should be tested by scrutinizing how the ASC establishes a barrier for the cross-slope transport (e.g., Bower et al., 1985) and how its structure responds to the coastal freshening. The role of the poleward SB shift is of particular interest as a possible trigger and accelerator for the feedback.

Figures and tables

Figure 1. Overview of the KY1804 hydrographic survey region. (a) Geographical locations of the CTD stations and climatological oceanic fronts. Green dots are the full-depth CTD stations with water sampling, and white dots are the XCTD measurement sites. The fronts are derived from the gridded climatology of Shimada et al. (2017). (b) Schematic of the three-dimensional structure of the horizontal and meridional circulations and water masses. The SB divides the Southern and Subpolar Zones, and the ASF divides the Subpolar and Continental Zones.

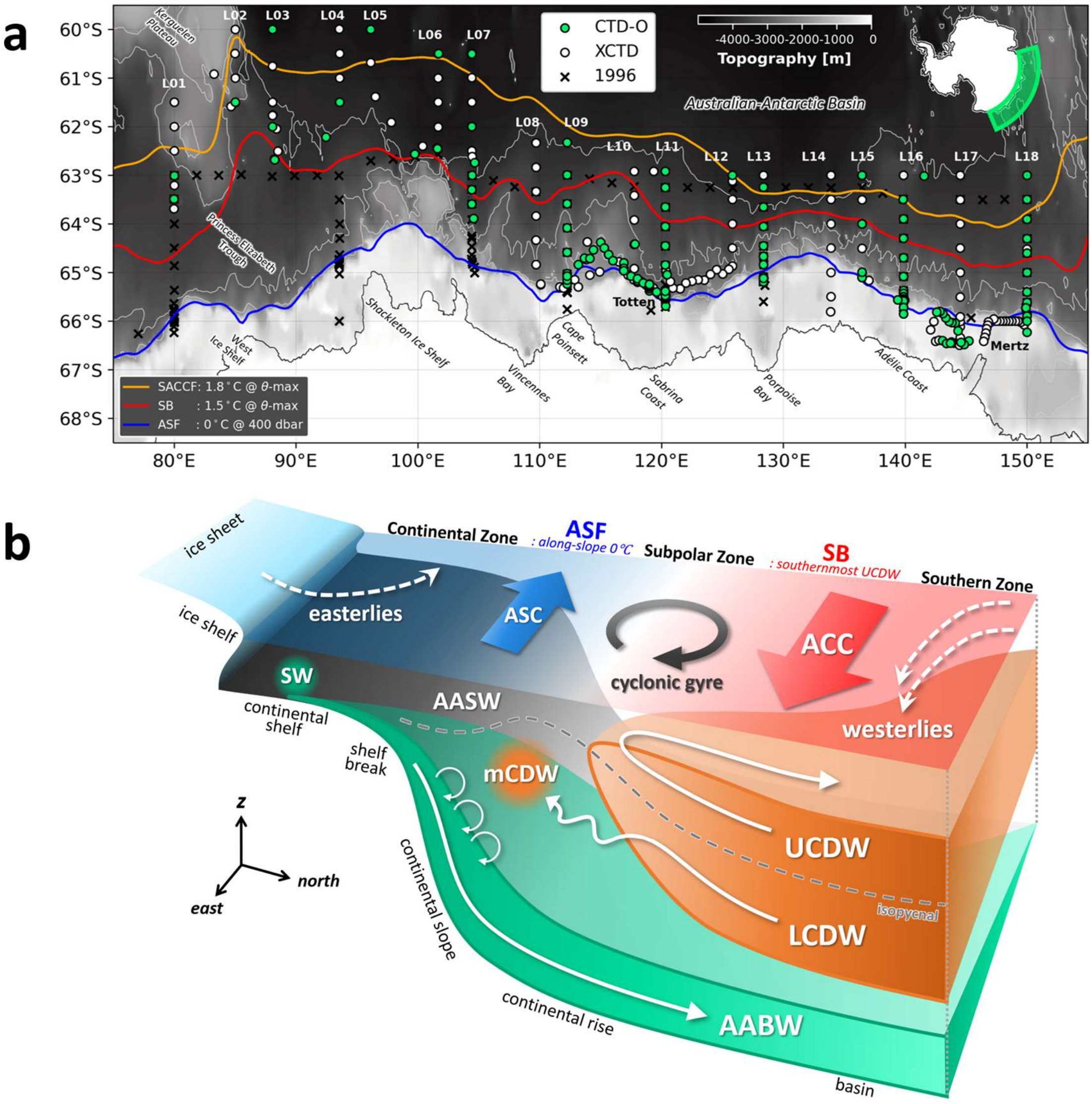

Figure 2. All vertical sections of Conservative Temperature from Leg 1 to Leg 18, focused on upper 1,000 dbar. Red (blue) contours are the 1.5°C (0°C) isotherms, whereas black contours indicate neutral density surfaces. Triangles at the bottom of each panel indicate the locations of full-depth CTD (green) and XCTD (white) stations.

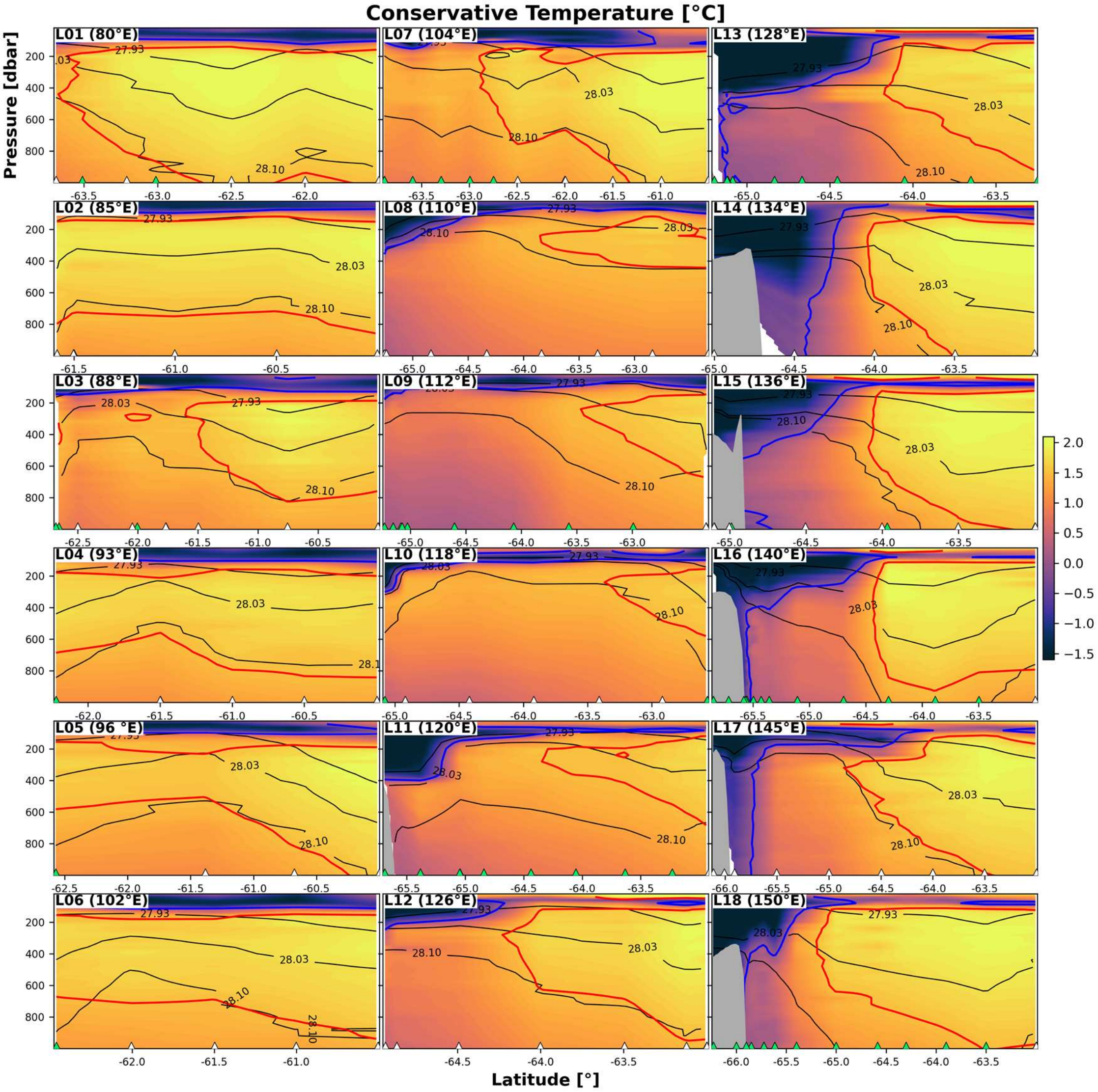

Figure 3. (a) Frontal positions inferred by isotherms of each dataset. Based on 2019 and 1996 positions, CTD stations are categorized into each frontal zone: (b) is from the KY1804 survey, and (c) is from the BROKE survey. Solid curves are the climatological fronts in Fig. 1 (Shimada et al., 2017). Topographic contours are shown with 1,000 m intervals.

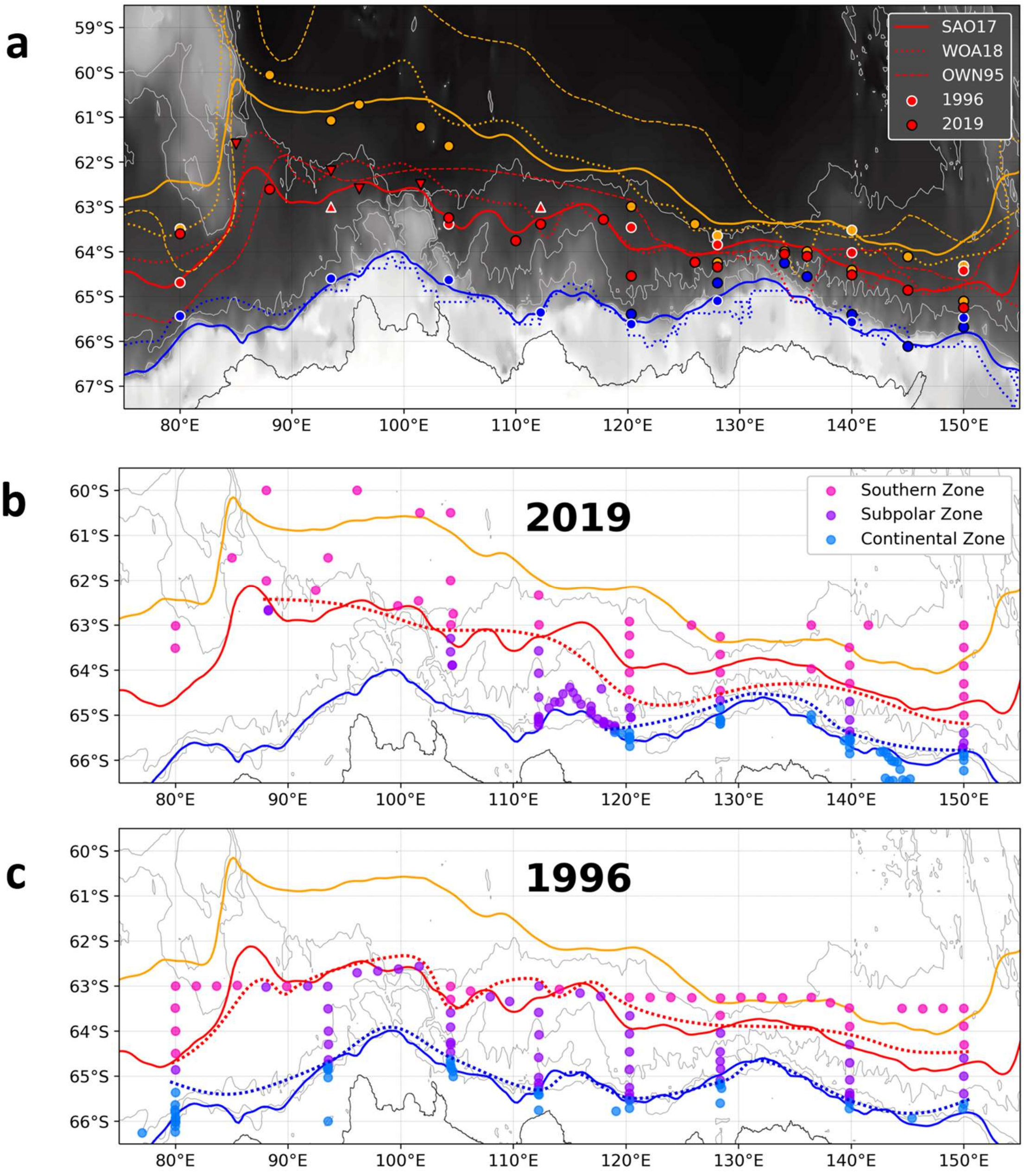

Figure 4. Conservative Temperature–Absolute Salinity plot for all full-depth CTD stations in the KY1804 survey, colored with their frontal zones. Neutral density contours are shown by black curves, whereas potential densities are shown by green curves. To eliminate the effect of spatial differences in the isopycnal averages, profiles in the Southern and Subpolar Zones are extracted from east of 100°E, and profiles in the Continental Zone are extracted from north of 66°S, east of 115°E.

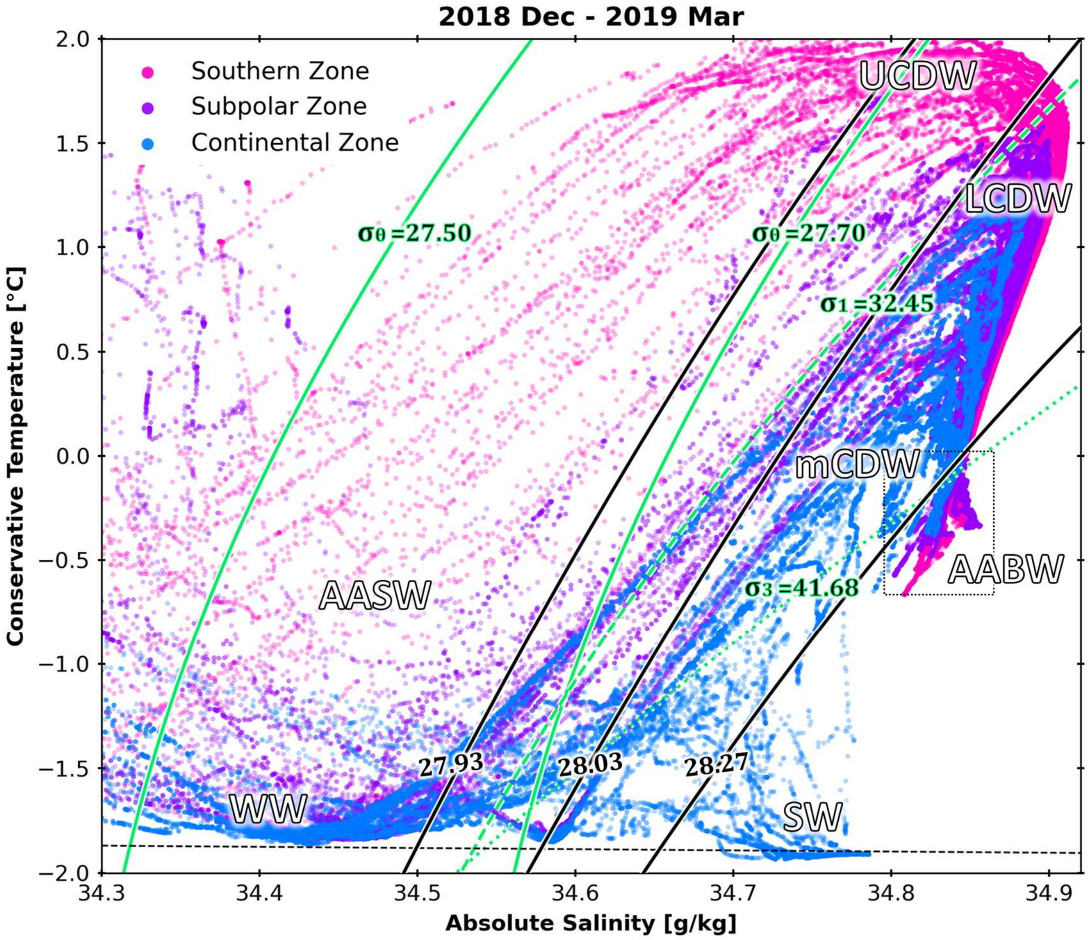

Table 1. Bounding neutral density, potential density, Conservative Temperature, and Absolute Salinity for the water mass definitions. Typical characteristics are denoted inside brackets.

	γ_n (kg/m^3)	σ_θ , σ_1 , σ_3 (kg/m^3)	Θ (°C)	S_A (g/kg)
AASW	(< 28.03)	$\sigma_\theta < 27.70$	($-1.84 < \Theta < 2.0$)	< 34.6
WW	(< 28.03)	$27.50 < \sigma_\theta < 27.70$	< -1.5	$34.3 < S_A < 34.6$
UCDW	$27.93 < \gamma_n < 28.10$	$\sigma_\theta > 27.70$, $\sigma_1 < 32.45$	> 1.5; Θ-max	> 34.6
LCDW	$28.10 < \gamma_n < 28.27$	$\sigma_1 > 32.45$, $\sigma_3 < 41.68$	($0 < \Theta < 1.8$)	> 34.85; S_A-max
mCDW	$28.03 < \gamma_n < 28.27$	$\sigma_1 > 32.45$	< 1.5	$34.6 < S_A < 34.85$
AABW	> 28.27	$\sigma_3 > 41.68$	$-1 < \Theta < 0$	($34.8 < S_A < 34.9$)
SW	> 28.27	($\sigma_\theta > 27.70$)	< -1.5	(> 34.65)

*AASW: Antarctic Surface Water, WW: Winter Water, UCDW: Upper Circumpolar Deep Water, LCDW: Lower Circumpolar Deep Water, mCDW: modified Circumpolar Deep Water, AABW: Antarctic Bottom Water, SW: Shelf Water

Figure 5. Vertical profiles of Conservative Temperature (a, c) Absolute Salinity (b, d) in pressure (a, b) isopycnal (c, d) coordinates, colored by the frontal zone. Thick curves indicate their isobaric/isopycnal averages for 2019 (solid) and 1996 (dashed).

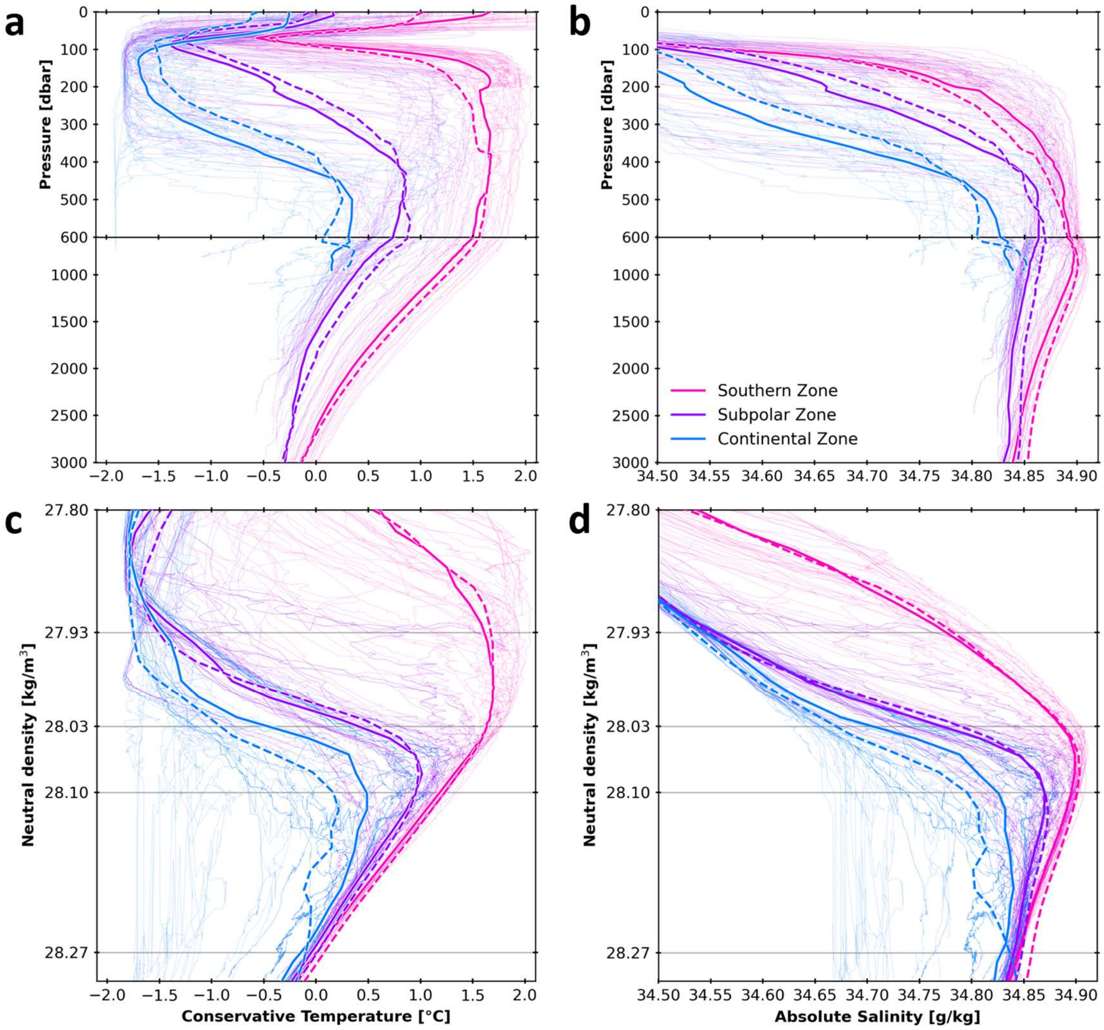

Figure 6. Vertical sections of Conservative Temperature change from 1996 to 2019 on pressure surfaces (a), upper 800 dbar (b), and on isopycnal surfaces (c), for Legs 9 (112°E), 11 (112°E), 13 (128°E), 16 (112°E), and 18 (150°E). The 1.5°C isotherms and neutral density surfaces in each measurement year are denoted as in Fig. 2; solid and dotted contours are from 2019 and 1996, respectively. Colormaps are shown in the uppermost panels. In (c), upper 100 dbar is hatched to hide surface transient features.

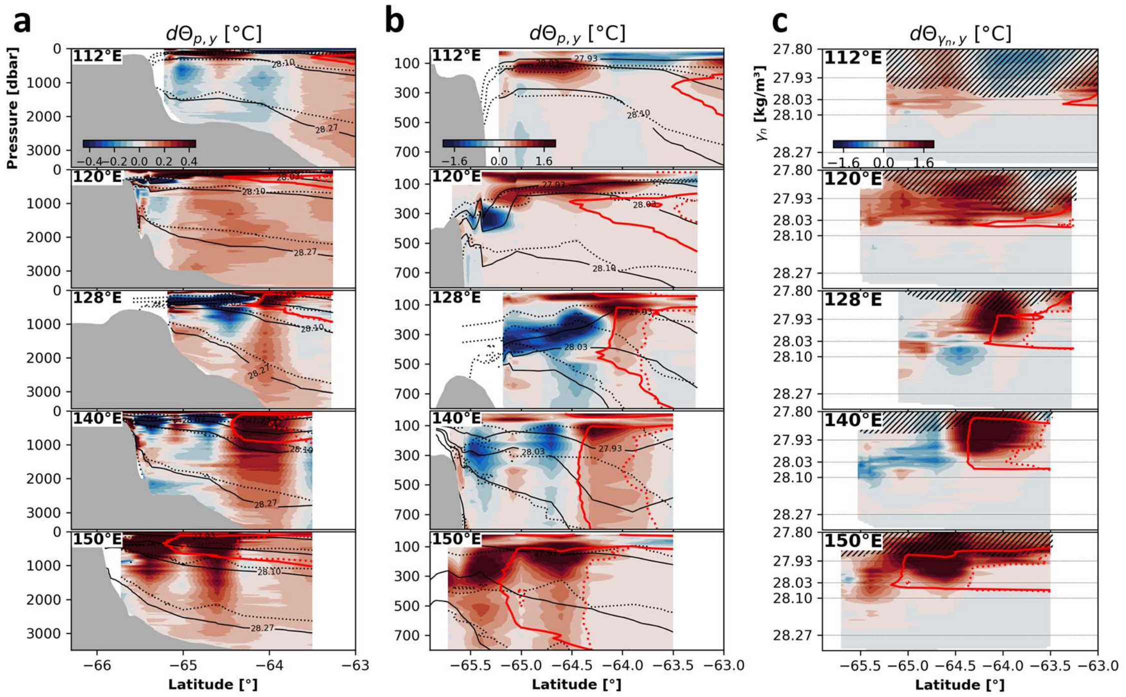

Figure 7. Same as Fig. 6, but for Absolute Salinity. Blue contours are the 34.89 g/kg isohalines, which represent the salinity maximum layer.

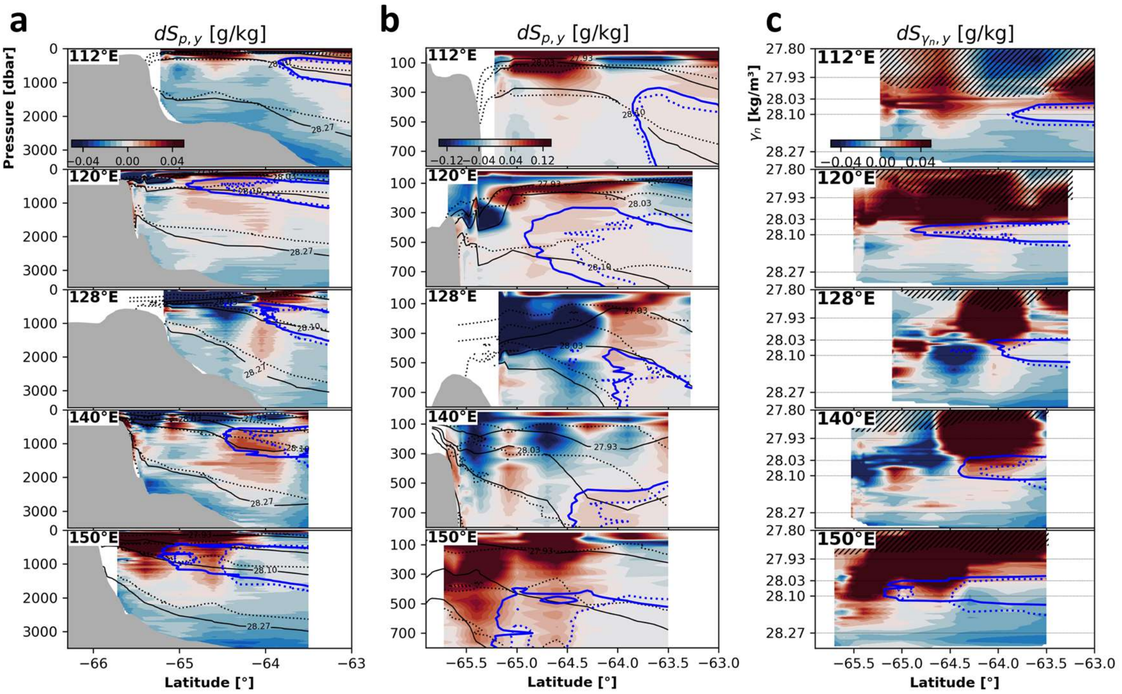

Figure 8. Same as Fig. 6, but for dissolved oxygen. Green contours are the 195 μmol/kg isopleths, which represent the oxygen minimum layer.

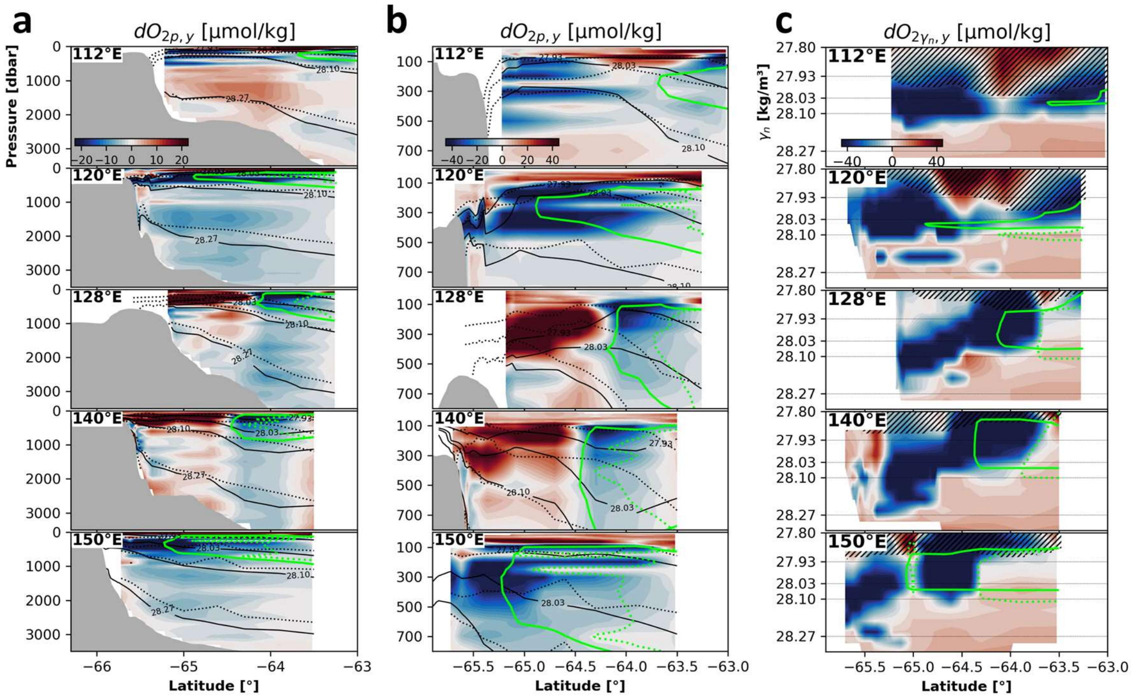

Figure 9. Velocity maps derived from the acoustic Doppler current profiler measurements. (a) Upper 200 m velocity vectors colored by the zonal component from the SADCP measurements (60 min. averages). (b) 200–1000 m averaged velocity from the LADCP measurements. (c) Same as (b) but averaged for 100 m from the seabed. In (b) and (c), black edged vectors denote absolute velocity larger than the half of error velocity. The position of SB in 2019 (red dots) and the topographic contours (gray) are also shown.

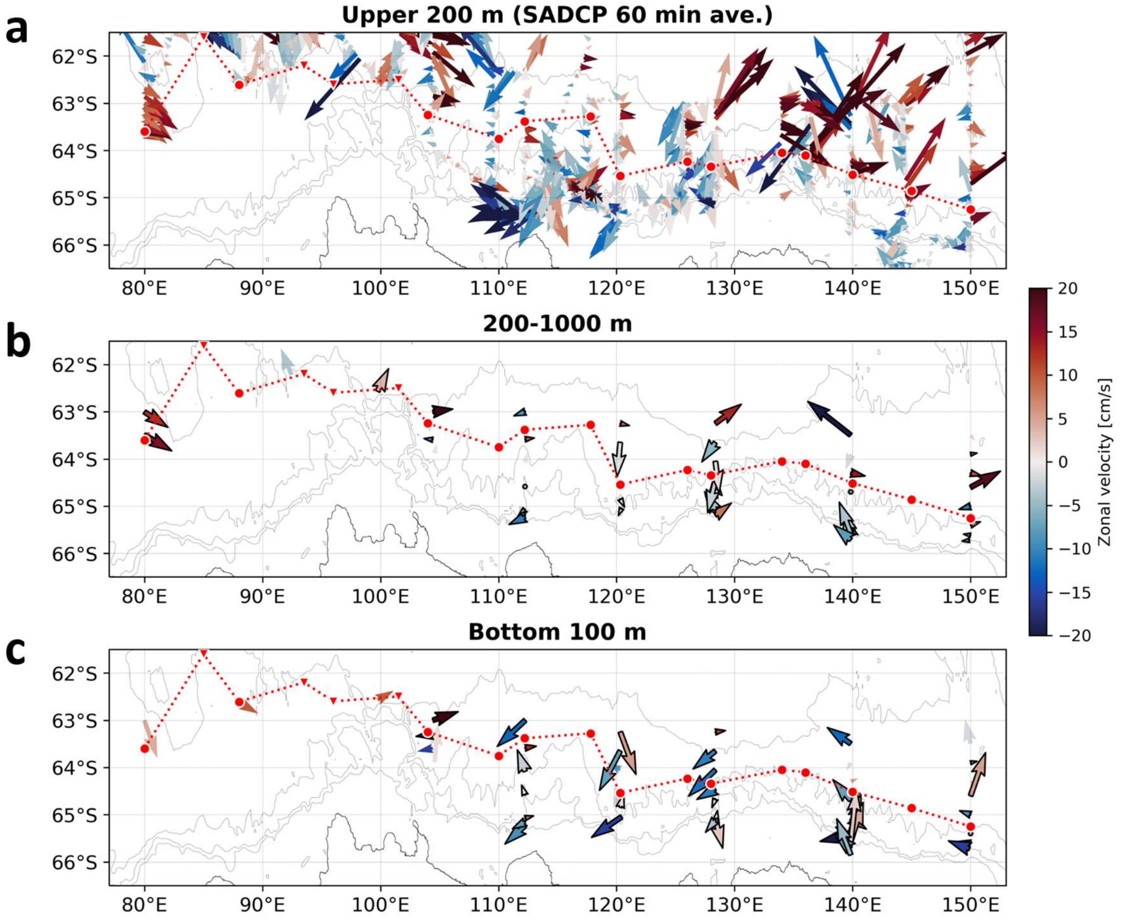

Figure 10. Zonal transport accumulated from the south for Legs 9 (112°E), 11 (112°E), 13 (128°E), 16 (112°E), and 18 (150°E). (a) Bottom-referenced geostrophic transport for 2019 (solid) and 1996 (dashed). (b) Absolute transport derived from the direct measurement by LADCP with 95% error bounds (dotted) and the SADCP measurement plus surface-referenced geostrophic transport (solid). Black circles indicate where the westward transport reaches its maximum. Previous estimates of the ASC transport by Bindoff et al. (2000; 'B00', white circle) and Pena-Molino et al. (2016; 'P16', star) are denoted (the latitudes of 'B00' indicate where westward flow became eastward, and the latitude of 'P16' indicates the center of mooring array.) Red vertical line is the SB location in 2019 (solid) and 1996 (dashed).

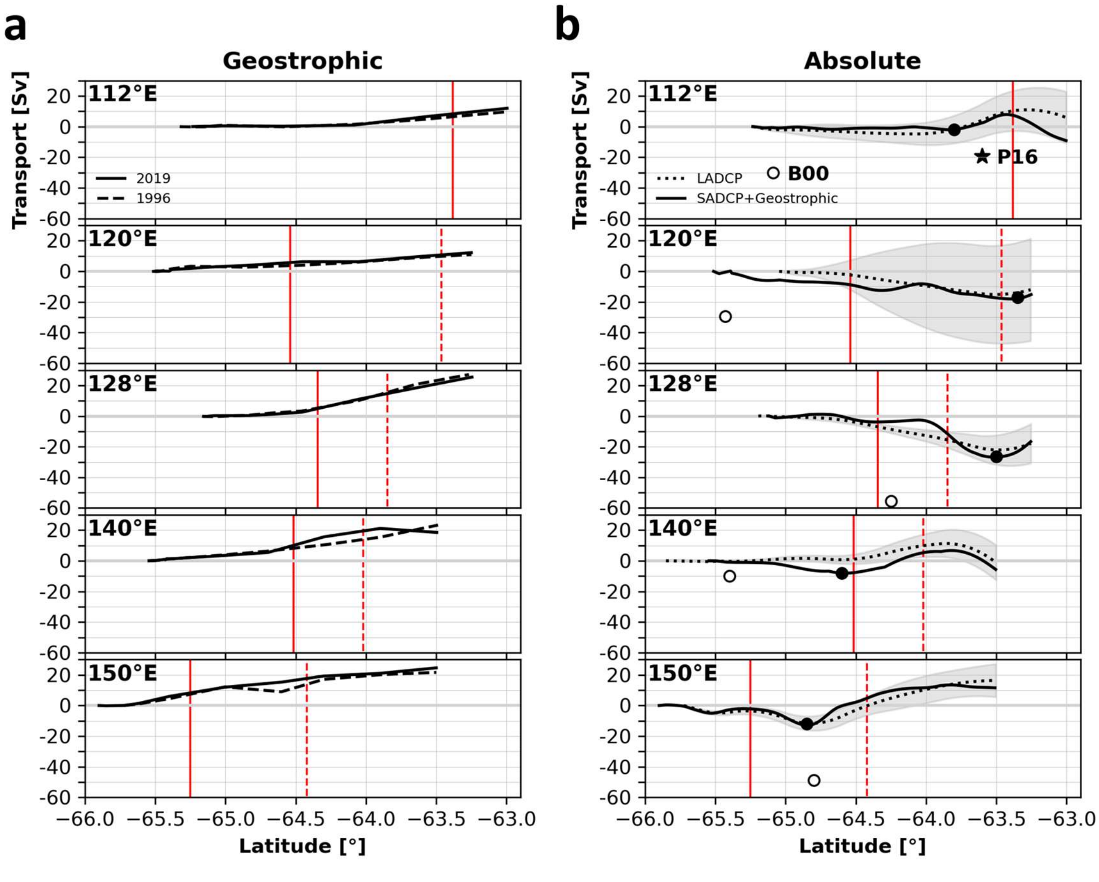

Figure 11. Dynamic topography. (a) Monthly average in 2019 January. Climatological frontal positions are denoted as in Fig. 3. (b) The interannual variation of the 1.95 m isoline from 2011 to 2020. Red scatters are the position of SB during the 1996 and 2019 occupations (white and black edgecolors, respectively). White dotted line corresponds to January 2019. Green dashed line indicates the longitude of cross-slope mooring array in 2010–2011 (Pena-Molino et al., 2016). (c) Zonal velocity anomaly in 2019 Janualy relative to the 2011–2020 January climatology, zonally filtered with 4° Blackman-Harris filter.

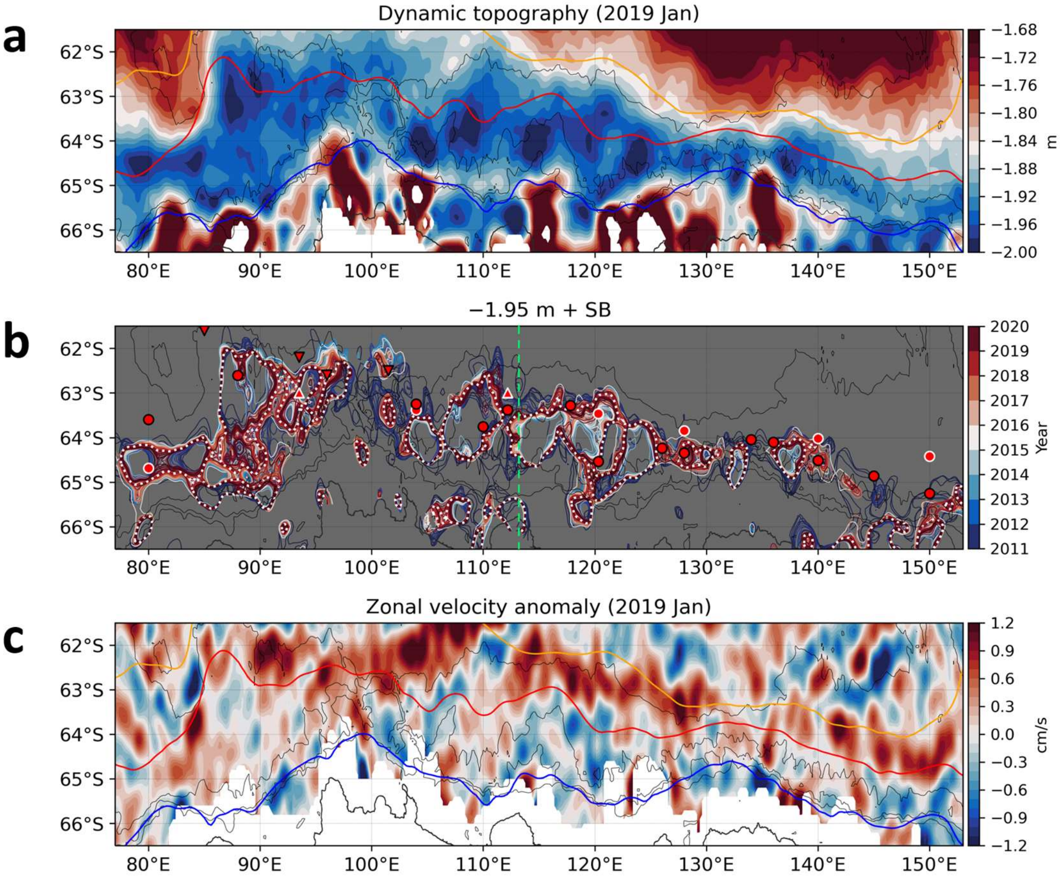

Figure 12. Summary of the observed changes from 1996 to 2019. Blue and red shades indicate westward ASC and eastward ACC, respectively.

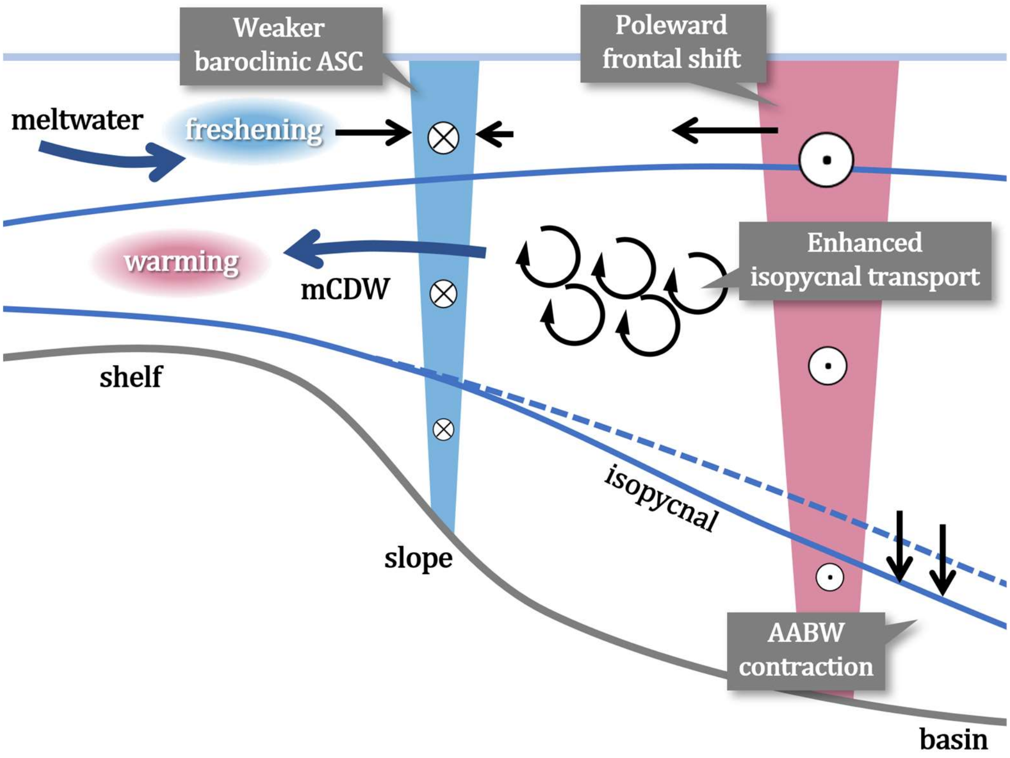

References and notes

Aoki, S., Sasai, Y., Sasaki, H., Mitsudera, H., and Williams, G. D. (2010). The cyclonic circulation in the Australian-Antarctic basin simulated by an eddy-resolving general circulation model. Ocean Dynamics, 60(3), 743–757.

Bensi, M., Kovačević, V., Donda, F., O'Brien, P., Armbrecht, L., and Armand, L. (2021). Water masses distribution offshore the Sabrina Coast (East Antarctica). Earth System Science Data Discussions, (July), 1–21.

Bestley, S., van Wijk, E., Rosenberg, M., Eriksen, R., Corney, S., Tattersall, K., and Rintoul, S. (2020). Ocean circulation and frontal structure near the southern Kerguelen Plateau: The physical context for the Kerguelen Axis ecosystem study. Deep-Sea Research Part II: Topical Studies in Oceanography, 174(July 2018), 104479.

Bindoff, N. L., Rosenberg, M. A., and Warner, M. J. (2000). On the circulation and water masses over the Antarctic continental slope and rise between 80 and 150°E. Deep-Sea Research Part II: Topical Studies in Oceanography, 47(12–13), 2299–2326.

Bower, A. S., Rossby, H. T., & Lillibridge, J. L. (1985). The Gulf Stream—barrier or blender?. Journal of Physical Oceanography, 15(1), 24-32.

Chapman, C. C., Lea, M.-A., Meyer, A., Sallée, J.-B., and Hindell, M. (2020). Defining Southern Ocean fronts and their influence on biological and physical processes in a changing climate. Nature Climate Change, 10(3), 209–219.

Fecher, T., Pail, R., Gruber, T., Schuh, W. D., Kusche, J., Brockmann, J. M., et al. (2017). GOCO05c: A New Combined Gravity Field Model Based on Full Normal Equations and Regionally Varying Weighting. Surveys in Geophysics, 38(3), 571–590.

Foppert, A., Rintoul, S. R., and England, M. H. (2019). Along-Slope Variability of Cross-Slope Eddy Transport in East Antarctica. Geophysical Research Letters, 46(14), 8224–8233.

Foster, T. D. (1995). Deep water formation off the eastern Wilkes Land coast of Antarctica. Antarctic Journal of the United States, 30(5), 110–111.

Garcia, H. E., and Gordon, L. I. (1992). Oxygen solubility in seawater: Better fitting equations. Limnology and Oceanography, 37(6), 1307–1312.

Giglio, D., and Johnson, G. C. (2016). Subantarctic and polar fronts of the Antarctic Circumpolar Current and Southern Ocean heat and freshwater content variability: A view from Argo. Journal of Physical Oceanography, 46(3), 749–768.

Gill, A. E. (1973). Circulation and bottom water production in the Weddell Sea. Deep-Sea Research and Oceanographic Abstracts, 20(2), 111–140.

Goddard, P. B., Dufour, C. O., Yin, J., Griffies, S. M., & Winton, M. (2017). CO2‐induced ocean warming of the Antarctic continental shelf in an eddying global climate model. Journal of Geophysical Research: Oceans, 122(10), 8079-8101.

Hazel, J. E., and Stewart, A. L. (2019). Are the near-Antarctic easterly winds weakening in response to enhancement of the southern annular mode? Journal of Climate, 32(6), 1895–1918.

Heywood, K. J., Sparrow, M. D., Brown, J., and Dickson, R. R. (1999). Frontal structure and Antarctic Bottom Water flow through the Princess Elizabeth Trough, Antarctica. Deep-Sea Research Part I: Oceanographic Research Papers, 46(7), 1181–1200.

Hirano, D., Mizobata, K., Sasaki, H., Murase, H., Tamura, T., and Aoki, S. (2021). Poleward eddy-induced warm water transport across a shelf break off Totten Ice Shelf, East Antarctica. Communications Earth and Environment, 2(1).

Hirano et al. (2023), Surface oceanography (80–150°E), *in preparation* to Special Issue in Progress in Oceanography.

Hood, E.M., Sabine, C.L. and Sloyan, B.M. (eds) (2010) The GO-SHIP Repeat Hydrography Manual: a collection of expert reports and guidelines, Version 1. (IOCCP Report 14), (ICPO Publication Series 134).

Jackett, D. R., and Mcdougall, T. J. (1997). A neutral density variable for the world's oceans. Journal of Physical Oceanography, 27(2), 237–263.

Jacobs, S. S. (1991). On the nature and significance of the Antarctic Slope Front. Marine Chemistry, 35(1–4), 9–24.

Kitade, Y., Shimada, K., Tamura, T., Williams, G. D., Aoki, S., Fukamachi, Y., et al. (2014). Antarctic bottom water production from the Vincennes Bay Polynya, East Antarctica. Geophysical Research Letters, 41(10), 3528–3534.

Lumpkin, R., and Speer, K. (2007). Global ocean meridional overturning. Journal of Physical Oceanography, 37(10), 2550–2562.

McCartney, M. S., and Donohue, K. A. (2007). A deep cyclonic gyre in the Australian-Antarctic Basin. Progress in Oceanography, 75(4), 675–750.

Meijers, A. J. S., Klocker, A., Bindoff, N. L., Williams, G. D., and Marsland, S. J. (2010). The circulation and water masses of the Antarctic shelf and continental slope between 30 and 80{ring operator} E. Deep-Sea Research Part II: Topical Studies in Oceanography, 57(9–10), 723–737.

Mizobata, K., Shimada, K., Aoki, S., and Kitade, Y. (2020). The Cyclonic Eddy Train in the Indian Ocean Sector of the Southern Ocean as Revealed by Satellite Radar Altimeters and In Situ Measurements. Journal of Geophysical Research: Oceans, 125(6).

Morrison, A. K., McC. Hogg, A., England, M. H., and Spence, P. (2020). Warm Circumpolar Deep Water transport toward Antarctica driven by local dense water export in canyons. Science Advances, 6(18), 1–10.

Murase, H., Abe, K., Matsukura, R., Sasaki, H., Driscoll, R., Driscoll, S., Schaafsma, F., van Regteren, M., Yang, Q., Ohshima, H., Ohshima, K., Sugioka, R., Tong, J., Yamamoto, N., Doiguchi, H., Briggs, E., Doi, K., Hirano, D., Katsumata, K., Kiuchi, M., Ko, Y., Nomura, D., Orui, M., Sato, H., Toyoda, S., Yamazaki, K., Ishihara, T., Hamabe, K., Kumagai, S., Miyashita, T., Yamada, N., Koyama, Y. and Sasaki, H. (2018). Cruise report of multidisciplinary ecosystem survey in the eastern Indian sector of the Antarctic (CCAMLR Division 58.4.1) with a focus on Antarctic krill during 2018/19 season by the Japanese survey vessel, Kaiyo-maru. WG-EMM-19/42 [available form the CCAMLR Secretariat]

Nakayama, Y., Greene, C. A., Paolo, F. S., Mensah, V., Zhang, H., Kashiwase, H., ... & Aoki, S. (2021). Antarctic Slope Current modulates ocean heat intrusions towards Totten Glacier. Geophysical Research Letters, 48(17), e2021GL094149.

Naveira Garabato, A. C., Williams, A. P., and Bacon, S. (2014). The three-dimensional overturning circulation of the Southern Ocean during the WOCE era. Progress in Oceanography, 120, 41–78.

Orsi, A. H., Whitworth, T., and Nowlin, W. D. (1995). On the meridional extent and fronts of the Antarctic Circumpolar Current. Deep-Sea Research Part I, 42(5), 641–673.

Pauthenet, E., Sallée, J. B., Schmidtko, S., and Nerini, D. (2021). Seasonal variation of the antarctic slope front occurrence and position estimated from an interpolated hydrographic climatology. Journal of Physical Oceanography, 51(5), 1539–1557.

Peña-Molino, B., McCartney, M. S., and Rintoul, S. R. (2016). Direct observations of the Antarctic Slope Current transport at 113°E. Journal of Geophysical Research: Oceans, 121(10), 7390–7407.

Shimada, K., Aoki, S., and Ohshima, K. I. (2017). Creation of a gridded dataset for the southern ocean with a topographic constraint scheme. Journal of Atmospheric and Oceanic Technology, 34(3), 511–532.

Sloyan, B. M., Wanninkhof, R., Kramp, M., Johnson, G. C., Talley, L., Tanhua, T., et al. (2019). The global ocean ship-base hydrographic investigations program (GO-SHIP): A platform for integrated multidisciplinary ocean science. Frontiers in Marine Science, 6(JUL), 1–21.

Sokolov, S., and Rintoul, S. R. (2007). Multiple jets of the antarctic circumpolar current South of Australia. Journal of Physical Oceanography, 37(5), 1394–1412.

McDougall, T. J., & Barker, P. M. (2011). Getting started with TEOS-10 and the Gibbs Seawater (GSW) oceanographic toolbox. SCOR/IAPSO WG, 127, 1-28.

Thompson, A. F., Stewart, A. L., Spence, P., and Heywood, K. J. (2018). The Antarctic Slope Current in a Changing Climate. Reviews of Geophysics, 56(4), 741–770.

Visbeck, M. (2002). Deep velocity profiling using lowered acoustic Doppler current profilers: Bottom track and inverse solutions. Journal of Atmospheric and Oceanic Technology, 19(5), 794–807.

Whitworth, T. (2002). Two modes of bottom water in the Australian-Antarctic Basin. Geophysical Research Letters, 29(5), 17-1-17–3.

Whitworth, T., Orsi, A. H., Kim, S.-J., Nowlin, W. D., and Locarnini, R. A. (2013). Water Masses and Mixing Near the Antarctic Slope Front. In Ocean; Ice; and Atmosphere: Interactions at the Antarctic Continental Margin; Antarctic Research Series; vol. 75; (Vol. 75, pp. 1–27).

Williams, G. D., Aoki, S., Jacobs, S. S., Rintoul, S. R., Tamura, T., and Bindoff, N. L. (2010). Antarctic bottom water from the adélie and George v Land Coast, East Antarctica (140-149°E). Journal of Geophysical Research: Oceans, 115(4), C04027.

Yamazaki, K., Aoki, S., Katsumata, K., Hirano, D., and Nakayama, Y. (2021). Multidecadal poleward shift of the southern boundary of the Antarctic Circumpolar Current off East Antarctica. Science Advances, 7(24), eabf8755.

Yamazaki, K., Aoki, S., Shimada, K., Kobayashi, T., and Kitade, Y. (2020). Structure of the Subpolar Gyre in the Australian-Antarctic Basin Derived From Argo Floats. Journal of Geophysical Research: Oceans, 125(8).

Yamazaki, K., Mizobata, K., Aoki, S., Onshore diffusion of Circumpolar Deep Water, *in preparation* for submitting to Journal of Geophysical Research: Oceans.

This chapter is adopted from

Yamazaki, K., Katsumata, K., Hirano, et al., Revisit of the circulation and water masses over the East Antarctic margin, *in preparation* to Special Issue in *Progress in Oceanography*.

(This page is intentionally set blank)

4

ONSHORE DIFFUSION OF CIRCUMPOLAR DEEP WATER

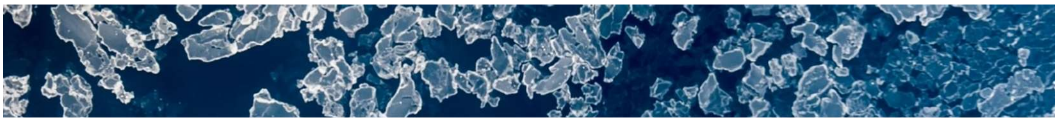

Abstract

Warm, salty Circumpolar Deep Water (CDW) has long been regarded as the climatological driver for Antarctica, but the mechanism of how it can reach the continental shelf remains unsettled. Motivated by the absence of observational eddy flux estimation in the Antarctic margin, we quantify isopycnal diffusivity of CDW by hydrographic variability and satellite altimetry under the mixing length framework. For comparison, spiciness and thickness are used as the isopycnal tracer, and two yield similar results. Over the extent of Antarctic Circumpolar Current, we find a general agreement with the mixing suppression theory and its exception in the lee of the topography as previously reported. In contrast, no mixing length's dependency on mean flow is obtained to the pole, reflecting a stagnant flow regime in the Antarctic margin. Eddy diffusion is likely enhanced where the CDW intrusion is localized by the recirculating gyres, mostly attributable to the small gradient of isopycnal thickness. Volume transport is then estimated in a GM-flux manner. Thickness-diffusive onshore heat flux over the continental slope is quantitatively consistent with cryospheric heat sinks (sea ice formation and ice shelf basal melt), suggesting that the isopycnal eddy advection is the main factor of the onshore CDW intrusion. We emphasize that the isopycnal thickness field is essential for determining the eddy fluxes in the Antarctic margin.

4.1 Background

Over the extent of the Antarctic Circumpolar Current (ACC), mesoscale eddies transport water masses across the streamlines, building up the adiabatic pathway of the global meridional overturning circulation (Marshall and Radko, 2003; Cessi, 2019). Isopycnal eddy diffusion is fundamental for the poleward heat flux in the Southern Ocean because the bottom enhanced diapycnal mixing (Kunze et al., 2006) and the surface water transformation (Abernathey et al., 2016) unlikely penetrates the intermediate and deep layers in the interior. Recent observations have indicated that mesoscale eddy plays a key role in bridging the Antarctic meridional overturning from deep ocean basins to the continental shelves (Thompson et al., 2014; Mckee et al., 2019), while the eddy condition from the ACC to the shoreward Antarctic Slope Current (ASC; Thompson et al., 2018) remains unconstrained.

Circumpolar Deep Water (CDW), the primary source of heat and salt for the Antarctic coasts, is transported across the ASC predominantly by mesoscale eddies in the absence of large-scale zonal pressure gradient (Stewart and Thompson, 2013). In reality, pressure gradient associated with topographic features generates standing eddies and meanders, facilitating the meridional water exchange (e.g., Hogg and Blundell, 2006). Topography-controlled geostrophic flows can transport CDW poleward in the continental margin (Morrison et al., 2020; Hirano et al., 2021). Meanwhile, the steep barotropic potential vorticity (PV) gradient on the upper continental slope (inshore of ~3,000 m isobaths) unlikely allows for the presence of the cross-slope mean flow, and hence eddy diffusion and/or tidal mixing might be essential for the onshore CDW flux near the shelf break (Stewart et al., 2018; Chapter 1). To the south of the ACC, the spatial distribution of eddy diffusion is yet to be described except few analyses (Foppert et al., 2019; FRE19 henceforth). From an observational standpoint, this study quests (1) to delineate the controlling factor of eddy diffusion in the Antarctic margin (portrayed as a poleward extension of Naveira Garabato et al., 2011; GFP11 henceforth) and (2) to quantify the isopycnal CDW flux by eddy diffusion towards the continental shelves.

The horizontal circulation in the Antarctic margin is shaped by the eastward ACC and the westward ASC, and in the transition zone between them exist clockwise subpolar gyres (e.g., Park and Gamberoni, 1995). The Weddell and Ross gyres are wide enough to isolate cold shelves from warm CDW, whereas ACC's proximity to the continent creates the eastward slope current in the eastern Pacific sector (Spence et al., 2017; Thompson et al., 2020) and standing eddies in the Indian sector (Mizobata et al., 2020; Chapter 1), resulting in the relatively warmer coastal conditions than the other sectors (Jenkins et al., 2016; Silvano et al., 2016). A lack of knowledge on the subpolar ocean circulation motivates further reanalysis of in-situ observations. Although FRE19 inferred the along-slope variability of eddy transport over the continental slope using seal-mounted conductivity-temperature-depth (CTD) data, the correspondence between the flow regime and eddy diffusion remains unclear. The present study approaches this question regarding the importance of eddy flux for the multidecadal change in the Antarctic thermal conditioning (Chapter 2). The East Antarctic margin (30–160°E; Fig. 1) is mainly targeted, where a sufficient amount of in-situ data exists thanks to ceaseless efforts of deploying profiling float and biologging. In this region, the eddy condition has recently been explored (FRE19; Stewart et al., 2018, 2019), lateral tidal mixing is weaker than the rest of the Antarctic margin (Beckman and Pereira, 2003), the frontal structure of ASC is relatively prominent (Pauthenet et al., 2021), and the onshore CDW flux collects attention for the future climate projection (Chapter 2; Hirano et al., 2021).

This paper is set out as follows. In Section 2, we review the theoretical background for observation-based eddy diffusivity calculation and introduce the concept of mixing length framework. In Section 3, we describe data and methods used for diffusivity calculation. In Section 4, mixing length, eddy diffusivity, and eddy fluxes are quantified, and their spatial variations are delineated with respect to the topographic structure in the continental margin. In Section 5, validity of presented results is assessed, and controlling factors of eddy diffusion are discussed. We conclude in Section 6.

4.2 Mixing length framework

This section briefly reviews arguments of the mixing length framework, which provides the basis for our analysis. The observational estimates of oceanic eddy diffusion may branch in four ways: hydrographic variability (Armi and Stommel, 1983; Naveira Garabato et al., 2011), altimetric eddy scaling (Klocker and Abernathey, 2014; Bates et al., 2014), tracer patch deformation (Marshall et al., 2006), and dispersion time scale (LaCasce and Bower, 2000; Sallée et al., 2011). The first two methods rely on the mixing length arguments (Taylor, 1921):

$$k = \Gamma U_{eddy} L_{mix} \qquad (1),$$

where Γ is mixing efficiency (or eddy transfer coefficient), U_{eddy} is characteristic eddy velocity measured by the standard deviation of downgradient velocity $\sigma(v)$, and L_{mix} is mixing length scale. This formulation rests on two major assumptions (quoted from Naveira Garabato et al., 2011): (i) tracer fluctuations are generated by local stirring of the large-scale tracer gradient, with the advection of tracer variance from upstream regions being weak; and (ii) the tracer gradient varies slowly over the distance L_{mix}.

The mixing length framework has widely been applied for the closure of geostrophic turbulence since the eddy tracer transport can be linked to a downgradient flux in Eulerian form. Diffusivity k of generalized tracer φ (which approximately follows PV contours) due to isopycnal stirring is parameterized as

$$\overline{v'\varphi'} = -k\frac{\partial \varphi}{\partial y} \qquad (2),$$

where the overbars indicate temporal average in the isopycnal layer, the primes indicate deviations from those averages, and the tracer gradient is assumed to be meridional. Here, it is *a priori* assumed that tracer φ mixes purely along isopycnals. This assumption is equivalent to the conditions that the mixing process is statistically steady, adiabatic, and solely caused by linear waves (e.g., Vallis, 2017). Although we may choose any passive tracer for φ, if the tracer concentration represents the PV field, its diffusion satisfies a requirement for the GM flux (Gent and McWilliams, 1990) mimicking baroclinic instability, and the scalar coefficient of downgradient PV flux may express the skew component of diffusivity tensor.

One possible choice for L_{mix} is characteristic eddy scale (Klocker and Abernathey, 2014; Bates et al., 2014), which can be determined by the altimetric velocity field. Another possible choice is a rather empirical way of using hydrographic data. Emulating arguments of Armi and Stommel

(1983), Naveira Garabato et al. (2011) derived L_{mix} in the Southern Ocean from hydrographic variability, i.e.,

$$L_{mix} = \frac{\sigma(\varphi)}{|\nabla\varphi|} \qquad (3).$$

Although they used isopycnal temperature for the conservative tracer φ, there exist other candidates (e.g., isopycnal spiciness and layer thickness). By the equations (1)–(3), the mixing efficiency follows as

$$\Gamma = \frac{\overline{v'\varphi'}}{\sigma(v)\,\sigma(\varphi)} \qquad (4),$$

that is identical to the correlation coefficient between v and φ. There are diverse estimates for Γ likely depending on the variety of L_{mix} definitions (generally ranging 0.01–0.4; Holloway and Kristmannsson, 1984; Visbeck et al., 1997; Karsten and Marshall, 2002). Naveira Garabato et al. noted the only observational estimate $\Gamma = 0.16$ provided by Wunsch (1999) may be used for the illustrating purpose.

The hydrographic estimate of eddy diffusivity by Naveira Garabato et al. is broadly consistent with a more direct estimation via Lagrangian tracer dispersion numerically advected with altimetric velocity (Marshall, 2006; Sallée et al., 2011), generally falling into 1500–3000 $\mathrm{m}^2\ \mathrm{s}^{-1}$ within the ACC core and higher values in its equatorward flank. The resulting map of diffusivity can be generally explained by the suppression theory deduced from weakly nonlinear wave–mean flow interaction (Ferrari and Nikurashin, 2010), interpreted as that advection reduces eddy's continuous action for the same water mass and suppresses mixing length. The suppression of eddy stirring ceases in "leaky jets", likely associated with non-parallel shear flows and meanderings steered by the topography (Naveira Garabato et al., 2011; Sallée et al., 2011; Tamsitt et al., 2018). Klocker and Abernathey (2014) conducted numerical simulations to test the quantitativeness of the mixing length framework. They remarked that, in a hypothetical unsuppressed mixing regime, diffusivity could equivalently be estimated by both the eddy scale/tracer-based mixing length formulations by choosing $\Gamma = 0.15$ for the tracer-based mixing length, supporting the estimate of Wunsch (1999). These studies rationalize to use the hydrographic variability method: the equations (1) and (3), and thus we proceed to apply them for quantifying eddy diffusion.

4.3. Data and methods

4.3.1 Altimetric velocity

An observational estimate of characteristic eddy velocity U_{eddy} can be given by altimetric velocity in the open ocean, while the satellite altimetry has previously been unavailable in the seasonal ice zone. Later, the advent of synthetic aperture interferometric radar altimeter enabled to measure sea ice freeboard remotely, and its application to dynamic ocean topography has recently been developed (Armitage et al., 2018; Mizobata et al., 2020). The present study adopts the monthly-reconstructed 0.2° grid dynamic ocean topography during 2011–2020 by Mizobata et al. (2020) to derive geostrophic velocities (Fig. 2). This dataset has an advantage over the product by Armitage et al. (2018) as its empirical orthogonal function filtering can remove spurious stripe patterns.

U_{eddy} is calculated as the standard deviation of altimetric flow speed (lower panel of Fig. 2). Its reliability is underpinned by the mooring measurements at 113°E (Pena-Molino et al., 2016), marking standard deviations of 0.04–0.06 m s^{-1} in zonal and meridional directions at the CDW depth (~500 dbar). The typical value of U_{eddy} is somewhat larger than the choice of FRE19 (0.017 m s^{-1}), as they adopted the temporal mean velocity from the same mooring data. In principle, U_{eddy} is standard deviation of the cross-frontal velocity. However, in contrast to the ACC's mainstream, the flow field in the Antarctic margin is stagnant, and the mean flow directions are ambiguous (upper panel of Fig. 2). To bypass this problem, we simply define U_{eddy} as the root-mean-squared velocity, accounting for its good agreement with the direct flow measurement (Pena-Molino et al., 2016).

Vertical variations of eddy velocity are neglected in this study. GFP11 treated this issue by applying the gravest empirical mode analysis to derive geostrophic shear. The gravest empirical mode scheme is very effective in the ACC domain, while it cannot be applied for the Antarctic margin as the dynamic topography does not descend poleward monotonically. Nevertheless, we consider that U_{eddy} adopted for CDW is acceptable because the vertical attenuation due to geostrophic shear is considerably small in the Antarctic margin by the quasi-barotropic flow structure (Pena-Molino et al., 2016; Mizobata et al., 2020; Chapter 1).

4.3.2 Hydrographic data

Mixing length L_{mix} is calculated from hydrographic variability by the equation (3). We assemble historical CTD profiles from World Ocean Database (https://www.ncei.noaa.gov/; for shipboard CTD), Argo Global Data Assembly Center (Argo, 2000), and Marine Mammals Exploring the Oceans Pole to Pole archive (https://www.meop.net/; Treasure et al., 2018). Data are extracted for December–March and 1990 onwards. After removing bad flagged data and fragmented profiles, 1-dbar Akima interpolation is performed for the CTD profiles. Surface data averaged within the neutral densities (Jacket and McDougall, 1997) are then constructed (Fig. 3), corresponding to CDW (defined as 28.0–28.1 kg m^{-3}) and Antarctic Surface Water (ASW; defined as 27.9–28.0 kg m^{-3}). The figures indicate that, in contrast to isopycnal temperature gradient of ASW stronger than CDW, isopycnal thickness gradient of CDW is generally stronger than ASW. Our focus is CDW, while a comparison to the ASW layer, with a larger number of data than the CDW layer, facilitates to check the layer dependency and the quantitativeness of k.

The previous studies adopted potential temperature and spiciness as the isopycnal tracer φ (GFP11; FRE19). However, it is unclear if these tracers yield diffusivity k conforming to volume transport expected by the downgradient PV diffusion (e.g., Marshall and Radko, 2003). Since the layer thickness is a possible candidate for the PV conservative variable (e.g., Vallis, 2017), the present study adopts both spiciness and layer thickness as the isopycnal tracer φ, and the diffusivities derived from the two variables are compared. Conservative Temperature, Absolute Salinity, and spiciness (at 0 dbar) are calculated using the Gibbs Sea Water Oceanographic Toolbox (http://www.teos-10.org/), and the layer thickness is derived from the pressure difference between the upper and lower isopycnal surfaces of each watermass.

Mapping surface data onto 0.2° grids is performed with the radius basis function interpolation (Chapter 1), which reproduces the best representative surface of noisy data nonparametrically in the least-squares sense. Grid data with less than 10 points inside a 75 km data radius are masked (gray area). Although the data coverage particularly reduces in 30–60°E, a sufficient number of data exist within the region of our interest (e.g., the continental slope of 1,000–3,000 m isobaths). Correspondence among the 3,000 m isobath, –0.15 kg m^{-3} CDW spiciness, and 300 m CDW thickness (Fig. 3 right panels) guarantees fidelity of the interpolation. After calculating deviations of surface data from the gridded climatological field, root-mean-squared tracer variations $\sigma(\varphi)$ are derived in each grid from the deviation data within the 75 km radius. This procedure minimalizes artifacts in $\sigma(\varphi)$ due to the spatial variation of the tracer field within the data radius. The choice of the radius size is a trade-off between the data amount and the resolution, while our choice is comparable to the discussion by GFP11 that “about 5–10 stations per 100 km” is a reasonable baseline required for the L_{mix} calculation to capture the basic distribution patterns.

4.3.3 Mixing efficiency

One of the largest uncertainties of diffusivity k rests within the mixing efficiency Γ. Based on the equations (1) and (3), FRE19 indicated the along-slope variability of eddy condition in the East Antarctic margin via mapping standard deviation of isopycnal spiciness, while their formulation did not include Γ and spatially variable U_{eddy}, leaving some ambiguities for the absolute value of k. For a trial, we directly calculate Γ from the correlation coefficient between v and φ, using a 17-month mooring record across the ASC (in 113°E for 2010–2011; Pena-Molino et al., 2016). Vertical/meridional linear gridding (by 50 dbar for 200–1500 dbar and by 0.1 degrees for 65.5–61.5°S) is performed for hourly meridional velocity and temperature profiles to yield 1040 grids in total. During the 12 months (8761 steps), their correlation coefficient is calculated for each grid, assuming that the temperature variation is approximately coherent with the PV change and its gradient directs northward on average.

From the histogram of Γ, the mean value is estimated as 0.12 for down-gradient cases and 0.10 for all cases (Fig. 4). The up-gradient cases are possibly irrelevant to the climatological eddy condition since the downgradient velocity must direct southward by the mean temperature field (Fig. 3). Wunsch (1999) derived $\Gamma = 0.16$ from a global inventory of mooring records, broadly consistent with our estimates but larger by 30–40%. We must admit that 12 months is too short to determine eddy statistics with certainty (additional low-pass filtering may effectively cut off uninterested short-term variations, but such filtering possibly leads to underestimation). Based on the general agreement of the local value with the global estimate, the present study adopts the mixing efficiency $\Gamma = 0.16$ by Wunsch (1999) consistently with previous investigations (GFP11; Klocker and Abernathey, 2014). The validity of our choice is further discussed in Section 4.5.1.

4.4. Result

4.4.1 Mixing length

Standard deviation and normed gradient of isopycnal tracer φ for spiciness and layer thickness of each watermass are shown in Figs. 5 and 6, respectively. The large gradient of spiciness is concentrated near the ACC's southern boundary (SB; defined as the southernmost extent of 1.5 °C isotherms) in ASW (27.9–28.0 kg m^{-3}), while in CDW (28.0–28.1 kg m^{-3}), it emerges over the upper continental slope to the south (Fig. 5; top panels). The large standard deviation of spiciness broadly corresponds to its steep gradient. Relative to the spiciness gradient, the thickness gradient is likely homogeneous, and the coherence between the standard deviation and the gradient is less noticeable (Fig. 6). As in the spiciness, the sharp thickness gradient of CDW is found in the proximity of the SB, indicating a poleward volume flux represented by thickness diffusion (Chapter 1). Rounded patchy patterns appearing in the thickness-based diagnostics are likely associated with the distribution of standing eddies, while those signals are not visible in the spiciness-based values.

The lowermost panels in Figs. 5 and 6 present the mixing length L_{mix} derived from the equation (3). The patchy patterns in the thickness-based diagnostics do not emerge for L_{mix}. The spatial distributions of the spiciness/thickness-based L_{mix} are analoguous in terms of their meridional variations. These estimates are quantitatively consistent with the previous estimate by GFP11, where L_{mix} can exceed 150 km in the unsuppressed part of the ACC. Even though the spiciness/thickness-based diagnostics are highly dependent on the choice of isopycnal layer, the two L_{mix} estimates for CDW and ASW exhibit the highest value of ~150 km in the ACC domain and its suppression near the SB. These results suggest the quantitative robustness of the L_{mix} estimates. The spatial variation of L_{mix} is generally consistent with the jet-induced suppression theory (Ferrari and Nikurashin, 2010) as discussed in the following, while near-boundary turbulent suppression or "law of the wall" likely becomes more influential over the Antarctic margin than in the ACC domain.

The dependency of L_{mix} on the flow regime is detailed in Fig. 7. Estimates of L_{mix} are averaged in bins of mean flow speed and individually shown for the ACC frontal zones categorized by Orsi et al. (1995; see Figs. 1 and 2). The frontal zones refer to the dynamic topography data of Mizobata et al. (2020); the Subpolar Zone (south of SACCF-S): < –1.85 m, the Southern Zone (from the SACCF-S to SACCF-N): –1.85 ~ –1.6 m, and the Antarctic Zone (from SACCF-N to PF): –1.6 ~ –1.0 m. Readers are advised to compare Fig. 7 with the result by GRP11 (their Fig. 10), which puts emphasis on the more energetic part of ACC to the north. In the Antarctic and Southern Zones, L_{mix} tends to decrease from 70–90 to 30–60 km as the flow speed increases from zero to 0.5 m s^{-1}, indicating suppressed mixing due to wave–mean flow interaction. In the Antarctic Zone, L_{mix} partly increases with the mean flow exceeding 0.5 m s^{-1}, corresponding to leaky jets in the lee of topographic features such as the Kerguelen Plateau (~80°E) and the Southeast Indian Ridge (~150°E; see Fig. 2). On the other hand, L_{mix} is not dependent of flow speed in the Subpolar Zone, ranging from 20 to 60 km. These results suggest that the jet-induced mixing suppression previously documented in the northern part of the ACC is less effective poleward. We posit that the mixing suppression in the Subpolar Zone is associated with the near-boundary turbulent suppression by the continental slope topography. We also confirmed that discussion for the L_{mix} dependency on the flow speed unchanged in case the inversion of suppression factor (Ferrari and Nikurashin, 2010) is taken as the horizontal axis. In Fig. 7, inter-layer dependencies are unclear, accounting for the different data coverages of ASW and CDW (Fig. 3). Meanwhile, the thickness-based L_{mix} for ASW in the Subpolar Zone is exceptionally large for strong flows with relatively large standard errors. Its difference from the spiciness-based estimates is possibly due to the less distinctive gradient of thickness than spiciness in ASW (Figs. 5 and 6). It should be noted that the hydrographic variability method can yield L_{mix} and isopycnal diffusivity k quantitatively consistent with the previous estimates, while the choice of the isopycnal tracer φ occasionally affects the outcome and thus requires some rationale (as considered in the next section).

To monitor the transition of L_{mix}'s controlling factor towards the Antarctic margin, a histogram of L_{mix} is plotted on $\sigma(\varphi)$–$1/|\nabla\varphi|$ space (Fig. 8), in which all coordinates are normalized by their averages, the isolines of $L_{mix} = 20$, 100 km are shown by white contours, and the averaged diagnostics for each layer/method are marked by plus. The poleward suppression of L_{mix} is readily observed by comparing the positions of population and plus among the frontal zones. In all presented layers and methods, modes and averages of L_{mix} are aligned with the $1/|\nabla\varphi|$ axis in the Antarctic Zone, and they migrate towards the $\sigma(\varphi)$ axis across the diagonal line as moving poleward. Significant learning drawn from this plot is that the inversed tracer gradient $1/|\nabla\varphi|$ becomes more influential poleward to the spatial variation of L_{mix} than $\sigma(\varphi)$ does (i.e., the variation of L_{mix} in the cross-isoline direction is hardly explained by $\sigma(\varphi)$ in the Subpolar Zone in contrast to the Antarctic and Southern Zones). This is because the poleward PV gradient becomes steeper (equivalently, the width of baroclinic zone becomes narrower) to the south, plausibly due to the continental slope topography. The topographic control of L_{mix} signifies a possibility to parameterize the eddy diffusivity using prescribed topographic information in an ocean model, as recently explored by idealized numerical simulations (Stewart and Thompson, 2016). We anticipate that, in the Subpolar Zone, L_{mix} and k can be predicted by the topographic gradient, and this idea will be assessed in the next section.

4.4.2 Isopycnal diffusivity

Based on the general agreement with the previous studies in the ACC domain, the diffusive parameters in the Antarctic margin are investigated more closely. Using the mixing length formulation of the equation (1), the isopycnal diffusivity k is calculated as the product of mixing efficiency Γ, eddy velocity U_{eddy}, and mixing length L_{mix}. Fig. 9 provides diffusivity maps for CDW diagnosed by spiciness and thickness, focusing on the Subpolar Zone. The climatological flow direction is represented by the mean dynamic topography overlaid, and contours characteristic to the subpolar circulation (–1.97 and –1.85 m) are highlighted in blue. The isopycnal diffusivity k typically ranges 100–500 m^2 s^{-1} in the Subpolar Zone for both tracer variables, and k likely becomes small near the SB, which shapes the transition zone from ACC to ASC. The spatial variation of k within the Subpolar Zone seems attributable to the spatial variation of L_{mix} (Figs. 5 and 6) rather than U_{eddy} (Fig. 2) and thus to the PV gradient change (as seen in Fig. 8). To visualize the along-slope variability of k, local maps of thickness-based diffusivity are shown in Fig. 10 with the isopycnal CDW temperature. Importantly, diffusivity is likely higher where the onshore CDW intrusion occurs: 70°, 90°, 110°, and 120°E (these intrusion pathways are documented in Chapter 1). Additionally, enhanced diffusivity is observed in 140°E (Fig. 9), where intervals between ACC and ASC become narrow and clockwise subgyres are meridionally squeezed. The mechanism for this nontrivial correspondence between the eddy diffusion and the onshore CDW intrusion will be argumented in Section 4.5.4.

The spatial variation of k results from those of L_{mix} and U_{eddy}, and its functional dependency varies in space. Analogously to Fig. 8, a histogram of k in U_{eddy}–L_{mix} coordinates is plotted for each layer and method (Fig. 11). In any frontal zone, neither of L_{mix} and U_{eddy} is a dominant controlling factor as the population and the center of mass are located close to the diagonal line. Still, we may state that k is more dependent on L_{mix} than U_{edd} in the Subpolar Zone, contrasting to the Southern and Antarctic Zones. The result supports the aforementioned idea that the spatial scale of tracer gradient can parametrize eddy diffusivity in the Antarctic margin via mixing length formulation. This idea is further tested by Fig. 12, in which k, L_{mix}, and the inversed topographic gradient within the Subpolar Zone are regressed onto the inversed tracer gradient $1/|\nabla\varphi|$, coordinated with nondimensionalized axes, and the scatters are colored by the altimetric mean velocity. Not surprisingly, significant correlations of k and L_{mix} with $1/|\nabla\varphi|$ are obtained (0.73 and 0.89 for spiciness; 0.81 and 0.92 for thickness, respectively). On the other hand, the correlation between the topographic and tracer gradients is insignificant for both tracers, implying that additional information is required to derive the climatological tracer gradient from the topographic data. Despite that controlling factors for the tracer gradient field remain veiled, the present result is encouraging since it allows us to predict eddy diffusion adequately if only we somehow determine the gradient of isopycnal tracers.

Compared to the spiciness-based estimation, the correlation of the thickness-based estimation with diffusivity is more statistically significant. The higher correlation of thickness implies that the thickness gradient better represents the PV gradient and the width of the baroclinic zone than the spiciness gradient does. This result seems quite reasonable provided that the ambient PV field is well approximated by the isopycnal layer thickness within the Subpolar Zone, where the flow condition is stagnant, and the relative vorticity likely becomes small. Predicated on these facts, we proceed to estimate the diffusive transport applying the thickness-based diffusivity to the isopycnal thickness field.

4.4.3 Volume transport

Assuming that the isopycnal thickness simply diffuses downgradient in a GM-flux manner, we can estimate diffusive volume flux of CDW (Fig. 13). Bolus transport ψ is calculated as

$$\psi = -k_H \nabla H \qquad (5),$$

where H and k_H are the isopycnal layer thickness and the thickness-based diffusivity, respectively. This is equivalent to the layer-integrated bolus velocity (in m^2 s^{-1}), and its horizontal integration gives a unit of transport. The zonal eddy transport likely directs downstream in the lee of topography and upstream in the other area (middle panel), indicative of the internal form stress balance within the ACC (Marshall et al., 2017). As a result of the thickness gradient, the volume transport generally directs shoreward in the Subpolar Zone, as represented by the transport vector direction and its meridional component (lower panel). We can observe the poleward CDW transport continuously extending from the eastern flank of the Kerguelen Plateau, where isopycnal eddies are favorably generated, to the continental margin. Along-slope variation of the meridional eddy transport is not so pronounced as k (Fig. 9), and the most significant poleward CDW transport is obtained around 140°E. This is because the magnitude of transport is $|\psi| = \Gamma U_{eddy}\sigma(H)$ by the equation (3) and is not proportional to the inversed thickness gradient (whether CDW flux becomes uniquely proportional to U_{eddy} is unclear even in zonally-symmetric configuration regarding possible variability of mixing efficiency; e.g., Stewart and Thompson, 2016). Partially northward eddy transport along the continental slope (e.g., around 70°E) likely reflects the multiple-cored ASC over the gentle continental slope, which has emerged in previous literature (Meijers et al., 2010; Stewart and Thompson, 2016).

The meridional component of ψ is zonally integrated to derive the cross-slope fluxes of volume and heat (Fig. 14; over the 1000–3000 m isobaths). Standard errors associated with the cross-slope variation are shaded, within which heat flux change due to the along-slope temperature variation safely falls. The gross onshore CDW transport is 0.39/0.12 Sv (= $m^3\ s^{-1}$) in the eastern/western Indian sectors (divided by the Princess Elizabeth Trough ~90°E), respectively, translated to the onshore heat fluxes of 3.6/1.2 TW. The interbasin contrast in thermal forcing seems consistent with the stratification regimes inshore, represented by warm Totten Ice Shelf and cold Amery Ice Shelf (Silvano et al., 2016).

Offshore transport of ASW to the west of 130°E is 0.15 Sv, balancing with ~40 % onshore volume flux by CDW. On the contrary, ASW eastward of 130°E is transported to the pole, and its contribution to the onshore heat flux (~0.4 TW) might not be negligible. As discussed in Section 4.5.2, these estimates are quantitatively consistent with the coastal heat sink due to sea ice formation and glacial melting.

4.5. Discussion

4.5.1 Diffusivity estimation

The present study is fundamentally based on the assumption that the mixing length framework is valid to the extent of our interest. One of the necessary conditions for the formulation (see Section 4.2) is a scale separation between L_{mix} and the spatial variation of $\nabla\varphi$. We estimated the typical value of L_{mix} to be 20–60 km in the Subpolar Zone (Fig. 7). $\nabla\varphi$ likely varies in the cross-slope direction by a scale comparable to or larger than the slope width (~100 km for the 1,000–3,000 m interval), so it is possible to regard this condition as holding in the Antarctic margin. The other necessary condition for L_{mix} estimation is that tracer fluctuations must reflect local eddy stirring rather than tracer anomalies advected from upstream. This condition also likely holds in the Antarctic margin, given the weaker nonlinearity than the ACC's mainstream (Fig. 3).

No significant difference is found between the thickness-based and spiciness-based L_{mix} (Figs. 5 and 6). To our knowledge, the present study is the first example to demonstrate that the two choices of tracer yield very similar L_{mix} estimates. This infers quantitativeness of a series of previous estimates, in which isopycnal tracers not necessarily dependent on PV have been adopted (GFP11; FRE19; Armi and Stommel, 1983). Meanwhile, a small but noticeable difference between the spiciness/thickness-based estimations is obtained; e.g., the large thickness-based (spiciness-based) k in 70°E (110°E) seems weak by the counterpart method. The flow dependency of L_{mix} also likely varies by choice of tracer (Fig. 7). These subtle contrasts generally pertain to the local difference in the tracer gradient, as the large diffusivities likely result from the weak tracer gradient. We found that the thickness gradient better represents the variations of L_{mix} and k than the spiciness gradient (Fig. 12) attributable to the PV-conservative nature of isopycnal thickness. The thickness-based L_{mix} and k rationalize the calculation of thickness-diffusive transport, accounting for the residual overturning theory (Marshall and Radko, 2003).

Although the estimated diffusivity of 100–500 m^2 s^{-1} is significantly smaller than the along-slope estimation of 950 ± 400 m^2 s^{-1} presented by FRE19 (based on spiciness variability), their estimate implicitly assumed the mixing efficiency Γ to be unity (far exceeding its previous estimates; 0.01–0.4) and hence seems incompatible as an absolute diffusivity estimation. In case $\Gamma = 0.16$ by Wunsch (1999) is consistently applied for their values, the isopycnal diffusivity of 90–220 m^2 s^{-1} is obtained from their result, rather smaller k than our estimate. Further, our estimation is quite consistent with previous studies in the ACC's mainstream, typically ranging for 500–2000 m^2 s^{-1} (Marshall et al., 2006) and 1500–3000 m^2 s^{-1} (Sallée et al., 2011) with a poleward decrease.

To investigate the meridional overturning circulation across the ASC jets in zonally symmetric configuration, Stewart and Thompson (2016) conducted idealized numerical experiments. They demonstrated that L_{mix} scaled by the slope width accurately predicts the simulated onshore flux of CDW ($R^2 = 0.89$). However, we found that L_{mix} is significantly correlated with the thickness gradient but not with the topographic gradient (Fig. 12). This dissociation with the topographic slope scale may be interpreted because of thickness control by the surface layer, expected from shelf water export in the clockwise subgyres (Chapter 1). We assume that the thickness field itself is strongly connected to the zonally asymmetric structures of circulation and topography (see Section 4.5.4).

The inaccessible but most uncertain part of our estimate is the spatial variability of mixing efficiency. Visbeck et al. (1997) argumented that eddy transfer coefficient, which determines the proportionality of diffusivity to the horizontal/vertical stratification and the width of baroclinic zone, is a universal constant (equal to 0.015) regardless of flow regime. Mixing efficiency is different from this coefficient by its formulation, but they are possibly associated with each other. Validity of $\Gamma = 0.16$ is dependent on, let alone mooring data analyzed in Section 4.3.3, discussion by Klocker and Abernathey (2014) that $\Gamma = 0.15$ is suitable for the tracer-based mixing length calculation to be consistent with diffusivity by altimetric eddy scale. Examination for its universality is a future task and requires a utility of numerical models. Although the spatial variation of Γ can alter the correspondence between the enhanced diffusivity and the CDW intrusions (Fig. 10), the presented result leastwise suggests that mixing length is large where CDW intrudes shoreward. Furthermore, it is presumable that its spatial variation is negligible when considering a basin-wide transport as in the next section.

4.5.2 Coastal transport and heat budgets

The estimated onshore heat/volume flux (Fig. 14) is quantitatively consistent with the previously reported coastal budgets. As for integration within the eastern Indian sector (90–160°E), the annually-cumulative sea ice production is 520 ± 75 km^3 (Tamura et al., 2016; a sum of Shackleton, Vincennes, Dalton, Dibble, and Mertz Polynyas), being translated to heat loss of 4.2–5.6 TW. The integrated ice shelf basal melt rate is 198 ± 39 Gt yr^{-1} (Rignot et al., 2013; a sum of Mertz, Dibble, Holmes, Moscow Univ., Totten, Vincennes, Conger, Tracy, and Shackleton Ice Shelves), being translated to 1.7–2.5 TW. Therefore, the CDW heat flux of 3.2–3.9 TW (within the 28.0–28.1 kg m^{-3} neutral density) compensates for nearly half of the cryospheric heat sink and thus is a major source of heat for the Antarctic coasts. Missing source of heat (~3 TW) and offshore heat advection is likely balanced by solar heating (~5 TW within 100 km from the coastline of 90–160°E; Tamura et al., 2011) and the partial onshore intrusion of ASW (to the east of 130°E; Fig. 14).

As connectivity of the on-shelf current over the Antarctic coastline is likely weak in the Indian sector (Dawson et al., 2021), the volume imbalance between CDW and ASW implies the local exporting volume of Antarctic Bottom Water. In this sense, the partial intrusion of ASW to the east (Fig. 14) is likely consistent with the intensive bottom water formation in the Adelie/Mertz region (Williams et al., 2010), which might be ~0.3 Sv on the annual mean basis (from a numerical simulation by Kusahara et al., 2017). To the west of 130°E, the ASW export only balances with ~40% of the CDW influx, so that the remaining volume (~0.2 Sv) may be attributable to the bottom water export in Vincennes Bay (Kitade et al., 2014), Cape Darnley (Ohshima et al., 2013), and the rest of minor formation sites. The CDW volume compensation for the bottom water export can be numerically simulated over the circumpolar domain (Morrison et al., 2020). This study provides the first observational implication for the phenomenon with the quantitative estimation of the coastal heat/volume budgets.

Results by Stewart and Thompson (2016) indicate a possibility to underestimate the onshore heat flux derived from the mixing length formulation solely based on the thickness-diffusive CDW flux (likely corresponding to "eddy advection"), as the isopycnal "eddy stirring" can also contribute to the heat flux without transporting water volume, especially near the shelf break. The remarkable heat budget closure pertains to the situation that, compared to the eddy advection, the eddy stirring and tidal mixing are not dominant over the targeted slope (1000–3000 m; Fig. 14), as indicated by a realistic simulation (Stewart et al., 2018), and most of the heat flux explained by eddy advection over the isobaths subsequently reaches the Antarctic coast beyond the shelf break. On the other hand, the poleward CDW transport by the cross-slope geostrophic current (measured in seaward of the 3000 m isobath; Mizobata et al., 2020) might be confined to the lower continental slope, consistent with the numerical model (Stewart et al., 2018) and the weak shoreward advection of profiling floats (Chapter 1).

4.5.3 Diapycnal fluxes

The divergence of ψ is also calculated to evaluate the diapycnal flux in the Antarctic margin (Fig. 15, top panel). It can be decomposed into the thickness squeezing term and the symmetric diffusion term:

$$\nabla \cdot \psi = -\nabla k_H \cdot \nabla H - k_H \nabla^2 H \qquad (6),$$

and both are explicitly computable (Fig. 15; middle and bottom panels, respectively). Since ∇k_H likely reflects the spatial variation of k_H at the upper surface (28.00 kg m^{-3}) rather than a tranquil deeper layer, divergent (convergent) thickness squeezing $-\nabla k_H \cdot \nabla H$ can be interpreted as upward (downward) diapycnal flux through the upper surface (left panel of Fig. 15). Likewise, since ∇H likely reflects its variation at the lower surface (28.10 kg m^{-3}) rather than undulation of shallower isopycnals, divergent (convergent) symmetric diffusion $- k_H \nabla^2 H$ can be interpreted as downward (upward) diapycnal flux through the lower surface. These ideas are translated to the diapycnal velocity over the Subpolar Zone; the net convergence of 1.0 ± 11 μm s^{-1} for the CDW density (28.00–28.10 kg m^{-3}) is decomposed into upward diapycnal fluxes of 1.8 ± 16 μm s^{-1} (at the upper surface) and 2.8 ± 21 μm s^{-1} (at the lower surface). Even though the spatial variability is quite large, these averaged values are very comparable to Ekman upwelling of ~2 μm s^{-1} typical in the Antarctic margin (Liang et al., 2017). This agreement might further underpin the quantitativeness of our estimation.

The net upward diapycnal flux due to the symmetric diffusion term $- k_H \nabla^2 H$ may be a manifestation of the convex curvature of the lower isopycnal (Fig. 15, right panel). On the other hand, the net upward diapycnal flux by the thickness squeezing term $-\nabla k_H \cdot \nabla H$ can be interpreted due to the seaward gradient of k_H. It is attributable to the gradual inclination of upper isopycnal from the SB to the continental shelf, since k_H is highly correlated with the magnitude of thickness gradient (Fig. 12). This situation is checked by the fact that $-\nabla k_H \cdot \nabla H$ tends to be positive to the south of SB (Fig. 15, middle panel). These arguments imply that, even though the isopycnal gradient is well correlated with that of topography (Chapter 1), the spatial distribution of CDW thickness is not simply determined by the structure of topography but also by the interface between CDW and ASW, so their discordance encountered in Fig. 12 appears to be reasonable.

The divergence of isopycnal eddy advection indicates the net upward diapycnal fluxes through the upper and lower surfaces of the CDW layer (Fig. 15, right panel). The net diapycnal upwelling seems consistent with the kinematic analysis of the layer thickness, in which both thickness squeezing and symmetric diffusion terms are controlled by thickness Laplacian as the isopycnal diffusivity k is highly dependent on the inversed thickness gradient (Fig. 12). These diapycnal fluxes are likely significant for modifying CDW along the isopycnal pathway over the continental slope, controlling the property of modified CDW inshore. Furthermore, the local diapycnal upwelling can explain why isopycnal/temperature surfaces tend to be shallow where the CDW intrusion occurs (Chapter 1; see its Figs. 8 and 10). Its vertical position relative to the topography is critical to whether the CDW isopycnal is bridged to the continental shelf. On the other hand, offshore advection of ASW might also play a crucial role in the vertical adjustment of CDW, and thus the effect of diapycnal flux needs to be further evidenced. Even though a basin-scale upwelling is naturally expected from the divergent wind stress in the Subpolar Zone, the presented result is valuable as an observational estimate of the climatological diapycnal flux, possibly demonstrating its spatial variation associated with the circulation and topography.

4.5.4 Circulation and eddy fluxes

We found that L_{mix} and k are likely large where the onshore CDW intrusion is localized (Fig. 10), indicating that the onshore CDW intrusion is achieved by the cross-slope eddy advection. Upon this result, we can speculate how the CDW intrusion is established. First, the recirculating gyres steered by the barotropic PV and horizontal shear between the ACC and ASC determine the location of shoreward intrusion. Offshore CDW then approaches the continental slope advected by a quasi-barotropic flow branched from the ACC. Due to the ambient PV constraint, the mean flow cannot reach the upper slope (inshore of ~3000 m); instead, this encroachment steepens the gradient of CDW isopycnal. The steepened isopycnal locally causes baroclinic instability, and, subsequently, the generated eddies facilitate the onshore eddy advection.

The explanation in the previous paragraph should be rationalized along with two facts: (i) the magnitude of ψ (i.e., $\Gamma U_{eddy}\sigma(H)$) is independent of ∇H and (ii) L_{mix} and k are "inversely" proportional to ∇H by the equations (1) and (3). The latter suggests that the inversed thickness gradient is associated with isopycnal tracer fluctuations and U_{eddy} (in short, "ability to mix") rather than the geostrophic stability. This infers that a steep thickness gradient is associated with the strong mean flow and likely prevents cross-frontal eddy transport, as schematized in Fig. 16. On the other hand, the former infers that the spatial variation of eddy transport ψ reflects that of tracer fluctuations and U_{eddy} rather than the ∇H field. Since U_{eddy} likely has a minor effect on the spatial variation (accounting for Fig. 11), we may interpret the large shoreward eddy transport in the intrusion sites as manifesting a large $\sigma(H)$ and L_{mix}, as suggested by FRE19. The baroclinic eddy generation accompanied by the cross-slope CDW flux is expected to occur intermittently, with a gentle thickness gradient on average. In contrast, the sharp thickness gradient is likely associated with a baroclinically stable part of the ASC, hence unintrusive (Fig. 16). This situation may be noticed by comparing the CDW thickness and isotherm (Chapter 1, 2020; its Fig. 10), where thicker CDW and its smaller gradient can be observed in the intrusion sites. The situation illustrated in Fig. 16 implicates that the ASC behaves as a barrier to the onshore CDW intrusion. The dynamical driver governing the thickness field remains unknown, yet we posit that ASW's property, as well as topographic steering, plays an indispensable role.

4.6 Summary

To investigate the controlling factor of onshore CDW intrusion across the Antarctic continental slope, the present study conducted an extensive analysis of hydrographic measurements and the satellite altimetry data taking advantage of the mixing length formulation. The spiciness/thickness-based estimations yielded qualitatively similar results, supporting the fidelity of the mixing length estimates previously made using hydrographic variability. The same analysis is applied for ASW, and its mixing length close to CDW was obtained. Over the ACC domain (Antarctic and Southern Zones), a general agreement with the mixing suppression theory and its exception in the lee of the topography is found, as previously reported (GFP11). In contrast, no mixing length's dependency on mean flow is obtained in the Subpolar Zone, reflecting a stagnant flow regime in the Antarctic margin. Eddy diffusion is likely enhanced where the CDW intrusion is localized by the recirculating gyres, which are steered by the barotropic PV (i.e., topography). This correspondence is primarily attributable to the spatial variation of diffusivity controlled by the isopycnal thickness gradient, and the gentle thickness gradient allows for ease of isopycnal mixing. Volume transport is estimated in a GM-flux manner, and it is shown that thickness-diffusive onshore heat flux over the continental slope is quantitatively consistent with cryospheric heat sinks (sea ice formation and ice shelf basal melt), suggesting that the isopycnal eddy advection is the main factor of the onshore CDW intrusion. Upward diapycnal fluxes across the CDW isopycnals are indicated by kinematic analysis of eddy flux divergence, in which thickness squeezing and symmetric diffusion terms cause upward fluxes in the upper and lower surfaces, respectively. The estimated diapycnal flux is broadly consistent with upwelling predicted by cyclonic wind stress, further supporting our quantification. Predicated on these findings, the mechanism of eddy flux localization is speculated, and the controlling factors of the onshore CDW intrusion are illustrated in Fig. 16. Our findings may break new ground on the Southern Ocean dynamics, in which a connection between the meridional overturning circulation and the coastal buoyancy budget has been hypothesized (e.g., Snow et al., 2016; Morrison et al., 2020).

As a concluding remark, we underscore that the isopycnal thickness field is essential for determining the eddy fluxes in the Antarctic margin. The presented results facilitate a possibility to predict the eddy diffusivity by solely determining the layer thickness. This idea might be valuable for simulating CDW transport in global climate models, where subgrid effects of eddy fluxes need to be parameterized. Detailed reproduction of eddy flux is substantial for the multidecadal variability of onshore CDW flux (Chapter 2) and is inevitable for climate projection with higher credibility.

Figures and tables

Figure 1. Circulation and topography in the East Antarctic margin. The 3,000 m isobath is highlighted in white. Polar Front (PF; green), Northern/southern branches of Southern ACC Front (SACCF-N/S; yellow/magenta), and subpolar gyres (blue) are derived from dynamic ocean topography (Section 3.1), and Southern Boundary (SB; red) and Antarctic Slope Front (ASF; cyan) are reproduced from temperature field of a climatological dataset by Shimada et al. (2017). The SACCF-S corresponds to the southernmost eastward jet of ACC (~4,000 m isobath), whereas the SB is located along the center of subpolar recirculating gyres (4,000–3,000 m) about zero lines of zonal velocity.

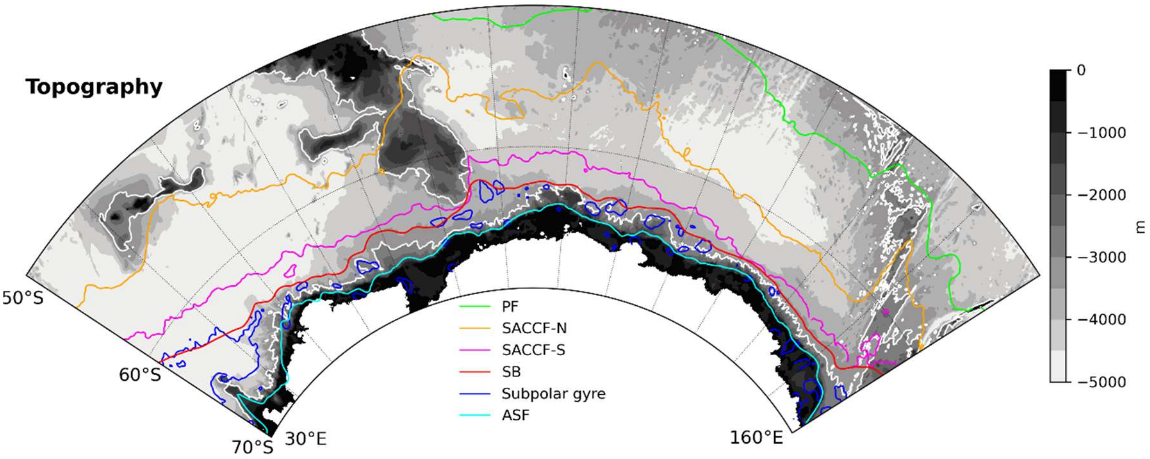

Figure 2. Altimetric velocities. Upper panel is the mean velocity by surface geostrophy, and lower panel is the eddy velocity as root-mean-squared speed. Frontal positions are drawn as in Fig. 1.

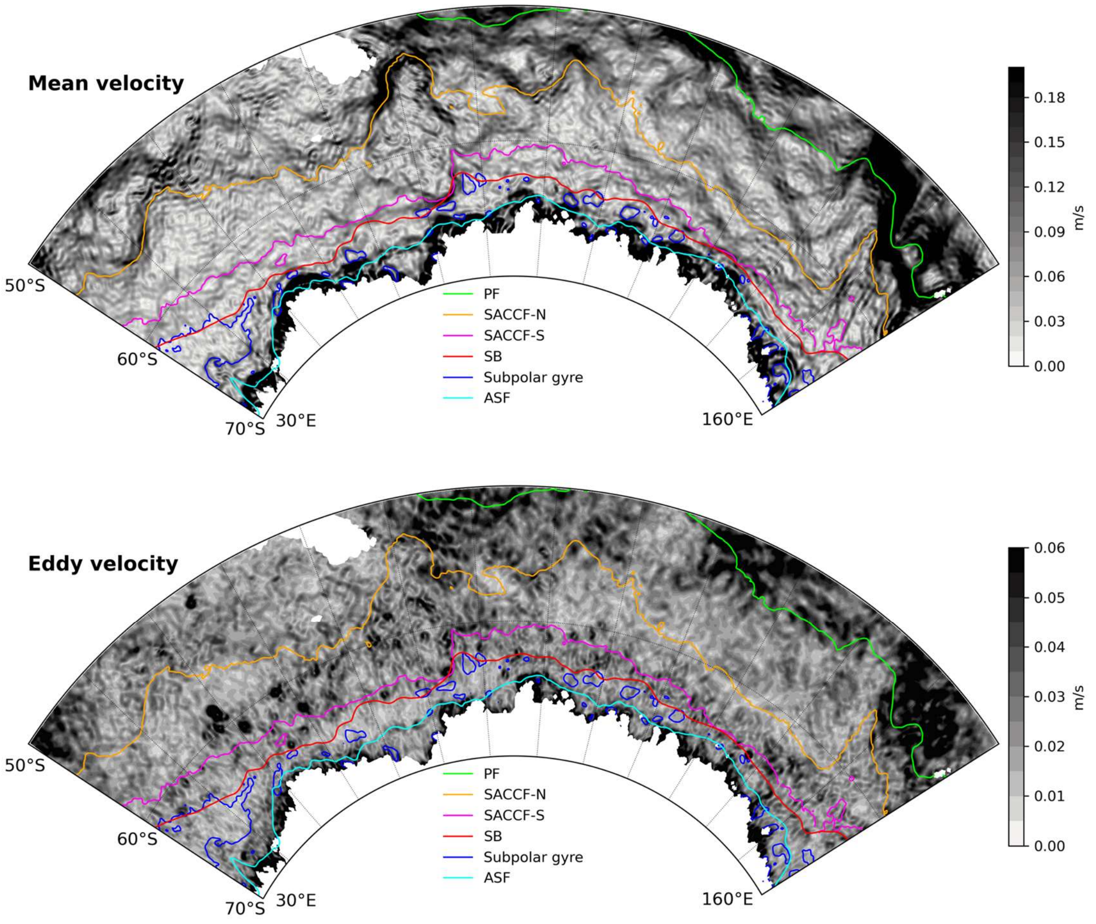

Figure 3. Hydrographic data description. Data density per 75 km data radius (top), Conservative Temperature (middle), and isopycnal pressure (bottom) are presented for ASW (left) and CDW (right). White contours in middle/bottom panels denote isopycnal spiciness/thickness (by 0.05 kg m^{-3}/100 m intervals), and thick contour is –0.15 kg m^{-3}/300 m, respectively. SB (red) and isobaths with 1,000 m intervals (black) are also shown.

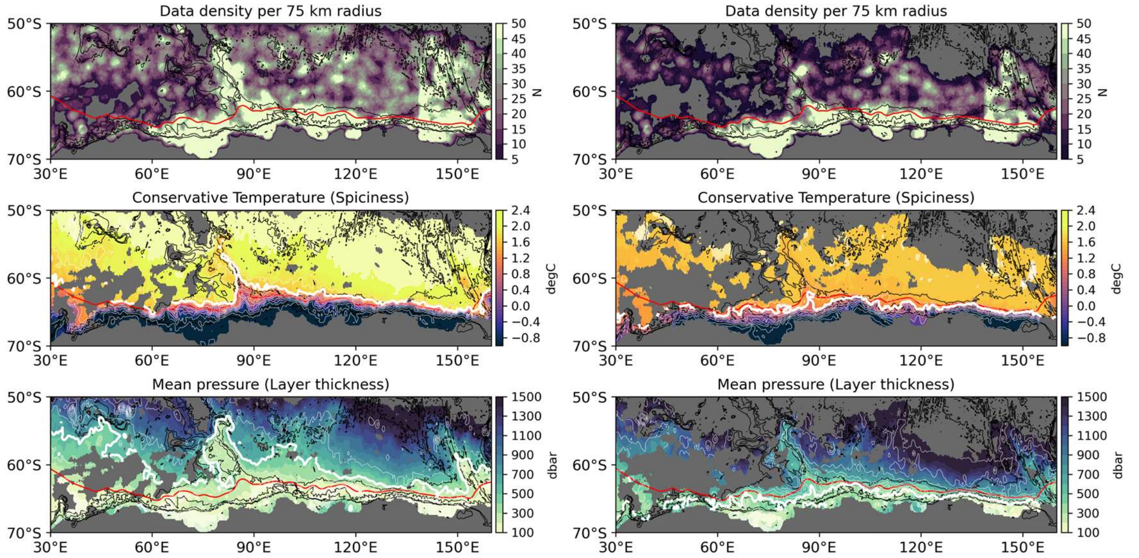

Figure 4. Histogram of the correlation coefficient between meridional velocity and temperature (or mixing efficiency) from the cross-slope mooring section in 113°E. “Down-gradient” denotes the correlation by southward velocity, and “up-gradient” means the correlation by northward velocity. Since the downgradient velocity must direct southward (shoreward), “up-gradient” possibly reflects transient events irrelevant to the climatological eddy condition. Hence, in addition to the whole mean (black line) and the previous estimate (dashed line; 0.16), the mean value only for the “down-gradient” is also presented (gray line).

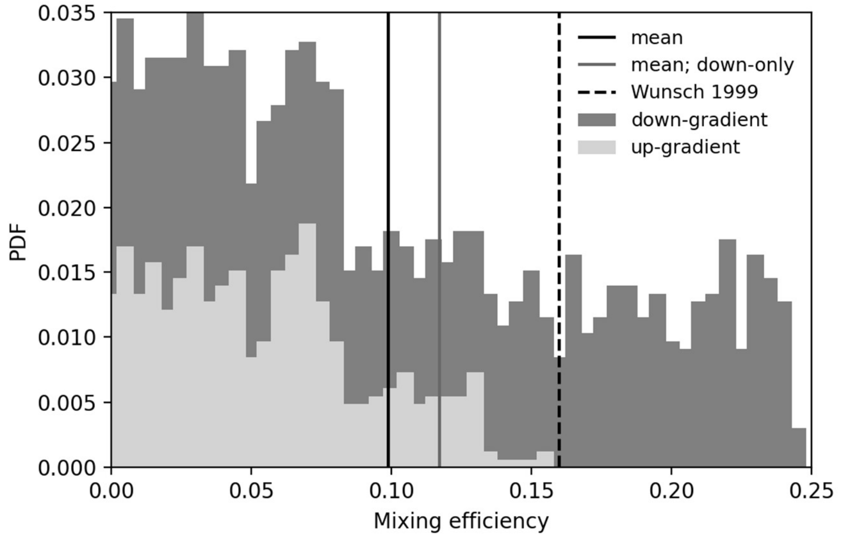

Figure 5. Mixing length calculation by isopycnal spiciness. Spiciness variability (top), normed spiciness gradient (middle), and mixing length (bottom) are presented for ASW (left) and CDW (right). White contours in top/middle panels denote isopycnal spiciness as in Figure 4.

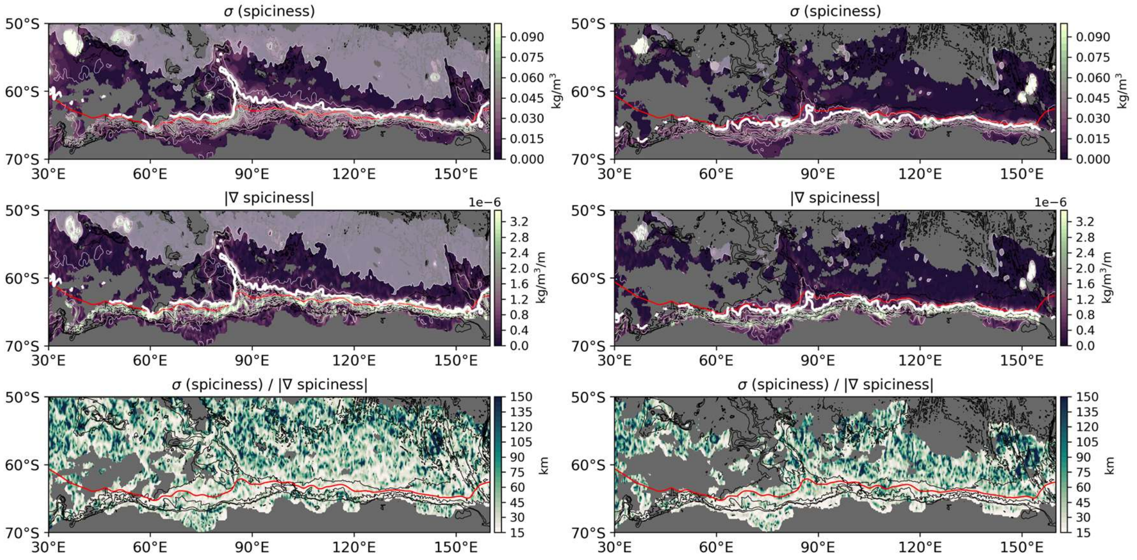

Figure 6. Mixing length calculation by isopycnal thickness. Thickness variability (top), normed thickness gradient (middle), and mixing length (bottom) are presented for ASW (left) and CDW (right). White contours in top/middle panels denote isopycnal thickness as in Figure 4.

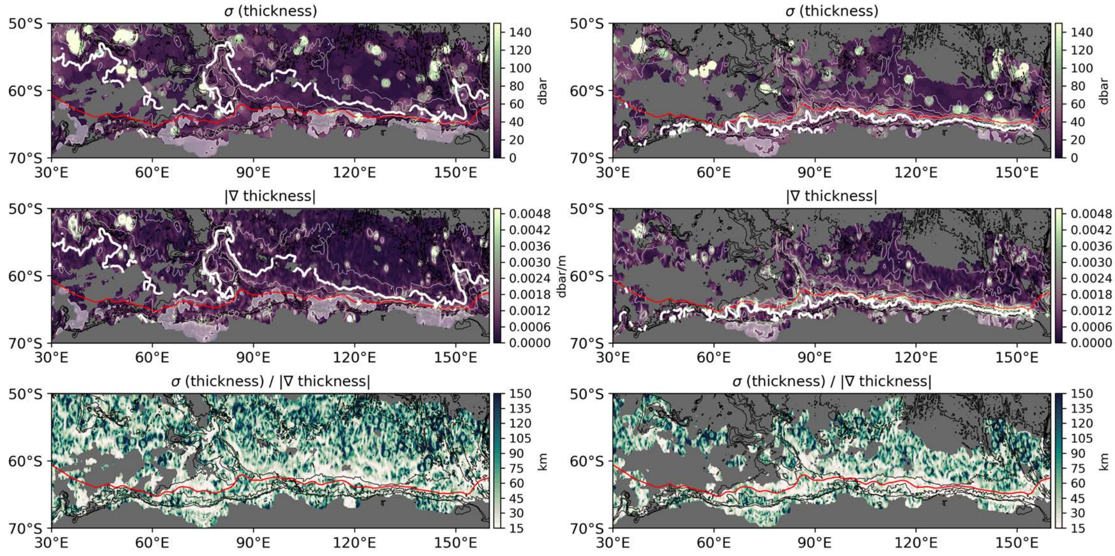

Figure 7. Mixing length dependency on mean flow. Upper and lower panels are based on spiciness and thickness, and left and right panels are for ASW and CDW, respectively. The results are separately shown for the three frontal zones: Subpolar (south of SACCF-S), Southern (from SACCF-S to SACCF-N), and Antarctic (from SACCF-N to PF) Zones. Standard errors due to the spatial variation are shaded.

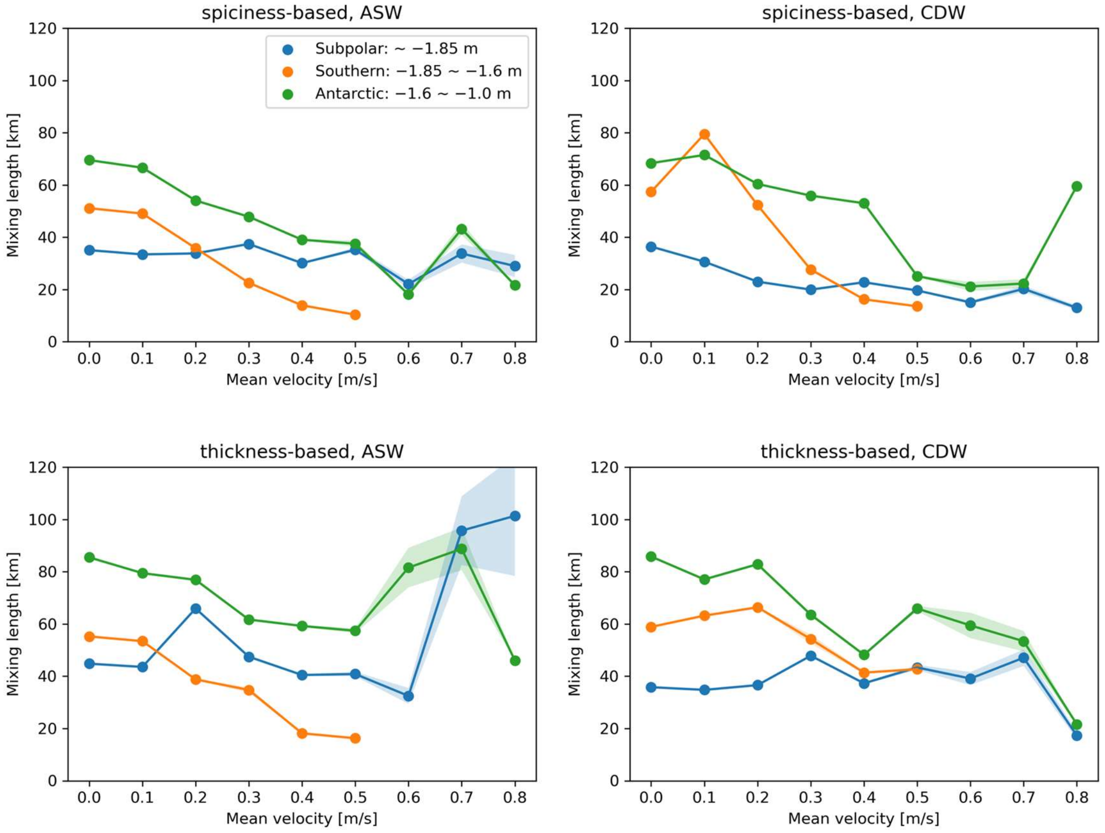

Figure 8. Two-dimensional histogram of mixing length coordinated by tracer variability (horizontal) and inversed tracer gradient (vertical), indicating relative dependency of mixing length on the two variables. Rows correspond to the methods (spiciness and thickness) and layers (ASW and CDW), whereas columns correspond to the three frontal zones. Color shade is normalized to unity, and yellower indicates a larger data population. The axes are also normalized to illustrate their functional dependency. White cross denotes the averaged value of tracer variability and inversed tracer gradient, and white contours are the mixing length of 20 and 100 km. The diagonal dotted line indicates where controls by the two variables become comparable.

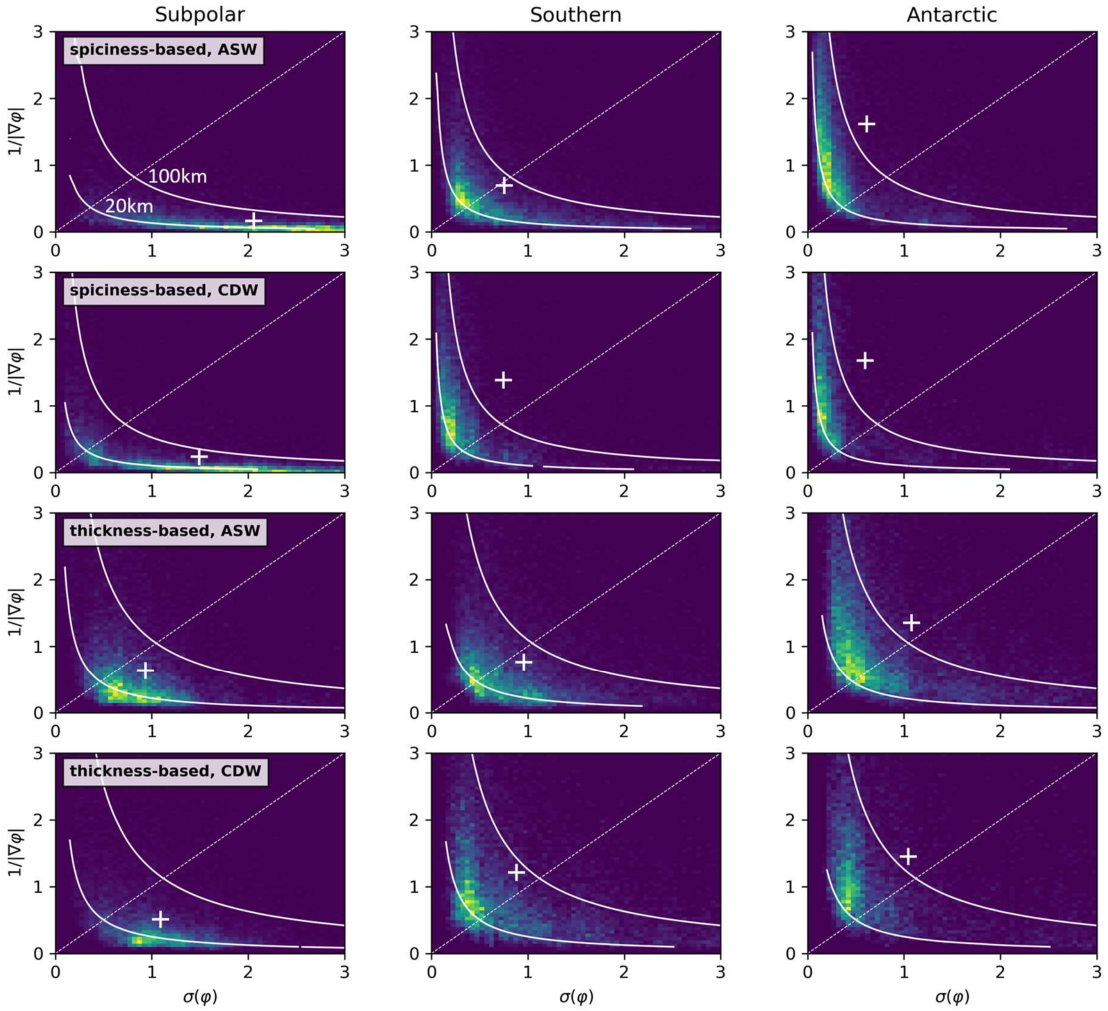

Figure 9. Spatial distribution of isopycnal diffusivity for CDW. Upper and lower panels are based on spiciness and thickness, respectively. In addition to SB and isobaths, dynamic topography is overlaid by 2 cm intervals (white contours). Characteristic contours are highlighted in blue (thick: subpolar gyre as –1.97 m, thin: SACCF-S as –1.85 m).

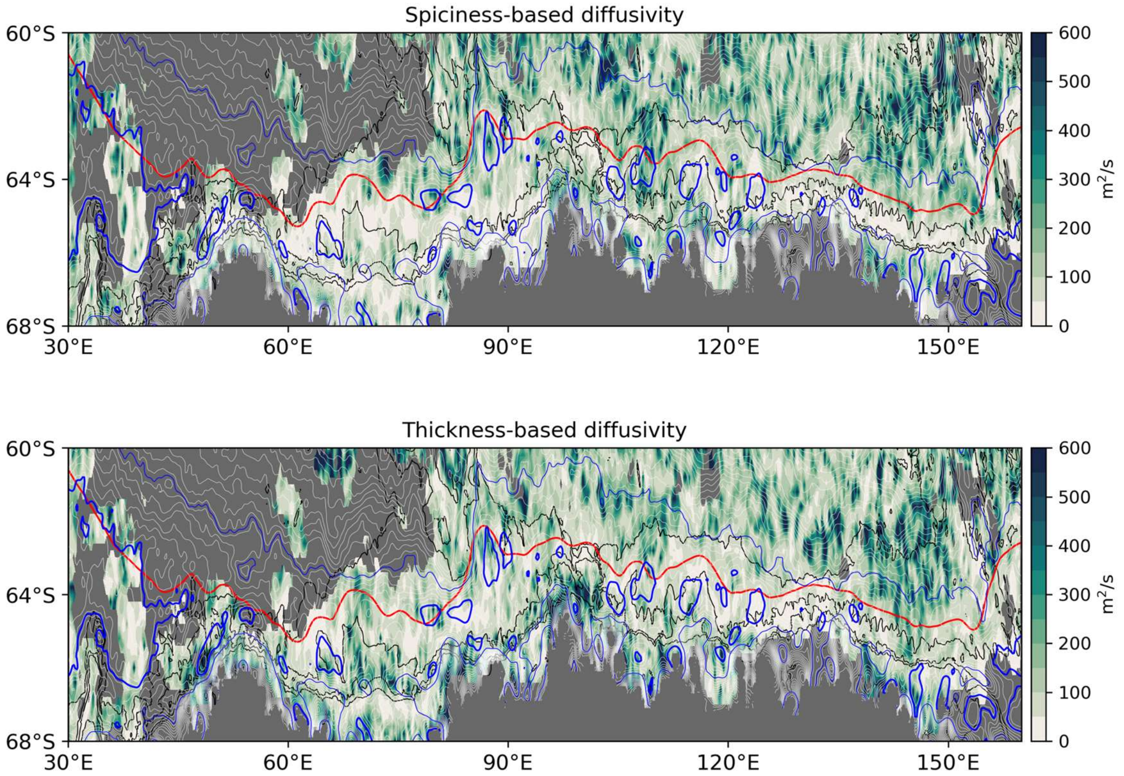

Figure 10. Eddy diffusion and CDW intrusion. Top: same as the lower panel of Fig. 9 (thickness-based diffusivity for CDW), magnified for three continental margins (Prydz Bay, Princess Elizabeth Trough, and off Wilkes Land). Middle: isopycnal CDW temperature (same as Fig. 3, right-middle panel). Vectors annotate where the CDW intrusion well corresponds to the large isopycnal diffusivity. Bottom: schematic of relationship between the eddy flux and CDW intrusion. Continental slope topography controls the barotropic PV field and thus the horizontal structure of subpolar recirculating gyre and intrusion sites.

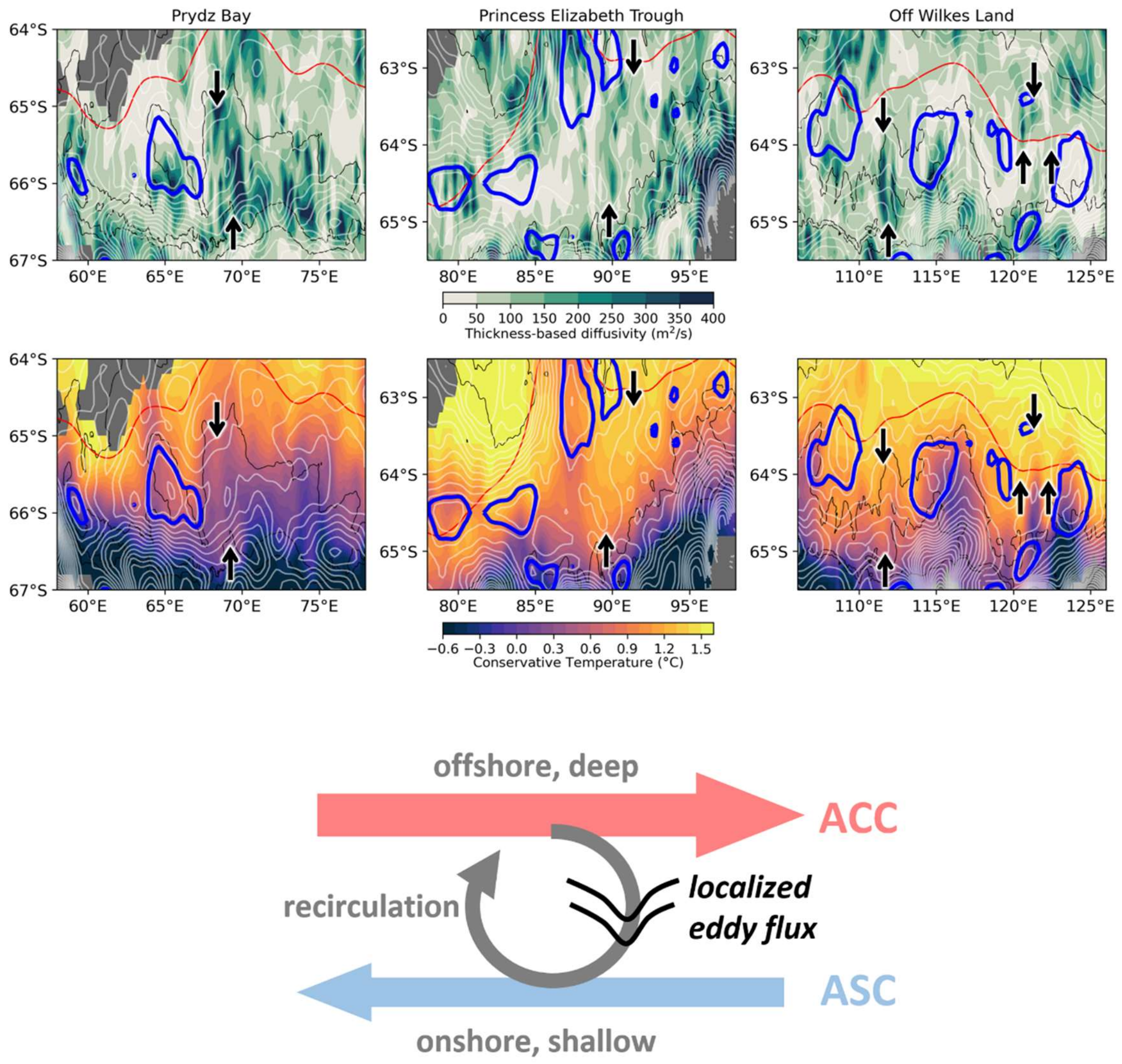

Figure 11. Histogram of isopycnal diffusivity on phase diagram coordinated with eddy velocity (horizontal) and mixing length (vertical), analogously to Fig. 8. White contours denote 100 and 500 $m^2 s^{-1}$.

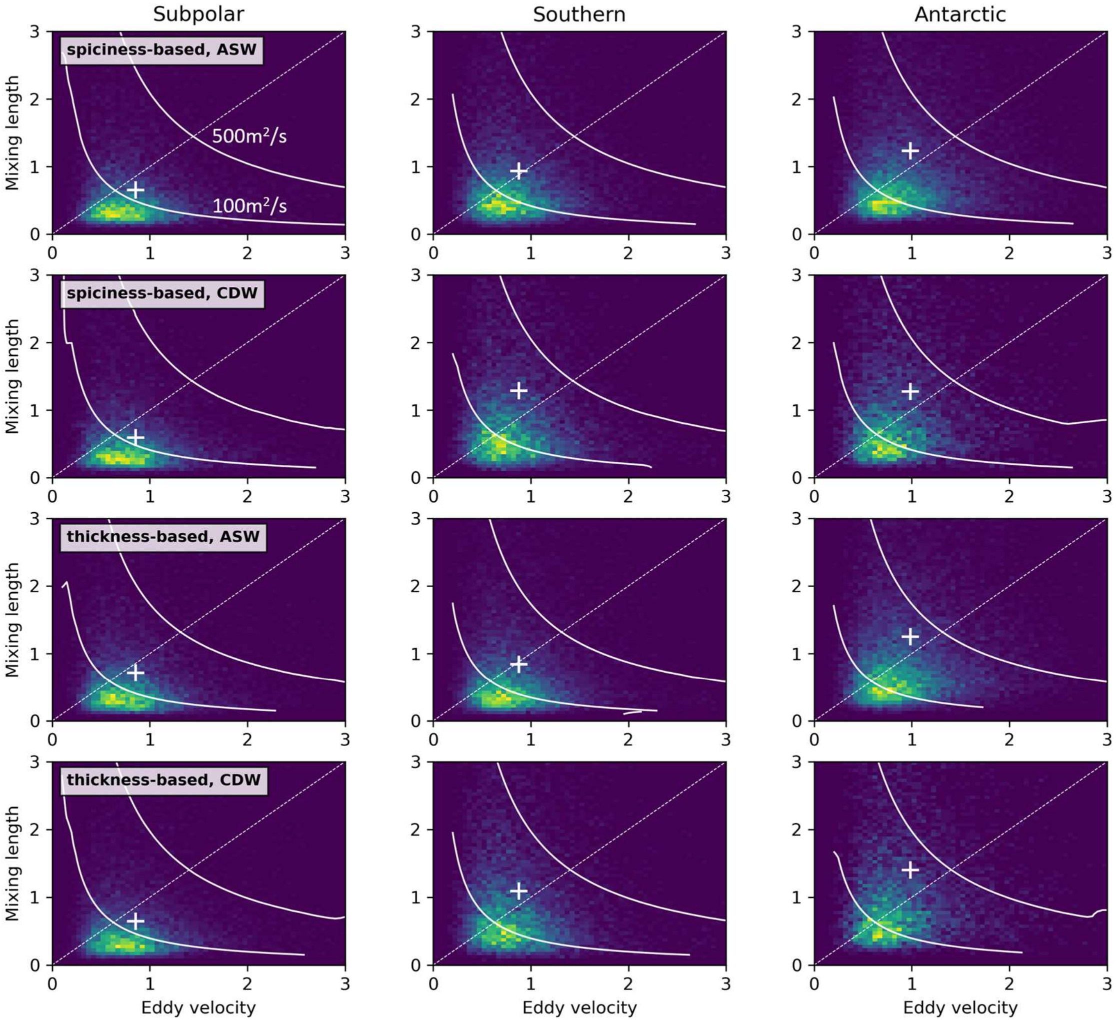

Figure 12. Tracer gradient control of CDW diffusion. Isopycnal diffusivity (top), mixing length (middle), and topographic gradient (bottom) over the 1000–3000 m isobath are regressed onto inversed tracer gradient as spiciness (left) and thickness (right). Scatters correspond to each grid point, colored by mean flow speed. Horizontal and vertical axes are normalized.

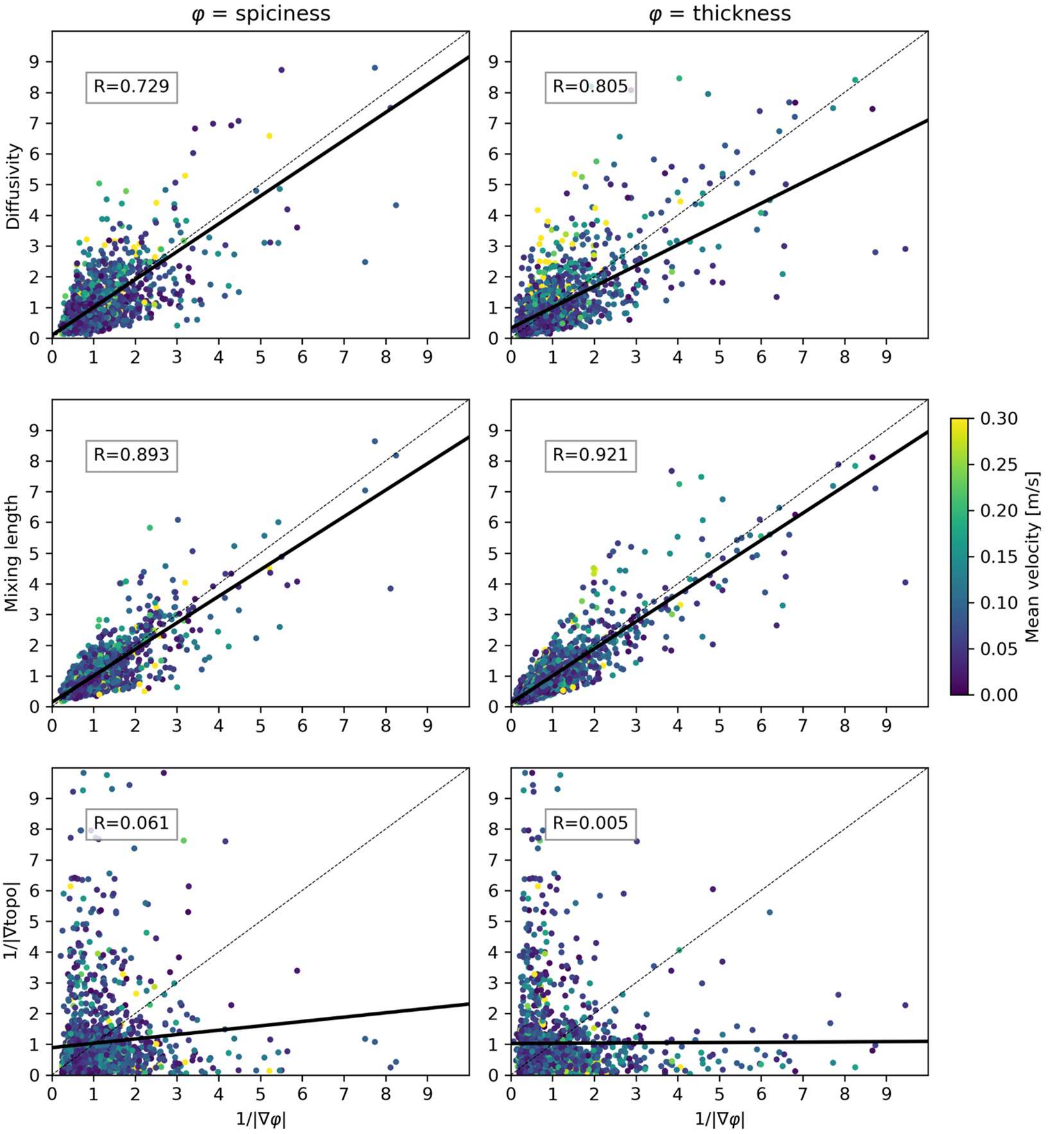

Figure 13. Eddy CDW fluxes. Top, middle, and bottom panels are transport vector (with its magnitude), zonal transport, and meridional transport, respectively. SB, isobaths, and dynamic topography are denoted as in Fig. 9. For illustrative purposes, colormap for the meridional transport is flipped.

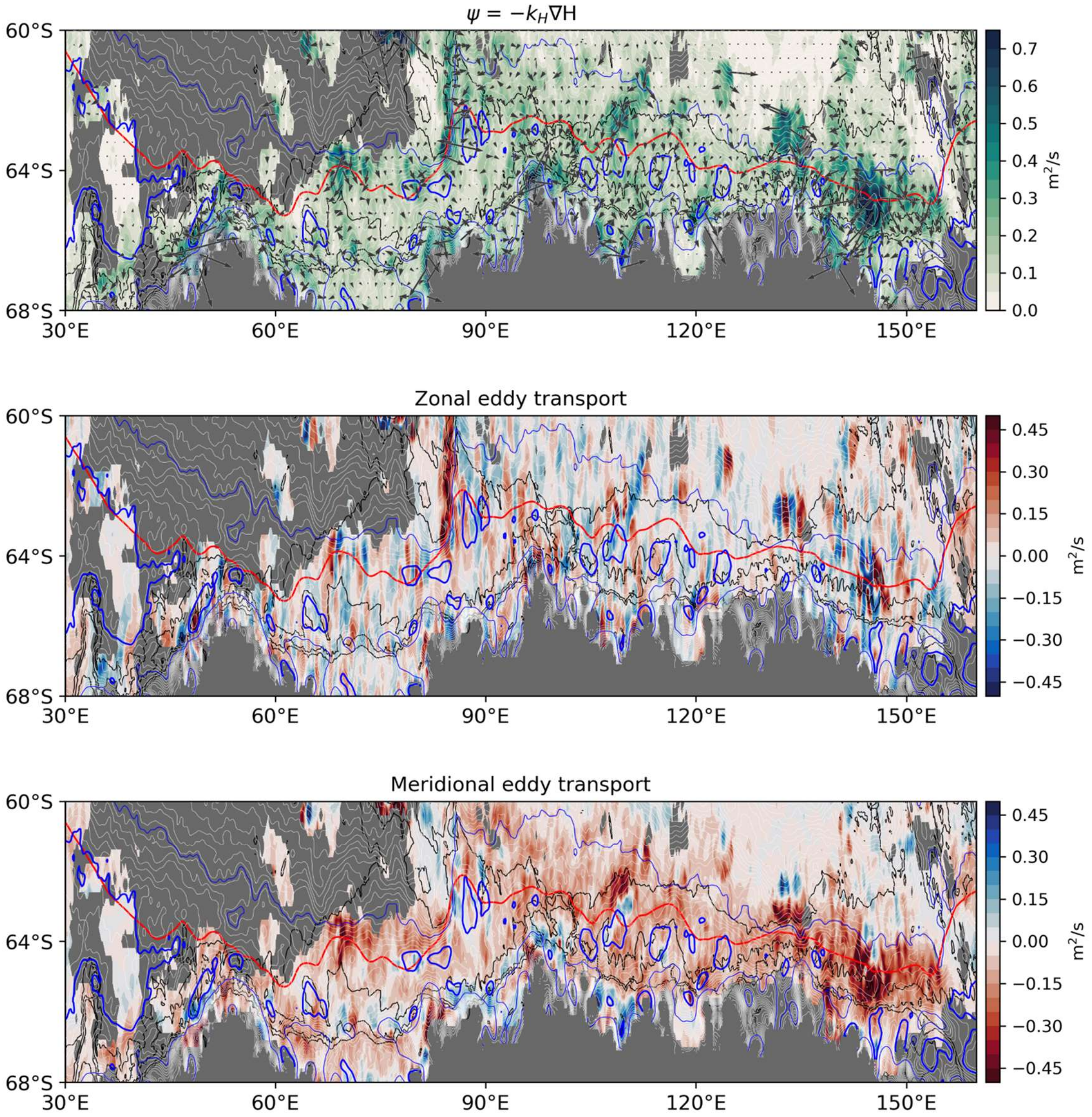

Figure 14. Cross-slope volume/heat transport. Meridional eddy transports for ASW and CDW (averaged within 1° bin in longitude over the continental slope; 1,000–3,000 m isobaths) are zonally integrated. Standard errors due to the cross-slope variation are shown by shade. Volume transport can precisely be translated to heat flux using the mean temperature of CDW and ASW as indicated by ticks to the left. The 90°E meridian for CDW corresponds to the interbasin boundary between eastern/western Indian sectors, while 130°E is transitional longitude for the ASW transport direction.

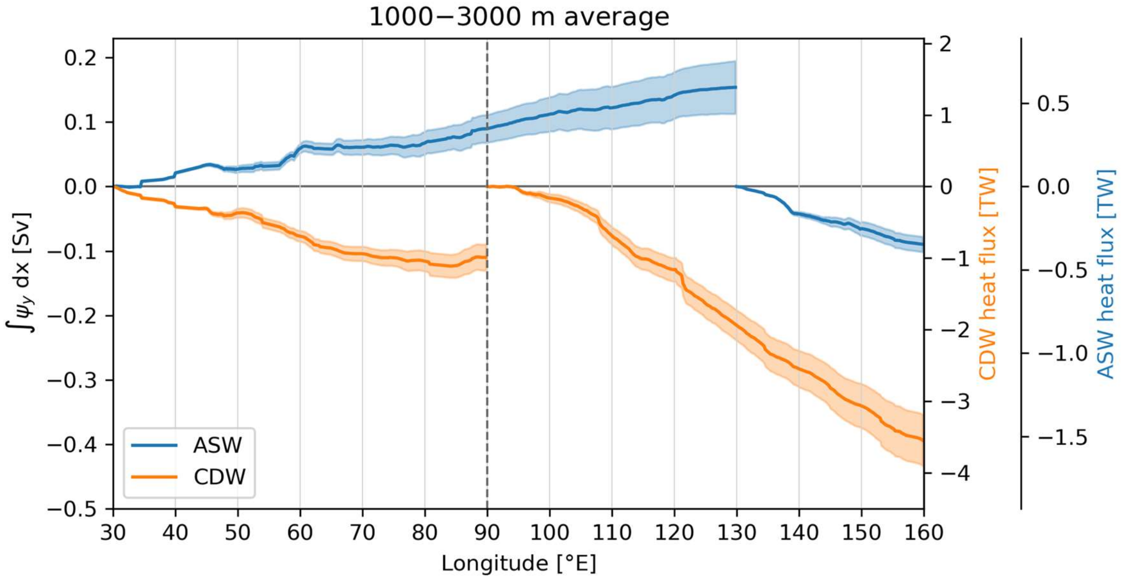

Figure 15. Diapycnal fluxes across CDW. Divergence of isopycnal eddy flux (top) was decomposed into thickness squeezing term (middle) and symmetric diffusion term (bottom). Based on kinematic analysis, the situation may be summarized as in the right panel, where the isopycnal thickness field primarily controls the eddy fluxes.

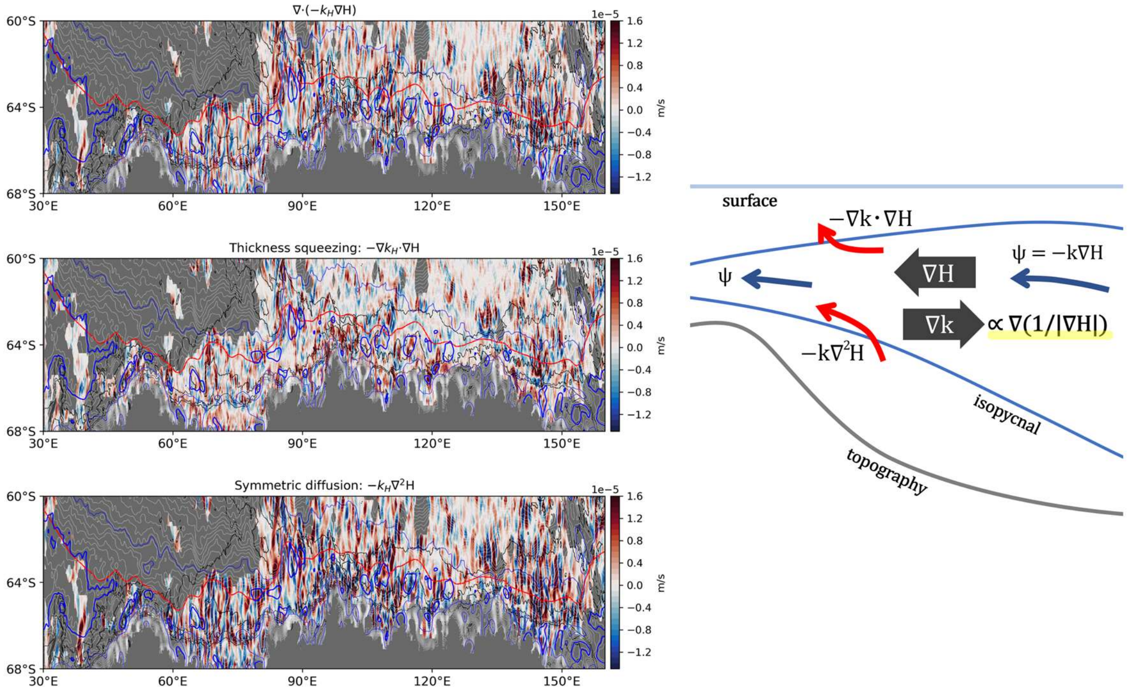

Figure 16. Diffusive CDW flux and isopycnal thickness. Enhanced eddy diffusivity and CDW intrusion are likely associated with small thickness gradient (right), whereas large thickness gradient is associated with suppressed diffusion and strong ASC, hence unintrusive (left).

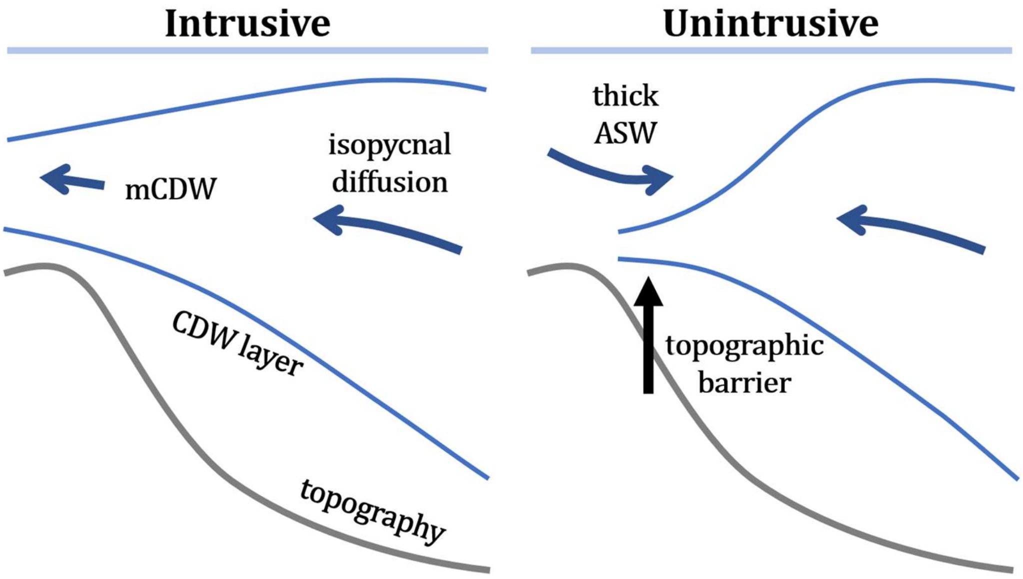

References and notes

Abernathey, R. P., Cerovecki, I., Holland, P. R., Newsom, E., Mazloff, M., and Talley, L. D. (2016). Water-mass transformation by sea ice in the upper branch of the Southern Ocean overturning. *Nature Geoscience*, *9*(8), 596–601.

Argo (2000). Argo float data and metadata from Global Data Assembly Centre (Argo GDAC). SEANOE. https://doi.org/10.17882/42182

Armi, L., and Stommel, H. (1983). Four Views of a Portion of the North Atlantic Subtropical Gyre. *Journal of Physical Oceanography*, *13*(5), 828–857.

Bates, M., Tulloch, R., Marshall, J., and Ferrari, R. (2014). Rationalizing the spatial distribution of mesoscale eddy diffusivity in terms of mixing length theory. *Journal of Physical Oceanography*, *44*(6), 1523–1540.

Beckmann, A., and Pereira, A. F. (2003). Lateral tidal mixing in the Antarctic marginal seas. *Ocean Dynamics*, *53*(1), 21–26.

Cessi, P. (2019). The global overturning circulation. *Annual Review of Marine Science*, *11*, 249–270.

Dawson, H., Morrison, A., Tamsitt, V., and England, M. (2021). Pathways and timescales of connectivity around the Antarctic continental shelf. In *EGU General Assembly 2021* (p. 14011).

Ferrari, R., and Nikurashin, M. (2010). Suppression of eddy diffusivity across jets in the Southern Ocean. *Journal of Physical Oceanography*, *40*(7), 1501–1519.

Foppert, A., Rintoul, S. R., and England, M. H. (2019). Along-Slope Variability of Cross-Slope Eddy Transport in East Antarctica. *Geophysical Research Letters*, *46*(14), 8224–8233.

Gent, P. R., and Mcwilliams, J. C. (1990). Isopycnal Mixing in Ocean Circulation Models. *Journal of Physical Oceanography*.

Hirano, D., Mizobata, K., Sasaki, H., Murase, H., Tamura, T., and Aoki, S. (2021). Poleward eddy-induced warm water transport across a shelf break off Totten Ice Shelf, East Antarctica. *Communications Earth and Environment*, *2*(1).

Hogg, A. M. C., and Blundell, J. R. (2006). Interdecadal variability of the Southern Ocean. *Journal of Physical Oceanography*, *36*(8), 1626–1645.

Holloway, G., and Kristmannsson, S. S. (1984). Stirring and transport of tracer fields by geostrophic turbulence. *Journal of Fluid Mechanics*, *141*, 27–50.

Jackett, D. R., and Mcdougall, T. J. (1997). A neutral density variable for the world's oceans. *Journal of Physical Oceanography*, *27*(2), 237–263.

Jenkins, A., Dutrieux, P., Jacobs, S., Steig, E. J., Gudmundsson, G. H., Smith, J., and Heywood, K. J. (2016). Decadal ocean forcing and Antarctic ice sheet response: Lessons from the Amundsen Sea. *Oceanography*, *29*(4), 106–117.

Karsten, R. H., and Marshall, J. (2002). Constructing the residual circulation of the ACC from observations. *Journal of Physical Oceanography*, *32*(12), 3315–3327.

Kitade, Y., Shimada, K., Tamura, T., Williams, G. D., Aoki, S., Fukamachi, Y., et al. (2014). Antarctic bottom water production from the Vincennes Bay Polynya, East Antarctica. *Geophysical Research Letters*, *41*(10), 3528–3534.

Klocker, A., and Abernathey, R. (2014). Global patterns of mesoscale eddy properties and diffusivities. *Journal of Physical Oceanography*, *44*(3), 1030–1046.

Kunze, E., Firing, E., Hummon, J. M., Chereskin, T. K., and Thurnherr, A. M. (2006). Global abyssal mixing inferred from lowered ADCP shear and CTD strain profiles. *Journal of Physical Oceanography*, *36*(8), 1553–1576.

Kusahara, K., Hasumi, H., Fraser, A. D., Aoki, S., Shimada, K., Williams, G. D., et al. (2017). Modeling ocean-cryosphere interactions off adélie and George V Land, East Antarctica. *Journal of Climate*, *30*(1), 163–188.

LaCasce, J. H., and Bower, A. (2000). Relative dispersion in the subsurface north atlantic. *Journal of Marine Research*, *58*(6), 863–894.

Liang, X., Spall, M., and Wunsch, C. (2017). Global Ocean Vertical Velocity From a Dynamically Consistent Ocean State Estimate. *Journal of Geophysical Research: Oceans*, *122*(10), 8208–8224.

Marshall, D. P., Ambaum, M. H. P., Maddison, J. R., Munday, D. R., and Novak, L. (2017). Eddy saturation and frictional control of the Antarctic Circumpolar Current. *Geophysical Research Letters*, *44*(1), 286–292.

Marshall, J., and Radko, T. (2003). Residual-mean solutions for the Antarctic Circumpolar Current and its associated overturning circulation. *Journal of Physical Oceanography*, *33*(11), 2341–2354.

Marshall, J., Shuckburgh, E., Jones, H., and Hill, C. (2006). Estimates and implications of surface eddy diffusivity in the Southern Ocean derived from tracer transport. *Journal of Physical Oceanography*, *36*(9), 1806–1821.

Mckee, D. C., Martinson, D. G., and Schofield, O. (2019). Origin and attenuation of mesoscale structure in Circumpolar Deep Water intrusions to an Antarctic shelf. *Journal of Physical Oceanography*, *49*(5), 1293–1318.

Meijers, A. J. S., Klocker, A., Bindoff, N. L., Williams, G. D., and Marsland, S. J. (2010). The circulation and water masses of the Antarctic shelf and continental slope between 30 and 80°E. *Deep-Sea Research Part II: Topical Studies in Oceanography*, *57*(9–10), 723–737.

Mizobata, K., Shimada, K., Aoki, S., and Kitade, Y. (2020). The Cyclonic Eddy Train in the Indian Ocean Sector of the Southern Ocean as Revealed by Satellite Radar Altimeters and In Situ Measurements. *Journal of Geophysical Research: Oceans*, *125*(6).

Morrison, A. K., McC. Hogg, A., England, M. H., and Spence, P. (2020). Warm Circumpolar Deep Water transport toward Antarctica driven by local dense water export in canyons. *Science Advances*, *6*(18), 1–10.

Naveira Garabato, A. C., Ferrari, R., and Polzin, K. L. (2011). Eddy stirring in the Southern Ocean. *Journal of Geophysical Research: Oceans*, *116*(9), 1–29.

Ohshima, K. I., Fukamachi, Y., Williams, G. D., Nihashi, S., Roquet, F., Kitade, Y., et al. (2013). Antarctic Bottom Water production by intense sea-ice formation in the Cape Darnley polynya. *Nature Geoscience*, *6*(3), 235–240.

Orsi, A. H., Whitworth, T., and Nowlin, W. D. (1995). On the meridional extent and fronts of the Antarctic Circumpolar Current. *Deep-Sea Research Part I*, *42*(5), 641–673.

Pauthenet, E., Sallée, J. B., Schmidtko, S., and Nerini, D. (2021). Seasonal variation of the antarctic slope front occurrence and position estimated from an interpolated hydrographic climatology. *Journal of Physical Oceanography*, *51*(5), 1539–1557.

Peña-Molino, B., McCartney, M. S., and Rintoul, S. R. (2016). Direct observations of the Antarctic Slope Current transport at 113°E. *Journal of Geophysical Research: Oceans*, *121*(10), 7390–7407.

Rignot, E., Jacobs, S., Mouginot, J., and Scheuchl, B. (2013). Ice-shelf melting around antarctica. *Science*, *341*(6143), 266–270.

Sallée, J. B., Speer, K., and Rintoul, S. R. (2011). Mean-flow and topographic control on surface eddy-mixing in the Southern Ocean. *Journal of Marine Research*, *69*(4–6), 753–777.

Shimada, K., Aoki, S., and Ohshima, K. I. (2017). Creation of a gridded dataset for the southern ocean with a topographic constraint scheme. *Journal of Atmospheric and Oceanic Technology*, *34*(3), 511–532.

Silvano, A., Rintoul, S. R., and Herraiz-Borreguero, L. (2016). Ocean-ice shelf interaction in East Antarctica. *Oceanography*, *29*(4), 130–143.

Snow, K., Hogg, A. M., Sloyan, B. M., and Downes, S. M. (2016). Sensitivity of Antarctic Bottom Water to changes in surface buoyancy fluxes. *Journal of Climate*, *29*(1), 313–330.

Speer, K., Rintoul, S. R., and Sloyan, B. (2000). The diabatic Deacon cell. *Journal of Physical Oceanography*, 30(12), 3212–3222.

Spence, P., Holmes, R. M., Hogg, A. M. C., Griffies, S. M., Stewart, K. D., and England, M. H. (2017). Localized rapid warming of West Antarctic subsurface waters by remote winds. *Nature Climate Change*, *7*(8), 595–603.

Stewart, A. L., Klocker, A., and Menemenlis, D. (2018). Circum-Antarctic Shoreward Heat Transport Derived From an Eddy- and Tide-Resolving Simulation. *Geophysical Research Letters*, *45*(2), 834–845.

Stewart, A. L., Klocker, A., and Menemenlis, D. (2019). Acceleration and overturning of the antarctic slope current by winds, eddies, and tides. *Journal of Physical Oceanography*, *49*(8), 2043–2074.

Stewart, A. L., and Thompson, A. F. (2013). Connecting antarctic cross-slope exchange with southern ocean overturning. *Journal of Physical Oceanography*, *43*(7), 1453–1471.

Stewart, A. L., and Thompson, A. F. (2016). Eddy generation and jet formation via dense water outflows across the Antarctic continental slope. *Journal of Physical Oceanography*, *46*(12),

Tamsitt, V., Drake, H. F., Morrison, A. K., Talley, L. D., Dufour, C. O., Gray, A. R., et al. (2017). Spiraling pathways of global deep waters to the surface of the Southern Ocean. *Nature Communications*, *8*(1), 172.

Tamura, T., Ohshima, K. I., Fraser, A. D., and Williams, G. D. (2016). Sea ice production variability in Antarctic coastal polynyas. *Journal of Geophysical Research: Oceans*, *121*(5), 2967–2979.

Tamura, T., Ohshima, K. I., Nihashi, S., and Hasumi, H. (2011). Estimation of surface heat/salt fluxes associated with sea ice growth/melt in the Southern Ocean. *Scientific Online Letters on the Atmosphere*, *7*(1), 17–20.

Taylor, G. I. (1922). Diffusion by Continuous Movements. *Proceedings of the London Mathematical Society*, *s2-20*(1), 196–212.

Thompson, A. F., Heywood, K. J., Schmidtko, S., and Stewart, A. L. (2014). Eddy transport as a key component of the Antarctic overturning circulation. *Nature Geoscience*, *7*(12), 879–884.

Thompson, A. F., Speer, K. G., and Schulze Chretien, L. M. (2020). Genesis of the Antarctic Slope Current in West Antarctica. *Geophysical Research Letters*, *47*(16).

Thompson, A. F., Stewart, A. L., Spence, P., and Heywood, K. J. (2018). The Antarctic Slope Current in a Changing Climate. *Reviews of Geophysics*, *56*(4), 741–770.

Treasure, A. M., Roquet, F., Ansorge, I. J., Bester, M. ., Boehme, L., Bornemann, H., et al. (2017). Marine Mammals Exploring the Oceans Pole to Pole. *Oceanography*, *30*(2), 132–138.

Vallis, G. K. (2017). *Atmospheric and Oceanic Fluid Dynamics*. Cambridge: Cambridge University Press.

Visbeck, M., Marshall, J., Haine, T., and Spall, M. (1997). Specification of Eddy Transfer Coefficients in Coarse-Resolution Ocean Circulation Models*. *Journal of Physical Oceanography*, *27*(3), 381–402.

Williams, G. D., Aoki, S., Jacobs, S. S., Rintoul, S. R., Tamura, T., and Bindoff, N. L. (2010). Antarctic bottom water from the adélie and George v Land Coast, East Antarctica (140-149°E). *Journal of Geophysical Research: Oceans*, *115*(4), C04027.

Wunsch, C. (1999). Where do ocean eddy heat fluxes matter? *Journal of Geophysical Research: Oceans*, *104*(C6), 13235–13249.

Yamazaki, K., Aoki, S., Katsumata, K., Hirano, D., and Nakayama, Y. (2021). Multidecadal poleward shift of the southern boundary of the Antarctic Circumpolar Current off East Antarctica. *Science Advances*, *7*(24), eabf8755.

Yamazaki, K., Aoki, S., Shimada, K., Kobayashi, T., and Kitade, Y. (2020). Structure of the Subpolar Gyre in the Australian-Antarctic Basin Derived From Argo Floats. *Journal of Geophysical Research: Oceans*, *125*(8).

Young-Hyang Park, and Gamberoni, L. (1995). Large-scale circulation and its variability in the south Indian Ocean from TOPEX/POSEIDON altimetry. *Journal of Geophysical Research*,

This section is adpoted from

Yamazaki, K., Mizobata, K., Aoki, S., Onshore diffusion of Circumpolar Deep Water, *in preparation* for submitting to *Journal of Geophysical Research: Oceans.*

(This page is intentionally set blank)

CONCLUDING REMARKS

Prior to the present studies, the pathway and mechanism of the poleward CDW transport off East Antarctica have been poorly specified. The deficiency of knowledge was associated with the deep ocean circulation over the Antarctic margin, which governs the fate of CDW transport. In Chapter 1, analyzing float data over the past decade, the traditional basin-wide picture of the subpolar gyre off East Antarctica (Bindoff et al., 2000; McCartney and Donohue, 2007) was updated to the circulation system consist of a series of subgyres regulated by the continental slope topography, that determine the location of CDW intrusion onto the Antarctic continental shelves.

As for the long-term trend of subpolar CDW, persistent warming at depths has been observed over the past half-century (Schmidtko et al., 2014; Aoki et al., 2005), whereas its cause was unconstrained, let alone the poleward influences of the regional shift of the ACC fronts in the Indian Ocean sector (Couldrey et al., 2013; Kim and Orsi, 2014; Katsumata et al., 2015). In Chapter 2, using hydrographic data, I found the subpolar CDW warming was associated with the poleward shift of the southern boundary of the ACC. Besides the frontal shift, it was first demonstrated that the Southern Ocean meridional overturning circulation is also critical to the multidecadal warming trend, highlighting the importance of the isopycnal eddy flux (Marshall and Speer, 2012). Warming due to the enhanced meridional overturning signifies the potential impact of ongoing/projected intensification of westerly, leading to more poleward CDW flux via isopycnal eddy diffusion reinforced by winds.

In Chapter 3, the hydrographic changes from 1996 to 2019 are delineated. In addition to the poleward SB shift, a decrease in the westward ASC transport concurrent with coastal freshening and onshore CDW intrusion is observed. This result supports the idea that the ASC acts as a barrier for the cross-slope transport (Thompson et al., 2018), and implicates that freshwater input due to glacial melting may weaken the ASC, allowing for more CDW access onto the shelves.

Across zonal streamlines of the ACC and the ASC, transient eddies achieve the poleward CDW transport. However, their connection from the ACC (Naveira Garabato et al., 2011) to the ASC (Foppert et al., 2019) and the eddy variability within the subpolar circulation system have been unexplored. In Chapter 4, taking advantage of the mixing length framework, the isopycnal eddy diffusivity over a wide range of the Antarctic margin is estimated from hydrographic variability and the newly-developed satellite laser altimetry. The thickness-based diffusivity for CDW yields its onshore volume flux, providing the first observational evidence for the closure of the coastal heat budget by the eddy CDW fluxes.

Outlining Chapters 1 to 4, concluding remarks on the poleward CDW transport follow:

1. The continental slope structure determines the shape of the subpolar gyre, the location of onshore CDW intrusion, and the variety of climatic responses to external forcing.
2. The adiabatic transport by the isopycnal eddy diffusion, which has been widely accepted for the ACC domain, plays a key role in the CDW flux over the Antarctic margin as well.
3. Temporal variability of the poleward CDW flux is regulated by the barotropic ACC front, the baroclinic overturning circulation, the recirculating gyres, and the inshore ASC.

These findings provide an observational basis for understanding the thermal conditioning for Antarctica, and thus fundamental for the global thermohaline circulation and the sea-level rise predictions. There remains a significant inter-model discrepancy in reproducing the subpolar Southern Ocean (Purich and England, 2021; Dias et al., 2021), primarily attributable to the uncertainty of CDW flux. For the next step, it would be essential to examine the consistency between observations and full-spec ocean simulations (e.g., Stewart et al., 2018).

To further extend our knowledge on the poleward CDW transport, particularly concerning the decadal-to-centennial climate prediction, we must prioritize addressing the following issues (ordered randomly):

- How the system responds to momentum flux by the intensified westerly?
- How the system responds to buoyancy flux by the meltwater discharge?
- External forcing vs. intrinsic variability.
- The effect of seasonal asymmetry in the climatic trends (winds etc.).
- Feedback mechanisms involved with global warming.

Additionally, in terms of ocean dynamics relevant to the poleward CDW transport:

- How baroclinity over the continental slope is shaped?
- Role of the ASC; barrier or blender?
- Role of tides in diffusion and current rectification.
- Multiscale interaction from circulations to eddies and tides.

Investigation for such issues is to be accompanied by further observations. Contrasting to the exploding data size of numerical simulations, the number of observations has never increased. This fact implies that simulations are getting more capable of fitting past observations. However, we should finally base our arguments on what we have observed indeed, and in-situ measurements are the last stand at this end. Efforts for Southern Ocean monitoring must be made in succession.

References

Aoki, S., Bindoff, N. L., & Church, J. A. (2005). Interdecadal water mass changes in the Southern Ocean between 30°E and 160°E. Geophysical Research Letters, 32(7), 1–5.

Bindoff, N. L., Rosenberg, M. A., & Warner, M. J. (2000). On the circulation and water masses over the Antarctic continental slope and rise between 80 and 150°E. Deep-Sea Research Part II: Topical Studies in Oceanography, 47(12–13), 2299–2326.

Couldrey, M. P., Jullion, L., Naveira Garabato, A. C., Rye, C., Herráiz-Borreguero, L., Brown, P. J., et al. (2013). Remotely induced warming of Antarctic Bottom Water in the eastern Weddell gyre. Geophysical Research Letters, 40(11), 2755–2760.

Dias, F. B., Domingues, C. M., Marsland, S. J., Rintoul, S. R., Uotila, P., Fiedler, R., et al. (2021). Subpolar Southern Ocean Response to Changes in the Surface Momentum, Heat, and Freshwater Fluxes under 2xCO2. Journal of Climate, 34(21), 8755–8775.

Foppert, A., Rintoul, S. R., & England, M. H. (2019). Along-Slope Variability of Cross-Slope Eddy Transport in East Antarctica. Geophysical Research Letters, 46(14), 8224–8233.

Katsumata, K., Nakano, H., & Kumamoto, Y. (2015). Dissolved oxygen change and freshening of Antarctic Bottom water along 62°S in the Australian-Antarctic Basin between 1995/1996 and 2012/2013. Deep-Sea Research Part II: Topical Studies in Oceanography, 114, 27–38.

Kim, Y. S., & Orsi, A. H. (2014). On the variability of antarctic circumpolar current fronts inferred from 1992-2011 altimetry. Journal of Physical Oceanography, 44(12), 3054–3071.

Marshall, J., & Speer, K. (2012). Closure of the meridional overturning circulation through Southern Ocean upwelling. Nature Geoscience, 5(3), 171–180.

McCartney, M. S., & Donohue, K. A. (2007). A deep cyclonic gyre in the Australian-Antarctic Basin. Progress in Oceanography, 75(4), 675–750.

Naveira Garabato, A. C., Ferrari, R., & Polzin, K. L. (2011). Eddy stirring in the Southern Ocean. Journal of Geophysical Research: Oceans, 116(9), 1–29.

Purich, A., & England, M. H. (2021). Historical and Future Projected Warming of Antarctic Shelf Bottom Water in CMIP6 Models. Geophysical Research Letters, 48(10), 1–15.

Schmidtko, S., Heywood, K. J., Thompson, A. F., & Aoki, S. (2014). Multidecadal warming of Antarctic waters. Science, 346(6214), 1227–1231.

Stewart, A. L., Klocker, A., & Menemenlis, D. (2018). Circum-Antarctic Shoreward Heat Transport Derived From an Eddy- and Tide-Resolving Simulation. Geophysical Research Letters, 45(2), 834–845.

Thompson, A. F., Stewart, A. L., Spence, P., & Heywood, K. J. (2018). The Antarctic Slope Current in a Changing Climate. Reviews of Geophysics, 56(4), 741–770.

ACKNOWLEDGEMENTS

Over the course of my Ph.D. life, I have been supported by many people in various ways.

I sincerely express gratitude to people in Institute of Low Temperature Science of HU, where I have belonged for the past five years. I was financially supported by ILTS as the research assistant. The following people have kindly supported me and/or spared me a long time for discussion (at the polar oceanography seminar etc.): for the professors, K. I. Ohshima, H. Mitsudera, N. Ebuchi, T. Toyota, M. Vigan, Y. Nakayama, D. Hirano, Y. Fukamachi, T. Nakamura, J. Nishioka, S. Aoki, and for the colleagues, H.W. Chou, M. Ito, P. Wongpan, Y. Nan, S. Hyogo, K. Kondo, S. Hata. Particularly, H. Mitsudera, H.W. Chou, T. Nakamura, and Y. Nan invited me a reading club on geophysical fluid dynamics, which critically helped me to reshape my understanding on ocean dynamics. I am especially grateful to the staffs who technically and mentally supported me: M. Wakatsuki, M. Kitagawa, K. Ono, and K. Kitagawa. The following people contributed to make my Ph.D. life enjoyable: H.W. Chou, M. Vigan, A. Kaminishizono, Y. Machimura, T. Takahashi, P. Wongpan, M. Ito, Y. Ohashi, Y. Koh, Y. Okouchi, S. Ota, S. Hyogo, S. Kishi, K. Narita, M. Ohshima, H. Sato, S. Gondo, H. Iida, M. Oda, and M. Hamaguchi.

During the Ph.D. course of Graduate School of Environmental Science of HU, professors who taught me a lot about oceanography and climate dynamics are A. Kubokawa, H. Mitsudera, K. I. Ohshima, S. Minobe, T. Toyota, R. Greve, F. Hasebe, M. Fujiwara, T. Horinouchi, J. Nishioka, K. Suzuki, Y. Tanimoto, N. Ebuchi, Y. Fukamachi, S. Aoki, G. Mizuta, and S. Sugiyama. Conversations with A. Kubokawa and T. Toyota, when I was a teaching assistant for their lectures on geophysical fluid dynamics, are especially impressive.

Researchers outside HU who taught me a lot about oceanography are K. Katsumata, T. Kobayashi, S. Kouketsu, S. Yasunaka (JAMSTEC), K. Shimada, K. Mizobata, Y. Kitade (Tokyo University of Marine Science and Technology), T. Tamura, D. Shimizu, S. Ushio, R. Makabe (National Institute of Polar Research), D. Hasegawa (Tohoku National Fisheries Research Institute), Y. Kawaguchi (Tokyo University), S.P. Xie, L. Talley (Scripps Institute of Oceanography), G.D. Williams (University of Tasmania), and A. Wåhlin (Göteborgs Universitet). T. Suga, K. Hanawa, S. Kizu, and S. Sugimoto, D. Ito, and R. Yamaguchi (Tohoku University) invited me to the world of oceanography when I was an undergraduate student. I deeply thank all coauthors and reviewers who sincerely advised me about paper writing.

I am also grateful to the R/V Kaiyo-maru (Japan Fishery Agency) captain and crew members for conducting the research cruise CCAMLR KY1804. Particularly, H. Murase, H. Sasaki, K. Abe, D. Nomura, M. Kiuchi, Y. Koh, H. Sato, H. Okamoto, S. Yamamoto, A. Yoshida, F. Schaafsma, E. Briggs, R. Driscoll, S. Driscoll, and other researchers, technicians, and participants assisted the physical oceanography observation.

My utmost gratitude is sent to supervisor S. Aoki in ILTS, who has been dedicated to guiding me for the five years. His posture to science has always been severe and sincere, from which I learned a lot about what a scientific researcher should be. Finally, I sincerely thank co-examiners A. Kubokawa, H. Mitsudera, K. I. Ohshima (in HU), and Y. Yoshikawa (in Kyoto University) for reading through the long lines and their valuable comments.

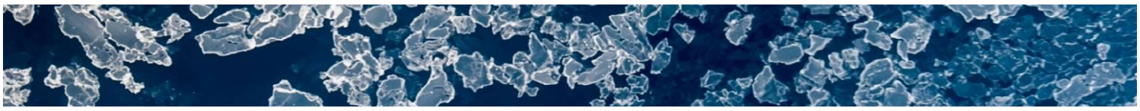

(This page is intentionally set blank)